BELGIAN SCIENTIFIC RESEARCH PROGRAMME
ON THE ANTARCTIC
SCIENTIFIC RESULTS OF PHASE TWO
(10/1988 - 05/1992)
VOLUME III

GLACIOLOGY
AND CLIMATOLOGY

EDITED BY S. CASCHETTO

**BELGIAN SCIENCE
POLICY OFFICE**

ANTARCTICA

BELGIAN SCIENTIFIC RESEARCH PROGRAMME ON THE ANTARCTIC

SCIENTIFIC RESULTS OF PHASE TWO (10/1988-05/1992)

VOLUME III

GLACIOLOGY - CLIMATOLOGY

EDITED BY S. CASCHETTO

LEGAL NOTICE

FOREWORD

In 1985, the Belgian government decided to launch a research programme to give tangible form to Belgium's desire to make an active contribution towards the international scientific effort on the Antarctic. This programme was designed as a coordinated thematic action targeting scientific problems identified by the Antarctic Treaty System as top-level priorities in pursuance of two objectives: protection of the Antarctic environment and ecosystems, and the role played by Antarctica and the Southern Ocean in global climate mechanisms. Particular attention was given to the complementarity of the different research projects, all covering a period of three years.

Development of the Belgian research effort continued between 1988 and 1992 during the Second Phase of the Programme, following the same general strategy and options. In particular, the same four fields of research were retained: (i) Plankton Ecology, (ii) Marine Biogeochemistry, (iii) Marine Geophysics and (iv) Glaciology-Climatology.

This volume sets out the results of the research projects carried out during the Second Phase of the Programme, on Glaciology-Climatology.

The results of the research conducted in the other fields within the Programme are the subject of two separate volumes (Volume I: Plankton Ecology and Marine Biogeochemistry and Volume II: Marine Geophysics).

At present, Belgium's involvement in scientific research on the Antarctic is covered by the Third Phase of the Programme, which commenced in the summer of 1992.

CONTENTS

ICE DYNAMICAL STUDIES IN THE SØR
RONDANE MOUNTAINS, DRONNING
MAUD LAND, EAST ANTARCTICA

F. Pattyn, H. Decleir and Ph. Huybrechts

SEA ICE AND CIRCULATION IN
THE WEDDELL SEA

B. Petit and C. Demuth

CONTENTS OF VOLUME I

PLANKTON ECOLOGY
AND MARINE BIOGEOCHEMISTRY

CONTENTS OF VOLUME II

MARINE GEOPHYSICS

CHEMICAL AND ISOTOPIC DISTRIBUTION IN ICE DUE TO WATER FREEZING IN ANTARCTICA

R. Souchez and J.-L. Tison

DÉPARTEMENT DES SCIENCES DE
LA TERRE ET DE L'ENVIRONNEMENT

Université Libre de Bruxelles
Av. F.D. Roosevelt, 50 CP 160/03
B-1050 Brussels, Belgium

Contents

Abstract

The isotopic and chemical properties of glacier ice in the Antarctic mostly reflect the climatic and environmental conditions under which snow was formed and transformed into ice. By constrast, ice due to water freezing has properties resulting from the action of completely different processes which characterize ice-ocean and ice-bedrock interfaces.

The two main factors which influence the isotopic and chemical signals in ice during a water/ice phase change are the freezing rate and the characteristics of the parent water.

When sea ice formation is governed by thermodynamical rather than dynamical processes, chemical and isotopic profiles fluctuating in opposite ways are the signatures of the dominant role played by a freezing rate effect. However, such situations are not always present. The isotopic and chemical characteristics of multi-year sea ice sampled in a rift of George VI Ice Shelf can only be understood if changes in parent water properties during the sea ice cover formation are taken into account. The dominating role of parent water effects over freezing rate effects result in sympathetic fluctuations between the two profiles : when ice is enriched in heavy isotopes, it is also enriched in salts and the reverse is equally true even at a small scale. In the case of the rift of George VI Ice Shelf, variable mixing of sea water with melt water from basal shelf ice plays the major role in explaining the distributions.

In some circumstances, liquid water is present only in small amounts such as at the base of the ice sheet. Basal ice was encountered in Terre Adelie in a core drilled through the ice sheet margin and in a ramp at proximity of the sea. An isotopic and chemical study of this ice reveals the presence of liquid water at crystal boundaries at subfreezing temperatures and the role of small scale freezing events which explain the main characteristics of basal ice. A new mechanism of basal ice formation is proposed.

Introduction

In the ice-covered Antarctic region, water freezing occurs in different environments.

In the periphery of the Antarctic ice sheets, surface melting can occur and, in this case, water percolates into the snow where it refreezes.

The basal zone of glaciers and ice sheets is sometimes at the pressure-melting point. In such a situation, water contributes significantly to the formation of basal ice and to the dynamics of these ice masses.

Sea water freezes either at the sea surface or within the water column and this ice is a major contributor to the floating ice cover around the Antarctic continent.

The study of the chemical and isotopic distribution in the ice formed under such circumstances can provide important information on the mechanisms involved.

Two different topics have been studied in such a context. A first chapter is concerned with the analysis of the chemical and isotopic distribution in an Antarctic multi-year sea ice cover in South George VI Ice Shelf area. The study of the formation of basal ice implying some liquid water at subfreezing temperatures in a site of Adelie Land is the objective of the second chapter.

I Stratigraphy, stable isotopes and salinity in multi-year sea ice from the Rift Area, South George VI Ice Shelf

1. Introduction.

Stratigraphy and salinity profiles in multi-year sea ice have been measured by several authors in the last decades, both in the Arctic (mainly the Northern Ellesmere Island area, Fram Strait and the Beaufort Sea - Schwarzacker, 1959; Cherepanov, 1966; Weeks and Ackley, 1986; Gow et al., 1987b; Meese, 1989) and the Antarctic (mainly in the McMurdo area and in the Weddell Sea - Weeks and Ackley, 1986; Gow et al., 1987a; Lange et al., 1989). However these studies were mainly focused on drifting pack ice, the properties and formation mechanisms of which are often quite different from landfast sea ice.

Combined salinity/stable isotopes analyses are less extensive in the litterature but have also been undertaken in both polar regions. One major advantage of the method is that it allows the discrimination of different parent water sources for the ice growth, as has been clearly demonstrated by previous authors (Friedman et al., 1961; Lyons et al., 1971; Gow and Epstein, 1972). Recently, the study of Jeffries et al. (1989) provides the first attempt to use the stable isotope ratio $^{18}O/$ ^{16}O as a tracer to detect fresh, brackish and sea water origins in multi-year landfast sea ice from the Canadian Arctic. Brackish ice was found there in significant amounts.

This chapter gives the results of a detailed textural, isotopic and chemical analysis performed on multi-year landfast sea ice located in large rifts affecting the southern part of the George VI Ice Shelf (Antarctic Peninsula). The properties of the ice samples are related to the melting processes at the surface and at the bottom of the ice shelf.

2. Sampling sites and analytical procedures.

Ten sea ice cores and two surface shelf ice cores were retrieved from the major rift closest to the southern active border of the George VI Ice Shelf as part of a joint Belgian/British project in the British Antarctic Survey 1987-1988 Antarctic field programme.

Two major sets of large surface waves affect the ice shelf surface where it thins in the south-western part and where the main outlet flow of the ice shelf from North-East meets the local southeasterly flow from the Plateau. One of these wave sets happens to be roughly parallel to the actively calving ice shelf edge and so the troughs are preferred sites for the opening of major rifts where sea water

reaches the surface. During the summer, open water areas are located where troughs from each wave system meet. The remaining bottom surface of the rift is covered with sea ice of variable thickness (1m to 5.5m). Away from the transverse depressions, the rift borders turn into sharp cliffs about 20m high. First-year sea ice started to cover the open water close to the sampling site at the end of February 1988.

Two different sets of sea ice cores were retrieved in the sampling area (fig. 1). One set was collected along a longitudinal profile South of the open water where the sea ice thicknesses varied from 0.97 m to 2.57 m (cores J to N) and the other set along a transverse profile a few kilometres to the North, where ice thicknesses fluctuated between 3.49 m and 5.54 m (cores F to I). In addition, one core was sampled in the multi-year sea ice from the transverse depression (B) and another in the freshly formed first-year sea ice (K). Finally, the surface shelf ice was sampled in two different locations (cores A and C). As the main focus was to study multi-year sea ice, the thickest core (H) has been selected for a first group of analyses.

The cores were sampled with a PICO drill, transferred into plastic bags and stored below -20°C in a small "sledge-fitting" freezer until transport by plane to Rothera Base. At Rothera and aboard RRS Bransfield on the journey to the U.K., the cores were again stored in freezers at -20°C. The following analytical techniques were performed in the cold laboratory (-25°C) in Brussels :

- Ice texture : Vertical thin-sections were taken along the whole profile to estimate the proportion of the different sea ice types and to guide the isotopic sampling.

- Sodium profile : for each individual part of the core the entire outside part of the cylindrical core sample was trimmed off with a band saw to avoid contamination which may have occurred during sampling in the field and during transport. A 1 cm-thick vertical slice has then been cut in samples of 0.5 cm width using standard methods to reduce contamination to the noise level of the VARIAN 300A atomic absorption spectrophotometer. A total of 1120 samples, regularly spaced in the core, have been measured for their Na content. The accuracy of the measurements is 5%. Sodium will be used here as a "proxy" of the global salinity, bearing in mind that the ratio Na/global salinity is 0.3074 in the oceans and independent of the salinity level for a large range of salinities (Riley and Skirrow, 1965) and that the same ratio is valid for sea ice as indicated by the dilution curves and statistical analyses performed by Meese (1989) on the sea-ice samples from the Beaufort Sea.

ANTAR
II/01

Legend:

- Multi-year sea ice
- ⊤⊤⊤⊤ Cliff
- ➘ Lead
- ⚑ Core location
- Open waters covered by first - year sea ice (February 1988)
- ⎯·⎯· Depression in the Ice Shelf
- ➘ p Small pressure ridge
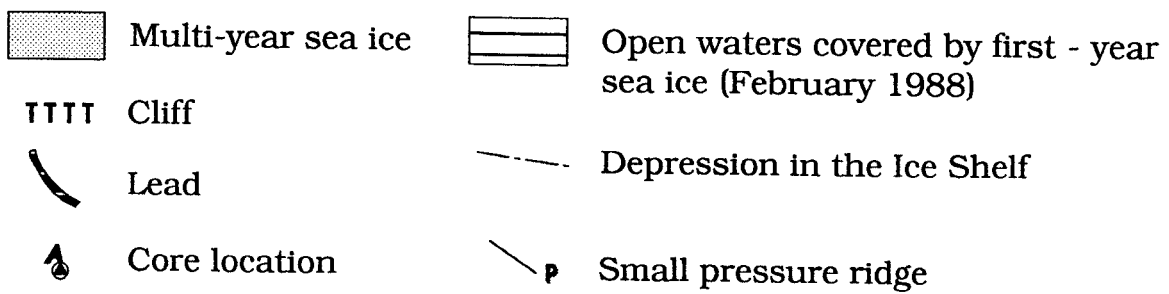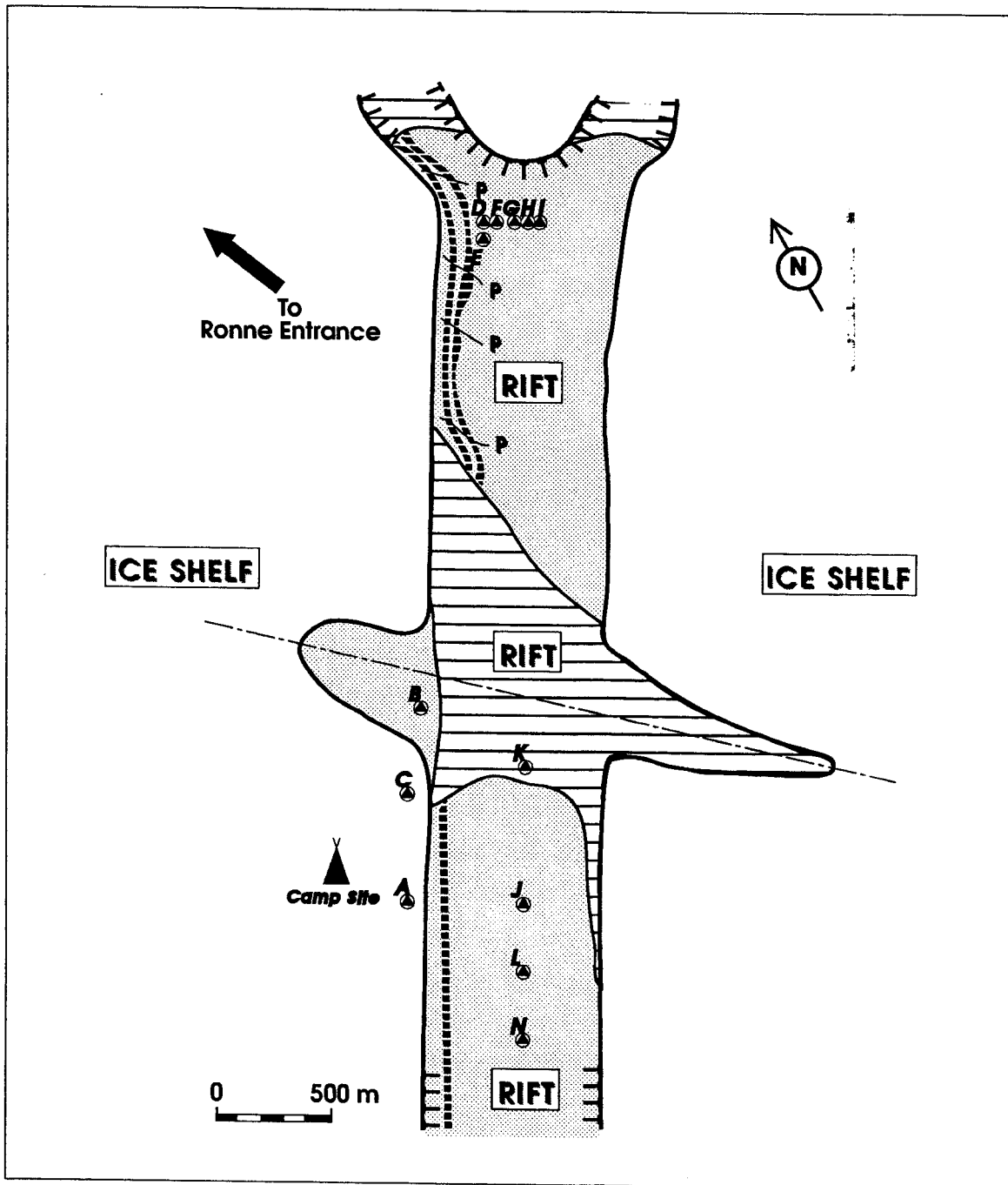
Figure 1. Sketch showing the location of the cores in the sampling area.

- <u>Isotopic profiles</u> : A second 1 cm-thick vertical slice of each individual part of the core was sampled in selected spots for co-isotopic analysis of deuterium and oxygen 18 (120 samples). The small amounts of ice necessary for the mass spectrometer measurements (0.3 ml) were collected using a microtome, allowing precise location of the samples and detailed profiling where required. The mass spectrometer analyses were performed at the Laboratoire de Géochimie Isotopique, Centre d'Etudes Nucléaires de Saclay, France. The accuracy is 0.5‰ for δD and 0.1‰ for δ^{18}O.

3. Results and discussion.

3.1. General features of the core H :

Figure 2 summarizes the textural, isotopic and chemical characteristics of the core. Na values have been smoothed with a running mean on 11 values to damp high frequency fluctuations and obtain a resolution similar to that of the δ^{18}O values. Two major observations can be made :

a. The core consists mainly of granular ice, which is essentially frazil ice, as will be discussed below. If we discard the 100 cm of porous granular ice at the top, which is certainly, as will be shown later, not the result of water freezing, granular ice occurs in 74% of the core, columnar ice in 19.4% and needle-like ice (platelet ice as described by Lange et al., 1989) in 6.6%.

b. The core presents a wide range of salinity and isotopic values. Na ranges from 0.00019‰ to 1.6‰ (e.g. a global salinity ranging from 0.00062‰ to 5.2‰), δD from -162.5‰ to 8.2‰ and δ^{18}O from -20.8‰ to 1.15‰. These ranges are comparable to those observed by Jeffries et al. (1989-Table II) for salinity and δ^{18}O, in landfast multi-year sea ice from the Canadian Arctic, although the variability within each individual core tends to be less important in their study.

3.2. Growth processes of the multi-year sea ice cover :

3.2.1. Dominance of parent water effects

A careful examination of figure 2 reveals a fair positive correlation between the salinity and isotopic profiles which is expressed by a regression coefficient of 0.78 in the δ^{18}O/Na diagram of figure 3a. This value is probably a low estimation of the strength of the correlation for two main reasons : (1) the diagram includes the samples from the top 130 centimeters of the core that forms a special unit where the salinities are negligible and result from different genetic processes

Figure 2. Textural, isotopic and chemical characteristics of core H.

and, (2) the dispersion of the salinities for the samples displaying high isotopic values is probably due to the combined effect of a slight shift between isotopic and chemical values related to the sampling techniques, and of a higher sensitivity of the salinity signal to the inclusions of sea water brines between frazil ice grains, as will be discussed later.

The behaviour of $\delta^{18}O$ and δD is very similar, as shown by the excellent linear regression of Figure 4a.

The two main factors which can influence the isotopic and chemical signals during a water/ice phase change in an open semi-infinite reservoir (e.g. the formation of sea ice) are :
(i) the characteristics of the parent water (eventually a "meteoric ice-sea water" mixture confined to the surface layer, in this case)
(ii) the rate of freezing.

Two major sources must be considered for the fresh water input to sea water at the sampling site : either melting of desalinated sea ice formed at a previous stage (low salinity, high δ values) or melting of snow and shelf ice (low salinity, low δ values).

In the first case, progressive dilution of sea water will produce a parent water showing decreased salinities and slightly increased δ values, since sea ice is enriched in heavy isotopes with regard to sea water, and since no fractionation occurs during melting (Friedman et al., 1964; Moser and Stichler, 1980). During growth of new sea ice from this diluted parent water, a reduction in the growth rate will further enhance salt rejection from the ice and heavy isotopes incorporation into the ice. Salinity and isotopic profiles fluctuating opposite ways will thus be the signature of such a process. A decreasing freezing rate during growth of sea ice from undiluted sea water will give similar results, but the salinity drop will be less important.

In the second case, the parent water will show decreasing salinities and decreasing δ values with increasing dilution. The freezing rate effect will, in this case, enhance the salt rejection from the new sea ice and impede the δ values decrease of maximum 3‰ in $\delta^{18}O$ and 20.8‰ in δD (maximum possible positive shift at very low freezing rates). Thus, for dilution events higher than 10% (and this is the worst case), this process will result in salinity and isotopic profiles in sea ice fluctuating in the same way. The large scale strong positive correlation between the two curves in our core thus suggests that there were major fluctuations in the composition of the parent water during the sea ice growth, and that this parent water results from dilution of sea water by melting from either
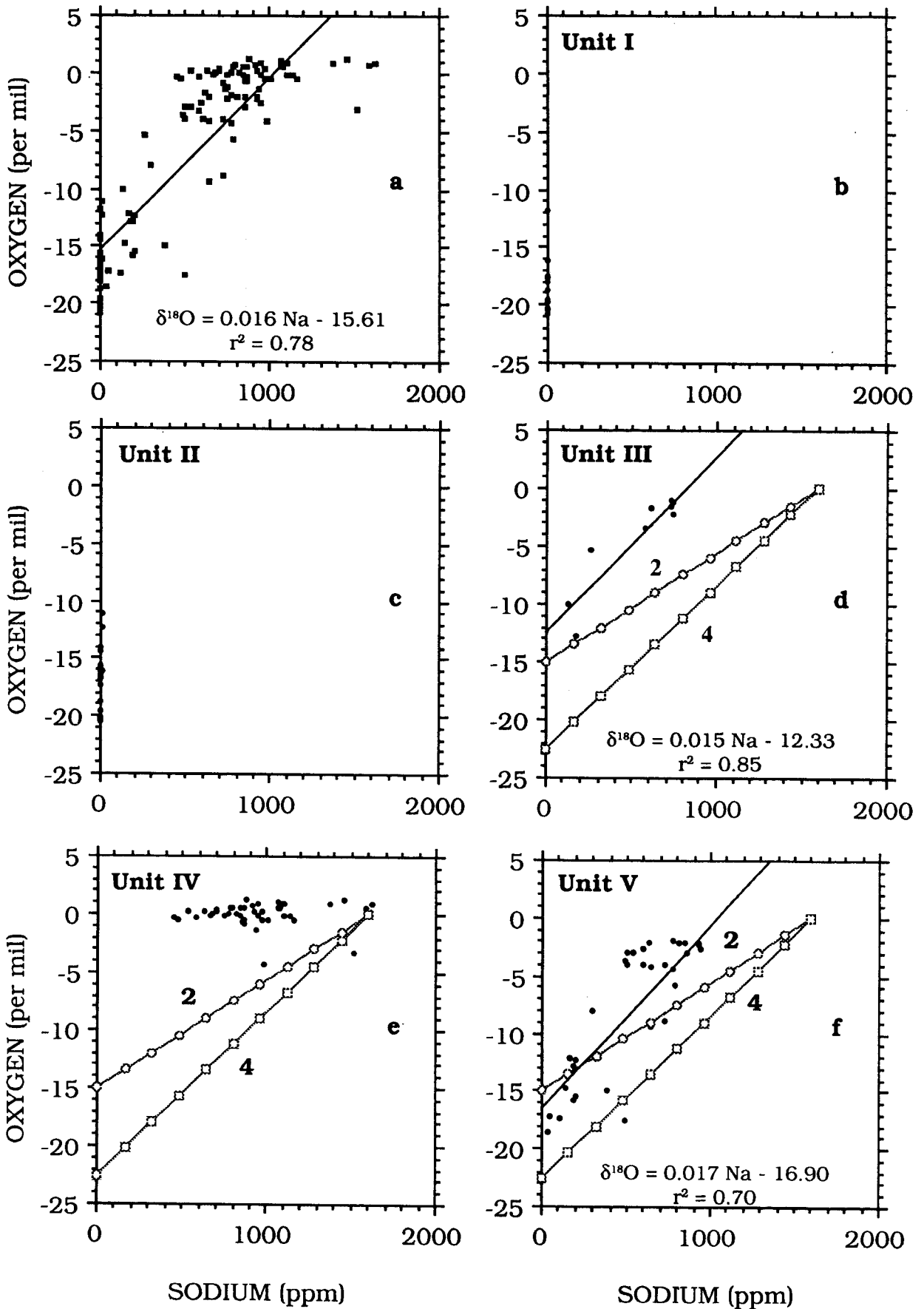
Figure 3. $\delta^{18}O$/Na diagrams for the samples from core H. The dotted line shows the linear regression and lines 2 and 4 correspond to those defined in figure 6

snow or surface/basal shelf ice.

The dominance of parent water effects over freezing rate effects can be pointed out from examination of the $\delta D/\delta^{18}O$ diagram in figure 4a, where all the samples lie on a line with a slope of 7.6 (correlation coefficient of 0.999) and δ ranges of 170‰ in deuterium and 23‰ in oxygen 18. If we plot, on such a diagram, all the possible samples resulting from mixing of pure sea water (V.S.M.O.W.) with glacial or snow melt waters from the local environment, the points will lie on a straight line, the slope of which will be slightly lower than the value of 8.0 characteristic of the Meteoric Water Line (MWL). Using the seasonal range of co-isotopic values of the snowfalls in the Rift area, typical slopes between 7.5 and 7.9 would be expected. If freezing rate effects are dominant the samples could also lie on a straight line, provided that the parent water remained unchanged while the freezing rate changed significantly. The "freezing slope" would correspond to the differential fractionation during the water/ice phase changes (Jouzel and Souchez, 1982; Souchez and Jouzel, 1984). However, a much shorter range in the isotopic composition of the ice would be obtained in this case. Thus, the slope of 7.6 and the high δ ranges observed in figure 4a, must mainly reflect the presence of a parent water with an isotopic composition evolving through time because of mixing between normal sea water and fresh melt waters.

The marked parallelism between the salinity and isotopic curves is also an indication that flushing out of the brine by downward percolation of surface melt waters has been very limited, because of the absence of summer melt at the top surface. In addition, the limited amount of columnar ice which, when present, is small-grained and lacks a brine layer/ice plate substructure, must strongly inhibit any brine drainage process. Small scale negative correlations between Na and δD were observed in congelation ice layers from the first half of the core, possibly indicating fluctuations in the freezing rate.

3.2.2. Origin of the different units

Five different units can be distinguished in the core, each corresponding to a distinct process of formation. The proposed limits between the different units are marked in figure 2 by vertical straight lines associated with the position of a sample. To ease the comparison with data previously mentioned in the literature, we choose to use $\delta^{18}O$ values in the discussion when only one isotope is considered.

Unit I (0 to 98 cm - figs. 3b and 4b) resembles the surface layers of the ice shelf. It is a low-density porous medium characterized by small polygonal crystals with
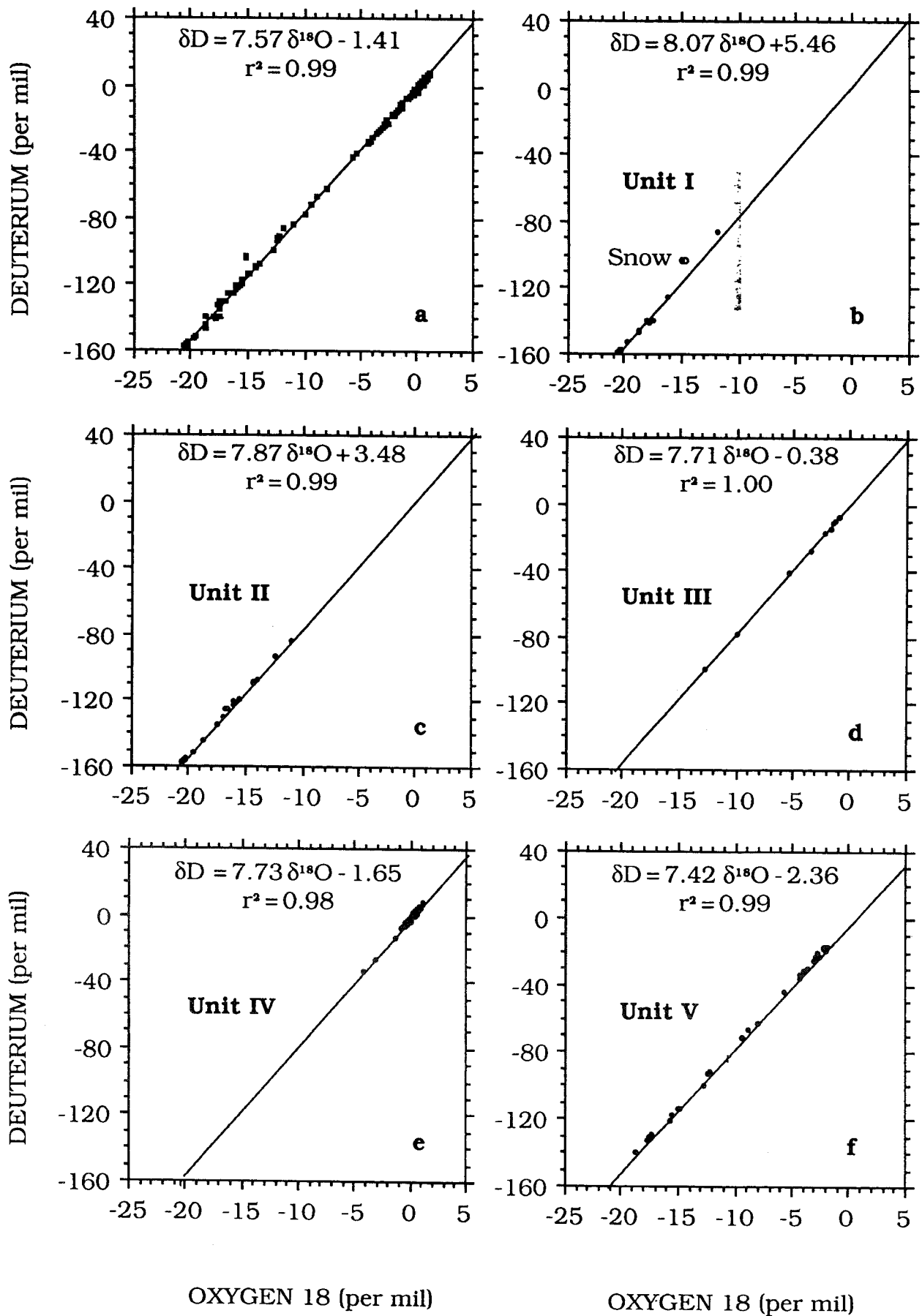
Figure 4.   δD/δ¹⁸O diagrams for the samples from core H.

many voids between them and it shows two localized layers of recrystallization (type 1). The salinity is negligible (0.19 to 4.29 ppm) and the $\delta^{18}O$ values are low (-11.8 to -20.8‰). This unit most probably corresponds to the snow accumulation during part of the year that followed the sea ice cover formation (from mid-winter 1987 to the end of the summer 1987-1988, when sampling occurred). The absence of bubbly or bubble-free ice layers in the unit and the preservation of the high porosity of the medium is further evidence of the restricted surface melting in the area during the summer. It should be noted that the slope of the regression line on the $\delta D/\delta^{18}O$ diagram of the figure 4b corresponds to the MWL (8.07).

Unit II (98 to 130 cm - figs. 3c and 4c) still displays a very low salinity (2.01 to 7.83 ppm Na) whereas the isotopic values are steadily increasing with depth from -20 to -10‰. Small-grained columnar ice is present probably indicating congelation effects. However, these congelation effects must be highly localised in the profile since the slope of 7.9 (correlation coefficient of 0.998) shown in the $\delta D/\delta^{18}O$ diagram of figure 4c is too high to be a freezing slope related to the decreasing of the freezing rate in a semi-infinite water medium with a constant isotopic value and a low salinity. The increasing isotopic values in the ice cannot be explained by an increasing share of normal sea water in the parent water, given the negligible salinities observed. Therefore, the most likely hypothesis is that this unit formed prior to unit I, and resulted from snow accumulation during the period that immediately followed the initial formation of the sea ice cover (end of summer 1986-1987 to mid-winter 1987).
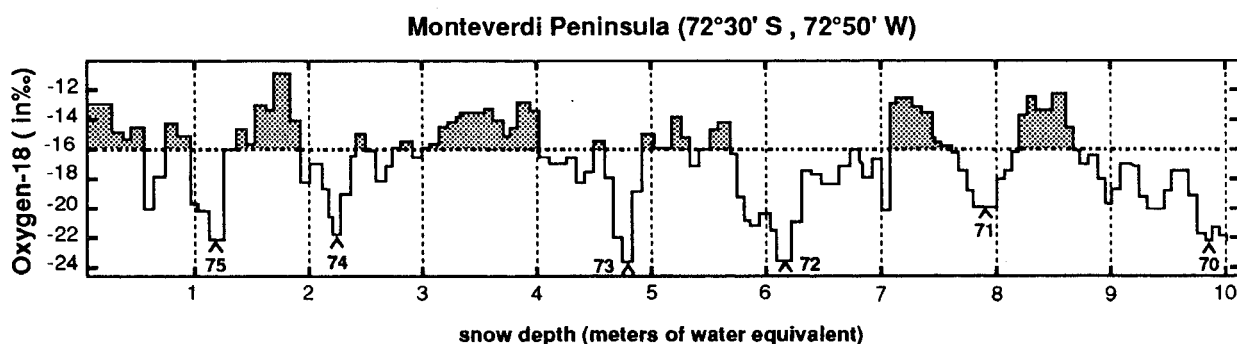
Figure 5. Oxygen 18 profile in a 10 m core from Monteverdi Peninsula (data from J.G. Paren, British Antarctic Survey). The arrows mark the years and the horizontal dashed line is the mean value in $\delta^{18}O$.

The C-shaped profile of the isotopic values from these two upper units can thus be considered as covering the net annual snow accumulation from summer to summer, between 1.00 and 1.30 my^{-1} with $\delta^{18}O$ values fluctuating between -11 and -20.8 ‰. These values correspond reasonably well to those observed by Potter et al. (1984) at Monteverdi Peninsula, not far from the rift area, in a 10 m ice core (fig. 5 - data from J. Paren, personal communication) with a mean annual accumulation of 0.95 my^{-1} and a range of -12 to -22‰ in $\delta^{18}O$. The preservation of the whole year's accumulation cycle in our core gives weight to the assertion that summer melting is very limited in the area.

A sharp transition from a $\delta^{18}O$ value of -13‰ to a value of 0‰ marks the beginning of **Unit III** (130 to 175 cm - figs. 3d and 4d). The linear regressions for $\delta D/\delta^{18}O$ (slope of 7.7 with $r^2 = 1.0$) and $\delta^{18}O/Na$ ($r^2 = 0.85$) clearly indicate the dominance of parent water effects over freezing rate effects.

Three main sources of fresh water to dilute the normal sea water can be considered :

a. melting of first-year sea ice from the previous year

b. melting of snow falling on the surface of the ice shelf and in the open sea water during the summer

c. melting of bottom shelf ice

Extensive melting of first-year sea ice from the previous year is highly improbable since most of the rift is covered with thick multi-year sea ice, with the exception of the restricted areas where depressions cross and open sea water forms during the summer. Also, mixing of melted sea ice with sea water would result in salinity and isotopic profiles fluctuating opposite way in the new sea ice formed, as discussed above.

Surface melt on the ice shelf during the summer is a possible source of fresh water. However, as discussed previously and as attested by annual mean temperatures estimated on Monteverdi Peninsula or Spaatz Island (Peel and Clausen, 1982), surface melting is probably much more limited here than in the northern part of the ice shelf (between 70°30'S and 72°S, Potter et al., 1984). Nevertheless, if the hypothesis proposed for the formation of Unit II is valid, partial dilution of surface sea water by snow falling in open waters should be considered. Potter et al. (1984) calculated a mean $\delta^{18}O$ value of -15.0 ± 0.9‰ for ice shelf accumulation in the southern part of the George VI Sound. This corresponds fairly well with the values of -15.10 and -15.20‰ measured in fresh

snow from two different precipitation events on the sampling site at the end of the summer (March 1988). Surface melting will only occur during the summer season and will mainly affect the more positive values of the annual accumulation cycle, as shown by the flatness of the summer peaks (above the mean) in the isotopic records of figure 5. The melt water that will eventually reach the sea ice/water interface will thus display isotopic values ranging between -12 and -16‰ in $\delta^{18}O$. A value of -15‰ will therefore be considered as typical of the melt either from the accumulation occurring at the surface of the ice shelf or from the snow falling in the open waters in the area.

The isotopic value of the melt from the base of the ice shelf is much more difficult to estimate. Potter et al.(1984) use a mean $\delta^{18}O$ value of -22.5 ±0.4‰ for the ice flux into the southern part of the ice shelf from the Inland Ice Sheet, estimated from an equilibrium mass and isotope balance partly using the temperature/$\delta^{18}O$ relationship established by Peel and Clausen (1982) for the Antarctic Peninsula. We shall assume that this value can be used as the average $\delta^{18}O$ value for ice at the base of the ice shelf.

Using the salinity value of 34.72‰ (10.67‰ in Na) and the $\delta^{18}O$ value of +0.16‰ proposed by Potter et al. (1984) for Warm Deep Water (WDW), the two mixing lines respectively of *surface* and *basal* meltwaters with WDW can be calculated. In both cases, we can discriminate between fresh (<0.5‰ global salinity), brackish (0.5 to 17‰) and sea water (>17‰) as proposed by Jeffries et al. (1989).

Reconstruction of the Na/$\delta^{18}O$ profile in the ice formed by freezing of these waters is complicated by non-equilibrium processes connected with fluctuations of the growth rates and by possible inclusion of liquid in the growing ice (Souchez and Jouzel, 1984; Souchez et al., 1987; Souchez et al., 1988). However, using a method similar to Jeffries et al. (1989), a broad envelope of possible values can be obtained by applying minimum and maximum apparent fractionation coefficients for Na and $\delta^{18}O$. For $\delta^{18}O$, extremely low freezing rates will allow the maximum equilibrium fractionation to occur with a positive shift of 3‰ (a = 1000+δ_i / 1000+δ_o = 1.003, where δ_i and δ_o are the δ values for ice and water respectively- O'Neil, 1968), and fast freezing will not yield any apparent fractionation. The effect of sea water inclusions on the isotopic signal of sea ice can be considered as negligible, as shown by Tison and Haren (1989). Na incorporation factors (S_i/S_o, where S_i and S_o are the salinity for ice and water respectively) as low as 0.04 to 0.05 have been observed at the bottom of first-year sea ice by the authors (Souchez et al., 1988) and a maximum value of about 0.15, as observed in our core, should cover most of the observations quoted in the

literature. This wide range of salinity fractionation factors is also thought to cover any alteration of the signal by sea water inclusions in the ice.

Figure 6 shows the four mixing lines obtained in the ice by applying the extreme values of the fractionation coefficients in Na (S_i/S_o) and in Oxygen 18 (a) to the two water mixing lines calculated above. The sample values are displayed in the background. The percentage of WDW varies from 100% to 0% along each mixing line. Curves 1 and 2 correspond to dilution of normal sea water by melt waters
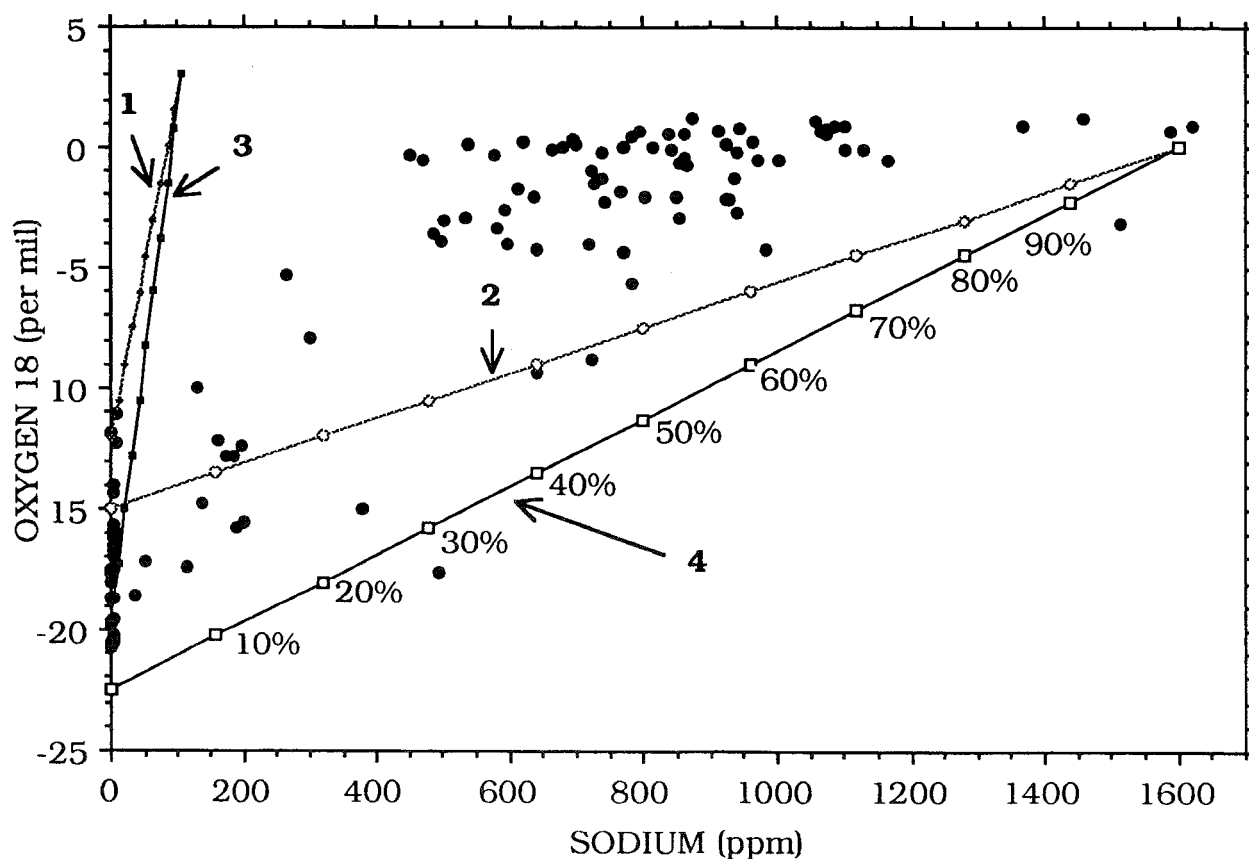
Figure 6. Mixing lines for ice formed by freezing of sea water diluted by fresh water from surface or basal melting of shelf ice and for extreme values of the fractionation coefficients. The % represent the proportion of normal sea water in the mix.
1. Fresh water = melt of surface snow and ice
   Slow freezing : Si/So = 0.01; α ^{18}O = 1.003
2. Fresh water = melt of surface snow and ice
   Fast freezing : Si/So = 0.15; α ^{18}O = 1.000
3. Fresh water = melt of basal ice from the ice shelf
   Slow freezing.
4. Fresh water = melt of basal ice from the ice shelf
   Fast freezing.

from the surface of the ice shelf and curves 3 and 4 to dilution by melt waters from the base of the ice shelf. Only curves 2 and 4 have been drawn on figures 3d, 3e and 3f, since curves 1 and 3 are very close to the ordinate axis and therefore not relevant in distinguishing the various parent water sources.

All the points from Unit III lie above the two mixing lines on figure 3d. This implies that these ice samples could either result from the freezing of sea water diluted by surface melt waters (with fresh water proportions ranging between 10 and 90 %) and/or from the freezing of sea water diluted by meltwaters from the base of the ice shelf (between 10 and 50 % of fresh water).

Unit IV (175 to 452 cm - figs. 3e and 4e) is the thickest unit in the core. It is characterized by the stabilization of Na and $\delta^{18}O$ around mean values of respectively 0.9‰ (900 ppm) and 0‰. However, it is clear in figure 2 that five major large scale sympathetic fluctuations of Na and $\delta^{18}O$ characterize the unit, with a minimum value at depths of 223, 258, 290, 330 and 390 cm (dashed lines in fig.2). It should be noted that this sympathetic response between Na and $\delta^{18}O$ does not show up as a good correlation in the $\delta^{18}O$/Na diagram of figure 3e. This is probably the expression of a different sensitivity of the chemical and isotopic signals to the liquid water inclusions during accretion of individual frazil ice crystals at the bottom of the pre-existing ice cover. Since at least 85% of the salts are rejected from the sea ice crystals as they form, slight fluctuations in the amount of parent water entrapped between the crystals as they accumulate at the base of the ice cover may cause important variations of the measured salinity in the core. This effect is negligible for the isotopic signal (Tison and Haren, 1989), since most of the signal results from the crystal itself. Thus, at two different locations in the core, similar changes in the isotopic signal will correspond to chemical changes of the same sign but of variable intensity.

Most of the samples in Unit IV could result from the freezing of sea water diluted by fresh water from each of the two possible sources, the proportions of fresh water input being of a few % (maximum 20 to 30 % in two point samples at depths of 223 and 258 cm, both corresponding to columnar ice - fig. 2). However, two arguments indicate a sub-shelf origin. Firstly, Units I and II correspond to the snow accumulation of a whole year with limited melting during the summer and Unit III results from the freezing of normal sea water which was less and less diluted by fresh water in the course of time. This last unit was thus growing down in the same time Unit II was piling up, at the beginning of the winter following the initial sea ice cover formation. This implies that Unit IV formed during the winter, when any surface melting is precluded. Secondly, one of the two stronger

dilution peaks is located below the two mixing lines (fig. 3e) and thus could only be produced by fresh water with a $\delta^{18}O$ value lower than -22.5‰. This could only be provided by melting at the base of the ice shelf.

Although dilution events are not always associated with textural differences (see, for example, the event at 390 cm) it should be noted that the only occurrence of platelet ice is located around two of the main dilution peaks (at 290 and 330 cm). Platelet ice is a special type of frazil ice usually associated with adiabatic expansion of sea water as it ascends from beneath ice shelves (see for example Robin, 1979; Lange et al., 1989). If dilution occurs at the bottom of the ice shelf, it is thus not surprising to trace it in the chemistry of the platelet ice in the core.

At 450 cm depth, the isotopic and chemical values drop sharply (from 741 ppm to 190 ppm in Na and from -0.25‰ to -15.75‰ in $\delta^{18}O$), and a last, fifth, unit of alternate columnar and granular ice occurs (**Unit V**, 452 to 553 cm figs. 3f and 4f) partly showing the characteristics of ice resulting from the freezing of brackish water. About one third of the samples from this unit can only be formed by freezing of waters resulting from the mixing of normal sea water with melt waters from the base of the ice shelf, as indicated by figure 3f. Dilution percentages as high as 80% fresh water/20% sea water can be observed. Contacts between individual grains are sharper and better defined than in the more saline units above. The higher dilutions correspond to the frazil layers that must therefore have been formed at depth, not far from the production zone, thus freezing in the chemical and isotopic signature of the fresh water before significant mixing with the normal sea water occurred. The presence of considerable amounts of columnar ice in this unit seems however to indicate that it partly forms by direct freezing of the brackish water layer at the bottom of the ice cover (congelation ice). The absence of brine layer/ice plate substructure in this columnar ice might be a trademark of brackish congelation ice.

Isotopic and chemical profiles of sea water, down to 15 meters (performed through the boreholes G and I (fig. 1)), confirm the sub-shelf origin for the fresh water. The water samples were taken just after the coring, while a considerable number of equigranular small frazil crystals were regularly floating up to the open water surface of the borehole. These frazil crystals were sampled separately and yielded isotopic values of -4.55‰ to -5.90‰ ($\delta^{18}O$)

and -33‰ to -46‰ (δD), sites G and I respectively. Under the ice cover, the isotopic and chemical values of the sea water are around 8000 to 8500 ppm of sodium, -1.1 to -1.8‰ (δ^{18}O) and -8 to -13‰ (δD). These isotopic values are too high to be responsible for those observed in the frazil ice at the extreme base of the core (-2‰ in δ^{18}O and -19‰ in δD), whatever the freezing rate. Similarly, the individual frazil ice crystals accumulating at the surface need a parent water with isotopic values fluctuating between -66‰ and -33‰ in δD and -9‰ to -4‰ in δ^{18}O. Such water was not observed under the sea ice cover and must result from the mixing of normal sea water with melt waters from the base of the ice shelf. The top of Unit V thus marks an increasing production of melt water at the base of the ice shelf, probably at the beginning of the austral summer 1987-1988.

4. Conclusion.

The major rifts developing in the southern part of the George VI Sound, where the ice shelf calves into huge tabular icebergs, are ideal traps for the water masses ascending in front of the ice shelf. These contribute to the accretion of sea ice at the open surface between the sides of the rift. Combined salinity and isotopic profiles of this sea ice allow the origin of the parent water to be traced. Results from a detailed profile of a 5.54 m - thick ice core sampled in the area show that it is probably second-year sea ice that has survived one melt season (Weeks and Ackley, 1986). Half of the core consists of sea ice, following the Jeffries et al. (1989) terminology, formed in the winter. Although, during this period, the parent water is close to normal sea water, the Na and δ^{18}O curves show a few sympathetic large scale fluctuations indicating dilution events reaching 20% of fresh water input that might reflect small variations in the basal melting of the ice shelf. A sharp transition from sea ice to brackish ice (450 cm depth) that must result from mixing with melt water from basal shelf ice, indicates the importance of this process during the summer period, with maximum dilution coefficients up to 80% of fresh water. Winter accretion consists almost exclusively of frazil ice production, while summer accretion alternates between frazil ice formed at depth close to the fresh water input location, (low salinity and low isotopic signal) and congelation ice formed by direct progression of a freezing front under the sea ice cover into a less diluted parent water. Further work on the multi-year sea ice formed in the rift area will aim to produce a semi-quantitative estimate of the fresh water output from the base of the George VI Ice Shelf at its southern ice front.

II Basal ice formation at the ice-bedrock interface in subfreezing temperature conditions, Adelie Land

1. Introduction

The study of the basal Ice Layers (B.I.L.), a common expression to describe the debris-laden ice layers is a key to understanding the mechanisms operating at the ice-bedrock interface. Several processes have been proposed to explain the B.I.L. genesis, based on stratigraphical, sedimentological, chemical, isotopic and crystallographic analyses.

There is a general consensus in the literature on the existence of two major mechanisms for debris entrainment at the sole of glaciers and larger ice masses. Pressure-melting regelation (Weertman; 1957, 1964) is induced by pressure melting fluctuations around bed protuberances. It usually yields low debris/ice ratios, with separated sequences of clear ice laminae alternating with thin debris layers. Boulton (1975) proposed that differential flow around the obstacle might bring this B.I.L. higher up above the bed, thus increasing its thickness from the usual decimetric scale to the metric scale. Freezing-on (Weertman, 1961) allows net accretion of ice at the glacier sole. It results from fluctuations of the pressure melting point (p.m.p.) isotherm with respect to the interface. A typical location where this process occur is at the limit between the central part of an ice sheet where the interface is at the p.m.p. and the outer part where the glacier sole is at sub-freezing temperature, or at the ice sheet margin where seasonal fluctuations occur. The mechanism will eventually yield very high debris/ice ratios where the interface consists of soft sediments.

Transport of rock particles along shear planes has been demonstrated by several authors (Goldthwait, 1951; Ward, 1952; Bishop, 1957; Souchez, 1967; Boulton, 1970; Andrews, 1971; Dilabio and Shilts, 1979), but the initial entrainment of debris into the ice by shearing is still conjectural. Weertman (1961), for example, is not convinced of the efficiency of such a process, given shear measurements across individual debris layers and debris layers geometry. However, recent work from Echelmeyer and Zhongxiang (1987) providing direct observation of basal sliding at sub-freezing temperatures report a detailed description of an ice-rock contact where shear-sliding is shown to occur, together with local debris entrainment in the form of thin alternating laminae of debris-rich ice and relatively clear ice.

2. Basal ice layers in Adelie Land

This work presents a detailed analysis of basal ice sequences observed in Adelie Land, near the margin of the East Antarctic Ice Sheet. The area is well documented thanks to the close vicinity of Base Dumont d'Urville. Physical, isotopic, chemical and sedimentological studies, further complemented with ice-sheet modelling, were performed since the middle sixties along the IAGP flow line joining Dome C to Dumont d'Urville (Merlivat et al., 1966; Merlivat et al., 1967, Lorius et al., 1968; Lorius et Merlivat, 1977; Raynaud et al., 1979; Yao et al, 1990). The area of Moraine Prudhomme was also invesigated (Lorius et Vallon, 1967) as well as a morainic deposits in drifting icebergs (Bellair et al, 1964).
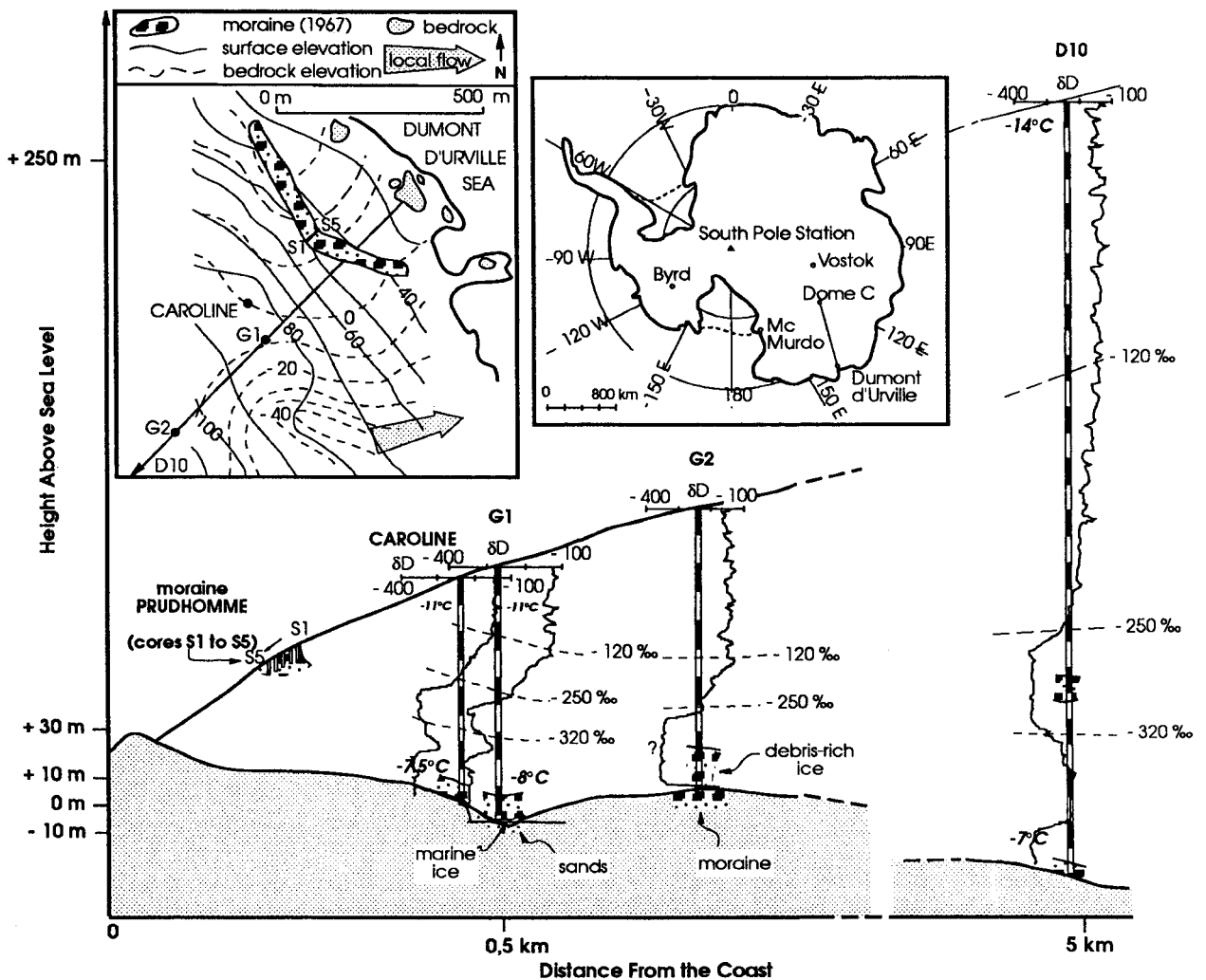
Figure 7. Summary of information from previous work in the Terre Adélie area along the IAGP line near the coast, and sampling sites for the present study (see text for references). Black and white strips on the core profiles are at 10 m depth intervals.

Figure 7 summarizes some of the results from previous studies along the flow line between core drilling D10, located approximately five km from the coast at 270m elevation and the coast (cores D10, G1, G2, C.A.R.O.L.I.N.E. and Moraine Prudhomme). Typical temperature ranges in the cores are between -14°C to -11°C near the surface and -7°C to -8°C at the ice-bedrock interface, which is thus at sub-freezing temperature throughout. Detailed isotopic profiles from all cores show strong similarities and reflect both dynamical and climatic effects along the flow line. Nearly constant isotopic values (about -140‰ in ∂D) in the upperpart of the cores correspond to the upper Holocene period. The gradual slow decrease of ∂D (down to approximately -250‰) characterizing the next stage still corresponds to ice from the Holocene period but for snow fallen in more inland area. A third stage with rapid decrease of ∂D values down to -360‰ reflects the combined effect of the climatic transition between full glacial period and the Holocene (Jouzel et al., 1987, 1989) and the correlative change in the origin of the ice occurring at a given depth, with concurrent lowering of the ice sheet. These isotopic results are backed up by microparticle concentration, crystal size and bubble concentration in the ice core (Yao et al., 1990). There is still some debate concerning the deeper layer with higher isotopic values, larger crystal sizes, lower bubble concentration and lower microparticle concentration, occurring between 55m and 65m in the C.A.R.O.L.I.N.E. ice core for example. It is not clear if this stage results from dynamical or climatic processes. Yao et al. (1990) favour the latter hypothesis on isotopic and bubble concentration grounds, but they find it difficult to relate this warming stage firmly to a given period. Assuming the dust peak found at 55m depth in the C.A.R.O.L.I.N.E. core corresponds to the 60 kyear BP dust peak observed on the Vostok record, they suggest that this (fourth) stage might fit the Vostok interstage E (73 to 106kyear BP). Another possible explanation is the occurrence of discontinuities in the ice sequence due to ice sheet thinning and formation of stagnant ice during warm periods. Nevertheless, if the climatic hypothesis is to be retained, then the lack of this fourth stage in the G2 ice core remains unexplained.

Marine ice was discovered at the very bottom of G1, in accordance with the local subglacial topography and the sediments forming the bedrock. They both show the existence of the head of a subglacial channel being part of the subglacial valley of the Glacier de l'Astrolabe, covered with sands reworked by coastal marine processes (Nougier and Lorius, 1969).

Debris-rich ice is present near the ice-bedrock interface in all four cores with thickness varying between 2m (D10) and 12.5m (G2). In addition internal debris-

rich ice layers found between 227 and 237m depth in D10 were used as an argument for a dynamical origin to the fourth warmer isotopic stage. A comparison between surface isotopic values along the IAGP flow line near the coast and the profiles of G1 and G2 suggests that the debris-rich ice layers cropping out at Moraine Prudhomme result from the overriding of stagnant ice, at least partly superimposed, by the B.I.L. observed at the bottom of G1, G2 ice cores (Lorius and Merlivat, 1977). For this reason, the B.I.L. from the C.A.R.O.L.I.N.E. ice core and the debris-rich ice layers feeding the Moraine Prudhomme can be considered as the same feature. Taking into account the easy access of the surface cores from Moraine Prudhomme, they can be advantageously used to back up the information provided by the C.A.R.O.L.I.N.E. ice core.

3. Analytical techniques and sampling procedures

As a first step, the 6 meters of B.I.L. from C.A.R.O.L.I.N.E. (see figure 7 for location) were sampled in the Laboratoire de Glaciologie de Grenoble for co-isotopic analyses of the ice both in ∂D and $\partial^{18}O$. A total number of 156 samples were collected with a resolution varying between 1 and 25cm depending on the core structures visible in transmitted light. The analyses were performed at the Centre d'Etudes Nucléaires de Saclay and the results are presented in ∂‰ values referring to SMOW. Accuracy of the measurements is 0.1‰ in $\partial^{18}O$ and 0.5‰ in ∂D. Moreover, a set of 7 representative samples were taken for total gas volume analyses and CO_2 analyses. The measurements were performed at the Laboratoire de Glaciologie de Grenoble. Precision of the measurements is 0.001 cm^3 g^{-1} for total gas volume and 5 ppmV (parts per million in volume) for CO_2 concentration.

The next step deals with a detailed crystallographic analysis (texture and c-axes measurements) at Brussels Laboratory on five 2 meters-long ice cores sampled across the «hinge» of the arcuate Moraine Prudhomme. Thin sections in debris-laden ice are difficult to prepare with standard microtomic procedures, which probably explains the paucity of information on B.I.L. ice-fabrics in the literature. To solve this problem, the laboratory has been equipped recently with an Ebner 5234 diamond-wire saw, and the authors are currently developing a new technique for cutting 800mm thin-sections, both through ice and rock particles, without damaging the section and/or the equipment whatever the debris/ice ratio.

Finally, selected debris samples from D10, C.A.R.O.L.I.N.E. and Moraine Prudhomme were prepared for light microscope and scanning electron microscope analyses (SEM) at York University, Toronto. The samples were wet washed to

separate the sand fraction (63μm-2mm) from silt and clay. Using the light microscope approximately 15 to 25 quartz grains were selected per subsample of coarse sand (1-2 mm) for detailed analyses by SEM. Altogether, 450 coarse quartz were analyzed. Other subsamples were prepared from the finer sand fraction (63-250μm) using several hundred grains of quartz plus other minerals per stub (for separation of fine sand, see Mahaney, 1991). The chemistry of all studied grains was verified by energy dispersive spectrometry (EDS). The samples were analyzed using a JEOL 840 SEM.

4. Results and discussion

4.1. Debris-rich ice at the base of the C.A.R.O.L.I.N.E. ice core :

The structure of the B.I.L. from the C.A.R.O.L.I.N.E. ice core consists of alternations of centimetric to decimetric layers of white bubbly ice devoid of particles and of pink bubbly amber ice with low to high debris/ice ratios. The white bubbly ice looks very much like the glacier ice observed in the upper part of the core. Although it is generally particle-free, in a few cases it occurs with thin millimetric layers of dispersed particles regularly spaced by a few centimeters. The pink color of the amber ice is given by the fine silty and sandy rock particles which mainly occur as aggregates (clots) reaching 0.6cm in diameter. The bubbles are smaller (<0.5mm) than in the glacier ice above and less dense. Sometimes a gross internal layering exists, for low ice/debris ratios, with typical individual layer thickness of 2 to 4cm. Rock fragments were also occasionally encountered in the profile. Generally, debris structure and characteristics are very similar to the one described by Gow et al. (1979) at the bottom of the Byrd ice core, but two major differences exist since at Byrd the debris-free ice was also clear-ice (devoid of air bubbles) and the pressure melting point was reached at the interface.

Figure 8a shows the results of the stable isotopes measurements in a ∂D-$\partial^{18}O$ diagram. No co-isotopic measurements are available for the upper part of the C.A.R.O.L.I.N.E. ice core. However, seven samples of bubbly debris-free glacier ice were taken in the 60 centimeters just above the first debris-laden ice layers (open circles in fig. 8a). Although these boundary glacier ice samples might be affected by the processes occurring at the interface, they provide our only estimate of the local precipitation slope. A linear regression for these sample points gives $\delta D = 7.32\ \delta^{18}O$ -30 ($r^2 = 0.96$). The slope of 7.32 is slightly lower than the usual value of 8, but this might be a bias from the small number of points. Deuterium excess calculated for each individual sample varies between -1.7 and +2.9. These values are compatible with the paleoclimatic interpretation of the
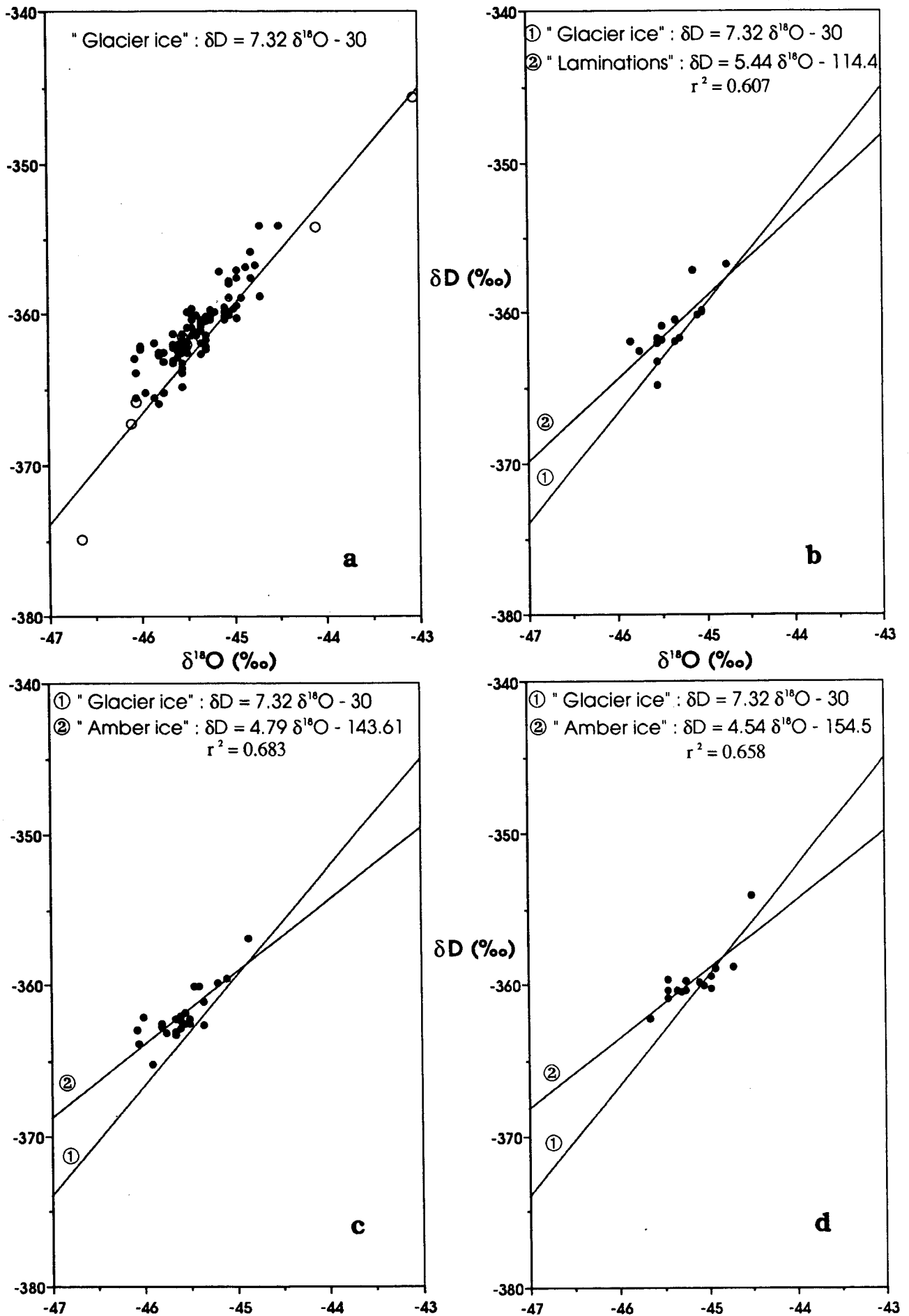
Figure 8. Co-isotopic results from the B.I.L. of C.A.R.O.L.I.N.E. ice core.

base of the ice core given previously (Yao et al., 1990), the very low isotopic values resulting from a pre-Holocene glacial maximum with expected higher relative humidity at the source area explaining our low deuterium excess (Jouzel et al., 1982).

All the B.I.L. samples are distributed in an elliptic cloud centered on the glacier ice samples. This dispersion is not particular to C.A.R.O.L.I.N.E. and was also observed amongst the most negative values measured at the base of G1 (Merlivat et al., 1967 - fig.7). No obvious «freezing slope» indicating freezing-on or regelation processes at the ice-rock interface is observed on fig. 8a. However, if individual debris layers, delimited by two successive white bubbly debris-free layers, are plotted separately (figure 8b for thin laminations of dispersed debris in white bubbly ice; figure 8c and 8d for two different sequences of pink amber ice) they define lower slopes (5.43, 4.79 and 4.54) but with considerable scattering (r^2 = 0.61, 0.68 and 0.66 respectively). Since theoretical freezing slopes should vary between 4.54 and 4.74 for the range of glacier ice observed above the B.I.L., these individual signatures could be interpreted as the result of modifications implying phase changes at the crystal boundaries, and yielding weaker co-isotopic relationships than in the case of freezing of a delimited water reservoir. Contact with freshly grounded hydroxyl-bearing clay minerals or micas could also explain lower slopes on a δD-$\delta^{18}O$ diagram (Souchez et al., 1990). They would however display much wider ranges of δ's and exclusively towards more positive values, with stronger correlations and even lower linear regression coefficients.

The occurrence of phase changes along crystal boundaries of the debris-laden ice is further supported by gas measurements summarized in Table I. There is a striking difference between debris-free and debris-laden ice both in total gas content and CO_2 concentration. The mean total gas value ($0.097cm^3/g$ of ice for debris-free ice and $0.052cm^3/g$ of ice for debris-laden ice) are in close agreement with previous measurements on G1 ice core performed by Lorius et al. (1968). These authors give values between $0.070cm^3/g$ and $0.110cm^3/g$ in white glacier ice and about $0.040cm^3/g$ in ice containing morainic debris. The same is valid for the CO_2 content, although recent developments seem to indicate that the «melting-refreezing» method for collecting CO_2, used by Lorius et al. in 1968, might overestimate CO_2 concentrations by favouring possible reactions with carbonate particles during the experimental procedure (Raynaud et al., 1982). Nevertheless, these authors measured a mean value of about 240ppmV CO_2 in the debris-free ice and a single value of 80 ppmV in debris laden ice, which are compatible with our concentrations listed in Table I (212 to 237ppmV and 7 to

85ppmV, respectively). The comparison of the two main types of ice in Table I shows that the total gas content is grossly halved, whilst the CO_2 is divided by a factor of 4 when debris is present. This favours the hypothesis of the presence of a liquid phase, at ice crystals boundaries, since only the higher dissolution rate of CO_2 with regard to the other atmospheric gases can explain its selective depletion.

SAMPLE	DESCRIPTION	TOTAL GAS VOLUME (cm3/g of ice)	CO2 CONTENT (ppmV)
TA 37 n°57	white bubbly glacier ice without debris	0.122	212
TA 37 n°92	" "	0.092	212
TA 37 n°96	pink amber ice	0.053	86
TA 37 n°98a	white bubbly ice without debris	0.077	237
TA 37 n°98b	pink amber ice with numerous particles	0.033	<7
TA 37 n°98c	light pink amber ice	0.067	33
TA 37 n°102	pink amber ice	0.055	85
mean	white bubbly ice without debris	0.097	220
mean	debris-laden ice	0.052	53

Table 1. Gas content and gas composition of basal ice in the C.A.R.O.L.I.N.E. ice core

The combined results of the stable isotope and gas analyses thus require a peculiar mechanism for debris entrainment allowing gas depletion in the presence of water, in a system different from that of progressive freezing in a finite reservoir at the ice-bedrock interface. Moreover, sedimentological studies on the particles forming the debris-rich ice layers suggest a local origin for the entrainment process which is thus occurring well below the pressure-melting point (between -7°C and -8°C, see fig. 7). Indeed, Nougier and Lorius (1969) in a geological and physico-chemical study of the debris in G1 and G2 showed that whilst the upper debris layers of both ice cores have chemical compositions close to that of a ferruginous mica-bearing sandstone (of the Beacon formation observed inland in the Transantarctic mountains), the bottom layers indicate a parent rock with a much lower proportion of silica and much richer in plagioclase feldspars. The latter can be compared either to the granite, diorite and migmatite outcropping near the coast, or to the dolerite boulders occurring in the ground

moraine below G2 and at the surface of Moraine Prudhomme.

Compared SEM analyses performed on sand particles from internal morainic layers at D10 (230m depth) on B.I.L. from the C.A.R.O.L.I.N.E. ice core and on debris-rich ice samples from Moraine Prudhomme strongly support the local origin for this debris entrainment process. Overall, the grains studied in the twenty subsamples from D10-230 consist largely of quartz and feldspar material (90%) with ancillary heavy minerals (mainly amphiboles). The microtextures observed on quartz grains include very high relief and high degrees of edge sharpness consistent with glacially-crushed grains reported elsewhere (Krinsley and Doornkamp, 1973; Mahaney, 1990a and 1991, Mahaney et al., 1988). About 80% of all grains studied showed extensive fracturing, over 70% of all glacially-crushed grains were abraded, some very intensively. High and low frequency fractures, thought to be related to ice thickness and hence cryostatic pressure (Mahaney, 1990a, 1990b), were observed on most of the grains studied. On the whole, high frequency fractures (number of fractures per surface area) dominate, which may be related to the vibrational energy released upon low velocity impact (Mahaney, 1991). The most common glacial-crushing features include subparralel linear and conchoidal fractures of variable high to low frequencies (Mahaney 1990a, 1990b), along with deep straight and curved grooves. The high degree of fracturing and the range of fractures observed suggest crushing by thick ice of continental proportions (Mahaney, 1990a) (>800m thickness). V-shaped percussion cracks, long considered to result from water transport (Krinsley and Doornkamp, 1973) were seen very infrequently on these subsamples. This suggests that water transport within or at the base of the ice is minimal. About 30% to 35% of the quartz grains studied show dissolution effects followed by renewed crushing, thus indicating weathering prior to entrainment and crushing by ice. However, the age of this weathering is still highly conjectural. Such weathering-crushing sequences have been identified elsewhere in Antarctica (Mahaney, 1991).

Samples from the very bottom of C.A.R.O.L.I.N.E. and from Moraine Prudhomme ice cores show different characteristics : especially a much higher proportion of plagioclases. Many particles from C.A.R.O.L.I.N.E. show old weathered surfaces side by side with freshly fractured and abraded surfaces and, in Prudhomme samples, most quartz is old, fractured and preweathered with only a few freshly fractured grains present. There is thus an overall impression gained of a much more local provenance for the debris picked up in the ice as one moves from D10

to the coast with a higher proportion of autochtonous minerals, a higher degree of weathering and a lower proportion of fresh fracturing under thick ice masses, the two last characteristics being possibly coupled with deglaciation/glaciation cycles affecting the area closer to the ice-cap border.

4.2. Debris-rich ice from surface ice core at Moraine Prudhomme

The five two meters long surface ice cores (S1 to S5 in fig. 7) were sampled on a straight line along the hinge of the arcuate Moraine Prudhomme in a downglacier direction to the coast. They were taken 4 to 6 meters apart from each other and probably correspond to most of the B.I.L. sequence at C.A.R.O.L.I.N.E., since no apparent debris-rich ice layer occurs either up glacier from S1 or down glacier from S5. Ice texture and debris characteristics are quite similar to those observed in the C.A.R.O.L.I.N.E. B.I.L. However, thanks to the available thin sections through debris-rich ice a better understanding of the debris entrainment processes can be gained. Three main ice populations are clearly visible.

White bubbly debris-free ice with very large crystals and numerous small (1mm in diameter) intracrystalline bubbles, mainly spherical, but sometimes slightly elongated in two mean directions, one of them being roughly parallel to the ice layering. It occurs in regular decimetric alternation with the other two ice types.

Pink bubbly debris-rich ice with large crystals: the pink coloured debris occurs as aggregates (clots), quite often made of a small pebble coated with a millimetric gangue of silty material. In some cases, the pebble is replaced by a few coarse sand particles in contact with each other. Debris concentrations vary between 0.2% and 3.4% in weight which is within the range of the values measured at the bottom of G1 and G2 (Nougier and Lorius, 1969). The ice crystals are often polygonal in shape and the air bubbles are smaller (down to 0.1mm) than in the debris-free ice and less numerous. Most of them are intracrystalline.

Pink bubbly debris-rich ice with small crystals is similar to the previous type in terms of bubbles and debris characteristics and concentrations. The crystal size is however clearly much smaller.

Crystal mean cross-sectional area (on at least 100 crystals), bubble and clot concentrations have been measured on enlarged thin-section photographs of each individual layer of a given ice type and the results are plotted on figure 9.
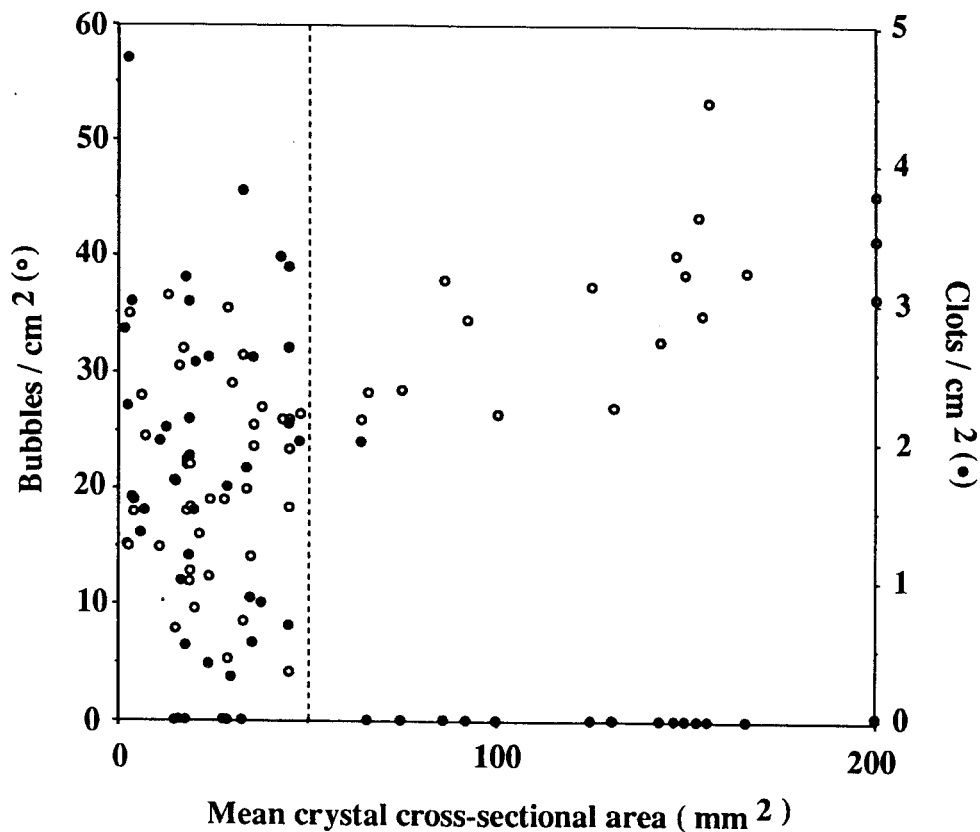
Figure 9. Bubble and clot concentrations (per cm²) as a function of the mean crystal cross-sectional area (in mm²) in surface ice cores at Moraine Prudhomme

Mean crystal cross-sectional area widely vary from 1 to 200mm2. This maximum value is higher than the one measured at shallower depths in the core, Yao et al (1990) reaching maximum values of 85mm^2 between 60 and 70 meters depth. This is probably the sign that the glacier ice near the margin of the ice sheet at Moraine Prudhomme has undergone a long history of post-cinematic recrystallization in a nearly stagnant state. There is a clear limit in figure 9, at about 50mm2 of cross-sectional area, beyond which debris-free ice with bubble concentration always higher than 25/cm^2 only occur. Debris-rich ice is thus always small grained and shows bubble concentrations ranging from values as low as 5/cm^2 to values not much different from the debris-free ice. There is however, in this small-grained population, no correlation between the mean crystal cross-sectional area and either the bubble concentration or the dirt content.

Ice fabrics (fig. 10) in the debris-rich ice differ from the one observed in the interlayered debris-free ice, although a general pattern of a wide girdle in the vertical plane containing the S1-S5 direction (tail of the arrow in the middle of each diagram) is a common feature for all samples. Debris-free ice shows a
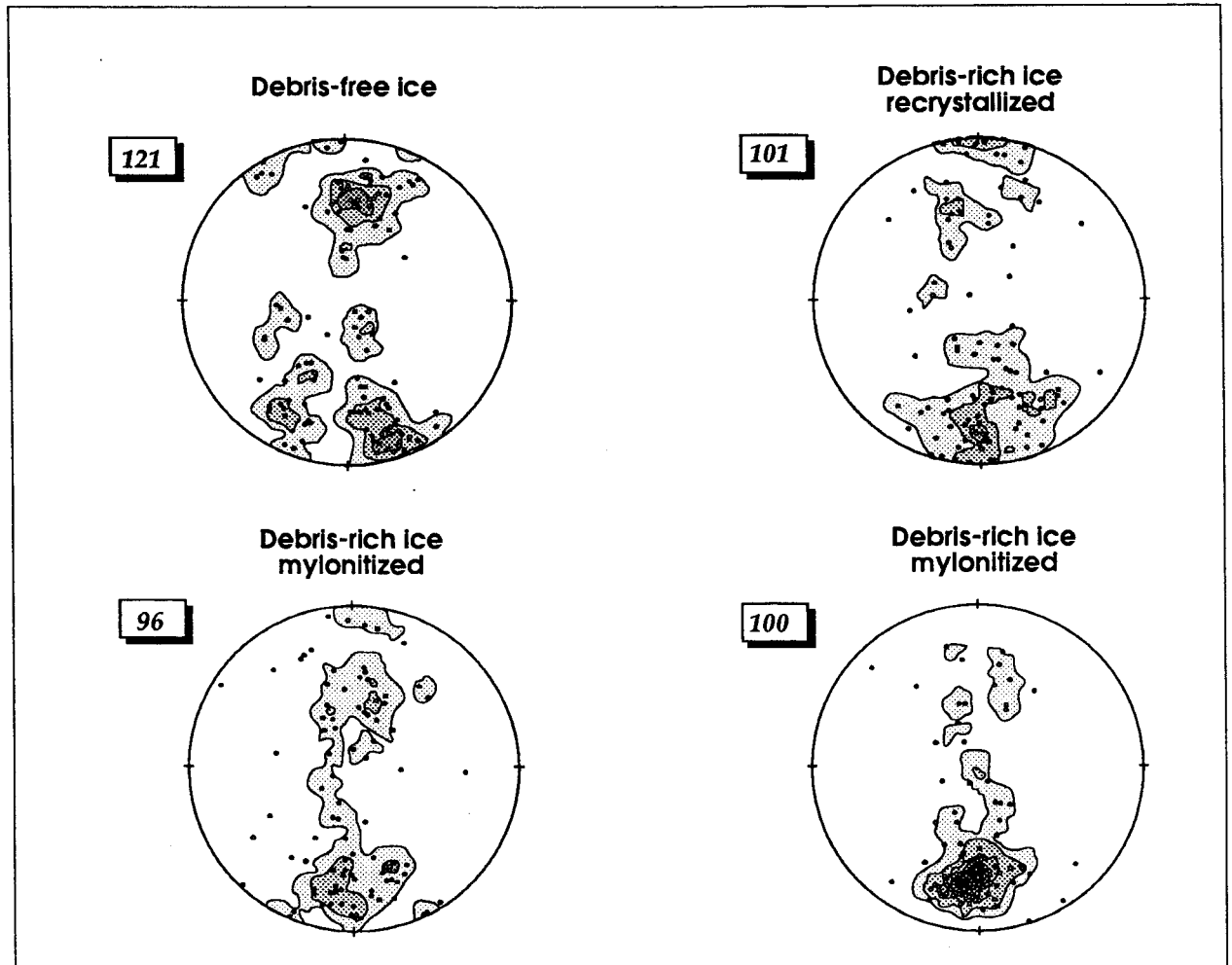
Figure 10. Ice fabric diagrams shown in the vertical plane and looking towards the coast (in the S1-S5 direction, figure 7). The number of c-axes measured is mentioned in the upper left corner of each drawing.

multiple maxima fabric which was also observed at 36.55 and 75m depth by Lorius and Vallon (1967) in the G1 ice core. In our case, however, they are grossly located in an elliptic girdle centered on the vertical and stretched in the vertical plane containing the S1-S5 direction. Following Alley (1988), this could be interpreted as a pure shear configuration with parallel flow (fig. 1c in Alley, 1988) where the vertical compression is balanced by an extension roughly following the main flow component of the glacier de l'Astrolabe (fig. 7). This fabric was probably acquired further up-glacier when the ice was still in the active fast flowing part of the Glacier de l'Astrolabe. Indeed, surface velocity measurements performed by the E.P.F. (personal communication) close to the Moraine Prudhomme yield values as low as 0.045my-1, with maximum values of about $2.3my^{-1}$ for the surrounding debris-free ice (surface ice velocity on the IAGP line between D24 and D10 ranges from 36 to $7my^{-1}$).

Fabrics in the debris-rich ice layers still display the girdle in the vertical plane, narrow in its central part, but they develop a typical single maximum which is commonly interpreted in the literature (Alley, 1988; Budd, 1972, Kamb, 1972), as the effect of a dominating basal shear stress near the glacier bed. The deviation of the center of the maximum at about 30° from the vertical is thought to be the result of a compressive stress superimposed to the simple shear, as the active glacier ice from upstream overrides slow moving ice near the border of the ice sheet, and is furthermore buttressed by the bedrock outcrops along the coast. In this case, the fine-grained texture of the debris-rich ice thus results from the activation of new local stress conditions near the glacier bed as the ice approaches the ice sheet margin, and not from crystal growth impedance by the debris load as it is in some cases suggested in the literature (Herron et al., 1979; Koerner and Fisher, 1979). Further arguments for this are the absence of correlation in figure 9, between dirt content and crystal size, and the fact that dozens of individual ice crystals usually exist between two neighbouring debris aggregates in the fine-grained amber ice. The single maximum is usually stronger in the finer-grained debris-rich ice, probably because the deformation fabric is essentially the result of grain rotation (Alley, 1988), whilst in the coarser-grained debris-rich ice, showing typical polygonal crystals, recrystallization has already taken place.

4.3. Discussion

The overall characteristics of the debris-rich ice at the base of C.A.R.O.L.I.N.E. ice core and at Moraine Prudhomme rule out pressure-melting regelation or freezing-on as possible mechanisms for debris entrainment at the glacier sole. Lithological and micromorphological signatures of the rock particles both indicate a local origin. Profiles in cores D10, G1 and C.A.R.O.L.I.N.E. all show temperatures well below the pressure-melting point (between -7.5°C and -8°C). Therefore, neither is a fresh meltwater input locally available for freezing-on processes, nor is the pressure-melting regelation possible around bed obstacles. This is further supported by the absence of a freezing slope on a dD-d18O diagram for the debris-rich ice population and by the persistence of intracrystalline bubbles even in the fine-grained amber ice. There is thus a clear need for a debris entrainment process acting at subfreezing temperature but allowing phase changes at crystal boundaries to explain small scale isotopic effects and considerable modifications in the total gas and CO_2 content of the ice.

Figure 11 illustrates such a possible mechanism that can be described as follows. Active glacier ice comes in from the inland, following the main flow
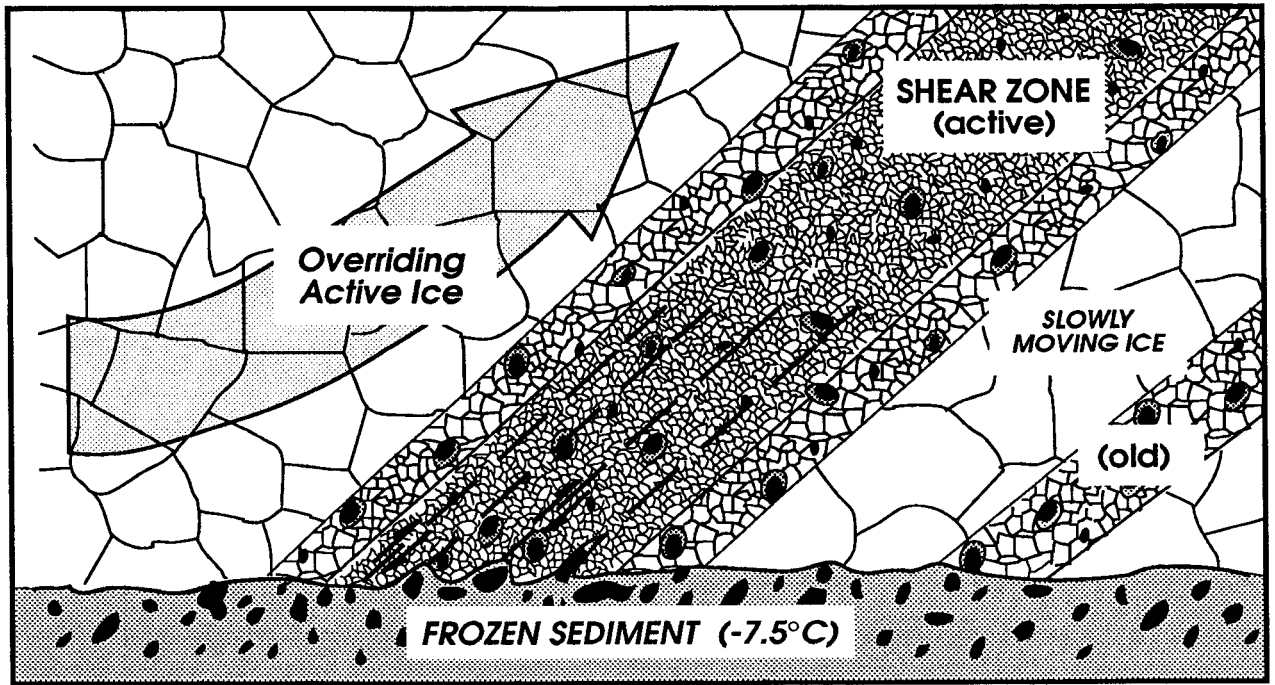
Figure 11. Sketch for a possible mechanism of debris entrainment in basal ice at subfreezing temperature (see text for details)

direction of the Glacier de l'Astrolabe in «parallel flow» conditions. As it reaches the edge of the ice sheet margin and as it is buttressed on the bedrock outcrops near the coast it is submitted to a strong compressive stress which combines with the basal shear stress near the interface. This local stress field causes the mylonitization of the active glacier ice as it overrides the dead, slow moving ice, near the margin. While some of the new crystals keep the signature of the previous stress field, most of them rotate to form a single maximum perpendicular to the new principal shear plane at about 30° from the horizontal. Similar mylonitized zones were described by Echelmeyer and Zhongxiang (1987) in basal ice layers at subfreezing temperatures at Urumqi Glacier N°1 in China. Thin sections taken just above the ice-sediment interface, where shear planes were proved to exist by detailed strain measurements, showed a non-gradational transition between coarse glacier ice and a 4-10mm layer of extremely fine-grained ice (<0.5mm grain size). In some places, like at the crest of a boulder embedded in the ice-laden basal drift and protruding 15cm into the ice above, the fine-grained ice layer was underlain by a few thin bands of debris-ice laminations extending 1-2m upward into the ice at an angle of 14-18°. The soft sediment frozen at the sole of the Glacier de l'Astrolabe near its coastal margin is most likely to be affected by the new stress field mentioned above. Large particles, eventually protruding at the interface on a small scale, are entrained in the ice by differential movement across them along the new principal shear

plane direction. As they tend to roll on themselves, a coating of fine particles adhering on their surface is progressively formed. These clots are further entrained in the ice by the movement of the surrounding small ice crystals in the shear zone. Eventually, under the combined influence of high temperatures (-10°C) and high strain rates (Alley, 1988), recrystallization will take place and form the coarser-grained debris-rich ice.

Fracture of the large glacier ice crystals into groups of smaller individuals will bring some of the intracrystalline bubbles in contact with water between the crystals. If this liquid phase is undersaturated in atmospheric gases, part of these gases can dissolve and eventually escape from the ice through fractures or squeezing. Frictional heat could also favour partial melting at grain boundaries, and enhance the whole process, which is affecting selectively the CO_2, given its higher dissolution rate. These phase changes at crystal boundaries and those which lead to the crystal growth by recrystallization are apparently strong enough to detect small scale isotopic fractionation as shown in figure 8 and discussed above.

5. Conclusions.

Ice texture and fabric, isotopic, total gas, CO_2 content and SEM measurements can be used together to indicate the feasibility of mechanical debris entrainment into basal ice by shearing at subfreezing temperature, at the margin of the Antarctic ice sheet in Terre Adelie. The debris-rich ice formed by such a process is characterized by :

a) a strong mylonitization of the ice crystals in the debris-rich ice together with the development of single-maximum fabrics

b) a moderate debris/ice ratio ranging from a fraction of a per cent to a few per cents

c) a typical structure of the debris in clots, consisting of a core made of larger particles in a fine coating of silts and clays

d) a lower total gas content (down to 30 % of its initial value in undisturbed glacier ice)

e) an even lower CO_2 content (down to 3.5 % of its initial value)

f) the subsistence of intracrystalline bubbles in the debris-rich ice

g) the absence of large scale isotopic fractionation, but the possibility of small scale «melting-refreezing» effects

h) increasing amounts of autochtonous glacially-crushed minerals from D10-230 to C.A.R.O.L.I.N.E. to Moraine Prudhomme.

It thus clearly differs from the B.I.L. studied at the base of the Byrd Ice Core by Gow et al. (1979) . There, the clear debris-rich ice, with negligible gas content throughout and with $\delta^{18}O$ values of the ice about 3‰ higher than the water collected in the drill hole at the ice-bedrock interface, was the signature of a «freezing-on» process. Although the general distribution pattern of the debris in the ice was quite similar to the one in this study, higher debris/ice ratios of 12 to 15% were observed.

We suggest from our observations in Terre Adelie that «freezing-on» at the ice-bedrock interface might not be the only major mechanism by which sediment is incorporated into polar ice sheets, as Gow et al. (1979) proposed. Indeed, dynamical conditions similar to those described in this study must be quite frequent along the Antarctic ice sheet border where no ice shelf is present and where the ice sheet terminus consists of a ramp or where it is buttressed by a coastal relief.

III General conclusions

Isotopic and chemical distribution in ice due to water freezing is a function of the freezing rate. This effect has been studied in the laboratory under controlled conditions. Salinity and isotopic profiles fluctuating opposite ways are displayed in this case. Such profiles have been found previously by our team in the Antarctic (Souchez et al, 1988). However, the application of this work to the study of Antarctic ice is only possible if, in fact, the freezing rate is the main factor influencing the isotopic and chemical signals during a water/ice phase change. This is not always the case.

The isotopic or chemical characteristics of multi-year sea ice sampled in a rift of the George VI Ice Shelf can only be understood if changes in parent water during the building of the ice cover have taken place. The dominating influence of parent water effects in this case explains why the Na content and $\delta^{18}O$ curves show large scale strong positive correlation and sympathetic fluctuations between the two curves. Mixing of sea water with meltwater from basal shelf ice representing a fresh water input is the main feature allowing the sea water in the rift to be modified in the course of time. This dilution affects the characteristics of sea ice formed during the summer but also some dilution events can be detected in sea ice formed during the winter period. While frazil and congelation ice are both formed during the summer, winter accretion consists almost exclusively of frazil ice production.

Isotopic (δD and $\delta^{18}O$), total gas, CO_2 content together with ice texture and fabric and SEM measurements have been used to study the debris-rich basal ice from the C.A.R.O.L.I.N.E. ice core and from the area of Moraine Prudhomme in Terre Adelie. The results shed some light on the process of basal ice formation in this region of Antarctica under subfreezing temperature conditions at the ice-bedrock interface and document further changes due to the presence of liquid water at crystal boundaries at these temperatures.

IV Acknowledgements

V References

Alley, R.B. 1988. Fabrics in polar ice sheets : development and prediction. Science, 240 : 493-495.

Andrews, J.T. 1971. Englacial debris in glaciers. Journal of Glaciology, Letter, 10 : 410.

Bell, J.D., Myatt, R.W. and Richards R.E. 1971. Proton magnetic resonance evidence of a liquid phase in polycrystalline ice. Nature, 230 : 91-92.

Bellair, P., Tourenq, J. and Vernet, S. 1964. Un échantillon de moraine interne du Glacier de l'Astrolabe (Terre Adélie). Revue de Géographie Physique et de Géologie Dynamique, VI, 2 : 115-121.

Bishop, B.C. 1957. Shear moraines in the Thule area, northwest Greenland. U.S. Snow, Ice and Permafrost Research Establishment. Research Report 17.

Boulton, G.S. 1970. On the origin and transport of englacial debris in Svalbard glaciers. Journal of Glaciology, 9 : 213-229.

Boulton, G.S. 1975. Processes and patterns of subglacial sedimentation : a theoretical approach. In : Ices ages : ancient and modern. Wright, A. and Moseley, F. (Eds). Seel House Press, Liverpool : 7-42.

Budd, W.F. 1972. The development of crystal orientation fabrics in moving ice. Zeitschrift für Gletscherkunde und Glazialgeologie, 8 : 65-105.

Cherepanov, N.V. 1966. Structure of sea ice of great thickness. Defense Research Establishment, Ottawa, Translation 448R, 6p.

Dilabio, R.N.W. and Shilts, W.W. 1979. Composition and dispersal of debris by modern glaciers, Bylot Island, Canada. In : Moraines and Varves, Origin, genesis and classification. Schlüchter, Ch. (Ed). Balkema, Rotterdam : 145-155.

Echelmeyer, K. and Wang Zhongxiang. 1987. Direct observation of basal sliding and deformation of basal drift at sub-freezing temperatures. Journal of Glaciology, 33 : 83-98.

ANTAR
II/01

Friedman, I., Redfield, A.C., Schoen, B. and Harris, J. 1964. The variation of the deuterium content of natural waters in the hydrological cycle. Reviews of Geophysics, 2 : 177-189.

Friedman, I., Schoen, B. and Harris, J. 1961. The deuterium concentration in arctic sea ice. Journal of Geophysical Research, 66 : 1861-1864.

Goldthwait, R.P. 1951. Development of end moraines in east-central Baffin Island. Journal of Geology, 59 : 567-577.

Gow, A.J., Ackley, G.F., Buck, K.R. and Golden, K.M. 1987a. Physical and structural characteristics of Weddell Sea pack ice. CRREL Report, 87-14, 75 p.

Gow, A.J. and Epstein, S. 1972. On the use of stable isotopes to trace the origins of ice in a floating ice tongue. Journal of Geophysical Research, 77 : 6552-6557.

Gow, A.J., Epstein, S. and Sheehy, W. 1979. On the origin of stratified debris in ice cores from the bottom of the Antarctic Ice Sheet. Journal of Glaciology, 23 : 185-192.

Gow, A.J., Tucker III, W.B. and Weeks, W.F. 1987b. Physical properties of summer sea ice in the Fram Strait, June-July 1984. CRREL Report, 87-16, 87 p.

Herron, S. and Langway, C. 1979. The debris-laden ice at the bottom of the Greenland ice-sheet. Journal of Glaciology, 23 : 193-207.

Jeffries, M.O., Krouse, H.R., Sackinger, W.M. and Serson, H.V. 1989. Stable-isotope ($^{18}O/^{16}O$) tracing of fresh, brachish and sea ice in multiyear land-fast sea ice, Ellesmere Island, Canada. Journal of Glaciology, 35 : 9-16.

Jouzel, J., Lorius, C., Petit, J.R., Jenton, C., Barkov, N.I., Kotlyakov, V.N. and Petrov, V.M. 1987. A continuous isotope temperature record over the last climatic cycle (160000 years). Nature, 329 : 403-408.

Jouzel, J., Merlivat, L. and Lorius, C. 1982. Deuterium excess in an East Antartic ice core suggests higher relative humidity at the oceanic surface during the last glacial maximum. Nature, 299 : 688-691.

Jouzel, J., Raisbeck, G., Benoist, J.P., Yiou, F., Lorius, C., Raynaud, D., Petit, J.R., Barkov, N.I., Korotkevitch, Y.S. and Kotlyakov, V.M. 1989. A comparison of deep Antarctic ice cores and their implications for climate between 65,000 and 15,000 years ago. Quaternary Research, 31 : 135-150.

Jouzel, J. and Souchez, R. 1982. Melting-refreezing at the glacier sole and the isotopic composition of the ice. Journal of Glaciology, 28 : 35-42.

Kamb, W.B. 1972. Experimental recrystallization of ice under stress. In : Flow and fracture of rocks. Heard H.C. et al. (Eds). American Geophysical Union (Geophysical Monograph 16), Washington D.C. : 211-241.

Koerner, R.M. and Fisher, D.A. 1979. Discontinuous flow, ice texture, and dirt content in the basal layers of the Devon Island Ice Cap. Journal of Glaciology, 23 : 209-221.

Krinsley, D. and Doornkamp, J. 1973. Atlas of quartz sand surface textures. Cambridge University Press, Cambridge, U.K., 91 p.

Kvlividze, V.I., Kiselev, V.F., Kurzaev, A.B. and Ushakova, L.A. 1974. The mobile water phase on ice surfaces. Surface Science, 44 : 60-68.

Lange, M.A., Ackley, S.F. and Wadhams, P. 1989. Development of sea ice in the Weddell Sea. Annals of Glaciology, 12 : 92-96.

Lorius, C. 1968. A physical and chemical study of the coastal ice sampled from a core drilling in Antarctica. Commission of snow and ice, General Assembly of Bern, September/ October 1967. I.A.H.S. Publication 79 : 141-148.

Lorius, C. and Merlivat, L. 1977. Distribution of mean surface stable isotope values in East Antarctica : observed changes with depth in the coastal area. Isotopes and impurities in snow and ice, Proceedings of the Grenoble Symposium August/ September 1975, I.A.H.S., Publication 118 : 127-137.

Lorius,C., Raynaud, D. and Dolle, L. 1968. Densité de la glace et étude des gaz en profondeur dans un glacier antarctique. Tellus, XX, 3 : 449-459.

Lorius, C. and Vallon, M. 1967. Etude structurographique d'un glacier antarctique. C.R. Academie des Sciences. Série D, Tome 265 : 315-318.

ANTAR II/01

Lyons, J.B., Savin, S.M. and Tamburi, A.J. 1971. Basement ice, Ward Hunt Ice Shelf, Ellesmere Island, Canada. Journal of Glaciology, 10 : 93-100.

Mader, H.M. 1990. Water veins in polycrystalline ice. Ph. D. Thesis, Faculty of Science, Department of Physics, University of Bristol, 190 p.

Mahaney, W.C. 1990a. Macrofabrics and quartz microstructures confirm glacial origin of Sunnybrook drift in the Lake Ontario Basin. Geology, 18 : 145-148.

Mahaney, W.C. 1990b. Ice on the Equator. Wm. Caxton Ltd., Sister Bay, Wisconsin, 386 p.

Mahaney, W.C. 1991. Glacial crushing, weathering and diagenetic histories of quartz grains inferred from scanning electron microscopy. In : Glacial Environments - processes, sediments and landforms. Menzies, J. (Ed). Pergamon Press, New York, in press.

Mahaney, W.C., Vortisch, W.B. and Julig, P. 1988. Relative differences between glacially-crushed quartz transported by mountain and continental ice - some examples from North America and East Africa, American Journal of Science, 288 : 810-826.

Meese, D.A. 1989. The chemical and structural properties of sea ice in the Southern Beaufort Sea. CRREL Report, 89-25 : 134 p.

Merlivat, L., Lorius, C., Majzoub, M. Nief, G. and Roth E. 1967. Etudes isotopiques en profondeur d'un glacier en Antarctique, Isotopes in Hydrology, International Atomic Energy Agency, Vienna : 671-681.

Merlivat, L., Lorius, C. and Nief, G. 1966. Etudes isotopiques d'un glacier en Antarctique, Comptes Rendus de l'Académie des Sciences, 263 : 414-416.

Moser, H. and Stichler, W. 1980. Environmental isotopes in ice and snow.In : Handbook of environmental isotope geochemistry. Fritz, P. and Fontes, J.C. (Eds). Elsevier, New York, 1 : 141-178.

Nougier, J. and Lorius, C. 1969. Etude géologique et physico-chimique de carottes profondes de glace (Terre Adélie). Revue de géographie physique et de géologie dynamique. 11 : 165-170.

O'Neil, J.R. 1968. Hydrogen and Oxygen isotope fractionation between ice and water. Journal of Physical Chemistry, 72 : 3683-3684.

Paren, J.G. and Walker, J.C.F. 1971. The influence of limited solubility on the electrical and mechanical properties of ice. Nature, 230 : 77-79.

Peel, D.A. and Clausen, H.B. 1982. Oxygen-isotope and total beta-radioactivity measurements on 10 m ice cores from the Antarctic Peninsula. Journal of Glaciology, 28 : 43-55.

Potter, J.R., Paren J.G. and Loynes, J. 1984. Glaciological and oceanographic calculations of the mass balance and oxygen isotope ratio of a melting ice shelf. Journal of Glaciology, 30 : 161-170.

Raynaud, D., Delmas, R., Ascencio, J.M. and Legrand, M. 1982. Gas extraction from polar ice cores: a critical issue for studying the evolution of atmospheric CO_2 and ice-sheet surface elevation. Annals of Glaciology, 3 : 265-268.

Raynaud, D., Lorius, C., Budd, W.F. and Young, N.W. 1979. Ice flow along an I.A.G.P. flow line and interpretation of data from an ice core in Terre Adélie, Antarctica. Journal of Glaciology, 24 : 103-115.

Riley, J.P. and Skirrow, G. 1965. Chemical Oceanography. Academic Press.

Robin, G. de Q. 1979. Formation, flow, and disintegration of ice shelves. Journal of Glaciology, 24 : 259-271.

Schwarzacher, W. 1959. Pack-ice studies in the Arctic Ocean. Journal of Geophysical Research, 64 : 2357-2367.

Shreve, R.L. 1984. Glacier sliding at subfreezing temperature. Journal of Glaciology. 30 : 341-347.

Souchez, R.A. 1967. The formation of shear moraines: an example in South Victoria Land, Antarctica. Journal of Glaciology, 6 : 837-843.

Souchez, R. and Jouzel, J. 1984. On the isotopic composition in δD and $\delta^{18}O$ of water and ice during freezing. Journal of Glaciology, 30 : 369-372.

Souchez, R., Lemmens, M., Lorrain, R., Tison, J.-L., Jouzel, J. and Sugden D. 1990. Influence of hydroxyl-bearing minerals on the isotopic composition of ice from the basal zone of an ice sheet. Nature, 345 : 244-246.

Souchez, R., Tison, J.-L. and Jouzel. 1987. Freezing rate determination by the isotopic composition of the ice. Geophysical Research Letters, **14** : 599-602.

Souchez, R., Tison, J.-L. and Jouzel, J. 1988. Deuterium concentration and growth rate of Antarctic first-year sea ice. Geophysical Research Letters, 15 : 1385-1388.

Tison, J.-L. and Haren J. 1989. Isotopic, chemical and crystallographic characteristics of first-year sea ice from Breid Bay (Princess Ragnhild Coast - Antarctica). Antarctic Science, 3 : 261-268.

Ward, W.H. 1952. The glaciological studies of the Baffin Island expedition, 1950. Part II. The physics of deglaciation in central Baffin Island. Journal of Glaciology, 2 : 19-22.

Wang, J., Robinson, C. and Edelman, I. 1953. Self-diffusion and structure of liquid water. III. Measurement of the self-diffusion of liquid water with H2, H3, and O18 as tracers. Journal of the American Chemical Society, 75 : 466-470.

Weeks, W.F. and Ackley, S.F. 1986. The growth, structure, and properties of sea ice. In : The geophysics of sea ice. Untersteiner, N. (Ed). NATO ASI Series B: Physics vol. 146. Plenum Press, New york : 9-164.

Weertman, J. 1957. On the sliding of glaciers. Journal of Glaciology, 3 : 33-38.

Weertman, J. 1961. Mechanism for the formation of inner moraines found near the edge of cold ice caps and ice sheets. Journal of Glaciology, 3 : 965-978.

Weertman, J. 1964. The theory of glacier sliding. Journal of Glaciology, **5** : 287-303.

Yao, T.D., Petit, J.R., Jouzel, J., Lorius, C. and Duval, P. 1990. Climatic record from an ice margin area in East Antarctica. Annals of Glaciology, 14 : 323-327.

NUMERICAL SIMULATIONS OF WIND-DRIVEN FLOWS IN THE ANTARCTIC COASTAL ZONES

M. Fettweis, C.-H. Yu
and J. Berlamont

Contents

Abstract

This paper gives a summary of the results obtained during the Antar02/II contract. Two hydrodynamic numerical models are presented. The first one consist of a 2.5D baroclinic model and the second one of a 3D barotropic model. The 2.5D model solves the 3D hydrodynamic equations on a vertical plane, the derivatives perpendicular to the plane are considered to be zero. Both models are explicit in time and make use of the MAC method to solve the equations. The 2.5D model is used to calculate the influence of stratification on the wind induced currents on the continental shelf and the shelf break in presence of an ice cover. and to simulate the currents off the coast of Adélie land forced by a katabatic wind. The 3D model has been applied to a coastal area at Terra Nova. The ocean is again forced by a katabatic wind. Interesting to note is that the surface flow calculated by both models is in agreement with the theory of coastal polynia formation.

1   Introduction

The purpose of this study is to simulate the ocean circulation in the Antarctic coastal zone. To do this two numerical models have been developed and applied to two different zones off the Antarctic coastal zone.

The first model is a so-called 2.5D model. The model is first used to investigate the influence of stratification on the wind induced flows in the vicinity of coastal boundaries and marginal sea-ice edges. The second application is dealing with the study of the hydrodynamic behaviour of the coastal zone at Adélie land forced by a katabatic wind. The second model consist of a 3D model. The model is applied to the Terra Nova coastal area (175 km by 36 km) where the flow due to katabatic winds is simulated.

ANTAR II/02

The models are driven for two application by katabatic winds. Katabatic winds are gravity driven currents forced by the cooling of air on a sloped surface. The importance of this phenomenon consist of, if the forcing is sufficiently strong, the formation of coastal polynias. The hydrodynamic and thermodynamic processes occurring in these open water zones are responsible for the formation of bottom water. The surface wind data for these simulation have been produced by the atmospheric models of the Institut d'Astronomie et de Géophysique G.Lemaitre from the Université Catholique de Louvain(UCL).

This paper gives a summary of the obtained results. The models and the numerical schemes used are described and discussed. In the next chapter the 2.5D model is presented together with an application dealing with a stratified ocean. Chapter 3 is devoted to the description of the 3D model and to the presentation of some simple test calculations. The 3D model is available for both "Cartesian" and "spherical" coordinates. The results of the katabatic wind forcing can be found in the fourth chapter. The conclusion and the final remarks are given in chapter 5.

2 2.5D Ocean Model

2.1 Basic model equations

The 2.5D model solve the 3D hydrodynamic equations in the form presented below. All the derivatives with respect to the y-direction, *i.e.* the uniform direction, are considered to be zero. The pressure is assumed to be hydrostatic and the energy loss due to friction is parameterized by means of eddy viscosity coefficients. The models is baroclinic and is using the Boussinesq approximation.

The equations of continuity and momentum are

$$\frac{\partial u}{\partial x} + \frac{\partial w}{\partial z} = 0 \tag{1}$$

$$\frac{\partial u}{\partial t} + u\frac{\partial u}{\partial x} + w\frac{\partial u}{\partial z} + \frac{1}{\rho}\frac{\partial p}{\partial x} - fv = \frac{\partial}{\partial x}(A_h\frac{\partial u}{\partial x}) + \frac{\partial}{\partial z}(A_v\frac{\partial u}{\partial z}) \tag{2}$$

$$\frac{\partial v}{\partial t} + u\frac{\partial v}{\partial x} + w\frac{\partial v}{\partial z} + \frac{1}{\rho}\frac{\partial p}{\partial y} + fu = \frac{\partial}{\partial x}(A_h\frac{\partial v}{\partial x}) + \frac{\partial}{\partial z}(A_v\frac{\partial v}{\partial z}) \tag{3}$$

the hydrostatic equation is

$$\frac{\partial p}{\partial z} - \rho g = 0 \tag{4}$$

and under the assumption that density and salinity are in a linear relationship we can use density in the transport equation and write the density equation as follows

$$\frac{\partial \rho}{\partial t} + u\frac{\partial \rho}{\partial x} + w\frac{\partial \rho}{\partial z} = \frac{\partial}{\partial x}(K_h\frac{\partial \rho}{\partial x}) + \frac{\partial}{\partial z}(K_v\frac{\partial \rho}{\partial z}) \tag{5}$$

where:

t	: is time;
x	: is the coordinate in eastward direction;
y	: is the coordinate in northward direction;
z	: is the vertical coordinate, positive downward;
u	: is the velocity component in eastward direction $(\mathrm{ms^{-1}})$;
v	: is the velocity component in northward direction $(\mathrm{ms^{-1}})$;
w	: is the vertical velocity component $(\mathrm{ms^{-1}})$;
p	: is the pressure $(\mathrm{Nm^{-2}})$;
ρ	: density of the water $(\mathrm{kgm^{-3}})$;
A_h	: is the horizontal eddy viscosity coefficient $(\mathrm{ms^{-2}})$;
A_v	: is the vertical eddy viscosity coefficient $(\mathrm{ms^{-2}})$;
K_h	: is the horizontal eddy diffusion coefficient $(\mathrm{ms^{-2}})$;

K_v : is the vertical eddy diffusion coefficient (ms^{-2});

g : is the acceleration due to gravity $(=9.81\ ms^{-2})$;

f : is the Coriolis parameter (s^{-1}).

The pressure gradient normal to the vertical plane, *i.e.* $\partial p/(\rho\partial y)$, is problem specific (taken as external forcing, computed according to some additional assumptions, ...), see Yu *et al.*(1990) where it has been calculated by a 2D horizontal model. The boundary conditions have been chosen as follows. At the coastal walls u and v are supposed to be zero, at the bottom all the three velocity components are zero. At an open boundary the horizontal velocity gradients are set to zero. At the sea surface the rigid lid boundary condition (*i.e.* $w=0$) is applied and the vertical diffusion terms are written as $-A_v\partial u/\partial z = \tau_x/\bar{\rho}_o$ and $-A_v\partial v/\partial z = \tau_y/\bar{\rho}_o$. τ_x and τ_y are the wind stresses in x- and y- direction respectively. In order to prevent unstable stratification the vertical advection is implicitly treated using the convective adjustment scheme, *i.e.* if the upper layer has a higher density than the lower one the density value in both layers is replaced by the weighted average over both layers. This procedure has been used by *e.g.* Bryan(1969).

ANTAR
II/02

2.2 The numerical model

The variables which have to be solved are u, v, w, and p. In case of the rigid lid assumption the hydrostatic equation (4) is integrated from the undisturbed surface to the bottom to give:

$$p = g\int_0^z \rho dz' + C \tag{6}$$

The constant of integration corresponds to the pressure at the sea surface ($z = 0$), *i.e.* p_a and the pressure on the rigid lid due to the flow, *i.e.* p_l, we obtain thus

$$p = p_a + p_l + gz\bar{\rho}_o \tag{7}$$

where

$$\bar{\rho}_o = \frac{1}{z}\int_0^z \rho dz' \tag{8}$$

We assume that the air pressure at the surface is constant and the first term from eq. (6) can be dropped. Taking the gradient in x-direction and dividing eq. (6) by ρ and putting the term in eq. (2) gives

$$\frac{\partial u}{\partial t} + u\frac{\partial u}{\partial x} + w\frac{\partial u}{\partial z} + \frac{1}{\rho}\frac{\partial p_l}{\partial x} + \frac{gz}{\rho}\frac{\partial \bar{\rho}_o}{\partial x} - fv = \frac{\partial}{\partial x}(A_h\frac{\partial u}{\partial x}) + \frac{\partial}{\partial z}(A_v\frac{\partial u}{\partial z}) \tag{9}$$

The set of equations which we have at our disposal is (1), (9) and (3). The rigid lid approximation eliminates surface waves and allows thus to use bigger timesteps, the stability condition is now (Niebauer, 1982):

$$\Delta t \le \frac{\Delta z^2}{2A_v} \tag{10}$$
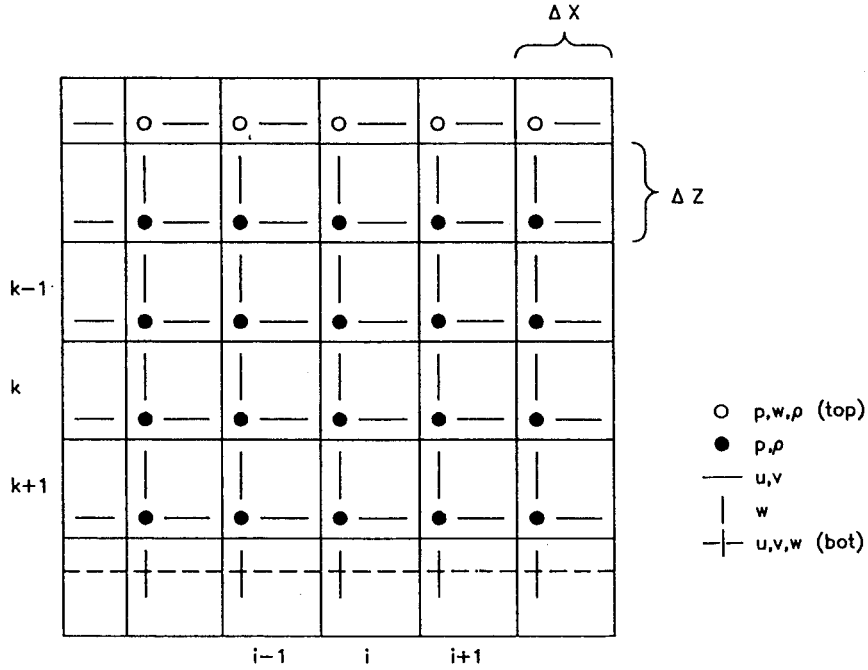
Figure 1: Numerical grid (B-grid) used by the 2.5D model.

2.2.1 Finite difference equations

The equations (1), (7) and (3) are solved using an explicit scheme, (Fettweis *et al.*, 1990). The variables are described on a staggered grid system (B-grid), see figure 1. The finite difference representation of the continuity equation and the momentum equations are presented using the notation of figure 1. The subscripts i, k are the space coordinates of the grid in x and z direction respectively, the superscript n indicates the time level and Δx is the horizontal and Δz the vertical distance between two successive u/v points. Δz is not necessarily constant, but in order to make the equations not to complicated it is assumed to be constant in the following description of the finite difference equations. The equations are valid away from the boundaries.

Continuity equation

$$\frac{u_{i,k}^{n+1} - u_{i-1,k}^{n+1}}{\Delta x} + \frac{w_{i,k+1}^{n+1} - w_{i,k}^{n+1}}{\Delta z} = 0 \tag{11}$$

Momentum equations

$$\frac{u_{i,k}^{n+1} - u_{i,k}^n}{\Delta t} + adu_{i,k}^n - fv_{i,k}^{n+1} - \frac{A_h(u_{i+1,k}^n - 2u_{i,k}^n + u_{i-1,k}^n)}{\Delta x^2}$$

$$- \frac{A_v(u_{i,k+1}^n - 2u_{i,k}^n + u_{i,k-1}^n)}{\Delta z^2} + \frac{1}{\rho_o}(\frac{\partial p_l}{\partial x})_i^{n+1} + \frac{gz}{\rho_o}(\frac{\partial \bar\rho_o}{\partial x})_i^n = 0 \qquad (12)$$

and

$$\frac{v_{i,k}^{n+1} - v_{i,k}^n}{\Delta t} + adv_{i,k}^n + fu_{i,k}^n - \frac{A_h(v_{i+1,k}^n - 2v_{i,k}^n + v_{i-1,k}^n)}{\Delta x^2}$$

$$- \frac{A_v(v_{i,k+1}^n - 2v_{i,k}^n + v_{i,k-1}^{n+1})}{\Delta z^2} + \frac{1}{\rho_o}(\frac{\partial p}{\partial y})_i = 0 \qquad (13)$$

where $adu_{i,k}^n$ and $adv_{i,k}^n$ are the advection terms they are replaced by a first order upwind scheme.

The density equation is written in finite differences as follows:

$$\frac{\rho_{i,k}^{n+1} - \rho_{i,k}^n}{\Delta t} + ad\rho_{i,k}^n - \frac{K_h(\rho_{i+1,k}^n - 2\rho_{i,k}^n + \rho_{i-1,k}^n)}{\Delta x^2}$$

$$- \frac{K_v(\rho_{i,k+1}^n - 2\rho_{i,k}^n + \rho_{i,k-1}^{n+1})}{\Delta z^2} = 0 \qquad (14)$$

where $ad\rho_{i,k}^n$ are the advection terms (1st order upwind). In order to prevent unstable stratification the vertical advection is implicitly treated using the convective adjustment scheme, *i.e.* if the upper layer has a higher density then the lower one the density value in both layers is replaced by the (weighted) average over both layers, (see *e.g.* van Ypersele, 1986).

2.2.2 Computational scheme

Equation (13) can be solved directly since all the terms are explicit. Solving the u-momentum equation (12) takes more computations, it cannot be solved directly because of the pressure gradient term which is supposed to be implicit. This pressure gradient term is calculated in the following way:

The velocity in x-direction is splitted in two parts, a part containing the explicit terms (and the Coriolis term which contains already v at $n+1$) and another one containing the implicit ones:

$$u_{i,k}^{n+1} = u_{i,k}' + u_{i,k}'' \qquad (15)$$

where u' and u'' are equals to:

$$u_{i,k}' = u_{i,k}^n + (-advec_{i,k}^n + diff_{i,k}^n + fv_{i,k}^{n+1})\Delta t \qquad (16)$$

$$u''_{i,k} = -\frac{1}{\rho_o}(\frac{\partial p_l}{\partial x})^{n+1}_i \Delta t \tag{17}$$

$advec^n_{i,k}$ are the advective terms and $diff^n_{i,k}$ the diffusion terms. To calculate the pressure gradient the continuity equation (1) is integrated over the vertical (from top, $k = 1$, to $k = hz - 1$, with hz the bottom coordinate). The vertical velocity at the surface and at the bottom is zero (rigid lid condition) so that the vertical integrated continuity equation at timestep $n + 1$ and written in finite differences takes the form

$$h_{i+1} \sum_{k=1}^{hz-1} (\omega_k u^{n+1}_{i+1,k}) - h_i \sum_{k=1}^{hz-1} (\omega_k u^{n+1}_{i,k}) = 0 \tag{18}$$

where ω_k is a weighting factor depending on the vertical grid size, in case of constant vertical grid size: $\omega_1 = 0.5\Delta z/h_i$ and $\omega_2...\omega_{hz-1} = \Delta z/h_i$. Equation (15) is put in eq. (18) and together with eqs.(16) and (17) the following relationship is obtained between the pressure gradient at $i + 1$ and i

$$(\frac{\partial p_l}{\partial x})^{n+1}_{i+1}\Delta t = \frac{\rho_o}{h_{i+1}}(h_{i+1} \sum_{k=1}^{hz-1} (\omega_k u'_{i+1,k}) - h_i \sum_{k=1}^{hz-1} (\omega_k u'_{i,k}) + \frac{h_i}{\rho_o}(\frac{\partial p_l}{\partial x})^{n+1}_i \Delta t) \tag{19}$$

Starting from a lateral boundary and using the lateral boundary condition the pressure gradient can be calculated from eq. (19). Having obtained the pressure gradient the u-velocity can be calculated using equation (15).

After u and v have been calculated for the whole domain for $n + 1$, the vertical velocity is obtained by solving the continuity equation (11) from bottom to top. The vertical velocity is thus the result of fulfilling the continuity equation. The last step consist of calculating the new density values.

2.3 Application: Upwelling along a shelf break in a stratified ocean

The sudden change in bathymetry at a continental margin forms a kind of barrier for the ocean currents and can result, depending on the direction of the currents, in upwelling along the shelf break. Upwelling in an open ocean is usually induced by wind blowing over the water surface (O'Brien et al., 1977). Oceans in high latitudes are seasonally covered with sea ice. Along the ice edges oceanic frontal systems occur due to large horizontal density gradients. The first to report about the phenomenon of ice edge upwelling as a result of a measurement campaign in the Arctic ocean were Buckley et al.(1979). The ice edge is acting similar to wind forcing as a continental boundary, see Røed and O'Brien(1983) and Røed(1983) and the upwelling is depending on the wind direction, force and duration. The deep ocean is involved as a driving force for the circulation on the shelf with interactions taking place across the shelf break.

The purpose of this application is to present the results of simulating the interaction occurring at an shelf break with a shelf covered with sea ice and to look at the coupled upwelling due the ice edge and the continental slope, see also Fettweis *et al.*(1991b). In order to separate the different effects, such as varying bathymetry, ice cover and density stratification, melting, two different cases have been set up with different bathymetries. The cases are idealized and thus not realistic but they can give information about the real situations.

Most of the existing numerical models of coastal upwelling are based on the application of Ekman's theory. Smith(1980) concluded from measurements done in the coastal regions off Oregon, northwest Africa and Peru that the flow patterns are consistent with this theory. Modelling upwelling along a shelf break requires the incorporation of the bathymetry, the stratification of the ocean, time variability and the effect of the bottom friction in the model. A review of numerical models of shelf break dynamics is presented by Johnson and Rockliff(1986). They divide the various models depending on their complexity, *i.e.* from simple steady state barotropic models to continously stratified unsteady models. Previous studies about ice edge upwelling are *e.g.* Niebauer(1982), who investigated the response of a shallow sea covered with a non moving ice layer to wind forcing and Ikeda(1985) who allowed the ice to move and included a deep ocean in the calculation but did not take into account any thermodynamics of ice.

ANTAR
II/02

2.3.1 Description of the cases

Two cases have been set up, the first one (Case 1) consist of a flat basin 500 km long and 400m deep. For the second one (Case 2) a shelf, shelf break and ocean are considered. The shelf is 400 m and the ocean 4000 m deep. The shelf zone extents over 160 km and is interrupted by a continental slope of 5 percent (*i.e.* 3800 m in 72 km), see figure 2a. These dimension are a idealized version of the one found off the coast of Adelie land in Antarctica. The horizontal grid size is 4km and the vertical one is 10 m for Case 1 and 20 m to 200 m for Case 2. The Coriolis parameter is constant (at 67.5°S), the horizontal eddy viscosity has been chosen as 5000 ms^{-2}, the vertical one as 0.01 ms^{-2}, the horizontal eddy diffusivity of density is 100 ms^{-2} and the vertical one 0.01 ms^{-2}. The density diffusion values are low, so that advection is the main process for density transportation. A wind of 10 ms^{-1} is blowing parallel to the coast in the direction that favours upwelling and continues until day 30. The ocean has or a constant density (1026 kgm^{-3}) or is stratified with density varying between 1026 and 1027 kgm^{-3}, see figure 2b. The surface of the ocean can be covered by a non moving ice layer, the ice cover is 160 km long and is thus covering whole the shelf zone of Case 2. Melting of ice is taken into account by lowering the density under the ice layer (from 1026 to 1024 kgm^{-3}).

2.3.2 Results of case 1

As was mentined above, the purpose of this experiment is to examine the effect of bathymetry, density and ice on the wind induced upwelling. Different runs have been
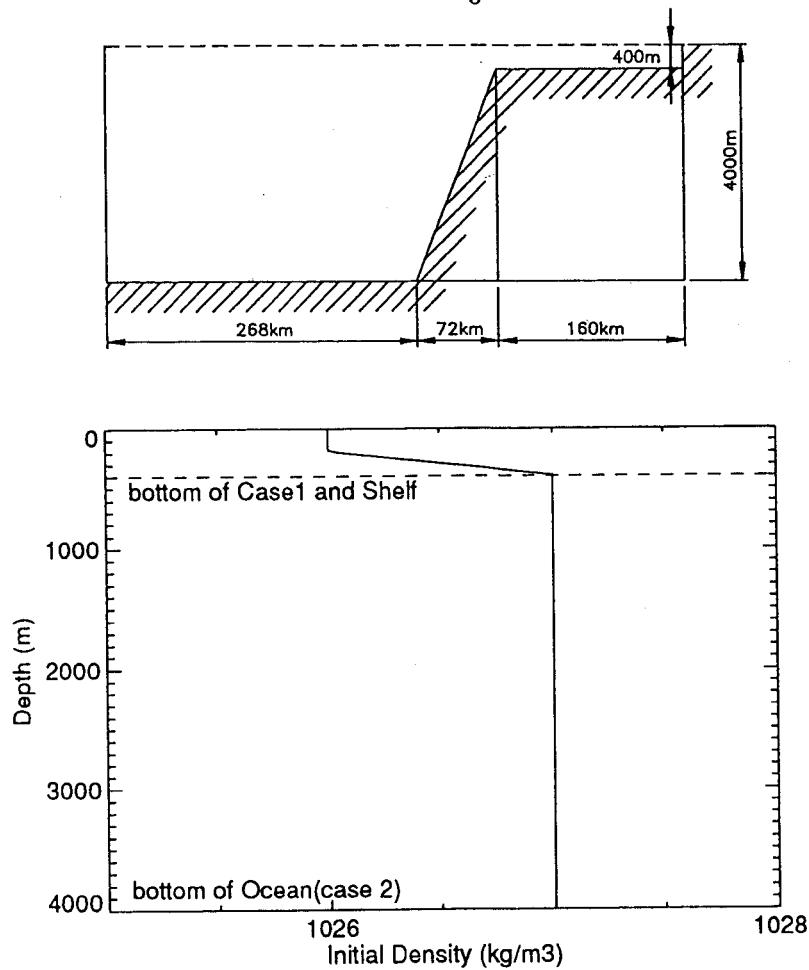
Figure 2: (a) Dimension of the basin for Case 2. (b) Initial density stratification.

carried out in order to separate the effects.

In figure 3 is shown the flow field for the ice free shelf with constant density (a) and variable density (b) distribution. One can distinguish a relatively strong top and bottom Ekman layer and upwelling at the coast. Due to this upwelling density is transported upward (for the variable density case), see the isopycnal lines of figure 4a, resulting in a wider upwelling zone due to flow of lighter water from the open sea towards the coast. The higher density in the deeper part of the sea is however restricting upwelling and we can observe a lower vertical velocity especially in the deepest 200 m.

For the next run the ocean is covered by an ice layer, the ice is acting as a continental boundary and is inducing upwelling. The density field is constant, variable or variable with melting of ice. The same remarkes as for the ice free case are valid, *i.e.* the density stratification is decreasing the upwelling velocity but horizontally extending the upwelling zone. The effects of melting have little influence on the flow field. We can distinguish the following differences when compared with the no-melting/variable density case: Under the ice the horizontal velocity is a little higher (due to the bigger density gradient) and at and under the ice edge upwelling is smaller (decreasing of density at top). In figure 5 the

flow field for constant density (a) and for variable density with melting (b) are presented. In figure 4b the density distribution for the melting case is shown.

2.3.3 Results of case 2

In this section the results of the shelf/ocean model are presented. Again in the first runs the ocean is ice free and has a constant or variable density. The flow field for these two situations is shown in figure 6. We can see that along the slope upwelling is occurring with downwelling above the starting of the slope. The flow in the deep part is almost zero except at the top and at the bottom where a week Ekman layer is present. The density stratification has a strong influence on the upwelling where the sudden density variation occurs (at about 200 m). A double vertical eddy has been formed at both sides of the continental break for the constant density case. With varying density the flow is slow down by the pycnocline and the eddy is not reaching the surface.

When the shelf is covered with ice, we observe for the constant density case a smaller upwelling along the slope than for the ice free situation. The reason can be found in the fact that because the ice is protecting the water from the wind the surface flow near the ice edge is smaller giving thus smaller upwelling. Melting has again only little influence on the flow. An enlargement of the flow in the shelf break region for the constant and the variable density case is presented in figure 7 and the stratification for both variable density cases in figure 8.

2.3.4 Discussion

The 2.5D baroclinic model presented in this chapter has been used to simulate the upwelling process along the slope and along a marginal ice edge. The wind is blowing parallel to the ice edge/coast in upwelling favorable direction. A flow perpendicular to the ice edge/coast is generated due to the Coriolis force. The upwelling is carrying denser water upward, a horizontal density gradient is formed and the resulting density current decreases the upward flow.

For the flat bottom case (Case 1) the initial density stratification is sufficiently high to decrease the magnitude of the upward flow and to enlarge the upwelling zone. Melting has little influence on the flow structure but changes (of course) the density field due to diffusion. The ligther water under the ice is mixed with the denser water under it and at the ice edge a high horizontal density gradient is occurring, see figure 8b.

Upwelling characteristics along the slope (Case 2) are strongly influenced by the presence of an ice cover, upwelling is reduced substantially with ice. The initially strong density variation is also not stimulating the upwelling flow. The denser water which is upwelling at the break is deviated and increasing the bottom flow over the shelf when compared with the constant density cases. Although the ice is simulated in a simplified way, the model is able to produce the main features occuring at an ice edge and at a continental slope.
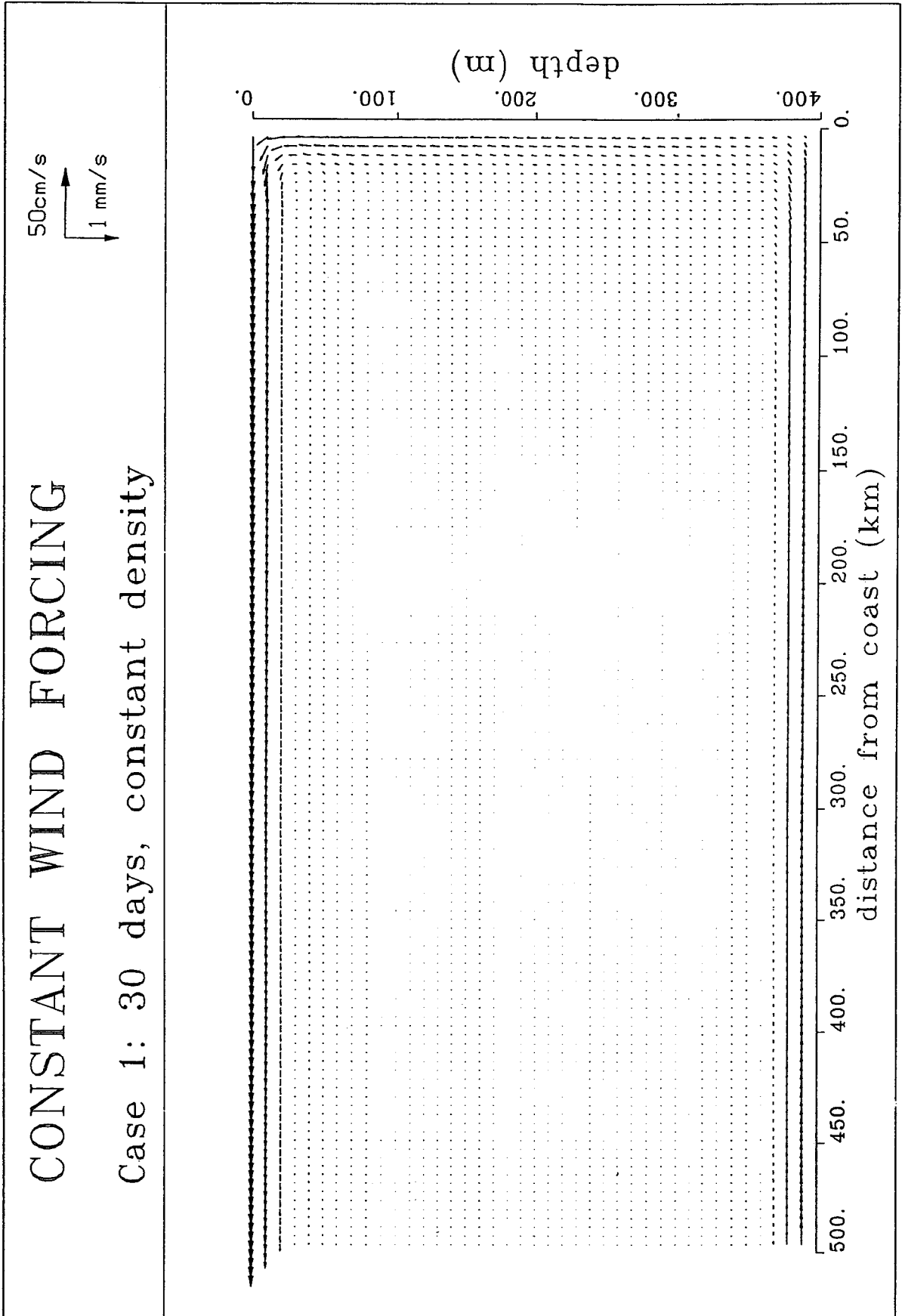
Figure 3a: Flow field of Case 1 - ice free shelf with constant density.
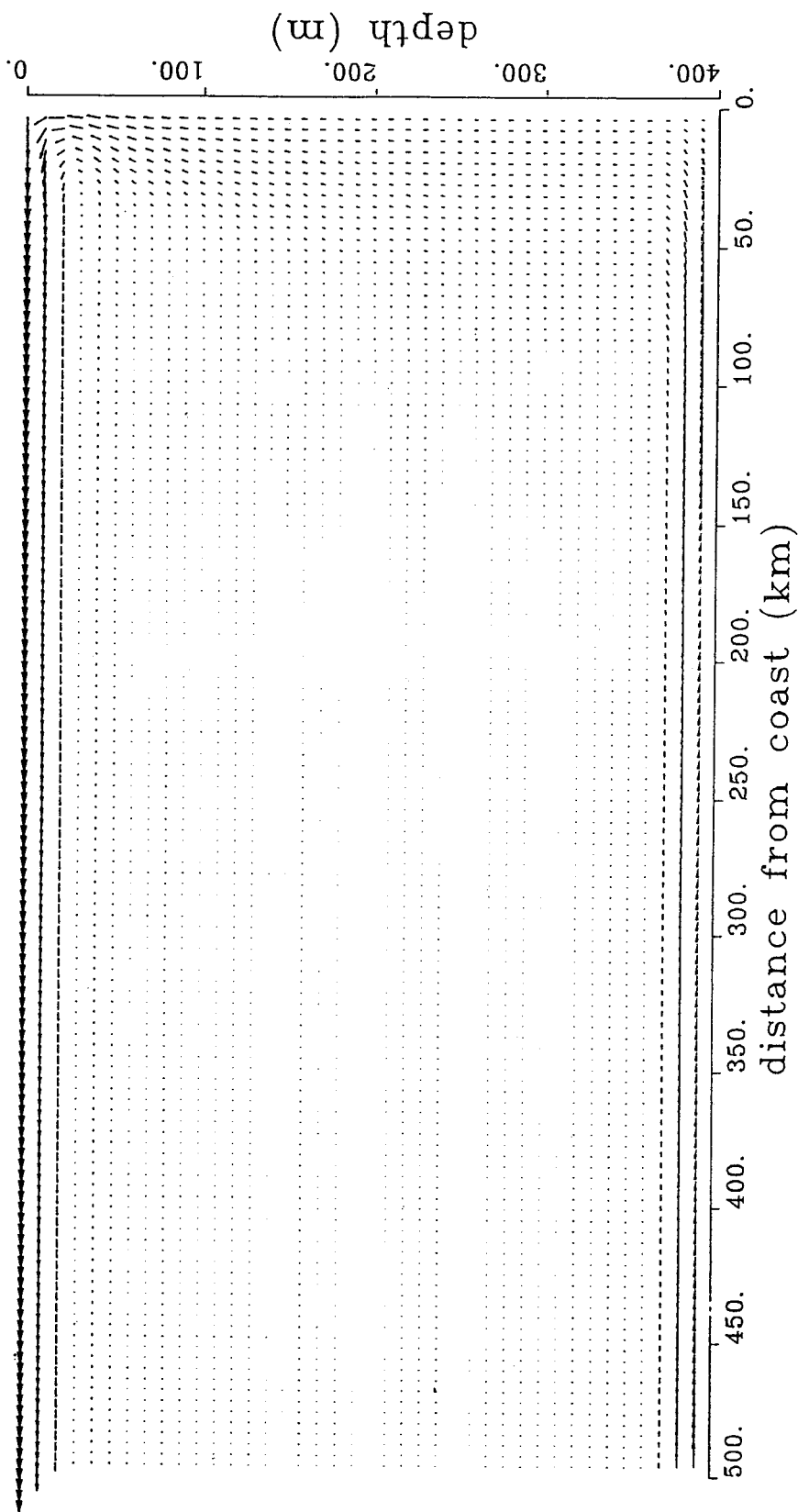
Figure 3b: Flow field of Case 1 - ice free shelf with variable density.

Case 1: 30 Days, ice cover

Density (kg/m3)

1026.1 — 1026.1

1026.5 — 1026.5

1026.9 — 1026.9

Distance from coast in km

Case 1: 30 Days, ice cover, melting

Density (kg/m3)

1025.5

1026.1

1026.1

1026.1

1026.7 — 1026.7 —

Distance from coast in km
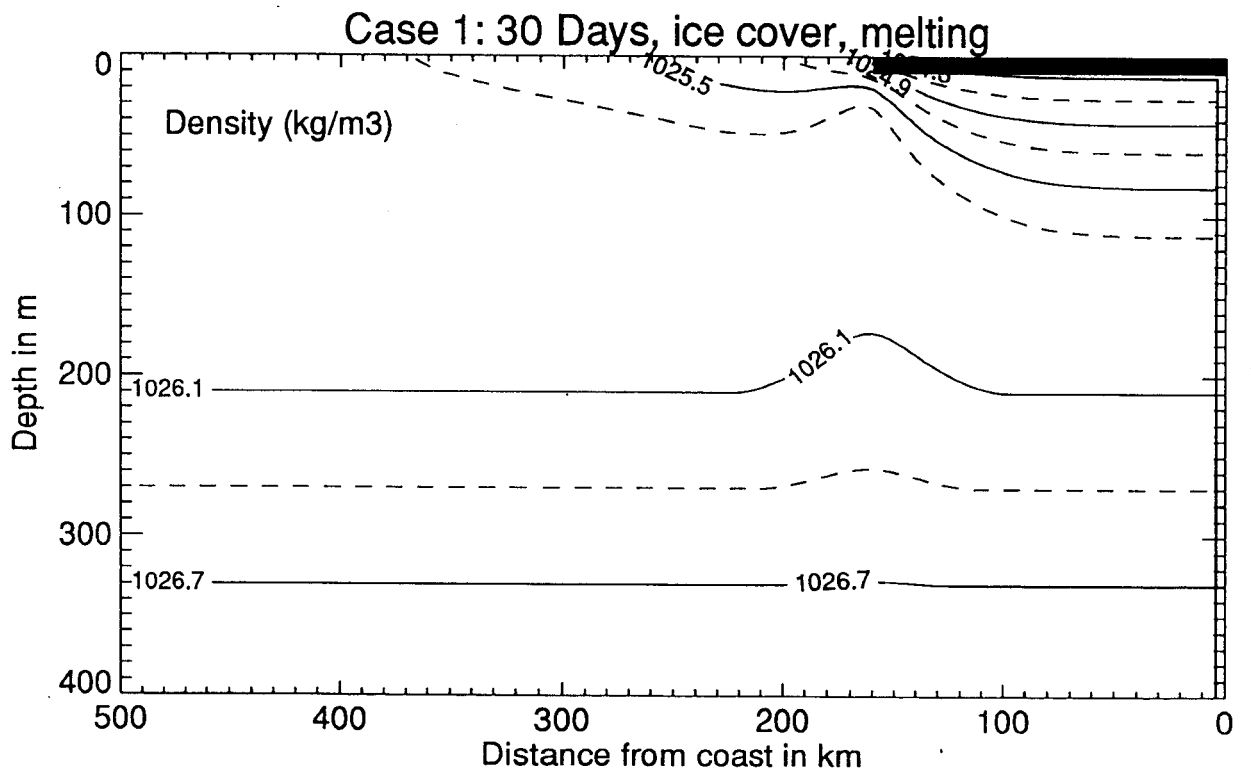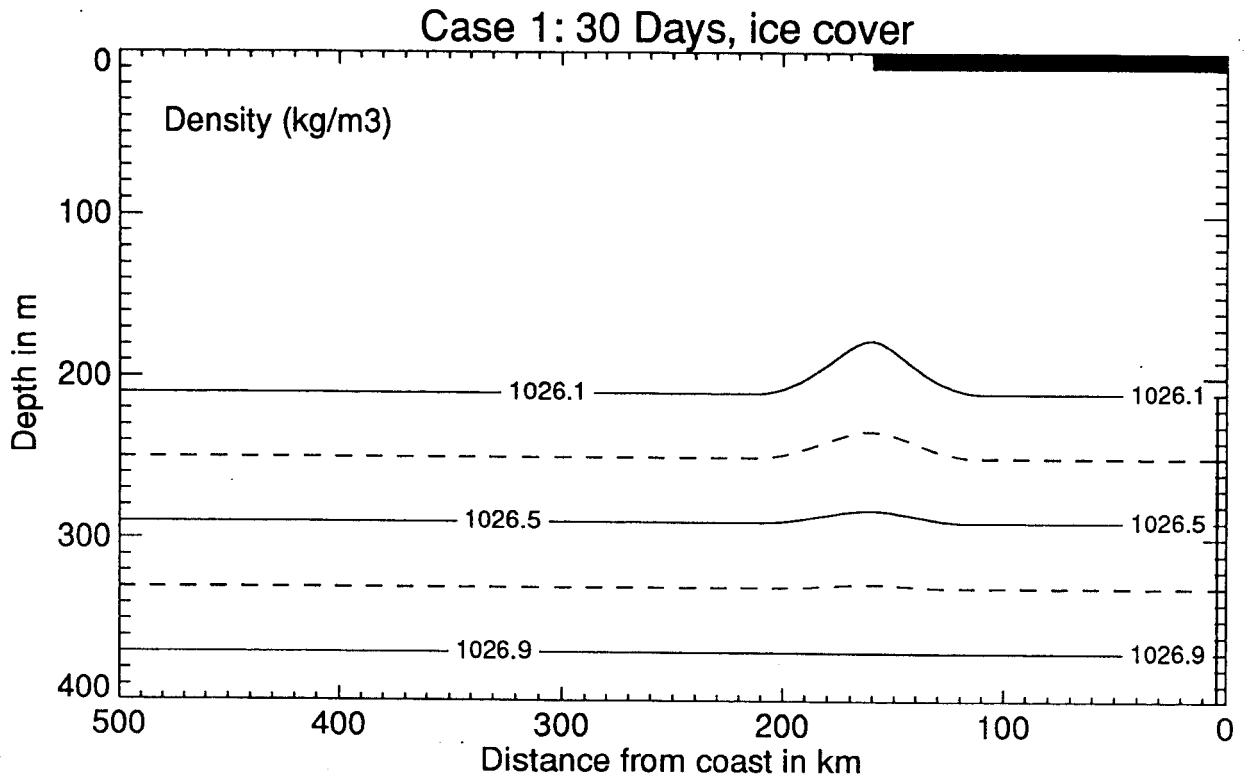
Figure 4: Isolines of density (Case 1) (a)variable density (b)variable density with melting.
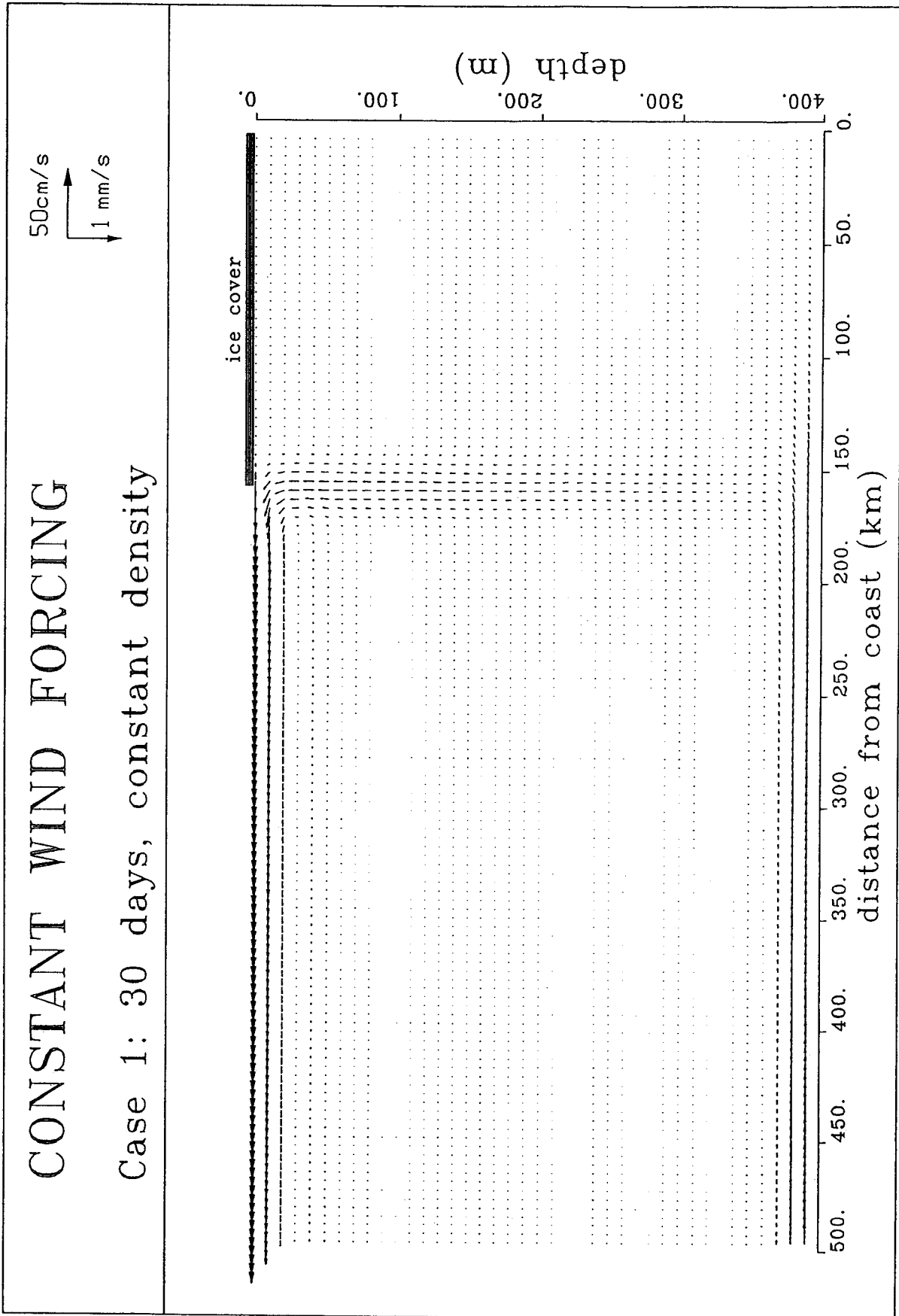
Figure 5a: Flow field of Case 1 - ice covered shelf with constant density.
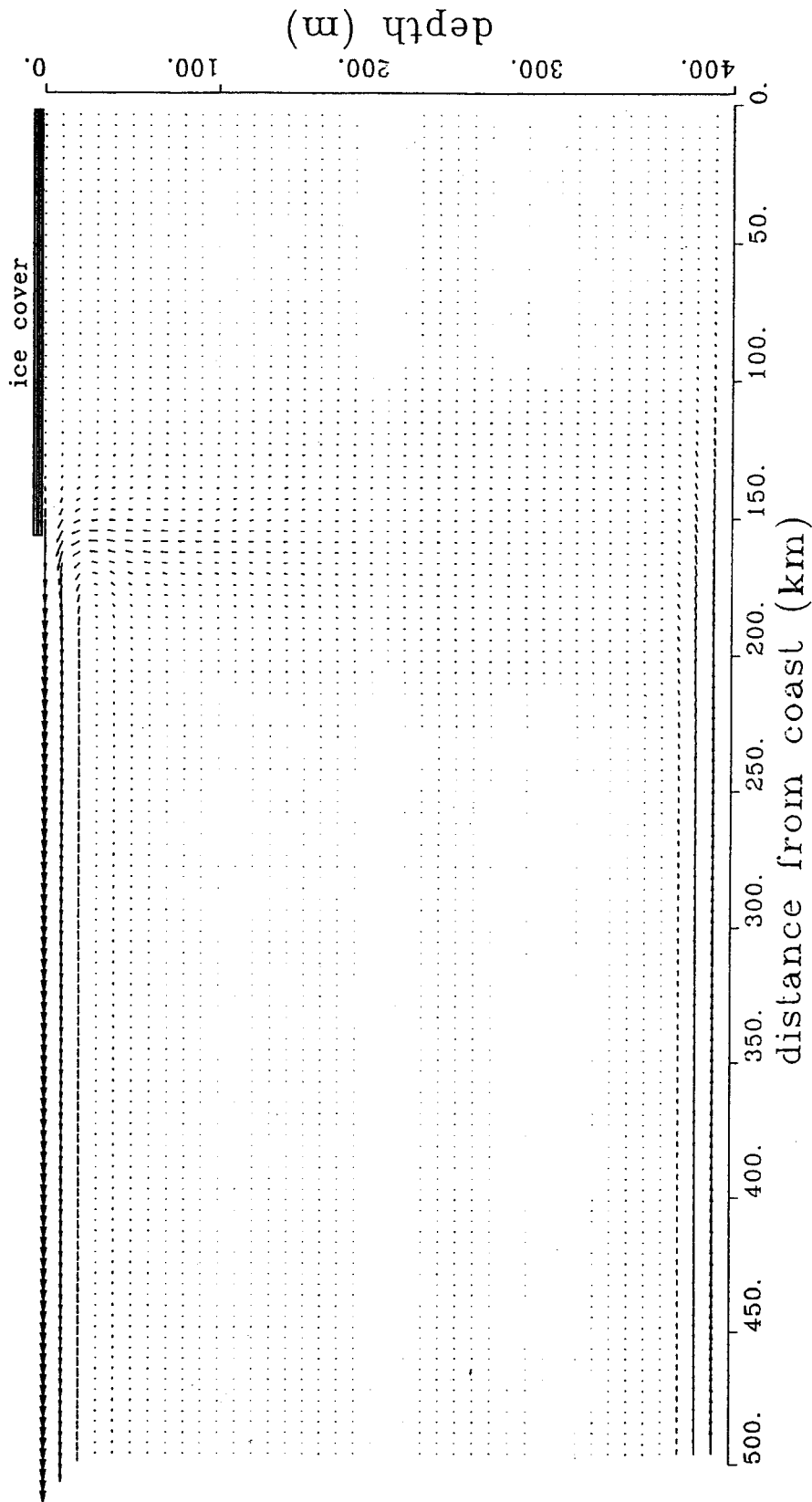
Figure 5b: Flow field of Case 1 - ice covered shelf with variable density and melting.
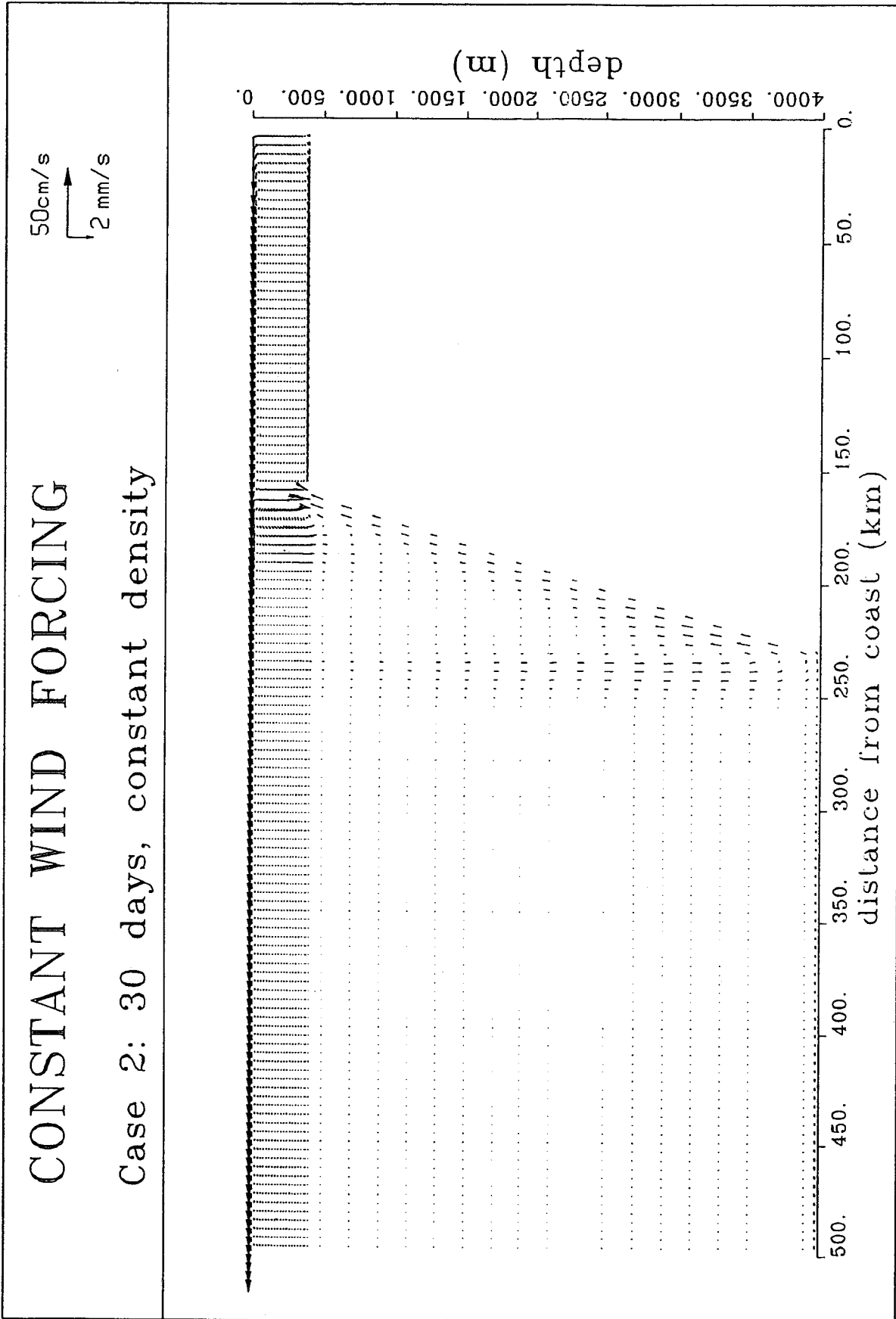
Figure 6a: Flow field of Case 2 - ice free with constant density.
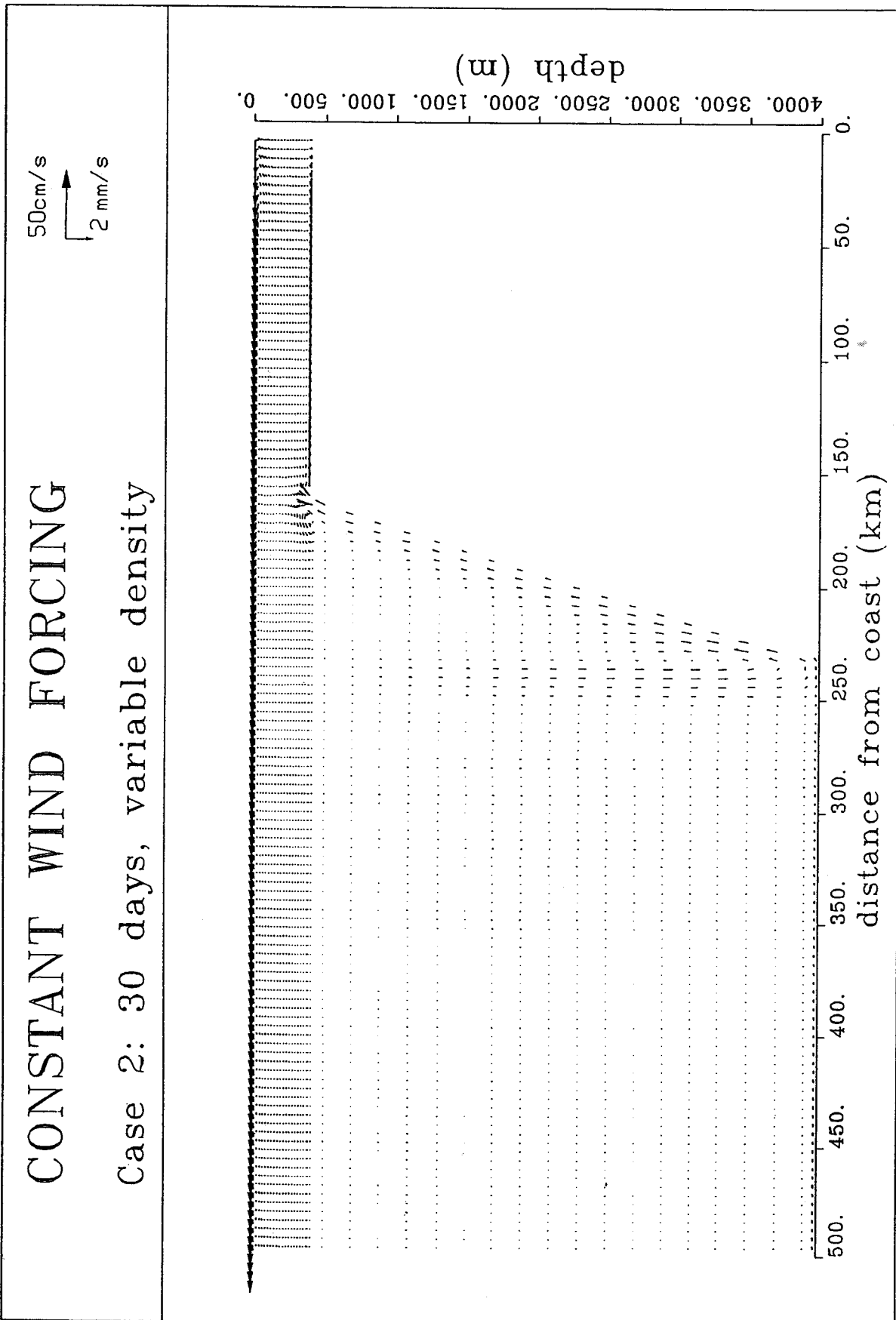
ANTAR
II/02

Figure 6b: Flow field of Case 2 - ice free with variable density.
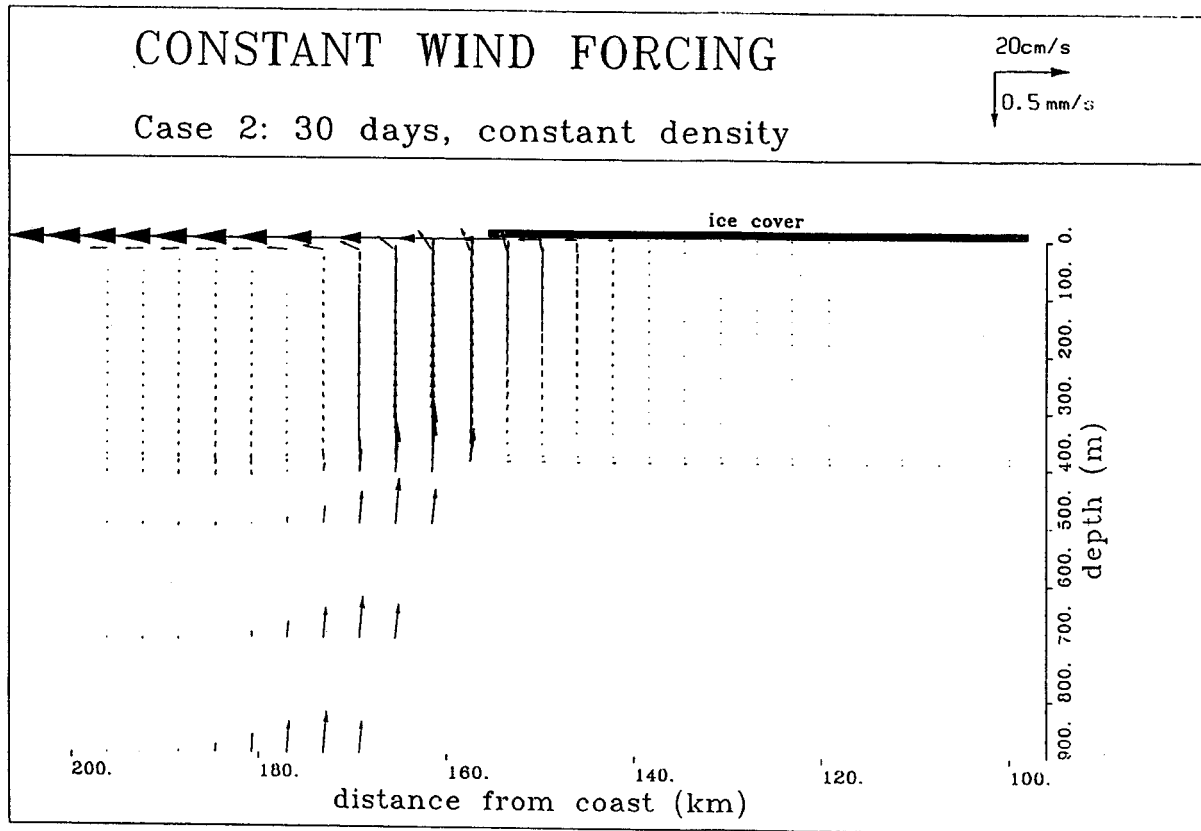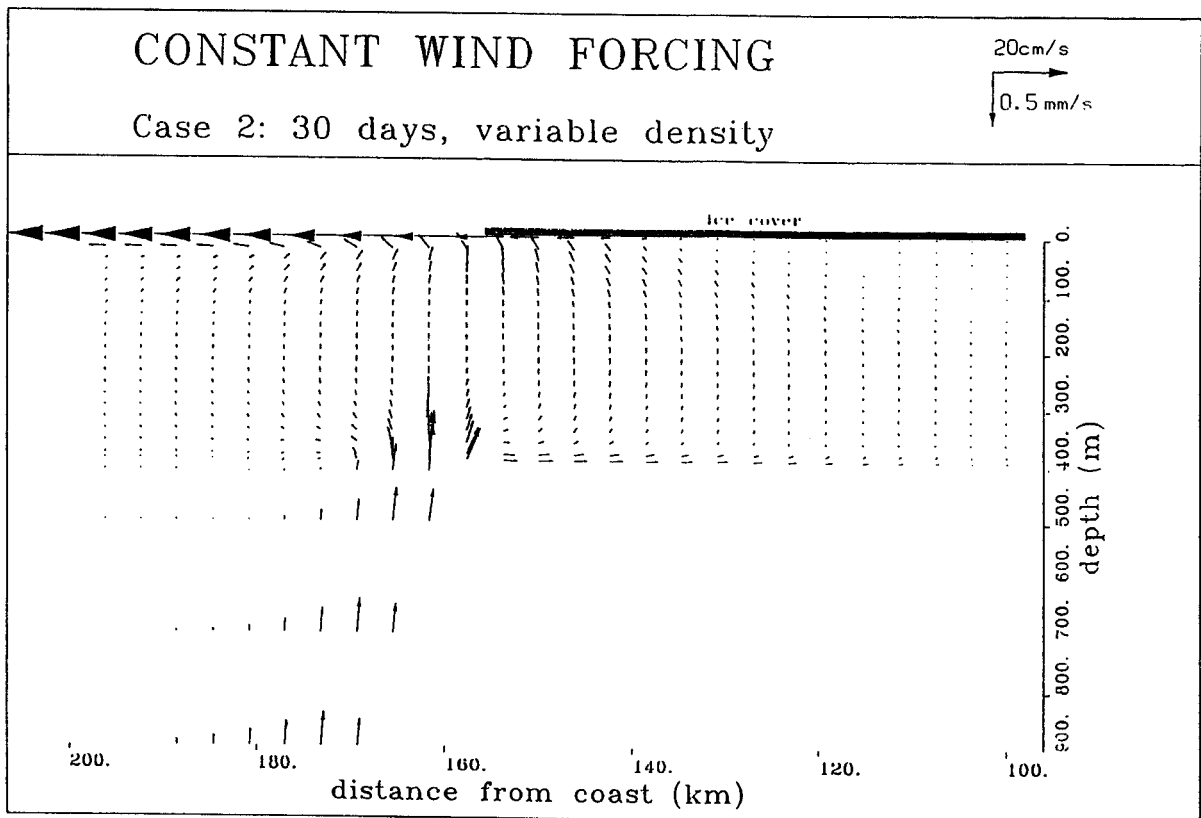
Figure 7: Flow field (Case 2), ice cover (a) constant density (b) variable density with melting.
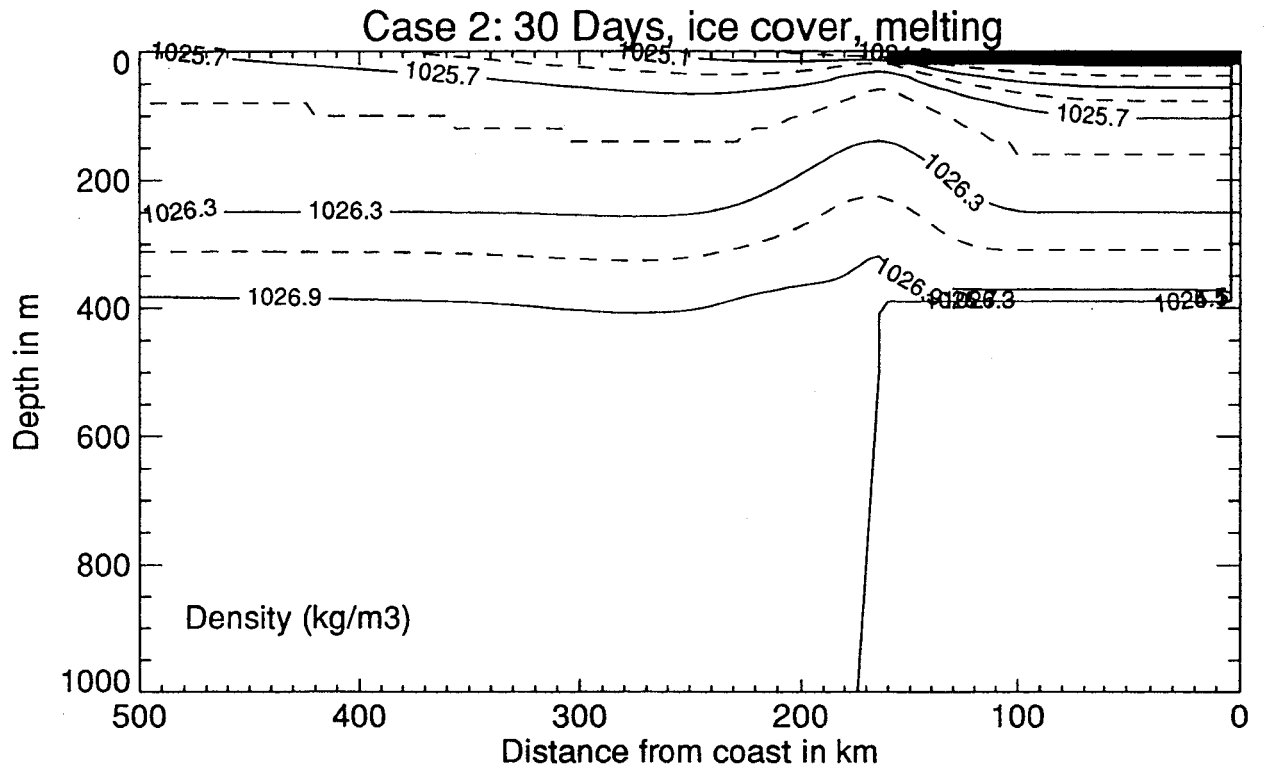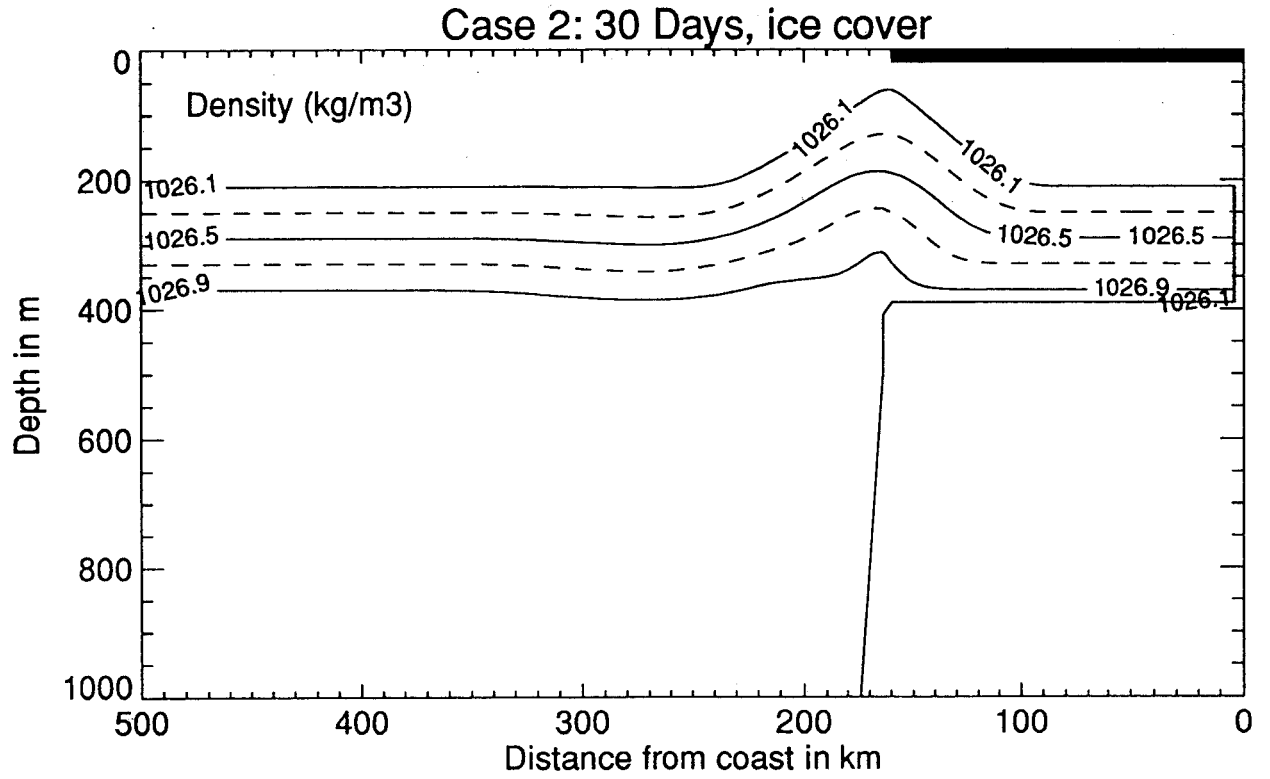
Figure 8: Isolines of density (Case 2) (a) variable density (b) variable density with melting.

3 3D Ocean Model

3.1 Basic model equation

The governing equations are derived from the three dimensional Navier-Stokes equations. The simplifications made are: hydrostatic pressure and Boussinesq approximations and the use of eddy coefficients for the turbulent momentum fluxes. These assumption are commonly used in the modelling of oceans, see *eg*. Bryan(1969), The hydrostatic assumption reduces the effort to calculate the pressure from a three dimensional elliptic equation to a two dimensional one. The Boussinesq approximation means that the water is treated as incompressible. Turbulence is introduced by means of eddy coefficients. The horizontal ones are constant whereas the vertical one can be variable. The model as presented here is barotropic. The equations of continuity and momentum in Cartesian coordinates are

$$\frac{\partial u}{\partial x} + \frac{\partial v}{\partial y} + \frac{\partial w}{\partial z} = 0 \tag{20}$$

$$\frac{\partial u}{\partial t} + u\frac{\partial u}{\partial x} + v\frac{\partial u}{\partial y} + w\frac{\partial u}{\partial z} + \frac{1}{\rho}\frac{\partial p}{\partial x} - fv = \frac{\partial}{\partial x}(A_h\frac{\partial u}{\partial x}) + \frac{\partial}{\partial y}(A_h\frac{\partial u}{\partial y}) + \frac{\partial}{\partial z}(A_v\frac{\partial u}{\partial z}) \tag{21}$$

$$\frac{\partial v}{\partial t} + u\frac{\partial v}{\partial x} + v\frac{\partial v}{\partial y} + w\frac{\partial v}{\partial z} + \frac{1}{\rho}\frac{\partial p}{\partial y} + fu = \frac{\partial}{\partial x}(A_h\frac{\partial v}{\partial x}) + \frac{\partial}{\partial y}(A_h\frac{\partial v}{\partial y}) + \frac{\partial}{\partial z}(A_v\frac{\partial v}{\partial z}) \tag{22}$$

the hydrostatic equation is

$$\frac{\partial p}{\partial z} - \rho g = 0 \tag{23}$$

where:

t	:	is time;
x	:	is the coordinate in northward direction;
y	:	is the coordinate in eastward direction;
z	:	is the vertical coordinate, positive downward;
u	:	is the velocity component in northward direction (ms^{-1});
v	:	is the velocity component in eastward direction (ms^{-1});
w	:	is the vertical velocity component (ms^{-1});
p	:	is the pressure (Nm^{-2});
ρ	:	density of the water (kgm^{-3});
A_h	:	is the horizontal eddy viscosity coefficient (ms^{-2});
A_v	:	is the vertical eddy viscosity coefficient (ms^{-2});
g	:	is the acceleration due to gravity $(=9.81\ \mathrm{ms}^{-2})$;
f	:	is the Coriolis parameter (s^{-1}).

Considering the boundaries of the model, the velocity at the coastline is set equal to zero (no-slip) and at open boundaries the velocity gradient is set equal to zero. At the sea surface wind is blowing and the vertical diffusion terms are written as $-A_v \partial u / \partial z = \tau_x / \rho$ and $-A_v \partial v / \partial z = \tau_y / \rho$. τ_x and τ_y are the wind stresses in x - and y - direction respectively. At the sea surface the rigid lid boundary condition ($w = 0$) is used and at the sea bottom a no-slip condition. The consequence of the rigid lid approximation is that surface gravity waves are filtered out, allowing thus to use bigger time-steps.

3.2 Numerical procedure

We have to solve the momentum equations (21, 22) with the pressure replaced by equation (7). If we are supposing that the air pressure and the density are constant the equations do not change. The dependent variables, *i.e.* u, v, w and p are defined on a numerical C-grid, see figure 9. An explicit finite difference scheme is used to define the discretisation in time.

3.2.1 Finite difference equations

The finite difference equations are presented using the notation of figure 9. The subscripts i, j and k are the space coordinates of the grid in x, y and z direction respectively, the superscript n indicates the time level and Δx, Δy and Δz are the horizontal and vertical space distances between two successive grid points. Δz is not constant, in order to simplify the writing of the equations it is assumed to be constant. The equations are valid away from the boundaries.

Continuity equation

$$\frac{u_{i,j,k}^{n+1} - u_{i-1,j,k}^{n+1}}{\Delta x} + \frac{v_{i,j+1,k}^{n+1} - v_{i,j,k}^{n+1}}{\Delta y} + \frac{w_{i,j,k+1}^{n+1} - w_{i,j,k}^{n+1}}{\Delta z} = 0 \tag{24}$$

Momentum equations

$$\frac{u_{i,j,k}^{n+1} - u_{i,j,k}^{n}}{\Delta t} + adu_{i,j,k}^{n} - f\bar{v}_{i,j,k}^{n+1} - \frac{A_h(u_{i+1,j,k}^{n} - 2u_{i,j,k}^{n} + u_{i-1,j,k}^{n})}{\Delta x^2}$$

$$- \frac{A_h(u_{i,j+1,k}^{n} - 2u_{i,j,k}^{n} + u_{i,j-1,k}^{n})}{\Delta y^2} - \frac{A_v(u_{i,j,k+1}^{n} - 2u_{i,j,k}^{n} + u_{i,j,k-1}^{n})}{\Delta z^2}$$

$$+ \frac{1}{\rho_o}(\frac{\partial p_l}{\partial x})_{i,j}^{n+1} = 0 \tag{25}$$

and

$$\frac{v_{i,j,k}^{n+1} - v_{i,j,k}^{n}}{\Delta t} + adv_{i,j,k}^{n} + f\bar{u}_{i,j,k}^{n} - \frac{A_h(v_{i+1,j,k}^{n} - 2v_{i,j,k}^{n} + v_{i-1,j,k}^{n})}{\Delta x^2}$$

$$- \frac{A_h(v_{i,j+1,k}^{n} - 2v_{i,j,k}^{n} + v_{i,j-1,k}^{n})}{\Delta y^2} - \frac{A_v(v_{i,j,k+1}^{n} - 2v_{i,j,k}^{n} + v_{i,j,k-1}^{n})}{\Delta z^2}$$

Δx

Δy

j+1

j

j−1

i−1   i   i+1

horizontal plane

● p
— u
| v

top

k+1

k

k−1

bottom

i−1   i   i+1

vertical plane

○ p,w at top
— u (or v)
● p
-|- u(v),w at bottom
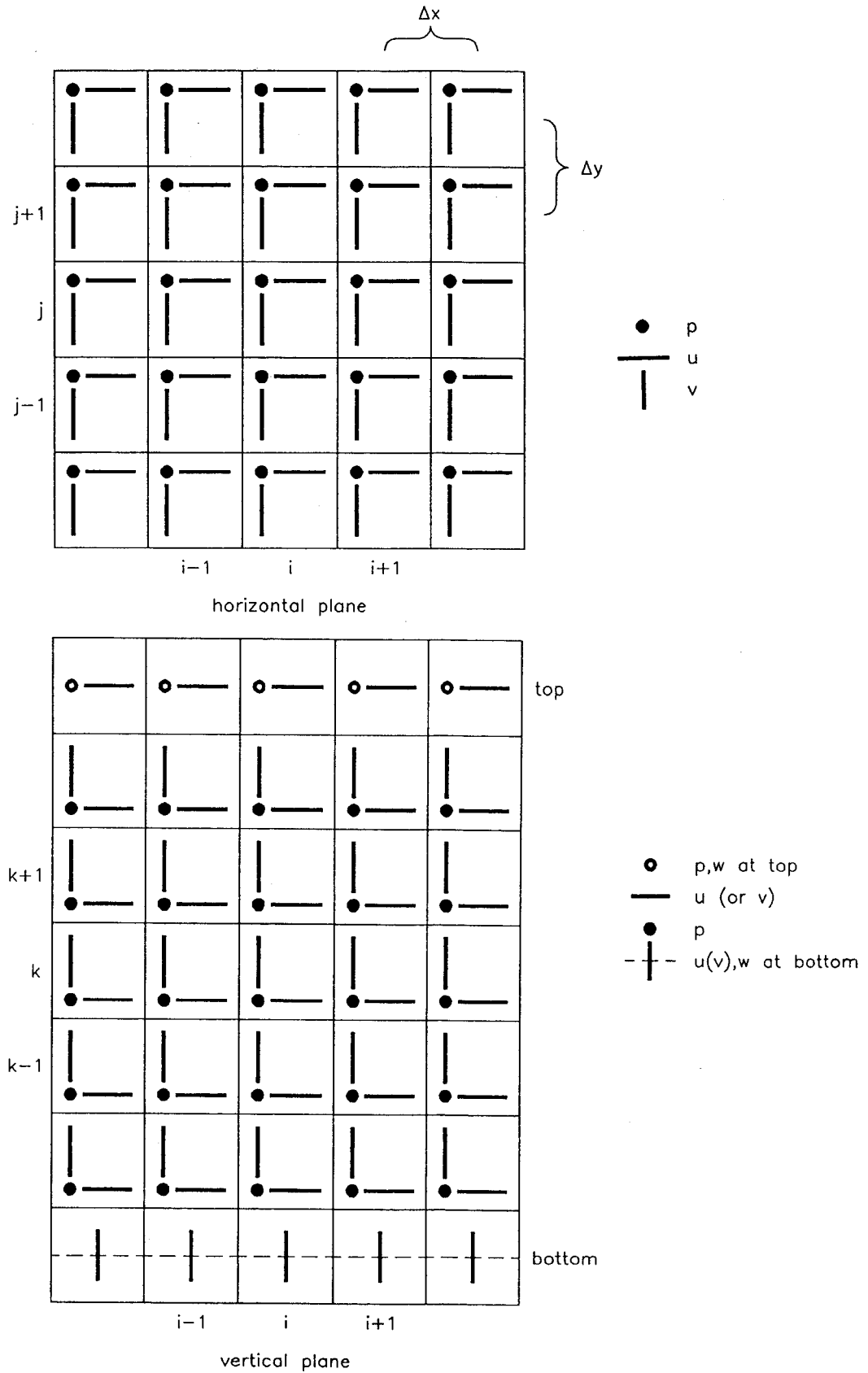
Figure 9: Numerical grid (C-grid) used by the 3D model.

$$+ \frac{1}{\rho_o}(\frac{\partial p_l}{\partial y})_{i,j}^{n+1} = 0 \tag{26}$$

where $adu_{i,j,k}^n$ and $adv_{i,j,k}^n$ are the advection terms they are replaced by a 1st order upwind scheme. $\bar{u}_{i,j,k}$ and $\bar{v}_{i,j,k}$ are equal to:

$$\bar{u}_{i,j,k} = (u_{i,j,k} + u_{i-1,j,k} + u_{i,j-1,k} + u_{i-1,j-1,k})/4 \tag{27}$$

$$\bar{v}_{i,j,k} = (v_{i,j,k} + v_{i+1,j,k} + v_{i,j+1,k} + v_{i+1,j+1,k})/4 \tag{28}$$

3.2.2 Computational scheme

The numerical procedure is based on the so-called MAC method, see Peyrot and Taylor(1986) and Jamart et al.(1982). The idea is to split the horizontal velocities in two parts, one containing the pressure term and one containing the rest (explicit terms).

$$u_{i,j,k}^{n+1} = u'_{i,j,k} + u''_{i,j,k} \tag{29}$$

$$v_{i,j,k}^{n+1} = v'_{i,j,k} + v''_{i,j,k} \tag{30}$$

where u', u'', v' and v'' are equals to:

$$u'_{i,j,k} = u_{i,j,k}^n + (-advec_{i,j,k}^n + diff_{i,j,k}^n - f\bar{v}_{i,j,k}^n)\Delta t \tag{31}$$

$$u''_{i,j,k} = -\frac{1}{\rho_o}(\frac{\partial p_l}{\partial x})_{i,j}^{n+1}\Delta t \tag{32}$$

$$v'_{i,j,k} = v_{i,j,k}^n + (-advec_{i,j,k}^n + diff_{i,j,k}^n + f\bar{u}_{i,j,k}^n)\Delta t \tag{33}$$

$$v''_{i,j,k} = -\frac{1}{\rho_o}(\frac{\partial p_l}{\partial y})_{i,j}^{n+1}\Delta t \tag{34}$$

$advec_{i,j,k}^n$ are the advective terms and $diff_{i,j,k}^n$ the diffusion terms. to calculate the pressure gradient the continuity equation (20) is integrated over the vertical (from top, $k = 1$, to $k = hz - 1$, with hz the bottom coordinate). The vertical velocity at the surface and at the bottom is zero (rigid lid condition) so that the vertical integrated continuity equation at timestep $n + 1$ and written in finite differences takes the form

$$(h_{i+1,j}\sum_{k=1}^{hz-1}(\omega_k u_{i+1,j,k}^{n+1}) - h_{i,j}\sum_{k=1}^{hz-1}(\omega_k u_{i,j,k}^{n+1}))\frac{1}{\Delta x} + (h_{i,j+1}\sum_{k=1}^{hz-1}(\omega_k v_{i,j+1,k}^{n+1})$$

$$- h_{i,j}\sum_{k=1}^{hz-1}(\omega_k v_{i,j,k}^{n+1}))\frac{1}{\Delta y} = 0 \tag{35}$$

where ω_k is a weighting factor depending on the vertical grid size, in case of constant vertical grid size: $\omega_1 = 0.5\Delta z/h_{i,j}$ and $\omega_2...\omega_{hz-1} = \Delta z/h_i$. Equations (29) and (30) are

put in eq. (35) and together with equations (32) and (34) the following relationship is obtained (we suppose that $\Delta x = \Delta y$)

$$h_{i+1,j} \sum_{k=1}^{hz-1} (\omega_k u'_{i+1,j,k}) - \frac{h_{i+1,j}}{\rho_o}(\frac{\partial p_l}{\partial x})^{n+1}_{i+1,j}\Delta t - h_{i,j} \sum_{k=1}^{hz-1} (\omega_k u'_{i,j,k})$$

$$+\frac{h_{i,j}}{\rho_o}(\frac{\partial p_l}{\partial x})^{n+1}_{i,j}\Delta t - h_{i,j+1} \sum_{k=1}^{hz-1} (\omega_k v'_{i,j+1,k}) + \frac{h_{i,j+1}}{\rho_o}(\frac{\partial p_l}{\partial y})^{n+1}_{i,j+1}\Delta t$$

$$- h_{i,j} \sum_{k=1}^{hz-1} (\omega_k v'_{i,j,k}) + \frac{h_{i,j}}{\rho_o}(\frac{\partial p_l}{\partial y})^{n+1}_{i,j}\Delta t = 0 \tag{36}$$

if we replace the pressure gradients by

$$(\frac{\partial p_l}{\partial x})_{i,j} = \frac{p_{i+1,j} - p_{i,j}}{\Delta x} \tag{37}$$

and

$$(\frac{\partial p}{\partial y})_{i,j} = \frac{p_{i,j} - p_{i,j-1}}{\Delta y} \tag{38}$$

we obtain the following Poisson equation for pressure (in case of constant depth)

$$4p_{i,j} - (p_{i+1,j} + p_{i,j+1} + p_{i-1,j} + p_{i,j-1}) = -G\frac{\Delta x}{\Delta t} \tag{39}$$

with G equals to

$$G = h_{i+1,j} \sum_{k=1}^{hz-1} (\omega_k u'_{i+1,j,k}) - h_{i,j} \sum_{k=1}^{hz-1} (\omega_k u'_{i,j,k}) + h_{i,j+1} \sum_{k=1}^{hz-1} (\omega_k v'_{i,j+1,k}) - h_{i,j} \sum_{k=1}^{hz-1} (\omega_k v'_{i,j,k})$$

$$\tag{40}$$

Equation (39) is only valid for interior grid points. Since pressure is never situated at the boundary a similar equation can be used where the appropriate boundary conditions for velocity are incorporated. As an example, consider a continental boundary at the southern edge of the basin. Because of the no-slip condition the summation over the vertical of $v_{i,j}$ is equal to zero and we can drop this term from equation (35) resulting in an equation for the surface pressure along this line. The treatment for open boundaries is similar and also depending on the chosen boundary condition for velocity (e.g. velocity gradient equals to zero).

For solving the Poisson equation different solution techniques are available. The method implemented here is the Conjugate Gradient Method, see e.g. Golub and Van Loan(1989). The advantage of the C-grid is that less averaging is needed for deriving the Poisson equation. The disadvantages of the C-grid consist in the generation of spurious boundary layers, these effects can be avoided by using the Wet Points Only Method, as proposed by Jamart and Ozer(1986).

3.3 Application 1: Testing of the model

To illustrate the performance of and to test the model, some simple but representative simulation have been carried out. The example consist of a closed basin, it has been taken from the BSEX model intercomparison experiment, see Ozer *et al.*(1988). The basin is rectangular (600 x 1200 km) and closed at all sides. The water depth is equal to 100 m. The calculations starts with the water at rest, a wind is then suddenly blowing over the surface. Two different simulations have been performed, for the first one (Case A1) a constant southward wind is used with a surface stress of 0.1 Nm^{-2}, while for the second one (Case A2) the same wind is blowing in south-east direction. The horizontal grid sizes are 40 km, the vertical one is 5 m. The value of the horizontal eddy coefficient is 1000 m^{2}s^{-1} and of the vertical one 0.0065 m^{2}s^{-1}. the value of the Coriolis term has been taken at 55°N. The results have been compared with those published in the BSEX report. In order to get a more exact idea about the quality of the model a more elaborate comparison experiment should be carried out, *e.g.* comparison with data or with others models. From these preliminary testings however the following conclusions can be drawn:

- The surface velocity is to the right of the wind, the angle depends on the vertical resolution of the surface layer.

- The changing of the velocity direction with depth is consistent with the Ekman theory(1905).

- The total mass is constant during calculation, the numbers of points with a positive pressure are equal to those with negative pressure on the lid and the the maximum value of the pressure is equal to the absolute value of the minimum value of pressure.

The horizontal velocity fields at different depths are shown in figure 10 (Case A1) and in figure 11 (Case A2). The velocity field in the vertical plane at y=320 km is presented in figure 12 (Case A1) and figure 13 (Case A2).

3.4 Application 2: Spherical coordinate model

The basic equations for ocean modelling in a sperical coordinate system are:

$$\frac{\partial u}{rcos\phi\partial\lambda} + \frac{\partial v}{r\partial\phi} + \frac{\partial w}{\partial z} = 0 \tag{41}$$

$$\frac{\partial u}{\partial t} + \frac{1}{rcos\phi}\{u\frac{\partial u}{\partial\lambda} + v\frac{\partial ucos\phi}{\partial\phi}\} + w\frac{\partial u}{\partial z} - \frac{uvtan\phi}{r} + \frac{1}{\rho rcos\phi}\frac{\partial p}{\partial\lambda} - fv =$$

$$A_h\{\nabla^2 u + \frac{(1-tan^2\phi)u}{r^2} - \frac{2sin\phi}{r^2cos^2\phi}\frac{\partial v}{\partial\lambda}\} + A_v\frac{\partial^2 u}{\partial z^2} \tag{42}$$

$$\frac{\partial v}{\partial t} + \frac{1}{r\cos\phi}\{u\frac{\partial v}{\partial \lambda} + v\frac{\partial v\cos\phi}{\partial \phi}\} + w\frac{\partial v}{\partial z} + \frac{u^2\tan\phi}{r} + \frac{1}{\rho r}\frac{\partial p}{\partial \phi} + fu =$$

$$A_h\{\nabla^2 v + \frac{(1-\tan^2\phi)v}{r^2} + \frac{2\sin\phi}{r^2\cos^2\phi}\frac{\partial u}{\partial \lambda}\} + A_v\frac{\partial^2 v}{\partial z^2} \qquad (43)$$

the hydrostatic equation is

$$\frac{\partial p}{\partial z} - \rho g = 0 \qquad (44)$$

ANTAR
II/02

The notation is identical to that of the cartesian equations, the new symbols are r the earth radius, λ the east-west coordinate and ϕ the north south coordinate. The numerical model uses the same scheme as the cartesian one.

Up to now this model has only been used to calculate the wind induced currents in an enclosed basin. The dimension and the wind forcing are similar to the one presented in the first application. Therefore we want only to show the vertical flow field in longitudinal direction taken in the middle of the basin and due to a constant southward wind forcing (figure 14).
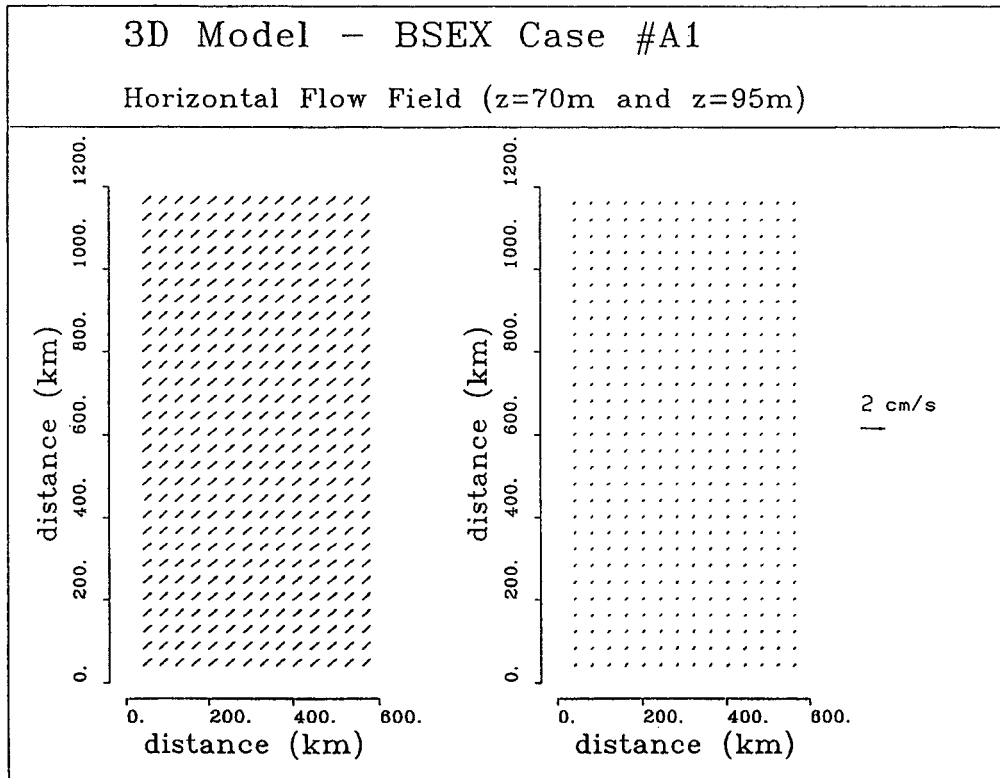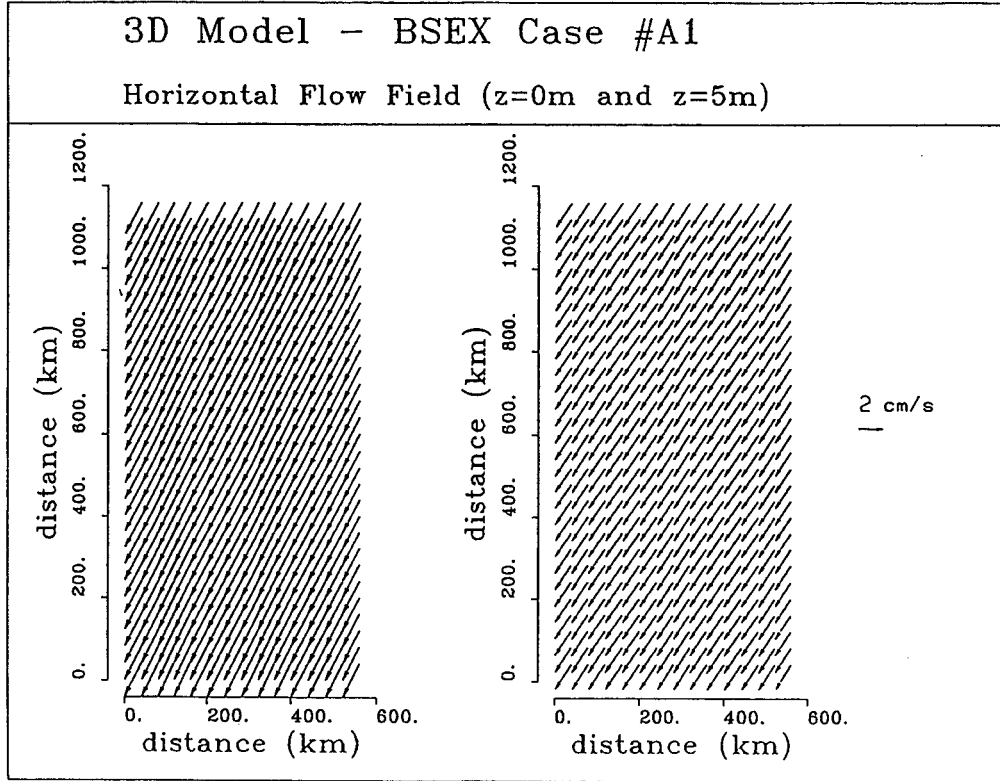
Figure 10: Horizontal velocity field, Case A1 (constant southward wind).
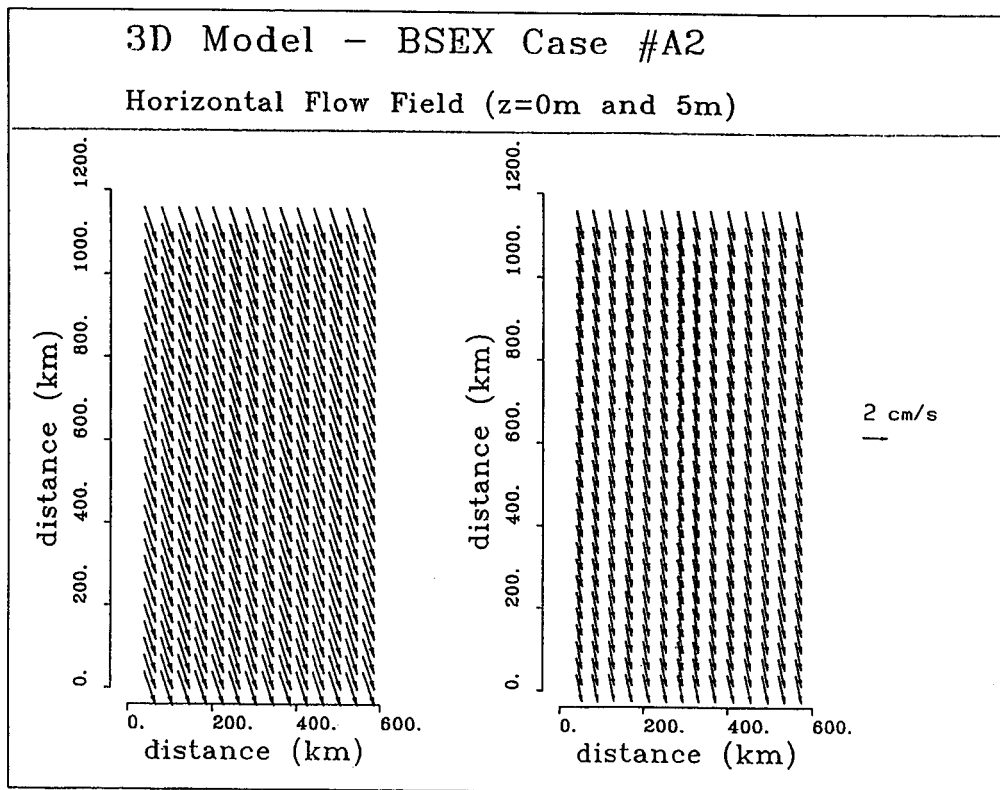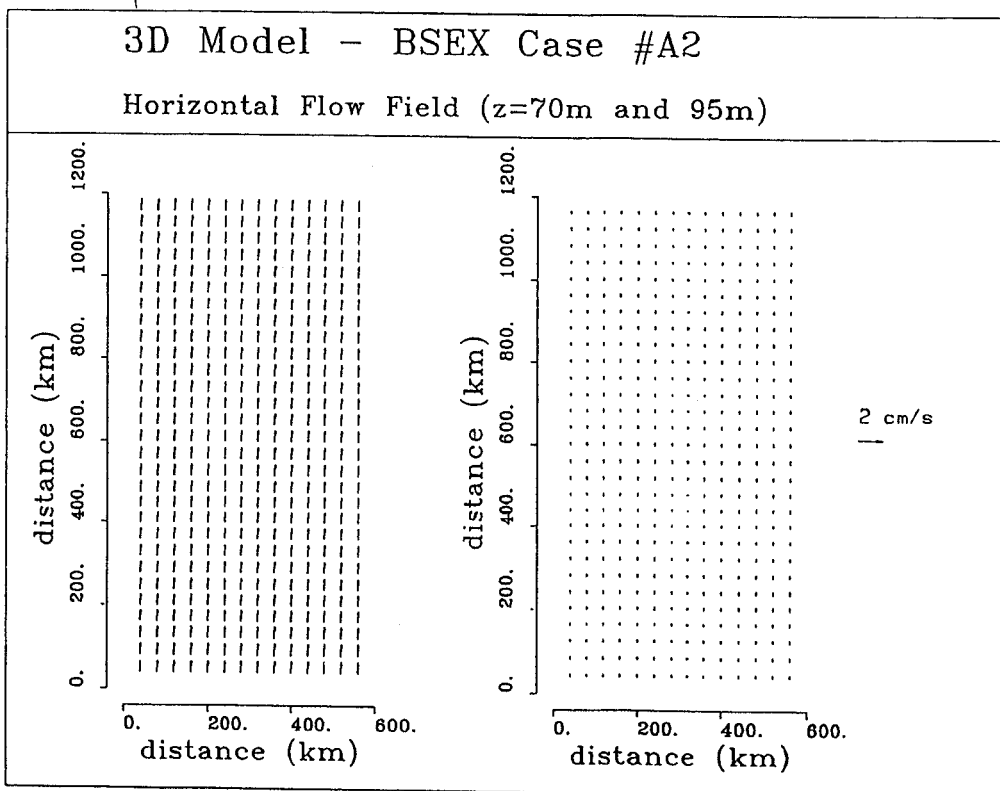
Figure 11: Horizontal velocity field, Case A2 (constant south-eastward wind).
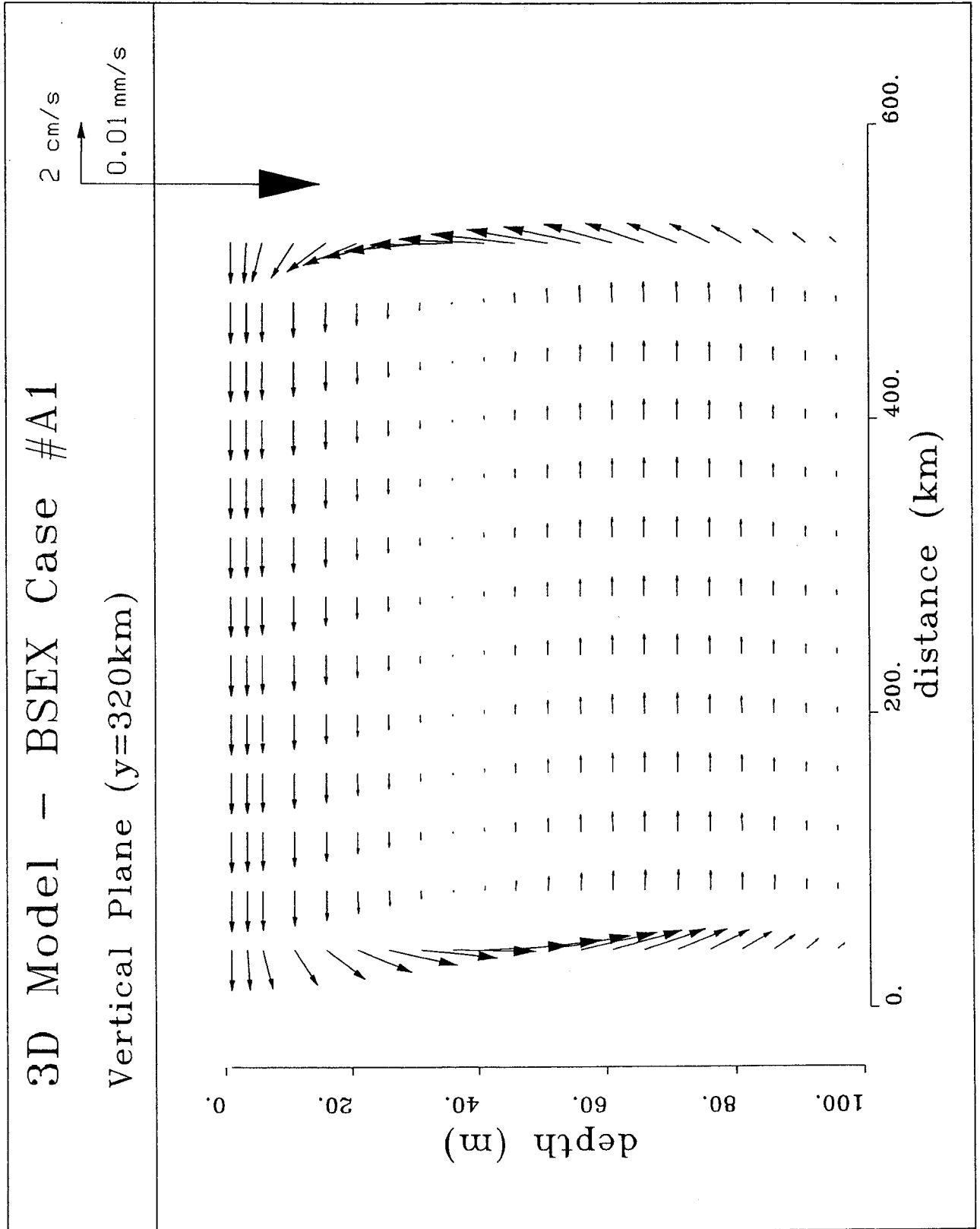
Figure 12: Vertical velocity field (EW plane), Case A1 (constant southward wind).

29
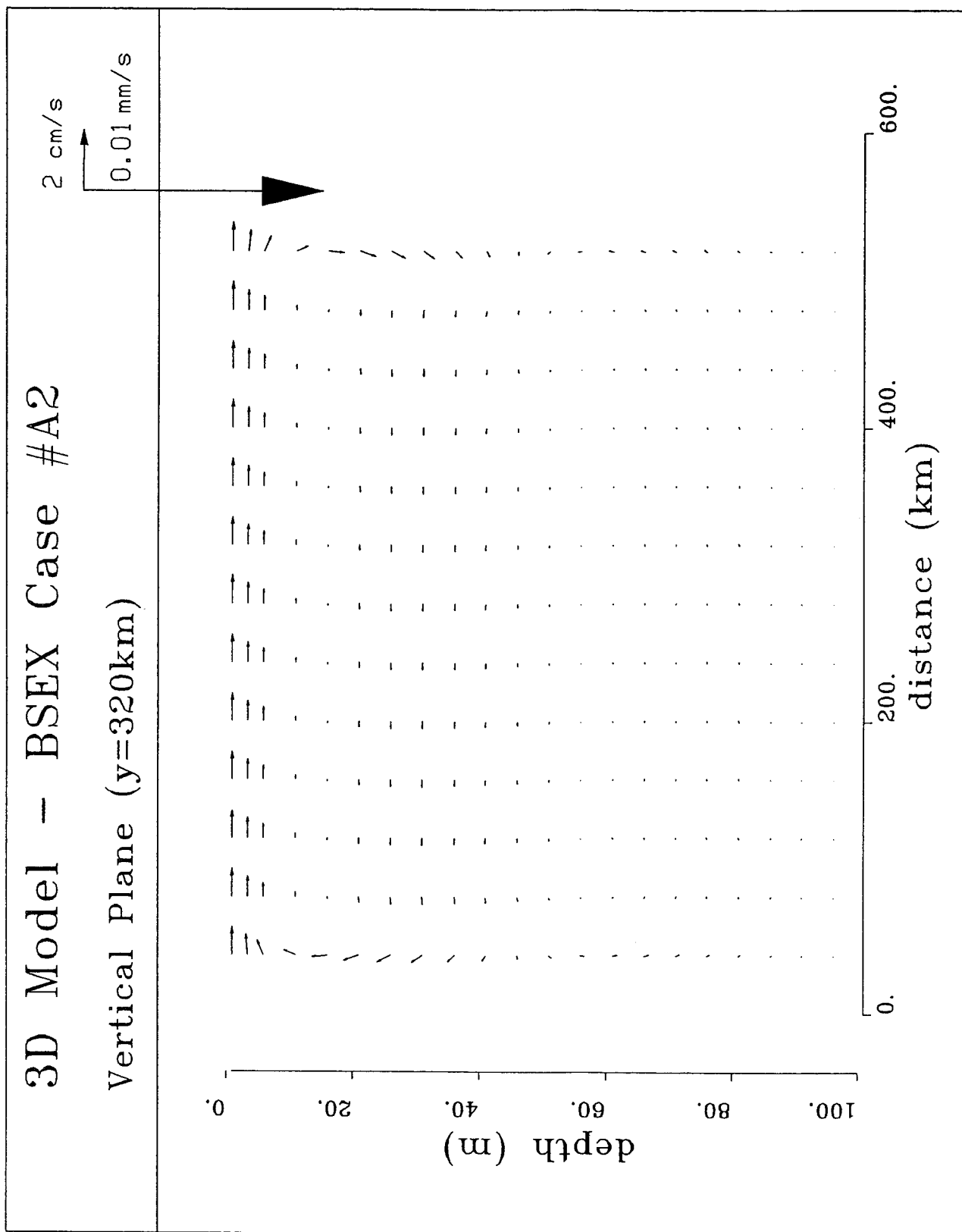
Figure 13: Vertical velocity field (EW plane), Case A2 (constant south-eastward wind).

3D Model – Spherical Code

vertical plane (NS) at x=300km
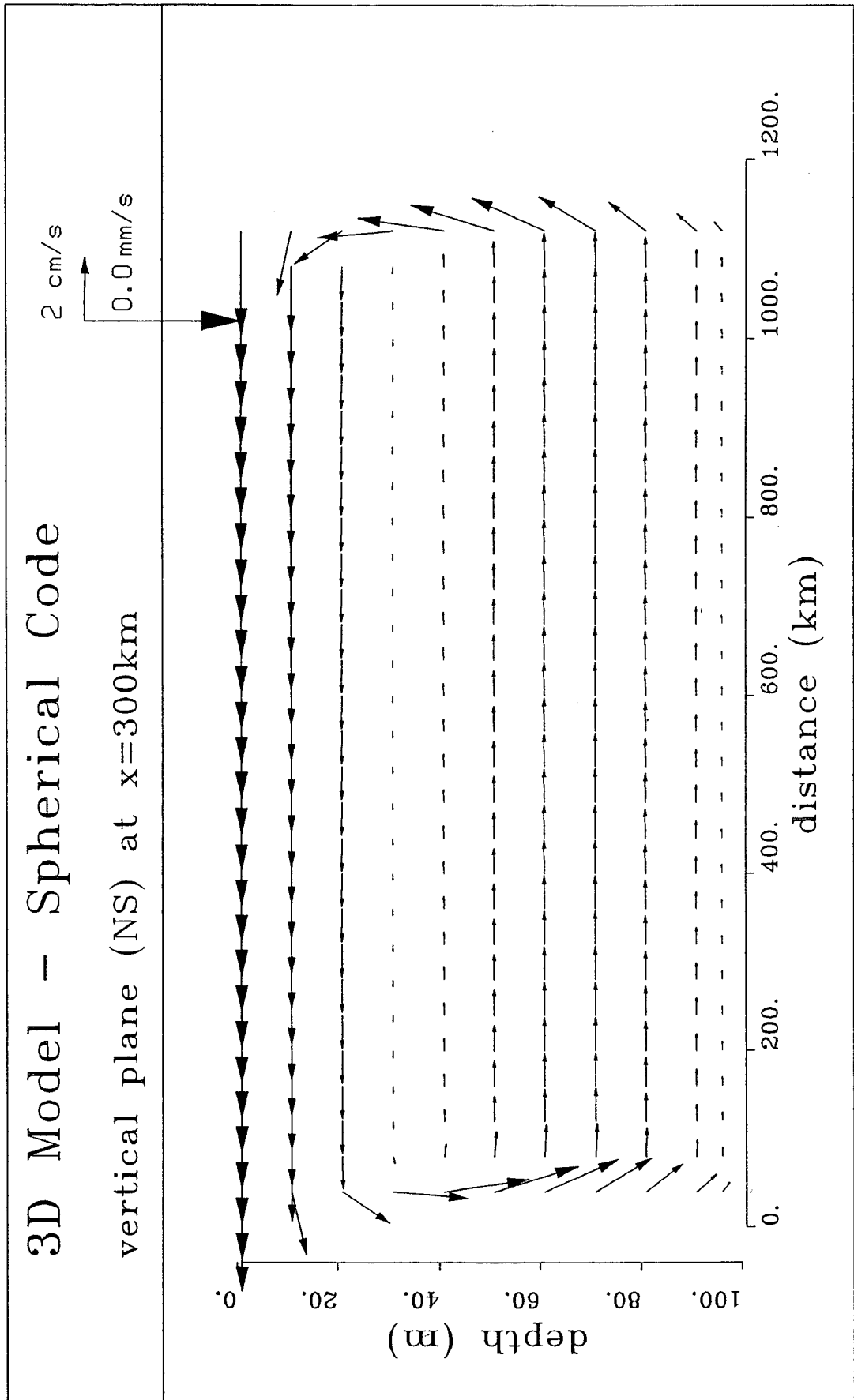
Figure 14: Vertical velocity field (NS plane), Case A1 (constant southward wind), spherical model.

4 Katabatic Wind Forcing

Katabatic winds are formed by cooling of air on a sloped ice covered surface. These winds can reach very high velocities in the coastal zones of the Antarctic continent. If the winds are strong enough coastal polynias can be formed. In these open water zones important energy exchanges occur between the water and the air leading to the formation of sea ice and dense water (Zwally and Comiso, 1985). It is believed that most of the bottom water of the oceans is formed by such an process. The purpose of this chapter is to simulate the hydrodynamic response of an ocean to katabatic wind forcing, the ocean is supposed to be ice free and barotropic. Two areas are considered, the first one is situated at the Adélie coast and the second one at the coast of Terra Nova. For these two areas we have at our disposal wind data calculated with the UCL atmospheric models, see Gallée et al.(1989). The particular interest of these two areas is situated in the fact that the katabatic winds are very strong there due to the presence of confluence topographic zones, which is the cause of this anomalous wind behaviour.

ANTAR II/02

The Adélie case was initially set up to simulate the currents in a vertical plane driven by a katabatic wind. This case has been used for comparison study between two 2.5D vertical plane models which are developed by the laboratory of hydraulics, K.U.Leuven(KUL) and the Management Unit of Mathematical Models of the North Sea and Scheldt Estuary(MUMM). The results of this comparison experiment have been published by Fettweis et al.(1991a) and therefore only a brief summary is given here.

It is clear that a fully 3D model is required to simulate the hydrodynamic behaviour of the flows forced by a katabatic wind. The reasons are many including the complexity of coastal boundaries and the strong variability of katabatic winds. The 3D model has been applied to an area along the coast of Terra Nova Bay.

4.1 A 2.5D model of the Adélie coastal area

4.1.1 Description of the cases

Four different cases have been set up, for all of them the vertical plane is 500km long, the horizontal eddy viscosity coefficient A_h is 200 m^{2}s^{-1}, the vertical one A_v is 0.01 m^{2}s^{-1}, g is 9.81 ms^{-2}, the Coriolis parameter f has been taken at 67.5 degrees South and the horizontal grid size is 4 km. A katabatic wind is blowing over the water surface. The sea is initially at rest. The waterdepth differs: Case 1 has a constant depth of 400 m, whereas for the second one the shelf of 400 m depth is interrupted by a shelf break with a slope of 5 percent, the depth outside the shelf and the shelf slope is 4000 m. Three different placements of the shelf edge have been proposed. Case 2s has a short shelf (80 km), Case 2o a medium shelf (160 km) and Case 2l a long shelf (280 km). The length of the shelf of Case 2o corresponds with the information read from the map. The wind is decreasing to zero at 200 km from the coast and is then blowing in opposite (eastward) direction, see figure 15. This turning point is situated above the shelf slope in Case 2o, in Case 2l the
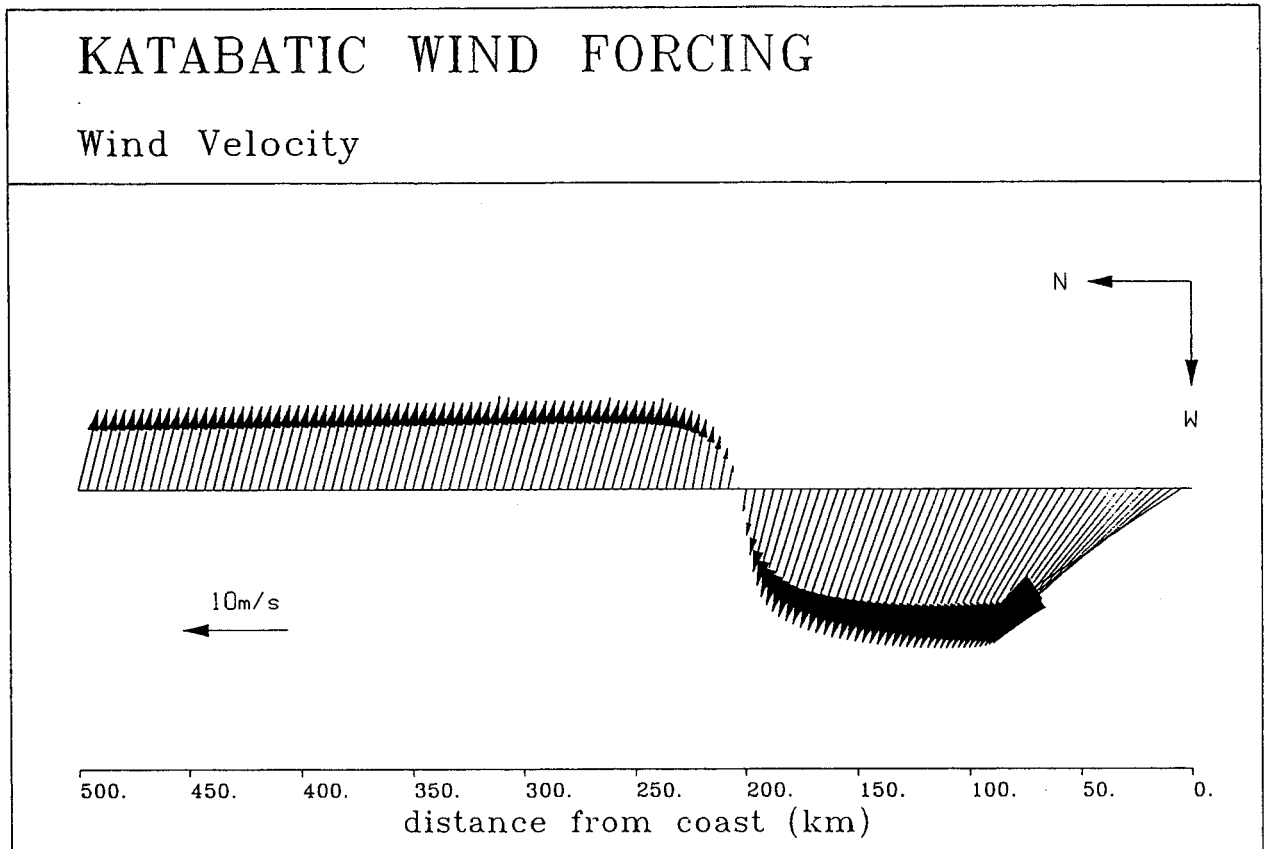
Figure 15: Katabatic wind: 2.5D model.

shelf slope is north of this point whereas for Case 2s it is put south of this point.

4.1.2 Case 1: flat bottom

The model starts with the calculations at $t = 0$ and continue until 50 days have been simulated. In figure 16a the flow fields in the vertical plane (northward and vertical currents) are shown. The flow pattern consists of two cells, in the first 200km the flow is directed on-shore in the top layer, except close to the continent, with downwelling at the continental margin, off-shore flow at the bottom and upwelling around 200 km. At about 50 m depth and close to the continent a vertical eddy exists. For the second cell (from 200 km to 500 km) the flow is in opposite direction, off-shore at the top and on-shore at the bottom. Figure 16b gives an enlargement of the first 80 km of the basin. It is noticeable on this figure that, although the flow in the surface layer is directed on shore, a seaward flow exists at the surface in the first 10 km. We do not intent to assert that the formation of coastal polynias could be fully explained by this result. Let us however mention that this behaviour of the surface flow near the coast, in agreement with the Ekman theory (Petit, 1991), can be considered as an indicator of the quality of the winds computed by the UCL model. It is clear that this result must be confirmed by a system of fully coupled models (atmospheric, sea-ice, ocean circulation). Further away from the coast the surface flow is directed towards the coast.

KATABATIC WIND FORCING

Case 1: 50 days (KUL)

20cm/s

0.5 mm/s

depth (m)

0. 50. 100. 150. 200. 250. 300. 350. 400.

0. 50. 100. 150. 200. 250. 300. 350. 400. 450. 500.

distance from coast (km)

ANTAR
II/02
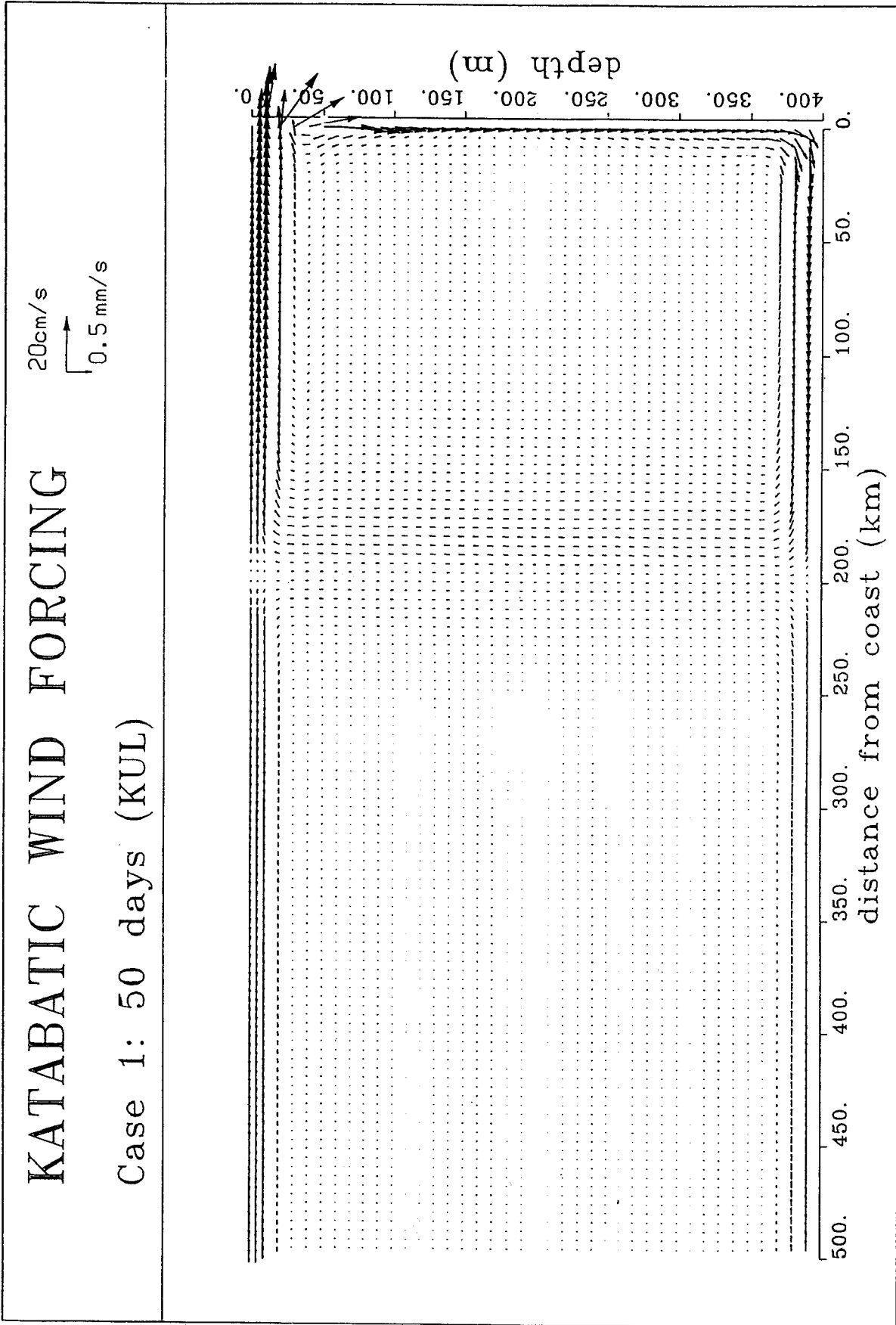
Figure 16a: Flow field simulated by the 2.5D model in the vertical plane after 50 days for Case 1. The vertical grid size is 10m.
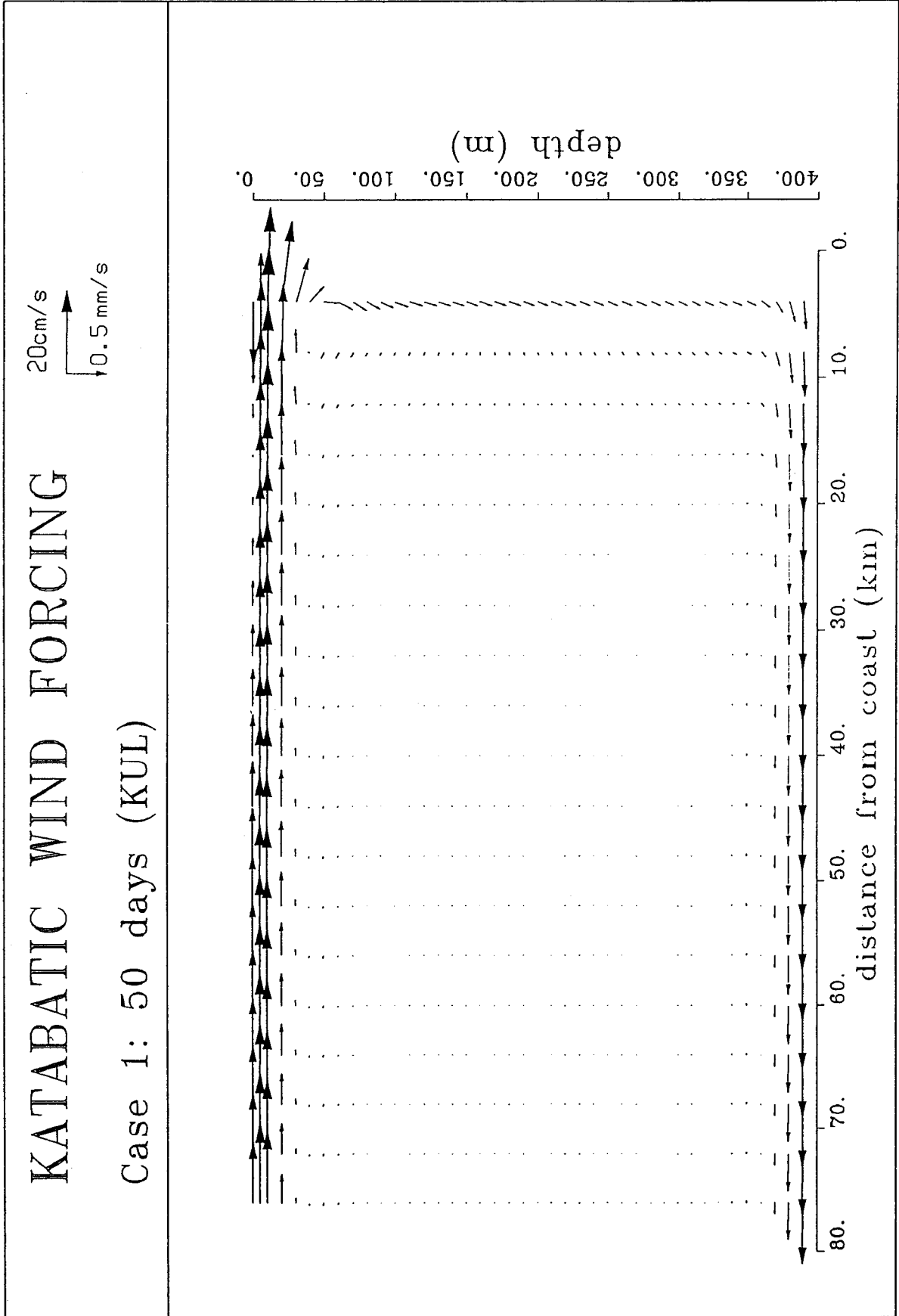
Figure 16b: Flow field near coast (enlargement of figure 16a).

4.1.3 Case 2: Shelf/ocean

As mentioned above three different cases have been treated consisting all of a shelf and a deep ocean part. We want to present only the general flow pattern in the vertical plane. The vertical grid size is not constant, the top and bottom layers have a finer grid size than the rest of the water column. As will be explained in the next chapter, it was observed that the choice of the grid size has a great influence on the accuracy of the result. Due to the finer resolution of the bottom and top the boundary layers are better resolved. The results presented are after 20 days. It should be noted that at this time-step the solution is not yet stationary. In the following a short description of the results of the three test cases is given.

a) Case 2s: Short Shelf

The shelf and the shelf slope are situated in (under) the area where the wind is blowing in northwest direction. Downwelling occurs along the slope followed by upwelling at about 150 km, *i.e.* the beginning of the slope, see figure 17a. The magnitude of this upwelling flow is gradually decreasing with decreasin depth. The flow on the coastal side of the shelf is similar with the results of Case 1.

b) Case 2o: Medium Shelf

The 200 km point, where the wind direction changes from northwest to southeast is situated in the middle of the slope. We can therefore see in figure 17b that in the higher part of the slope downwelling occur (see Case 2s) and in the lower part upwelling followed by downwelling at the beginning of the deep ocean. In the upper 400 m the flow is qualitatively similar with the one of Case 1.

c) Case 2l: Long Shelf

The slope for the long shelf case is completely situated in the southeastern wind blowing zone, see figure 17c. The wind is blowing in the opposite direction as in the first 200 km, along the slope upwelling occurs with downwelling at the ocean side of the slope. The upwelling is restricted to a small slope-bottom layer.

4.1.4 Comparison of two 2.5D models

As is already said, the purpose of this study was to compare the results of two ocean models, solving both the same equations, but differing in the way the equations are solved. The two models which participated in the comparison are the model presented in chapter 2 (referred to as KUL model) and the MUMM model (Spitz *et al.*, 1987 and Fettweis *et al.*, 1991a). The models solve the equations on a so-called B-grid using finite differences. The KUL model is basically explicit and has a fixed grid size in the vertical plane, whereas the MUMM model is semi-implicit (Crank-Nicholson scheme) using σ-coordinates for the vertical discretisation. Although both models are using a B-grid, differences occur in the position of the bottom. The bottom is going through w-points in the KUL model and through u/v-points in the MUMM model. The advection terms are treated by an explicit

first order upwind scheme in the KUL model and by an explicit second order central scheme in the MUMM model. The MUMM model makes use of a second order one side difference of the diffusion terms at the top, whereas the KUL model uses a first order one side difference. For the comparison experiment it was decided to focus only on Case 1. For this case the Ekman solution (Ekman, 1905) can be taken as the reference outside the lateral boundary layer.

In a first stage, a set of simulations has been done using the models in their original configuration. In these simulations, the forcing is the same but the bottom topography is different (either constant or variable with a different position of the shelf break). The conclusions of those first model runs can be summarized as follows. An overall agreement exists between the model solutions and, especially, the two models predict a seaward flow at the surface close to the continental margin. This result should be confirmed by a more realistic study including a coupled ocean-ice-atmosphere model. However, some discrepancies have been also observed between the model results, see the northward (figure 18) and the eastward velocity component profile (figure 19). These discrepancies have to be ascribed to the differences in the numerical procedures. Therefore, a set of additional simulations has been realized as an attempt to identify where the differences came from.

The results of those investigations can be summarized as follows. The differences between the finite difference analogs of the horizontal advection and of the horizontal diffusions do not contribute significantly to the discrepancies between the model results. For a given vertical resolution, the differences between the model solutions and the Ekman solution are partially due to the value of the horizontal diffusion coefficient. If this later is reduced, both model results converge towards the Ekman solution. It appeared clearly that the crux of the difficulties encountered came from the numerical procedures used along the vertical. An improvement of the results of the KUL model can be obtained by introducing a second order accurate analog of the vertical diffusion term at the surface and the bottom. A significant improvement of the two model results is obtained by reducing the grid spacing along the vertical. The results obtained with a vertical mesh size equal to 5m agree significantly better with the Ekman solution than those obtained with a grid spacing equal to 10m, see figure 20 (northward velocity) and figure 21 (eastward velocity). In this case, the convergence towards the exact solution is different for the two models, in the first 200km of the basin the MUMM model seems to convergence more rapidly, whereas in the other part of the basin the KUL model seems to be closer to the exact solution. We are still looking for a satisfying explanation of this point.
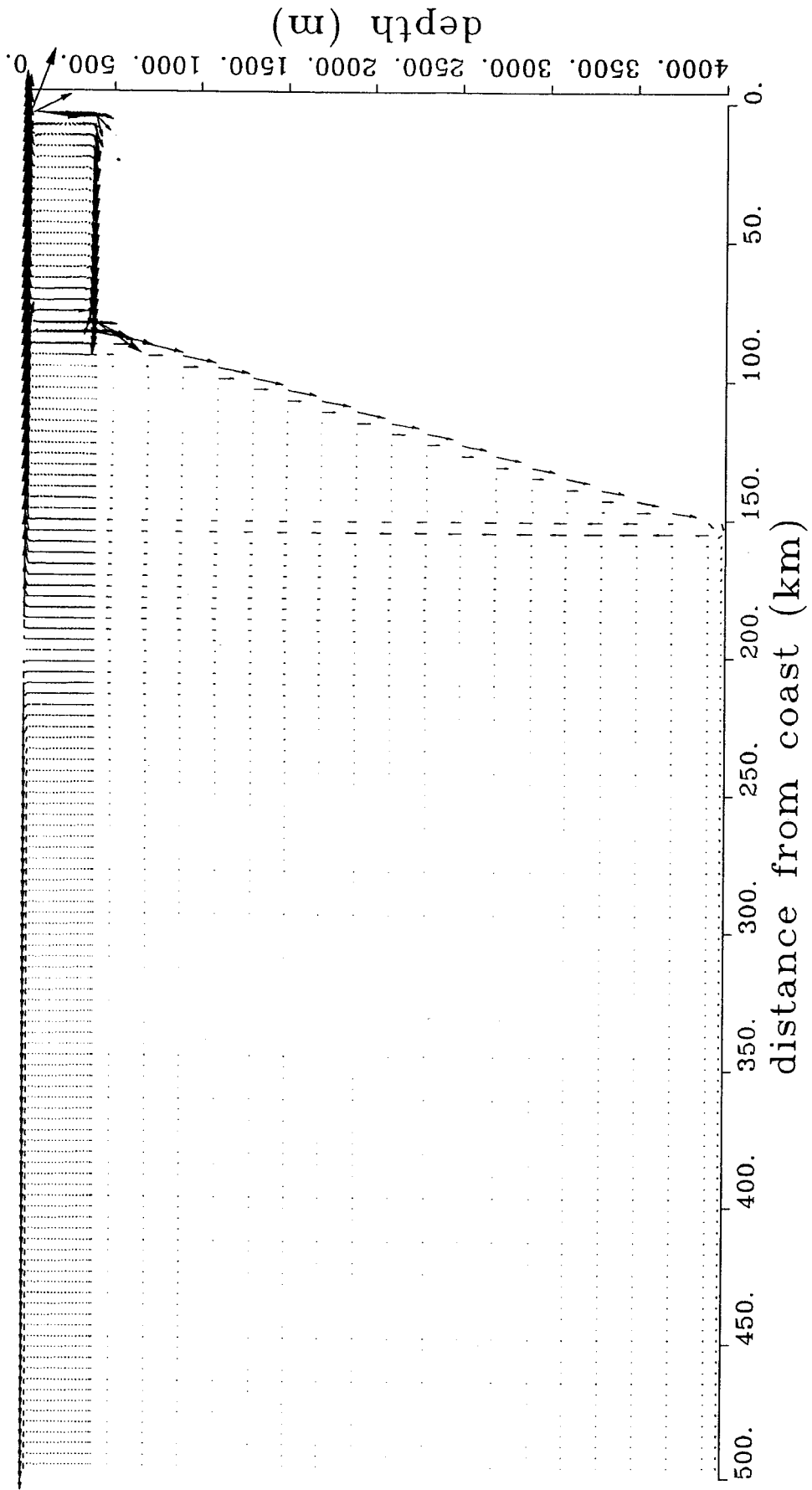
Figure 17a: Flow field in the vertical plane after 20 days for Case 2s by the 2.5D model.
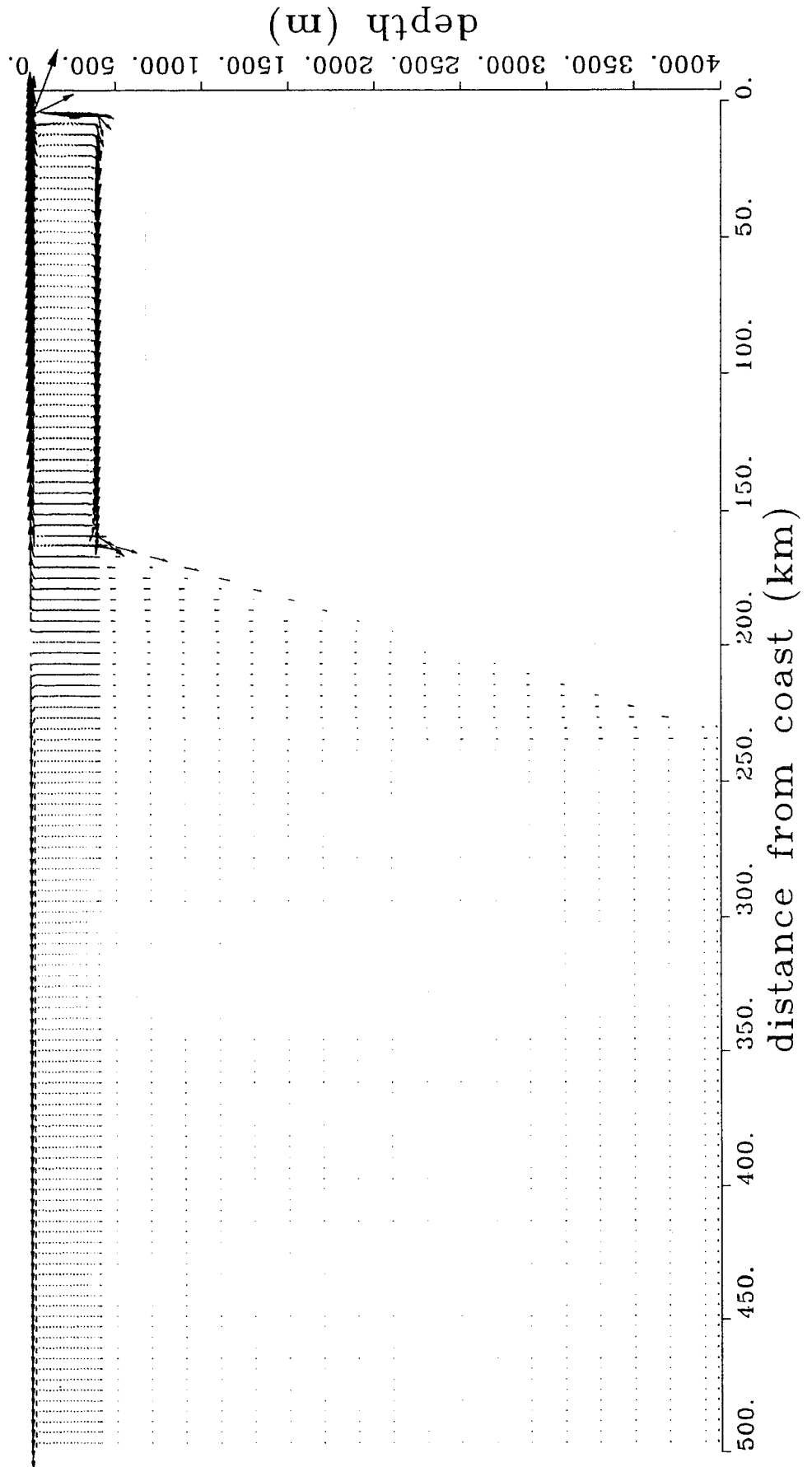
Figure 17b: Flow field in the vertical plane after 20 days for Case 2o by the 2.5D model.
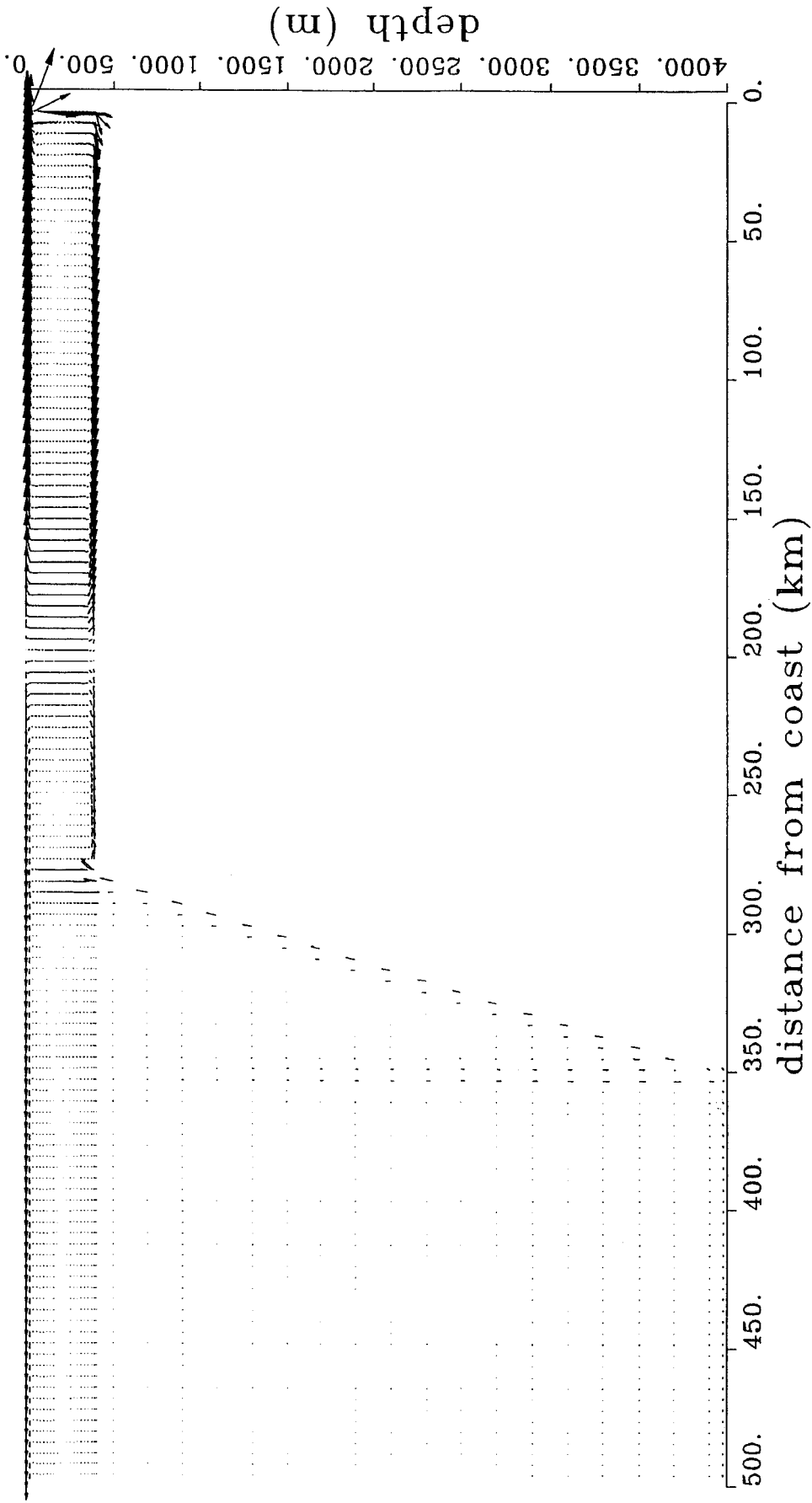
Figure 17c: Flow field in the vertical plane after 20 days for Case 2*l* by the 2.5D model.
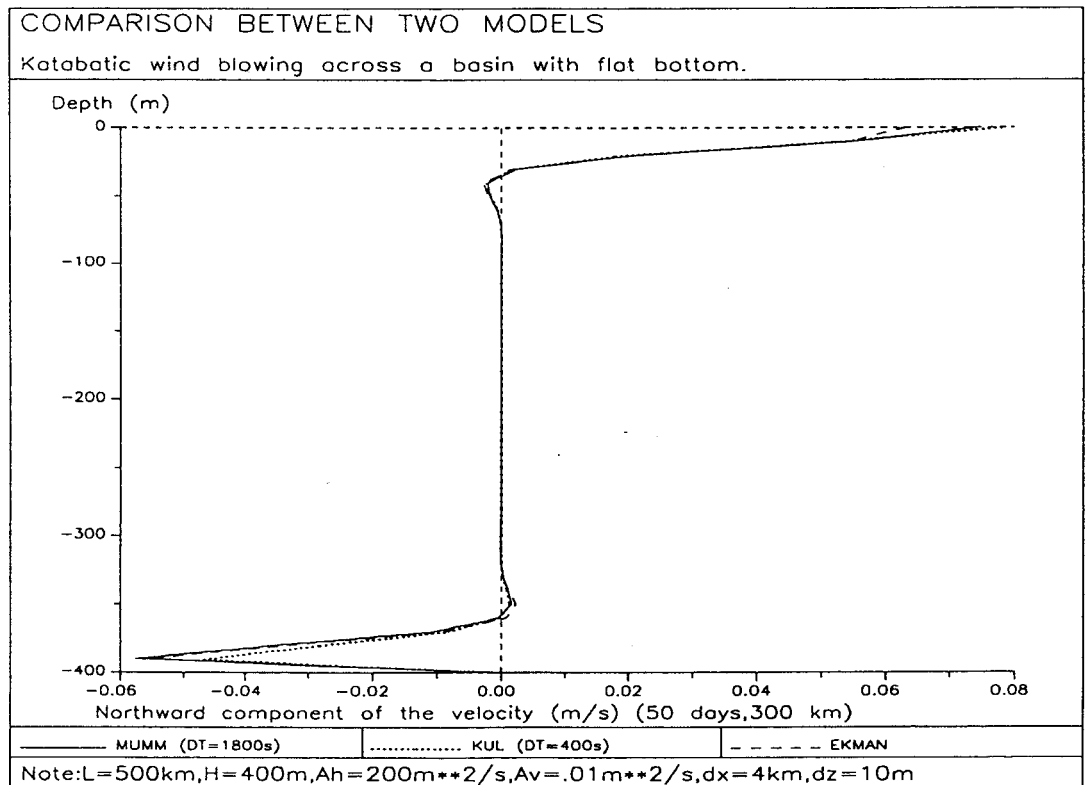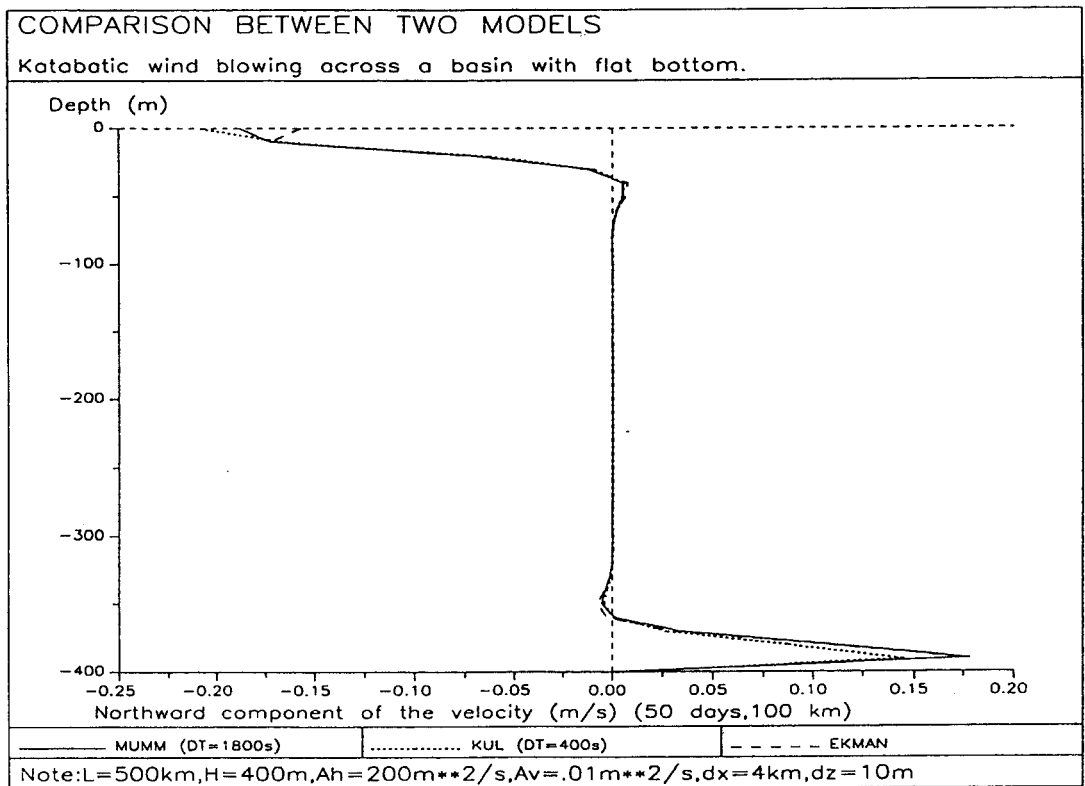
Figure 18: 2.5D model: Northward velocity component after 50 days for Case 1 at (a) 100 km and (b) 300 km. The vertical grid size is 10m.

COMPARISON BETWEEN TWO MODELS

Katabatic wind blowing across a basin with flat bottom.

Depth (m)

Eastward component of the velocity (m/s) (50 days,100 km)

——— MUMM (DT=1800s)   ·········· KUL (DT=400s)   _ _ _ _ EKMAN

Note:L=500km,H=400m,Ah=200m**2/s,Av=.01m**2/s,dx=4km,dz=10m

ANTAR
II/02

COMPARISON BETWEEN TWO MODELS

Katabatic wind blowing across a basin with flat bottom.

Depth (m)

Eastward component of the velocity (m/s) (50 days,300 km)

——— MUMM (DT=1800s)   ·········· KUL (DT=400s)   _ _ _ _ EKMAN

Note:L=500km,H=400m,Ah=200m**2/s,Av=.01m**2/s,dx=4km,dz=10m

Figure 19: 2.5D model: Eastward velocity component after 50 days for Case 1 at (a) 100 km and (b) 300 km. The vertical grid size is 10m.
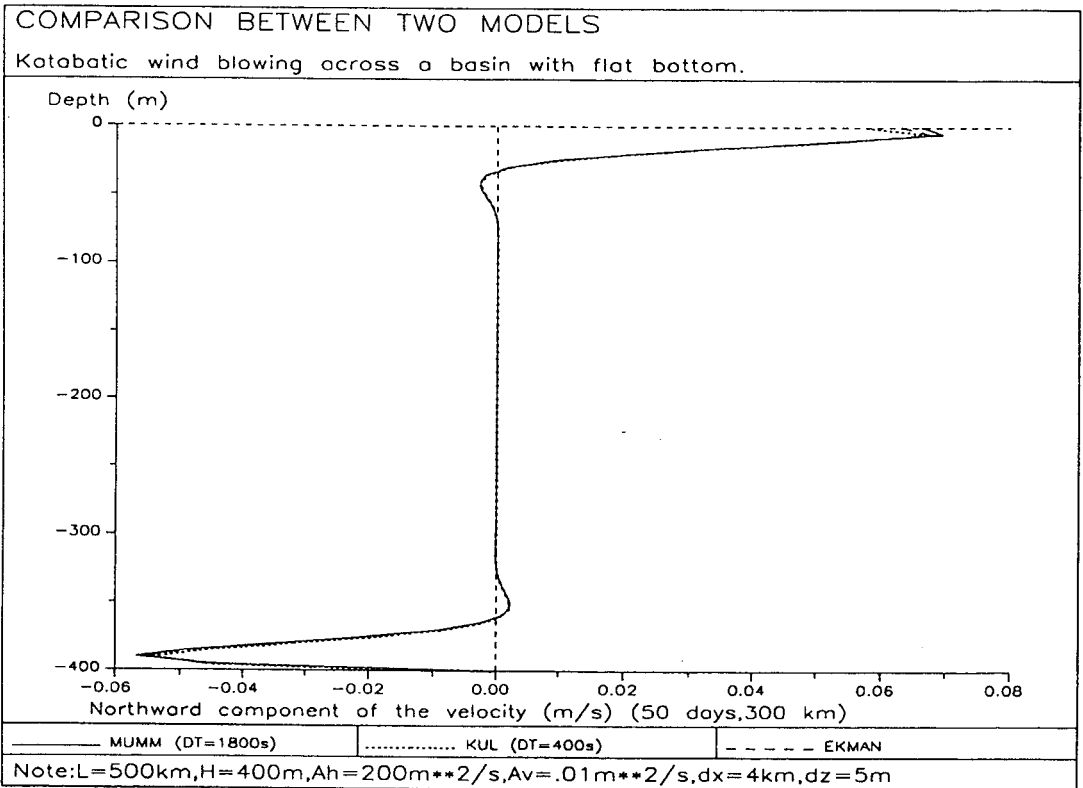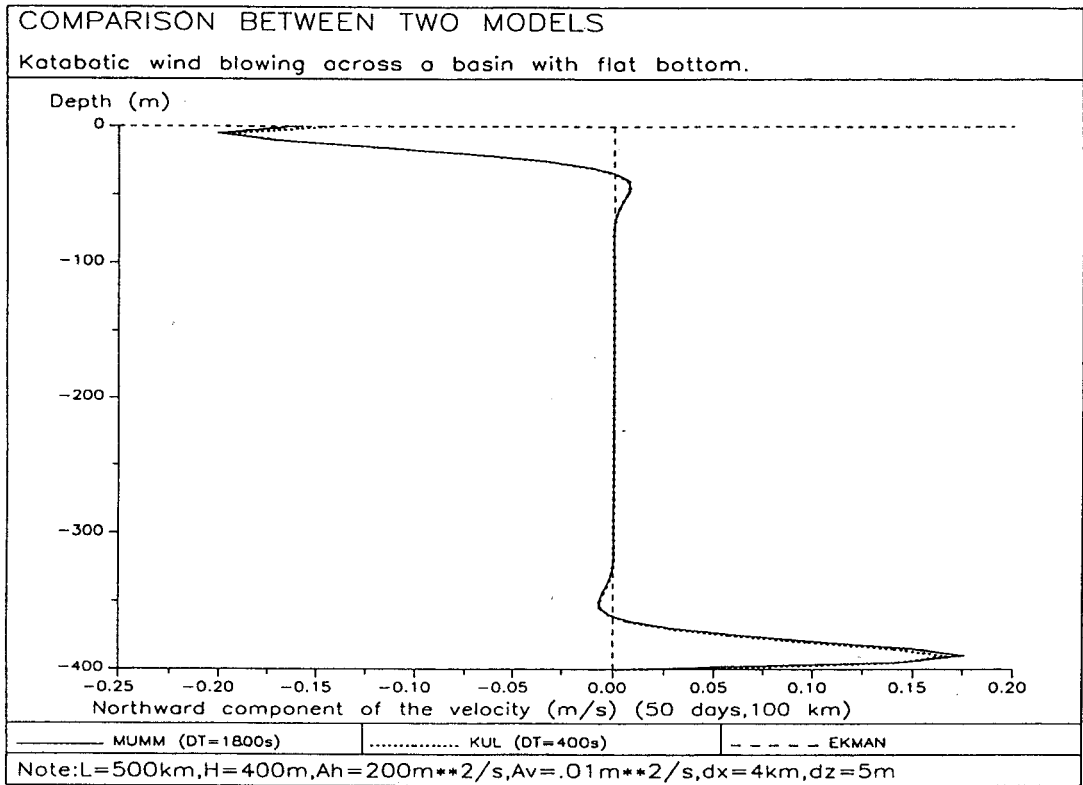
Figure 20: 2.5D model: Northward velocity component áfter 50 days for Case 1 at (a) 100 km and (b) 300 km. The vertical grid size is 5m.

COMPARISON BETWEEN TWO MODELS

Katabatic wind blowing across a basin with flat bottom.

Depth (m)

Eastward component of the velocity (m/s) (50 days,100 km)

MUMM (DT=1800s) KUL (DT=400s) EKMAN

Note:L=500km,H=400m,Ah=200m**2/s,Av=.01m**2/s,dx=4km,dz=5m

COMPARISON BETWEEN TWO MODELS

Katabatic wind blowing across a basin with flat bottom.

Depth (m)

Eastward component of the velocity (m/s) (50 days,300 km)

MUMM (DT=1800s) KUL (DT=400s) EKMAN

Note:L=500km,H=400m,Ah=200m**2/s,Av=.01m**2/s,dx=4km,dz=5m

ANTAR II/02

Figure 21: 2.5D model: Eastward velocity component after 50 days for Case 1 at (a) 100 km and (b) 300 km. The vertical grid size is 5m.
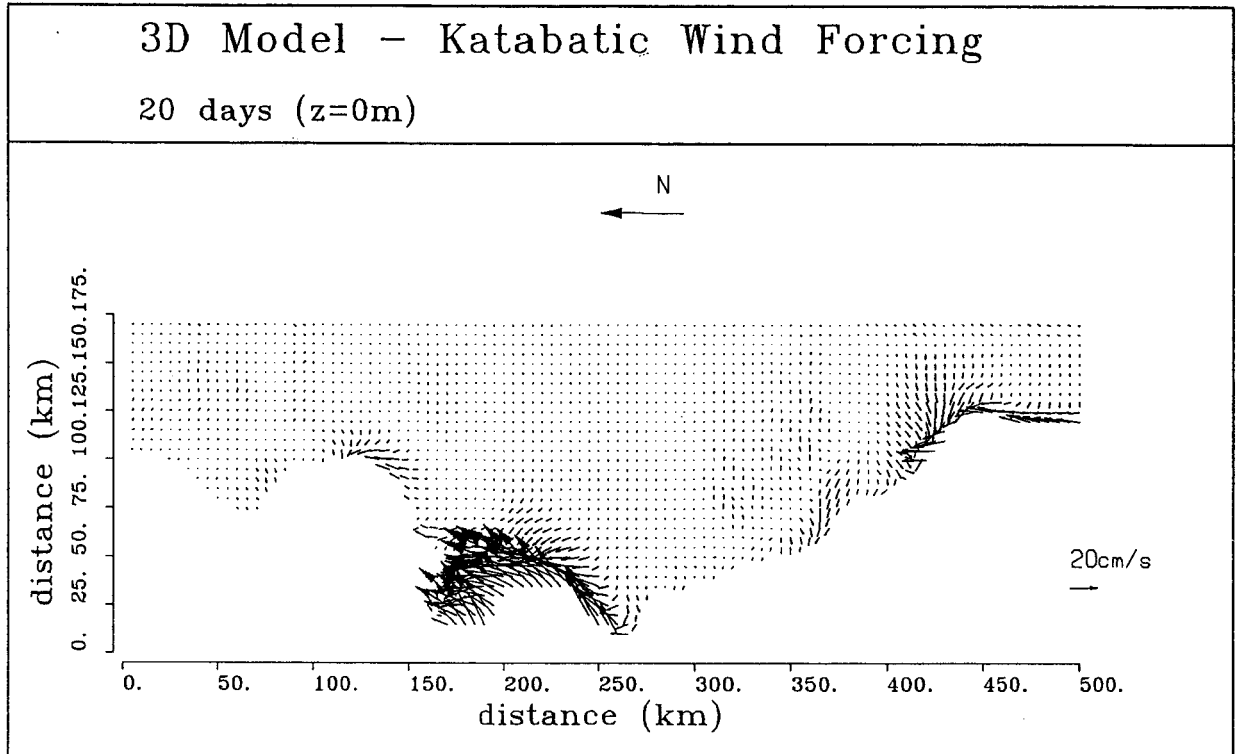
Figure 22: Katabatic wind : 3D model.

4.2 A 3D model of the Terra Nova coastal area

4.2.1 Description of the model area

The model area is situated along the coast of Terra Nova Bay (Antarctica) The dimension are 500 km in northward direction and 175 km in eastward dirction. The horizontal eddy viscosity is 1000 m^2s^{-1} and the vertical one 0.01 m^2s^{-1}. The Coriolis parameter has been taken at 70°S. The horizontal grid size is 5 km, the waterdepth is constant and equal to 1000 m. This value is approaching the waterdepth found off the coast of Terra Nova. The model is forced by katabatic winds, calculated by a 3D atmospheric model (UCL). In this model the geographical boundaries are taken into account. In figure 22 is displayed the wind forcing. Interesting to note is the strong concentration of the katabatic wind at certain areas along the coast. The differences with the 2.5D wind field are situated in the more extreme less continues values of the forcing. At about $x=200$ km the wind speed reaches up to 20 ms^{-1} near the coast and is then quickly decreasing to nearly zero stress. These strong variations are not found in the 2.5D wind forcing. Again the model starts the calculation at time 0 and continues until 20 days have been simulated. At this time steady state is not fully reached.

4.2.2 Results of the simulations

In figures 23 and 24 are shown the horizontal flow fields at different depth. The surface flow field (figure 23a) is characterised by the presence of some small and local areas with high flow values. At about $x=200$ km the water is flowing with a speed of about 50cms^{-1}. The flow field at the surface is is to the left of the wind direction. The wind and flow pattern near the coast are in agreement with the idea of coastal polynia formation by a combination of strong seaward winds and currents. At about $x=200$ km and $x=430$ km this seaward surface flow is clearly existing. The flow field is decreasing quickly with depth, see figure 23b for the horizontal flow at 20 m depth. The figures 24c and 24d are presenting the horizontal flow field at 400 m and 990 m depth. The flow pattern is more or less constant with depth and is build up of three eddies. The eddies are partially due to the coastal boundaries, see at $x=170$ km. The strong non uniform wind is inducing in the coastal zones divergence or convergences reulting in upwelling or downwelling away from the boundaries. These vertical flow structures can influence the density currents and the formation of dense bottom water. This subject must be investigated by a baroclinic model and could be made the subject of further research.

ANTAR II/02

4.3 Discussion

The subject of this chapter is the simulation of flows induced by katabatic winds. Two applications have been worked out. The first one consist of a vertical plane model taken at the coast of Adélie land and the second one is a 3D model of a costal zone of Terra Nova. The Adélie model has been the subject of an intercomparison excercise between the models of the KUL and the MUMM. The results of these investigations have been briefly described here, the reader interested in more details is referred to Fettweis *et al.*(1991a).

The katabatic winds have been simulated by the atmospheric models of the UCL. It was found that the strongest winds for both wind fields occur near the coast. Differences exist between both wind fields. The wind for the 2.5D model is decreasing smoothly with increasing distance from the coast (up to the inversion point at 200 km). The 3D wind field however shows much more irregularity. The strong winds are concentrated in some small areas along the coast and the wind is decreasing rapidly when leaving the coast.

The differences in wind forcing are (of course) reflected in the simulated currents. Interesting to note is that in both models a seaward flow exist near the coast. This result is supporting the idea of coastal polynia formation by a combination of wind and surface flow action.
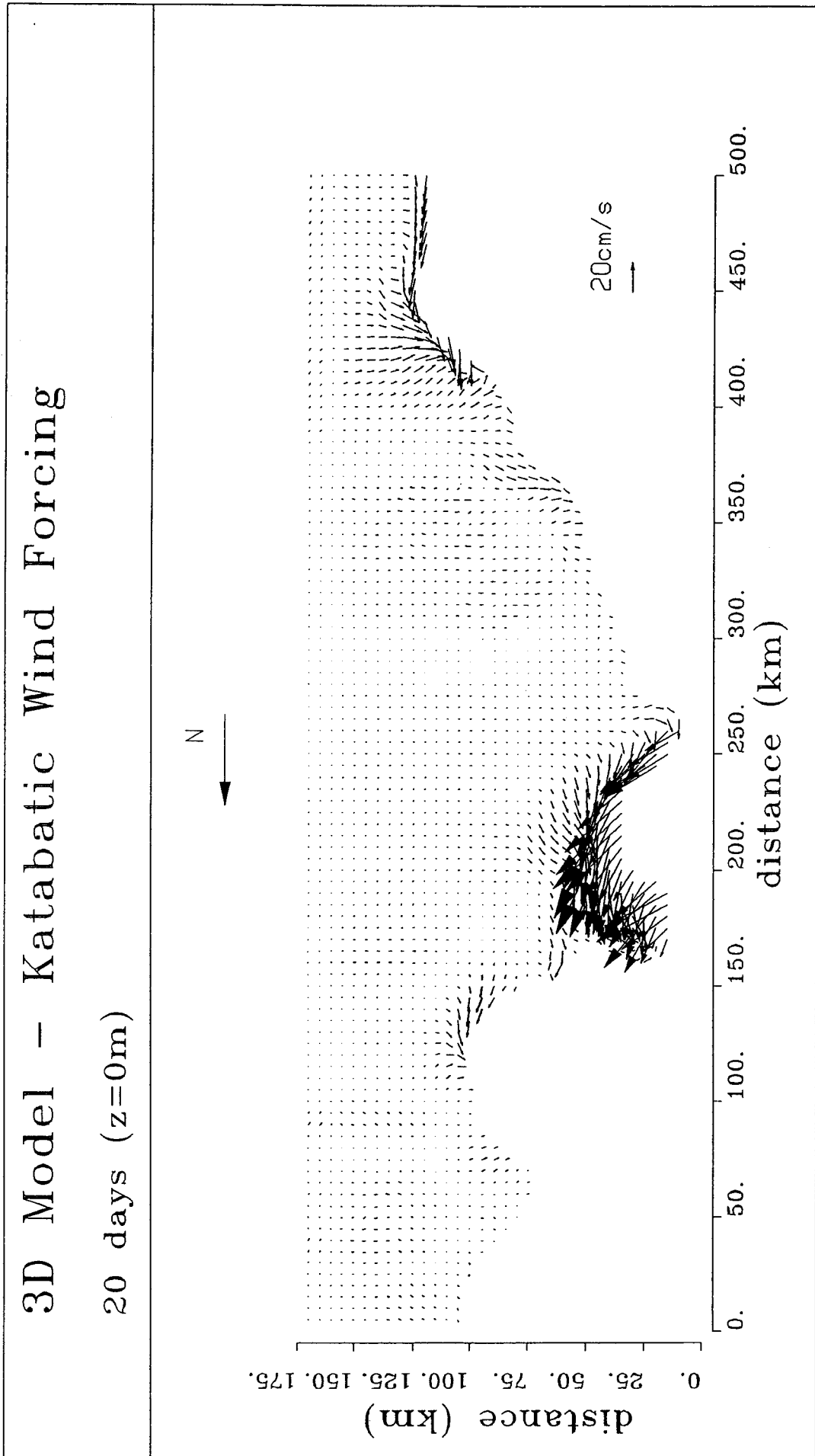
Figure 23a: Horizontal flow field at the surface calculated by the 3D model.

3D Model – Katabatic Wind Forcing

20 days (z=20m)
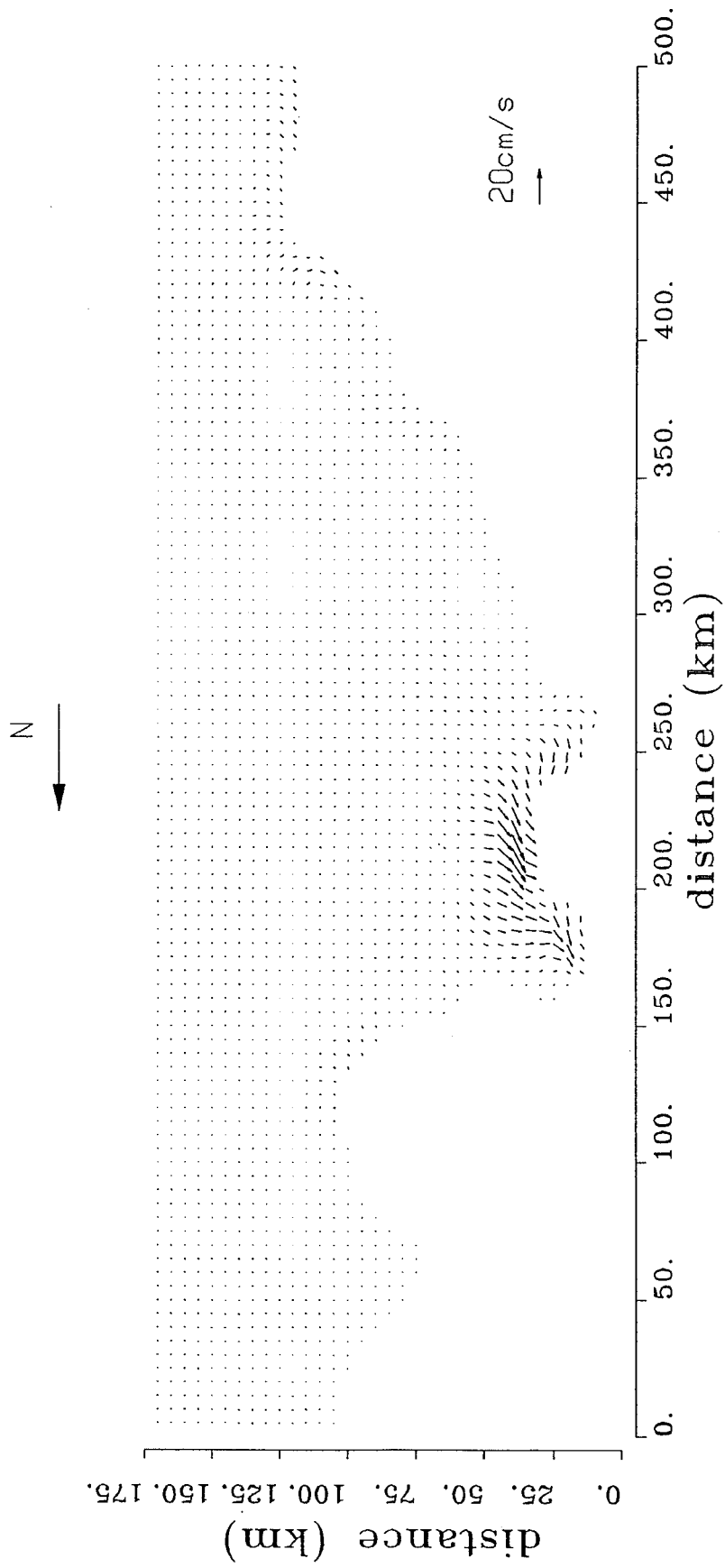
Figure 23b: Horizontal flow field at 20 m depth calculated by the 3D model.
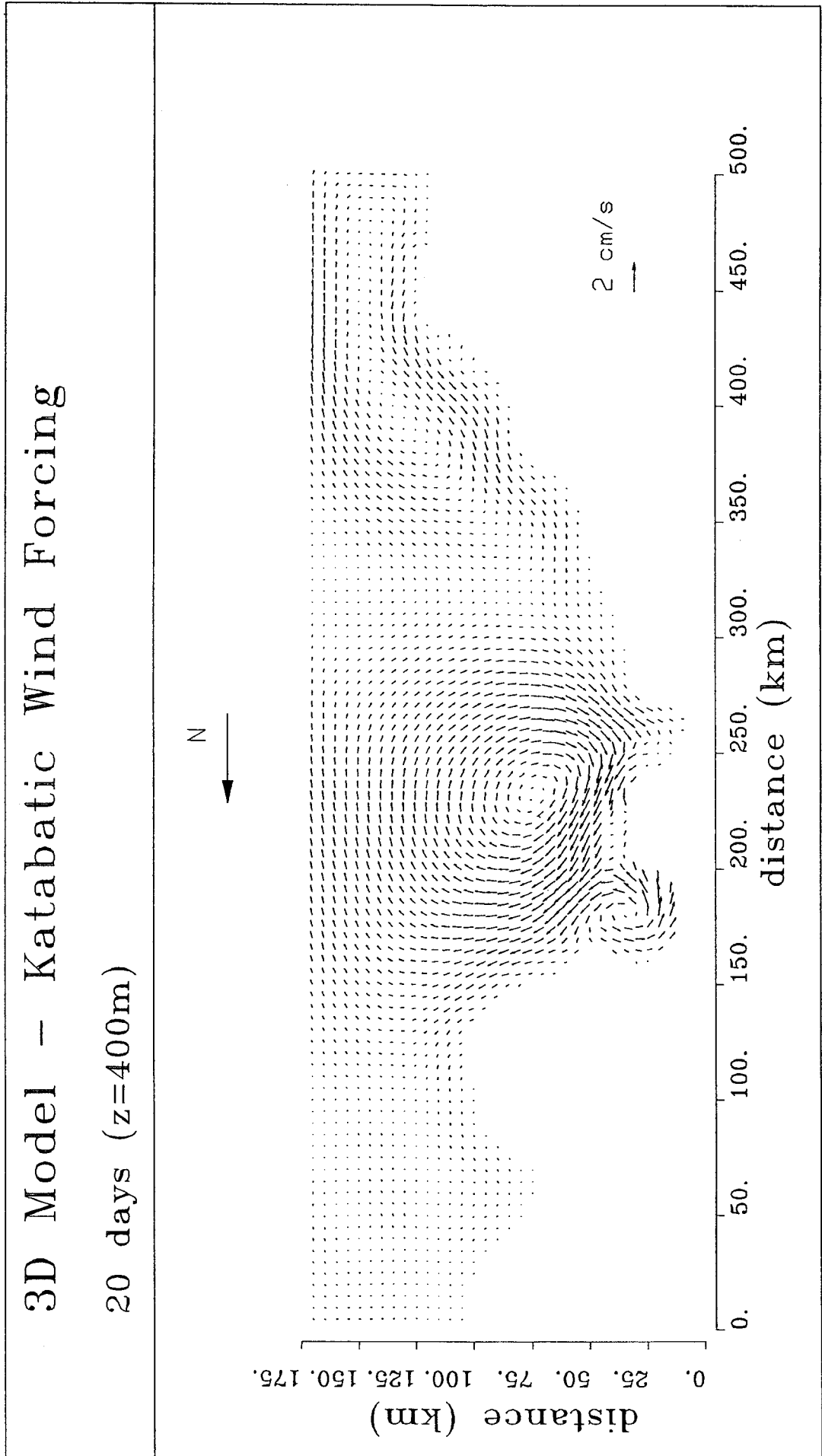
ANTAR
II/02

Figure 23c: Horizontal flow field at 400 m depth calculated by the 3D model.

3D Model — Katabatic Wind Forcing

20 days (z=990m)
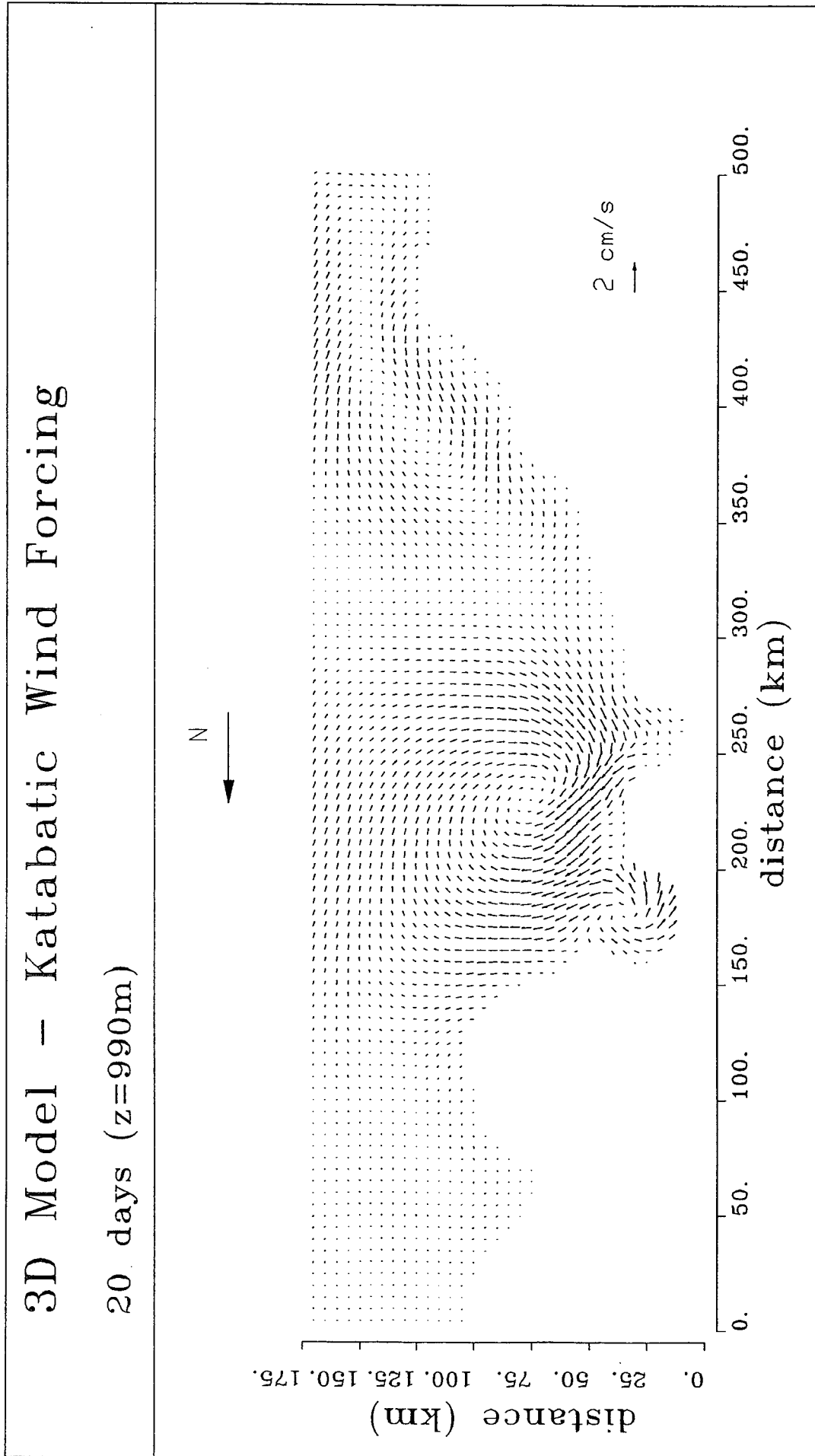
Figure 23d: Horizontal flow field at 990 m depth calculated by the 3D model.

ANTAR
II/02

5 Conclusions

In order to do numerical study of wind and density induced currents in the Antarctic coastal zones two numerical models have been developed. The first one can be described as a vertical plane (2.5D) baroclinic model. The second one fall into the class of fully 3D models. The 2.5D model has been applied to simulate the upwelling along a shelf break in an ice covered and stratified water. The second application as well as the 3D model application have as subject the flow structure due to katabatic wind forcing.

Every model which describes a physical phenomenon gives rise to inaccuracies, the results should therefore be taken as speculative as long as they are not validated by comparing them with reality. The results presented are reasonable in the sence that they are logical and are fulfilling the expectations. In order to say something about the quantitative aspect of the solution measurements are necessary for comparison. It was not possible to compare the results of the models with measurements for the simple reason that they are very scarce for Antarctic waters. Another possibility for evaluating the model performance is to test it with other models or with applications for which validation data are available. The "katabatic wind" results of the 2.5D model have been compared to the results of another model and to an (simplified) analytical solution. All the three results show an overall agreement and we can conclude that the 2.5D model is well simulating the ocean circulation.

From the comparison exercise it was learned that a good resolution of the top and bottom boundary layer is necessary in order to improve the results since the largest currents are calculated at the surface and (less) at the bottom.

Including variable density in the model can substantially alter the flow field. The introduction of baroclinic effects for the calculation of the currents for the katabatic wind driven models seems to be important. The incorporation of the hydrodynamic model in a coupled system of atmosphere, ocean and sea-ice is the next step which has to be taken for a more realistic study of coastal polynias.

In order to judge the quality of the results of the 3D model it was first applied to a simple test case. The results were encouraging us to start more complex applications. One of the difficulties encountered during the development of the 3D model was concerning the definition of (open) boundary conditions. The problem was related with the solution of the pressure equation. For some applications the model was unstable, it was found that this is related with the explicit definition of the Coriolis parameter. In order to avoid these problems the Coriolis term must be made (semi-) implicit.

The choice between a 2.5D model and a 3D model is related to the specific problem. For the two "katabatic wind" applications it is clear that the wind field is a consequence of the complex geometry and topography of the area. The flow field for the Terra Nova area can only be modelled correctly by a fully 3D model. The 2.5D model however remains

a tool which can give a good idea about the flow structure. Although the simulations treated here are all related to a very specific phenomenon occurring in some particular zones of the Southern ocean other applications of the models are possible. The models have been developed in such a way that they are general enough to be applied to other water bodies.

ANTAR
II/02

Acknowledgements

References

Bryan, K. 1969. A numerical method for the study of the circulation of the world ocean. J. Comp. Phys. 4: 347-376.

Buckley, J.R., Gammelsrød, T., Johannessen, J.A., Johanessen, O.M. and Røed, L.P. 1979. Upwelling: Oceanic structures at the edge of the Arctic ice peak in the winter. Science 203: 165-167.

Ekman, V.W. 1905. On the influence of the Earth's rotation on ocean currents. Ark. Mat. Astron. Fys 2(11).

Fettweis, M., Yu, C.S., Berlamont, J. and Rosso, M. 1990. A 2.5D and a 3D numerical ocean model for wind driven flows in a partially ice covered shelf sea. Interim Report ANTAR 02/II contract, Belgian Scientific Research Program on Antarctica, Services of the Prime Minister - Science Policy Office, 48p.

Fettweis, M., Yu, C.S., Petit, B., Ozer, J., Demuth, Cl. and Gallée, H. 1991a. Comparison of two 2.5D ocean models forced by a Katabatic wind. Report Antar 01,02 and 03/II contracts, Belgian Scientific Research Program on Antarctica, Services of the Prime Minister - Science Policy Office, 52p.

Fettweis, M., Yu, C.S. and Berlamont, J. 1991b. Modelling upwelling along a shelf break in high latitudes. Computer Modelling in Ocean Engineering 91, Proc. of the 2nd Int. Conf. on Computer Modelling in Ocean Engineering. Barcelona. Spain. BALKEMA: 21-31.

Galée, H., Berger, A., Schayes, G., Fichefet, T., Marsiat, I., Tricot C. and van Ypersele, J.P. 1989. Numerical study of the air sea interactions in the Antarctic coastal zone and their implications on deep sea formation in the case of katabatic wind. In: Antarctica. Vol 3. Glaciology and Climatology. Caschetto, S. (Ed). Belgian Scientific Research Program on Antarctica, Services of the Prime Minister - Science Policy Office. 40p.

Golub, G.H. and Van Loan, C.F. 1989. Matrix Computations. 2nd editon. The Johns Hopkins University Press, Baltimore and London.

Ikeda, M. 1985 A coupled ice-ocean model of a wind-driven coastal flow. J. Geoph. Res. 90(C5): 9119-9128.

Jamart, B.M. and Ozer, J. 1986. Numerical boundary layers and spurious residual flows. J. Geoph. Res. 91(C9): 10621-10681.

Jamart, B.M., Milliff, R., Lick, W. and Paul, J. 1982. Numerical studies of the wind-driven circulation in the Santa Barbara channel. Final Report to Exxon Production Research Company. 126p.

Johnson, J.A. and Rockliff, N. 1986. Shelf break circulation processes. In: Baroclinic Processes on Continental Shelves. Mooers, C.N.K. (Ed). Coastal and Estuarine Sciences 3, American Geophysical Union: 33-62.

Niebauer, H.J. 1982. Wind and melt driven circulation in a marginal sea ice edge frontal system: a numerical model. Cont. Shelf Res. 1(1): 49-98.

O'Brien, J.J., Clancy, R.M., Clarke, A.J., Crepon, M., Elsberry, R., Gammelsrød, T., MacVean, M., Røed, L.P. and Thompson, J.D. 1977 Upwelling in the ocean: two- and three- dimensional models of upper ocean dynamics and variability. In: Modelling and Prediction of the Upper Layer of the Ocean. Krauss, E.B. (Ed). Pergamon Press, Oxford and New York.

Ozer, J., Jamart, B.M. and Spitz, Y. 1988. Wind driven flows in an enclosed basin: a comparison of numerical model's. MUMM's Contribution to BSEX. Technical Report No. TRO6. 139p.

Petit, B. 1991. Programm de recherche sur l'Antarctique. Rapport d'activité del l'UGMM du 1 aout 1990 au 31 janvier 1991.

Peyret, R. and Taylor, T.D. 1983. Computational methods for fluid flow. Springer Verlag New York. 358p.

Røed, L.P. and O'Brien, J.J. 1983. A coupled ice-ocean model of upwelling in the marginal ice zone. J. Geoph. Res. 88(C5): 2863-2872.

Røed, L.P. 1983. Sensitivity studies with a coupled ice-ocean model of the marginal ice zone. J. Geoph. Res. 88(C10): 6039-6042.

Smith, R.L. 1980 A comparison of the structure and variability of the flow field in three coastal upwelling regions: Oregon, Northwest Africa and Peru. In: Coastal Upwelling. Richards F.A. (Ed). Coastal and Estuarine Sciences 1, American Geophysical Union: 107-118.

Spitz, Y., Ozer, J. and Jamart, B. 1987. Numerical experiments with a verticalplane 2.5D hydrodynamical model. MUMM's Contribution to BSEX. Technical Report No. TRO5. 106p.

van Ypersele, J.P. 1986. A numerical study of the response of the Southern ocean and its sea ice to a CO_2 induced atmospheric warming. Cooperative Thesis Université de Louvain, Belgium and National Center for Atmospheric Research, USA. 135p.

ANTAR
II/02

Yu, C.S., Fettweis, M., Rosso, M. and Berlamont J. 1990. A 2D model with changing land-water boundaries. Computational Methods in Surface Hydrology. Gambolati, G. *et al.*(Eds). Computational Mechanics Publications and Springer-Verlag: 101-106.

Zwally, H.J., Comiso, J.C. and Gordon, A.L. 1985. Antarctic offshore leads and polynias and oceanographic effects. Oceanology of the Antarctic Continental Shelf, Antarctic Research Series. 43: 203-226.

DEVELOPMENT OF A 3-DIMENSIONAL MESO-γ PRIMITIVE EQUATIONS MODEL : KATABATIC WINDS SIMULATION IN THE AREA OF TERRA NOVA BAY, ANTARCTICA

H. Gallée, G. Schayes
and A. Berger

Contents

Abstract : *The spatial evolution of Antarctic katabatic winds in the area of Terra Nova Bay is examined using the three-dimensional version of the UCL/MAR[1] mesoscale primitive equation model. The ability of the model to replicate classical linear and nonlinear mountain waves simulations is verified. Then, a three-dimensional experiment is performed using the terrain configuration of Terra Nova (Ross Sea coastal zone). Because of computational requirements, the discretization is chosen to be 5 km. Results are in good agreement with available observations and previous modeling work. In particular, the high resolution allows the model to represent the katabatic jet over Terra Nova Bay.*

**ANTAR
II/03**

---

[1]MAR: Modèle Atmosphérique Régional

1 Introduction

Atmospheric circulation over the Antarctic continent is dominated by katabatic winds. Katabatic wind occurs where air adjacent to a sloped surface is colder than directly above. In this case, the larger air density resulting from lower temperature is responsible for a gravity driven atmospheric current which horizontal scale is typically that of the slope. Because of the long polar night over Antarctica, the surface cooling is so important that a strong sloped inversion forms, causing the induced wind to reach a stormy character, especially in the Antarctic coastal zone, where the slopes are steeper. Moreover, although katabatic wind is observed all around the world [*Mather and Miller*, 1967] and generally classified as a mesoscale phenomenon, the horizontal scale of the Antarctic slopes is so important that Antarctic katabatic wind is perhaps the most remarkable climatic feature which has already been observed on polar ice caps [*Parish*, 1988].

The aim of the present research is to understand the physical mechanisms which are responsible for strong katabatic winds events in some regions of the Antarctic coastal zone, in order to provide in the future more insight into the impact of Antarctica on global climate. These impacts are numerous: for example Antarctic coastal polynyas (water area free of ice) are responsible for strong heat exchanges between the atmosphere and the ocean and are forced by winds coming from the continent [*Zwally et al.*, 1985]; mesocyclones which contribute to the Antarctic snow mass budget could be generated by katabatic winds events [*Heinemann*, 1990].

Model studies [*Parish and Bromwich*, 1987, 1991] have shown that katabatic winds are very strong in topographic confluence zones because of the large supply of negatively buoyant air. This is particularly true in Adélie Land and in the area of Terra Nova Bay.

Sudden decays of katabatic winds in the Antarctic interior have also been ob-

served [*Pettré and André*, 1991].

On the other hand, it has been inferred from thermal infrared satellite imagery that strong katabatic winds in the area of Terra Nova Bay can propagate horizontally for hundred of kilometers after passing the coast line [*Bromwich*, 1989]. Concerning air-sea interactions in polar regions, [*Pease*, 1987] has found that a seaward component of the wind exceeding 10 m s^{-1} is sufficient to maintain in the coastal zone a polynya.

It is believed that the presence of the stable, annually recurring Terra Nova Bay polynya is due to strong, persistent katabatic winds which blow far offshore [*Kurtz and Bromwich*, 1985]. Coastal polynyas like that of Terra Nova Bay are of particular importance. In these ice-free zones, strong heat exchanges occur between the cold atmosphere and the relatively warm ocean, with enhanced sea-ice formation and salt rejection in the water column [*Zwally et al.*, 1985]. For exemple, sea-ice formation in the Terra Nova Bay polynya contributes to no less than 10% of the total sea-ice formation in the region of the Ross Sea continental shelf [*Kurtz and Bromwich*, 1985].

Moreover, the presence of ice-free ocean near the Antarctic coast in winter modifies the energy and momentum budgets of the atmosphere and influences the general circulation and the Earth's climate [*Wendler et al.*, 1983; *Gordon*, 1988]. In spring, summer and fall, the high level of solar light at the open-water surface of a polynya (in contrast to under the surrounding sea ice) allows major biological productivity. Polynias are similar to oases in a terrestrial desert; within the sea-ice cover they allow access to open water and food. Marine mammals and birds use them variously as feeding, mating, and overwintering grounds.

In a previous paper [*Gallée and Schayes*, 1992], the katabatic wind evolution on idealized slopes representative of the coastal area of Antarctica, has been analyzed.

ANTAR
II/03

Some ideas about the kind of physical mechanisms that are responsible for the persistance or the weakening of katabatic wind in this area were given.

One purpose of this paper is to discuss katabatic winds simulation on more realistic slopes, using the three-dimensional version of the UCL/MAR meso-γ model. Katabatic winds over the complex topography of the region of Terra Nova (Ross Sea coastal zone) will be simulated. The results will be compared with available observations and previous simulations, with a particular attention to the katabatic winds decay in the area of Terra Nova Bay. The study will be restricted to the case of a pure katabatic wind event where the ocean is covered with sea-ice.

2   The Model

2.1   Equations of the Atmospheric Model

The atmosphere is simulated with a mesoscale primitive equations model in which the full continuity equation is taken into account. To express the surface boundary conditions in a way as easy as possible, and to allow a wide variety of applications, the pressure ratio σ-coordinate is used :

$$\sigma = \frac{p - p_t}{p_\star} \tag{1}$$

where p is pressure, p_t refers to the pressure at the top of the model, (set equal to 50 hPa), p_s is the surface pressure and $p_\star = p_s - p_t$

The use of the pressure ratio is preferred to the height ratio because this allows a more accurate integration of the hydrostatic equation, using the finite difference approximation [*Tanrikulu, Carroll and Liu*, personnal communication]. Horizontal equations for momentum are therefore :

$$\frac{\partial u}{\partial t} = -u\frac{\partial u}{\partial x} - v\frac{\partial u}{\partial y} - \dot{\sigma}\frac{\partial u}{\partial \sigma} + f(v - v_g) - \frac{\partial \phi}{\partial x}\mid_p + F_u \tag{2}$$

$$\frac{\partial v}{\partial t} = -u\frac{\partial v}{\partial x} - v\frac{\partial v}{\partial y} - \dot{\sigma}\frac{\partial v}{\partial \sigma} - f(u - u_g) - \frac{\partial \phi}{\partial y}\Big|_p + F_v \tag{3}$$

where x and y are the horizontal axis, t is time, u, v and $\dot{\sigma}$ are respectively the x, y and σ components of the wind, f is the Coriolis parameter, $\vec{V_g} = (u_g, v_g)$ is the geostrophic wind, written explicitly for generality, $\phi = gz$ is the mesoscale geopotential perturbation, g is gravity, z is altitude, $|_p$ means that the pressure gradient force $\left(-\frac{\partial \phi}{\partial x}, -\frac{\partial \phi}{\partial y}\right)$ is calculated on an isobaric surface. This avoids its development into the sum $-\frac{R_a T}{p_* + \frac{p_t}{\sigma}}\frac{\partial p_*}{\partial x} - \frac{\partial \phi}{\partial x}\Big|_\sigma$ which leads to severe truncation errors on steep topography [Alpert et al., 1982]. F_u and F_v are the divergences of the turbulent momentum fluxes :

$$F_u = -\frac{1}{p_*}\frac{\partial(p_* \overline{u'u'})}{\partial x} - \frac{1}{p_*}\frac{\partial(p_* \overline{v'u'})}{\partial y} - \frac{\partial(\overline{\dot{\sigma}'u'})}{\partial \sigma} \tag{4}$$

$$F_v = -\frac{1}{p_*}\frac{\partial(p_* \overline{u'v'})}{\partial x} - \frac{1}{p_*}\frac{\partial(p_* \overline{v'v'})}{\partial y} - \frac{\partial(\overline{\dot{\sigma}'v'})}{\partial \sigma} \tag{5}$$

where the overbar indicates time average. It must be pointed out that to preserve simplicity overbar is avoided except for the turbulent fluxes.

The vertical momentum equation is approximated by the hydrostatic equilibrium and after some algebra we get :

$$\frac{\partial \phi}{\partial(\frac{T}{\theta})} = -C_p \theta(1 + 0.85q) \tag{6}$$

where

$$\theta = T\left(\frac{p_0}{p}\right)^\kappa \tag{7}$$

is the definition of potential temperature, T is the air temperature, $p_0 = 1000$ hPa, $\kappa = \frac{R_a}{C_p}$, R_a is the perfect gas constant for dry air, C_p is the specific heat at constant pressure for dry air and q is the specific humidity.

The equation of state for humid air as a perfect gas is given by :

$$p = \rho R_a T(1 + 0.608q) \tag{8}$$

The full continuity equation is used and is expressed through the time tendency equation for $p_\star$

$$\frac{\partial p_\star}{\partial t} = -\int_0^1 \left(\frac{\partial(p_\star u)}{\partial x} + \frac{\partial(p_\star v)}{\partial y} \right) d\sigma \tag{9}$$

from which the vertical velocity in σ coordinates $\dot\sigma$ can be computed,

$$\dot\sigma = \frac{1}{p_\star} \left[\sigma \int_0^1 \left(\frac{\partial}{\partial x}(p_\star u) + \frac{\partial}{\partial y}(p_\star v) \right) d\sigma - \int_0^\sigma \left(\frac{\partial}{\partial x}(p_\star u) + \frac{\partial}{\partial y}(p_\star v) \right) d\sigma \right] \tag{10}$$

The thermodynamic energy equation is :

$$\frac{\partial \theta}{\partial t} = -u\frac{\partial \theta}{\partial x} - v\frac{\partial \theta}{\partial y} - \dot\sigma\frac{\partial \theta}{\partial \sigma} + \frac{\partial R_{IR}}{\partial \sigma} + F_\theta \tag{11}$$

where R_{IR} is the infrared radiative heat flux [*Sasamori*, 1968] and

$$F_\theta = -\frac{1}{p_\star}\frac{\partial(p_\star \overline{u'\theta'})}{\partial x} - \frac{1}{p_\star}\frac{\partial(p_\star \overline{v'\theta'})}{\partial y} - \frac{\partial(\overline{\dot\sigma'\theta'})}{\partial \sigma} \tag{12}$$

is the divergence of the turbulent heat flux.

The specific humidity conservation is expressed with the following equation :

$$\frac{\partial q}{\partial t} = -u\frac{\partial q}{\partial x} - v\frac{\partial q}{\partial y} - \dot\sigma\frac{\partial q}{\partial \sigma} + F_q \tag{13}$$

where

$$F_q = -\frac{1}{p_\star}\frac{\partial(p_\star \overline{u'q'})}{\partial x} - \frac{1}{p_\star}\frac{\partial(p_\star \overline{v'q'})}{\partial y} - \frac{\partial(\overline{\dot\sigma'q'})}{\partial \sigma} \tag{14}$$

is the divergence of the turbulent moisture flux.

Equations (2), (3), (6), (8)–(11) and (13) form a system of 8 equations for 8 unknows u, v, $\dot\sigma$, ϕ, $p_\star$, ρ, θ and q; p and T can be obtained from the definitions (1) and (7) of σ and θ respectively, and the turbulent fluxes introduced in (4), (5), (12) and (14) will be parameterized.

It should be noted that a two-dimensional version of this set of equations is easily obtained by eliminating all the terms containing a derivative with respect of y.

2.2 Upper and Lower Boundary Conditions

The boundary conditions at the top of the model, where $p = p_t$ ($\sigma = 0$), are :

$$\dot{\sigma} = 0 \tag{15}$$

$$\frac{\partial u}{\partial \sigma} = \frac{\partial v}{\partial \sigma} = 0 \tag{16}$$

$$\theta = \theta_{observed} \tag{17}$$

$$q = q_{observed} \tag{18}$$

To minimize reflection from the upper boundary, we use a viscous damping layer at the top of the domain, similar to that used by *Klemp and Lilly* [1978] to absorb vertically propagating waves. This absorbing layer takes the following form:

$$\begin{aligned} K_t &= 0 & , k \geq 5 \\ K_t &= K_{max}\frac{\sigma_b - \sigma_k}{\sigma_b} & , k < 5 \end{aligned} \tag{19}$$

ANTAR II/03

where K_t is added to the horizontal eddy exchange coefficient (see below) and $k = 1$ refers to the highest level of the model. Except otherwise stated, the nondimensional value used for K_{max} (i.e. $K'_{max} = K_{max}\frac{\Delta t}{\Delta x^2}$) is 0.1.

The boundary conditions at the surface ($\sigma = 1$) are :

$$u, v = 0 \tag{20}$$

$$T = T_s(t) \tag{21}$$

$$q = q_s(T_s) \tag{22}$$

where T_s is the predicted air surface temperature in function of time t (see below), and q_s is the saturation specific humidity corresponding to the air surface temperature T_s. This last choice is made because in our simulations, the surface is assumed to be covered by snow.

2.3 Lateral Boundary Conditions

To help suppress spurious boundary reflections, the following radiation condition are used:

$$\frac{\partial \psi}{\partial t} + c\frac{\partial \psi}{\partial x_i} = 0 \tag{23}$$

where $\psi = u, v, \theta$ or q and c is the wave velocity, $x_i = x$ and y for lateral boundaries on the x and y axis respectively. This scheme has been introduced by *Orlanski* [1976] and discussed later by *Miller and Thorpe* [1981]. The 3th order accurate in space formulation of *Miller and Thorpe* [1981] is used for determining c.

2.4 Parameterization of Subgrid Scale Fluxes

For each variable $\psi = u$, v , θ or q, the expression of the subgrid scale fluxes is of the form:

$$F_\psi = -\frac{1}{p_\star}\frac{\partial(p_\star\overline{u'\psi'})}{\partial x} - \frac{1}{p_\star}\frac{\partial(p_\star\overline{v'\psi'})}{\partial y} - \frac{\partial(\overline{\dot{\sigma}'\psi'})}{\partial \sigma} \tag{24}$$

Alpert and Neumann [1984] have obtained simple relationships between vertical subgrid scale fluxes in the rectangular coordinate system and in the σ system. To do this, the two following approximations have been made:

(i) Taking that the local variation of the geopotential is small, the expression for the vertical velocity in the rectangular coordinate system is

$$w = \frac{dz}{dt} \simeq \frac{1}{g}u\frac{\partial \phi}{\partial x} + \frac{1}{g}v\frac{\partial \phi}{\partial y} - \frac{p_\star\dot{\sigma}}{\rho g} \tag{25}$$

(ii) It is presumed that in regions of topography the terms $|\frac{\partial \overline{\phi}}{\partial x_i}|$ is larger than $|\frac{\partial \phi'}{\partial x_i}|$, with $x_i = x, y$. And one gets:

$$\overline{\psi'\dot{\sigma}'} = \frac{\rho g}{p_\star}\left[-\overline{\psi'w'} + \overline{\psi'u'}\frac{\partial \overline{z}}{\partial x} + \overline{\psi'v'}\frac{\partial \overline{z}}{\partial y}\right] \tag{26}$$

A convenient way for the expression of the 'horizontal' subgrid scale flux in the x direction is the use of an eddy exchange coefficient K_H. This could be done in the

rectangular coordinate system and then transformed into the σ system [*Alpert and Neumann*, 1984]:

$$\overline{\psi' u'} = -K_H \frac{\partial \overline{\psi}}{\partial x}\Big|_z = -K_H \left(\frac{\partial \overline{\psi}}{\partial x}\Big|_\sigma + \frac{\partial \sigma}{\partial x}\frac{\partial \overline{\psi}}{\partial \sigma} \right) \tag{27}$$

$$\overline{\psi' v'} = -K_H \frac{\partial \overline{\psi}}{\partial y}\Big|_z = -K_H \left(\frac{\partial \overline{\psi}}{\partial y}\Big|_\sigma + \frac{\partial \sigma}{\partial y}\frac{\partial \overline{\psi}}{\partial \sigma} \right) \tag{28}$$

The eddy exchange coefficient K_H parameterization is adapted from *Smagorinsky* [1963]:

$$K_H = K_t + (k_H l_H)^2 \left[\frac{1}{2}\left(\frac{\partial v}{\partial x} + \frac{\partial u}{\partial y} \right)^2 + \left(\frac{\partial u}{\partial x} \right)^2 + \left(\frac{\partial v}{\partial y} \right)^2 \right]^{1/2} \tag{29}$$

where $l_H = \triangle x$ is the assumed mixing length and k_H is a dimensionless constant, which value range between 0.2 and 0.4 [*Tag et al.*, 1979]; the value $k_H = 0.4$ has been taken. Although the formulation (29) seems plausible, it has not yet been verified for katabatic wind observations. This fact has to be taken into account when analysing our simulations.

After some algebra one gets from (24), (26), (27) and (28):

$$F_\psi = \underbrace{\frac{1}{p_\star}\frac{\partial}{\partial x}\left(p_\star K_H \frac{\partial \overline{\psi}}{\partial x} \right)}_{A_{\psi,x}} + \underbrace{\frac{1}{p_\star}\frac{\partial}{\partial y}\left(p_\star K_H \frac{\partial \overline{\psi}}{\partial y} \right)}_{A_{\psi,y}}$$

$$+ \underbrace{\frac{g}{p_\star^2}\frac{\partial}{\partial x}\left(\rho\alpha K_H \frac{\partial \overline{\psi}}{\partial \sigma} \right)}_{B_{\psi,x}} + \underbrace{\frac{g}{p_\star^2}\frac{\partial}{\partial y}\left(\rho\beta K_H \frac{\partial \overline{\psi}}{\partial \sigma} \right)}_{B_{\psi,y}}$$

$$+ \underbrace{\frac{g}{p_\star^2}\frac{\partial}{\partial \sigma}\left(\rho\alpha K_H \frac{\partial \overline{\psi}}{\partial x} \right)}_{C_{\psi,x}} + \underbrace{\frac{g}{p_\star^2}\frac{\partial}{\partial \sigma}\left(\rho\beta K_H \frac{\partial \overline{\psi}}{\partial y} \right)}_{C_{\psi,y}}$$

$$+ \underbrace{\frac{\partial}{\partial \sigma}\left(\left(\frac{\rho g}{p_\star}\alpha\right)^2 K_H \frac{\partial \overline{\psi}}{\partial \sigma} \right)}_{D_{\psi,x}} + \underbrace{\frac{\partial}{\partial \sigma}\left(\left(\frac{\rho g}{p_\star}\beta\right)^2 K_H \frac{\partial \overline{\psi}}{\partial \sigma} \right)}_{D_{\psi,y}} - \underbrace{\frac{\partial}{\partial \sigma}\left(\frac{\rho g}{p_\star}\overline{\psi' w'} \right)}_{E_\psi} \tag{30}$$

where $\alpha = \frac{\partial z}{\partial x}$ and $\beta = \frac{\partial z}{\partial y}$ (respectively the x and y slope components of the σ surface). Terms $A_{\psi,x}$ and $A_{\psi,y}$ are the horizontal diffusion terms on σ surfaces. Term E_ψ is the divergence of the vertical turbulent flux. Terms $B_{\psi,x}$, $B_{\psi,y}$, $C_{\psi,x}$, $C_{\psi,y}$, $D_{\psi,x}$ and $D_{\psi,y}$ are correction terms. The form of relations (30) is very similar to that of *Alpert and Neumann* [1984] and allows K_H to be variable in space and time.

2.4.1 Vertical Turbulent Diffusion above the Surface Layer

The parameterization of turbulence above the surface layer is done by expressing the double covariance term $\overline{\psi'w'}$ found in the development of (4), (5), (12) and (14) by the classical Austausch exchange formulation, and one gets

$$E_u = +\frac{g^2}{p_\star^2}\frac{\partial}{\partial\sigma}(\rho^2 K_z \frac{\partial\overline{u}}{\partial\sigma}) \tag{31}$$

$$E_v = +\frac{g^2}{p_\star^2}\frac{\partial}{\partial\sigma}(\rho^2 K_z \frac{\partial\overline{v}}{\partial\sigma}) \tag{32}$$

$$E_\theta = +\frac{g^2}{p_\star^2}\frac{\partial}{\partial\sigma}(\rho^2 K_{zh} \frac{\partial\overline{\theta}}{\partial\sigma}) \tag{33}$$

$$E_q = +\frac{g^2}{p_\star^2}\frac{\partial}{\partial\sigma}(\rho^2 K_{zh} \frac{\partial\overline{q}}{\partial\sigma}) \tag{34}$$

where K_z and K_{zh} are the vertical turbulent diffusion coefficients respectively for momentum and heat. They are expressed as follows :

$$K_z = l^2 \mid \frac{\triangle\overline{V}}{\triangle z} \mid F(R_i) \tag{35}$$

$$K_{zh} = l^2 \mid \frac{\triangle\overline{V}}{\triangle z} \mid F_h(R_i) \tag{36}$$

where

$$l = \frac{kz}{1 + \frac{kz}{\lambda}}$$

$$\frac{\triangle \overline{V}}{\triangle z} = [(\frac{\partial \overline{u}}{\partial z})^2 + (\frac{\partial \overline{v}}{\partial z})^2]^{\frac{1}{2}}$$

$$R_i = \frac{g}{\overline{\theta}}\frac{\frac{\partial \overline{\theta}}{\partial z}}{(\frac{\triangle \overline{V}}{\triangle z})^2}$$

are the mixing length, the wind shear and the Richardson number respectively. The functions $F(R_i)$ and $F_h(R_i)$ of the Richardson number are given by *Louis* [1979]. The value of λ is chosen to be 10 m.

2.4.2 Vertical Turbulent Diffusion in the Surface Layer

The parameterization of turbulence will be different for the surface layer. The turbulent fluxes in the surface layer may be assumed constant and it is possible to get from the observations a good parameterization of them, although it is computationally expensive.

The formulation is given by *Businger* [1973], who uses the scaling variables $u_\star$, $\theta_\star$, $q_\star$ and the Monin-Obukhov length L

$$u_\star^2 = -\overline{V'w'} \tag{37}$$

$$-\overline{u'w'} = \frac{\overline{u}}{\overline{V}}u_\star^2 \tag{38}$$

$$-\overline{v'w'} = \frac{\overline{v}}{\overline{V}}u_\star^2 \tag{39}$$

$$-\overline{\theta'w'} = u_\star\theta_\star \tag{40}$$

$$-\overline{q'w'} = u_\star q_\star \tag{41}$$

$$L = -\frac{\overline{\theta}u_\star^2}{kg\theta_\star} \tag{42}$$

where $k = 0.4$ is the von Kármán constant, w is the vertical velocity in z coordinates and $V = (u^2+v^2)^{\frac{1}{2}}$. Using universal functions, and taking into account the roughness length z_0 of the surface, the scaling variables are obtained through the values of the

corresponding variables at 10 m height, *Businger* [1973] providing the relationships between $u_{10\ m}$ and u_*, $\triangle q = q_{10\ m} - q_s(T_s)$ and q_*, $\triangle \theta = \theta_{10\ m} - \theta_s$ and θ_*, where θ_s is the potential temperature at the surface. It is therefore possible to use these relations and (37)–(42) in order to determine the contribution of the turbulent diffusions F_u, F_v, F_θ and F_q in the surface layer.

2.5 The Numerical Scheme of the Model

The conservation equation (9) for p_* is solved by using a numerical scheme centered, 2th accurate in time (leap frog) and centered, 4th accurate in space. Because spurious mass loss could occur in the model through the lateral boundaries, the correction proposed by *Yan and Anthes* [1987] is used, namely by restoring the model average $\overline{\overline{p_*}}$ of p_* to its initial value $\overline{\overline{p_{*,0}}}$. This is achieved by adding at each horizontal grid point the difference $K_r(\overline{\overline{p_{*,0}}} - \overline{\overline{p_*}})$, where $K_r = 1.157 \times 10^{-5}$ s^{-1}.

The numerical scheme used to solve the equations (2), (3), (11) and (13) for u, v, θ and q is based on splitting techniques [i.e. *Bornstein*, 1975]. The contribution of the pressure gradient force to the first horizontal momentum equation is achieved with a leap frog scheme. For the advection a semi-lagrangian scheme is used. This scheme is based on the cubic spline interpolation technique [e.g. *Pielke*, 1984] and has been improved by *Seibert and Morariu* [1991]. For the turbulent flux contributions, we prefer to use an explicit scheme rather than an implicit scheme, because the former does not introduce enhanced numerical diffusion and is not computationnaly expensive.

In order to avoid the generation of short scale spurious waves on σ-surfaces in the three-dimensional version of the model, the selective two-dimensional low-pass filter proposed by *Raymond and Garder* [1988] is used for the variables u, v, θ and q. We prefer to filter the difference $p_* - p_{*,0}$ rather than p_*, where $p_{*,0}$ is the value of p_*

at the beginning of the integration. This avoids spurious mass loss and a subsequent generation of instability where the slope varies. For the two-dimensional version of the model, the *Long et al.* [1978] filter is used. In fact, the *Raymond and Garder* [1988] filter is a generalized version of the *Long et al.* [1978] filter.

The weighting parameter of the filter is equal to 0.004. With such value, the contribution of the filter is much less than horizontal diffusion, except for 2 $\triangle$ x and 2 $\triangle$ y waves which are completely removed.

The horizontal grid spacing of the model is regular: for the two-dimensional mountain waves simulations, we have chosen $\triangle x = 10$ km, while for the three-dimensional simulation, $\triangle x = 5$ km. Vertical discretization is irregular to get more σ-levels close to the surface. For the mountain waves simulations, σ-levels are defined by $\sigma = 0.5\nu + 1.5\nu^2 - 1.0\nu^3$, with $\triangle\nu$ constant. For the katabatic winds simulation, the initial heights of the σ-levels over the ocean are $z = 10, 20, 40, 78, 152, 295, 560,$ 1034, 1833, 3082, 4870, 7217, 10082, 13420 and 17233 m. The time step is such that the Courant-Friedrich-Levy criterion is satisfied for fast gravity waves. $\triangle t = 10$ s was adopted in all experiments.

ANTAR II/03

2.6 The Surface Model

Ground surface temperature is predicted from the force restore slab model of *Deardorff* [1978]:

$$\frac{\partial T_s}{\partial t} = -C_1 \frac{H_A}{\rho_s c_s d_1} - C_2 \frac{T_s - T_2}{\tau_1} \tag{43}$$

with $C_1 = 3.72$, $C_2 = 7.4$, H_A (positive upward) is the sum of the heat fluxes coming from the atmosphere and absorbed at the ice sheet surface: the net infrared radiative fluxes, the sensible and latent heat turbulent fluxes. The surface parameters are those of the snow, which is assumed to cover the sea ice and the continental ice during the Antarctic winter : the specific mass : $\rho_s = 330$ kg m^{-3}, the heat capacity :

$c_s = 2\ 10^3$ J kg^{-1} K^{-1}, the thermal diffusivity : $\kappa_s = 0.27\ 10^{-6}$ m^2 s^{-1}, the depth reached by the diurnal temperature wave : $d_1 = (\kappa_s \tau_1)^{\frac{1}{2}} = 0.15$ m, with the length of the day : $\tau_1 = 86400$ s. Finally T_2 is the mean temperature of the ice and is assumed to be the average of T_s over the previous 24 hours.

3 Model Verification

In this Section one verify the ability of the model to simulate airflow over an idealized mountain. Both linear and nonlinear mountain wave simulations have been done.

3.1 Linear Hydrostatic Mountain Waves in an Isothermal Atmosphere

Linear mountain waves over bell-shaped mountains have been studied and analytical solutions have been found [e.g. *Queney*, 1948]. Although the numerical model is not linear, it should produce a steady solution that closely approximates the analytical solution when the height of the mountain is very small. A 'linear' experiment has been performed with the model by using a 1 m high mountain of 20 km halfwidth. The atmosphere is initially isothermal (250 K) and the geostrophic wind vector is $\vec{V_g} = (20,0)$ m s^{-1}. For this experiment, subgrid scale fluxes are not taken into account and the numerical filter is not used. A free slip condition is used at the lower boundary of the model. $\triangle x = 10$ km and $\triangle t = 10$ s. There are 30 levels in the vertical.

The perturbation velocity and potential temperature fields are compared, respectively in Fig.1 and Fig.2, with the results of the analytical solution for a 1 km high mountain. The numerical model results have been amplified by a factor of 1000 for purposes of visualization, and are shown after 12 hours of model time.

Figure 1: *Perturbation velocity (in m s^{-1}) from (a) the linear hydrostatic solution for a 1-km high mountain; (b) the numerical simulation for a 1-m high mountain (amplified by a factor of 1000).*

ANTAR
II/03
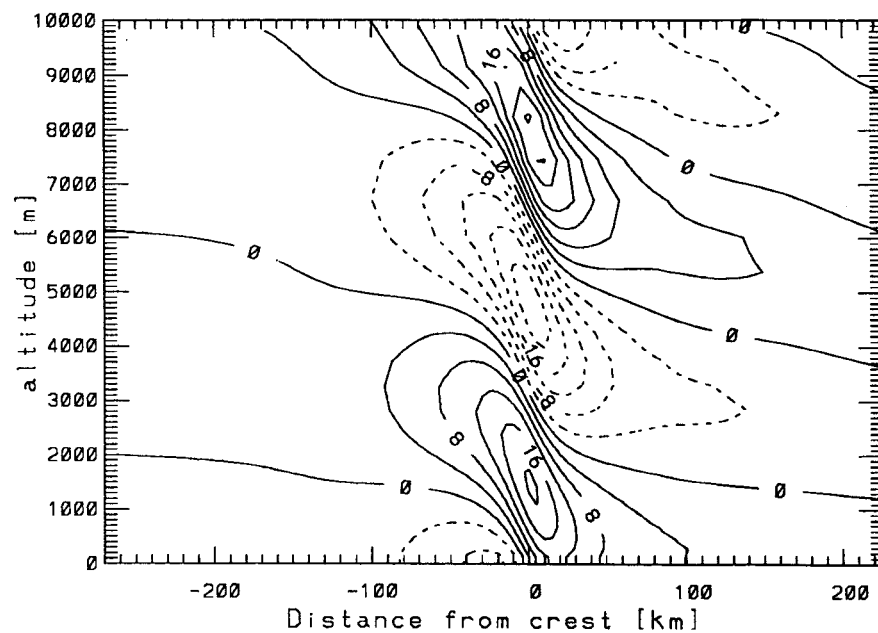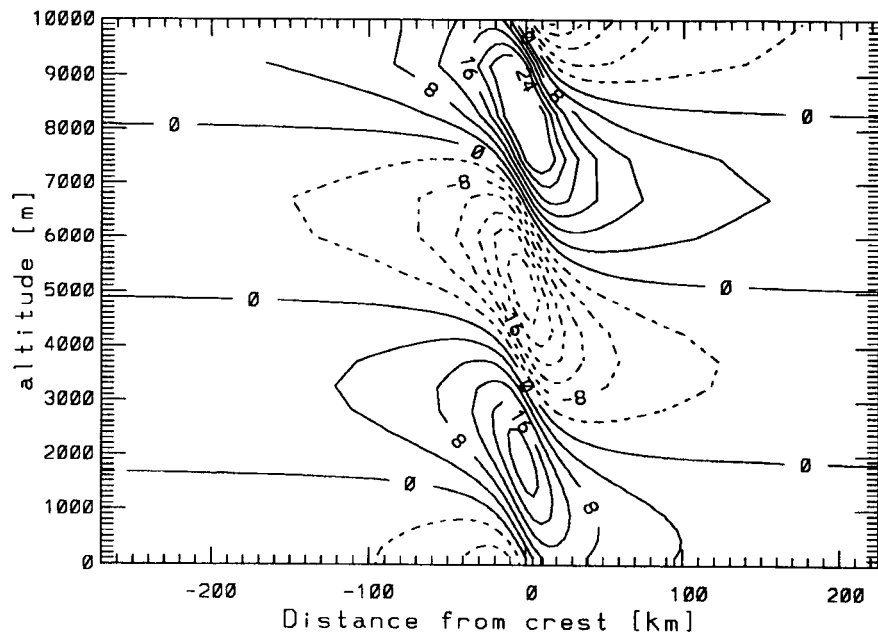
Figure 2: *As in Fig. 1, but for potential temperature (in K).*
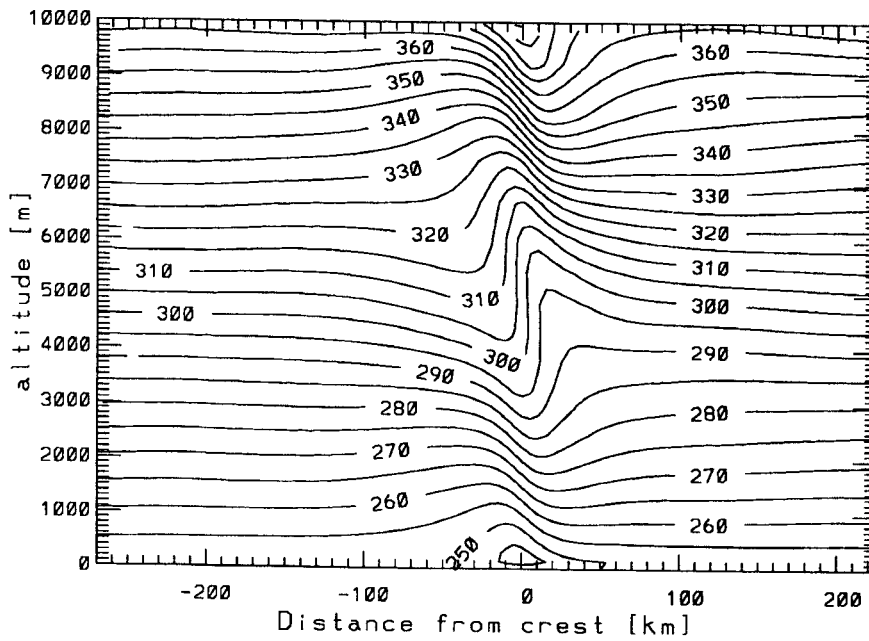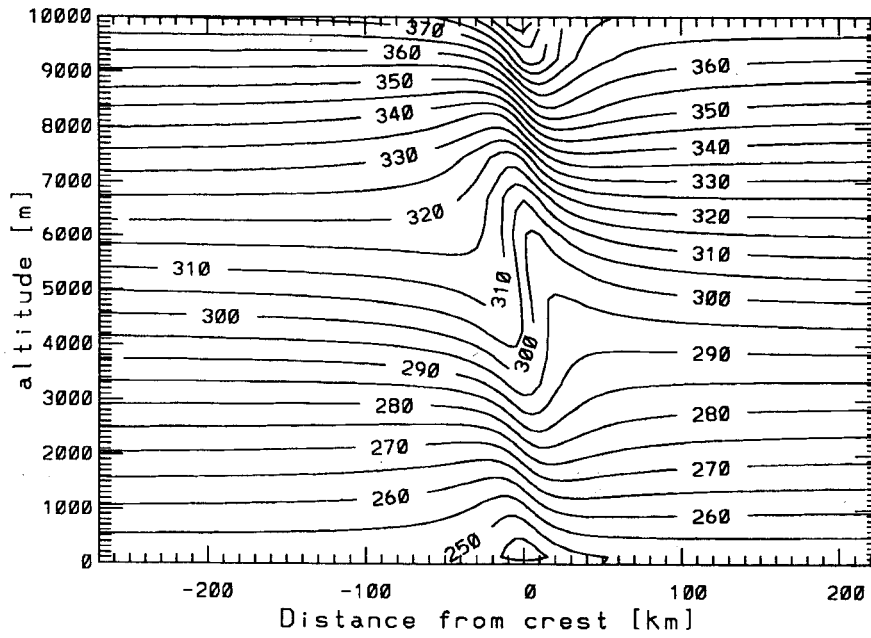
Figure 3: *Simulated horizontal velocity (in m s^{-1}) and potential temperature (in K) for a 1-km high mountain.*

ANTAR
II/03
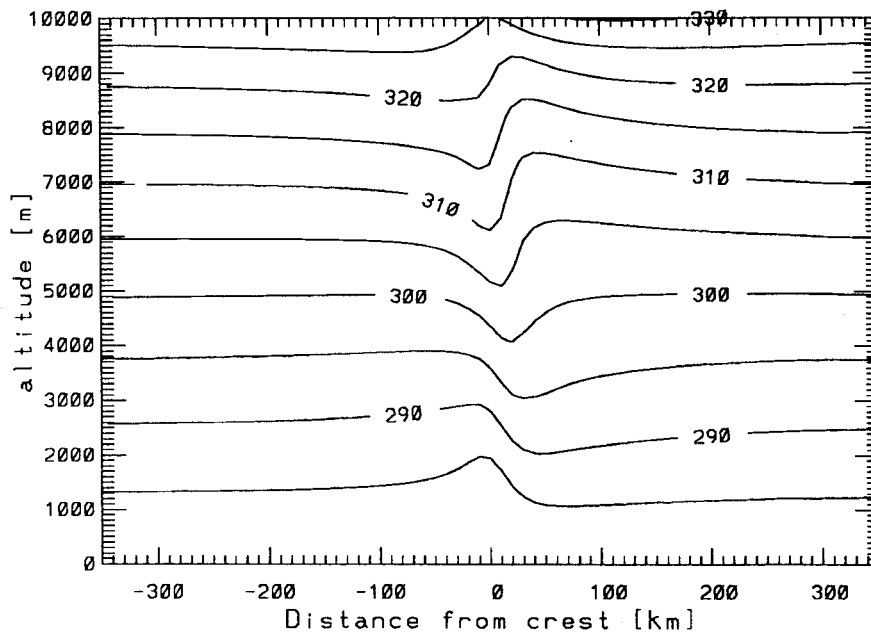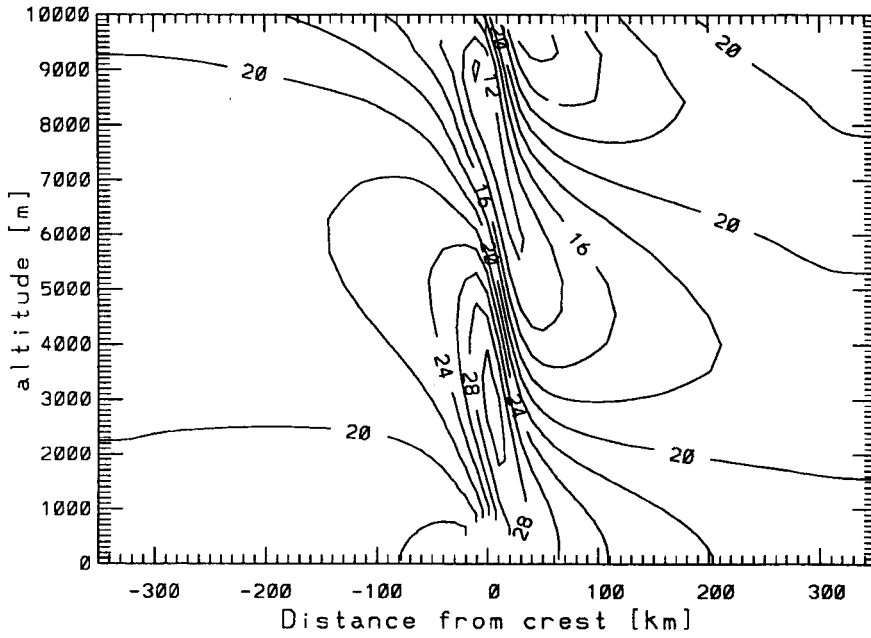
The agreement is quite good. In particular, no 2 $\triangle x$ waves are generated. The very stable numerical behaviour of the model is of particular importance, because this would not require strong numerical damping which could preclude an accurate simulation of drainage flows.

3.2 Nonlinear Hydrostatic Mountain Waves in a Two-Layer Atmosphere

In order to compare the impact of the nonlinear terms of the model with what is obtained in other models [e.g. *Klemp and Lilly*, 1978; *Mahrer and Pielke*, 1978], we have performed an experiment in which the height of the bell-shaped mountain is set to 1 km. In the lowest 700 hPa of the atmosphere, the temperature decreases at a constant rate of 6°C km^{-1} from a value of 280 K at zero elevation. In the upper part of the atmosphere, an isothermal profile is taken. The geostrophic wind vector is $\vec{V}_g = (20,0)$ m s^{-1}. The model discretization is the same as what was used in the linear mountain wave experiment. The subgrid scale fluxes are not included. The weighting parameter δ of the filter is set equal to 0.004.

The simulated velocity and potential temperature fields are displayed in Fig.3. They show a good agreement with the above mentioned studies.

4 Simulations of Katabatic Winds in the Area of Terra Nova Bay

Terra Nova Bay (75°S, 164°E) is in the Ross Sea. This area is located downwind of a pronounced confluence region in the Antarctic interior wind field simulated by *Parish and Bromwich* [1987].

Figure 4: *The terrain topography in the area of Terra Nova Bay. The height of the highest mountain is 2800 m [taken from* Drewry, *1983].*

ANTAR
II/03
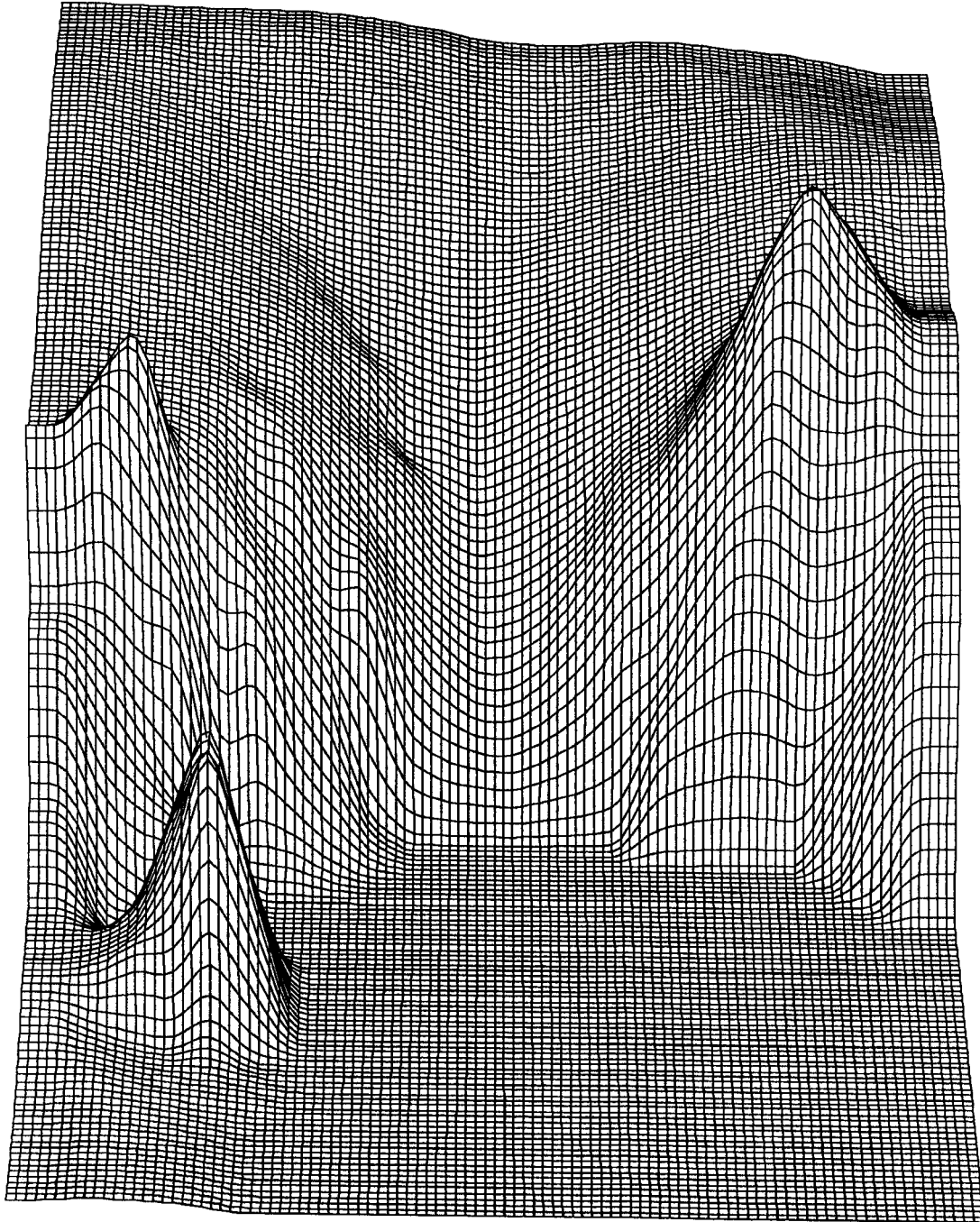
Figure 5: *Model katabatic wind vectors after 36-hour time integration for the lowest level of the model (10 m above the surface). Ice sheet elevation contours (in meters) are also plotted. Contour interval is 200 m. Vectors which norm is less than 1 m s^{-1} are not plotted. Vectors are plotted every 3 grid points. The arrow length at the right bottom corner of the graph represents wind speed amounting to 20 m s^{-1}.*
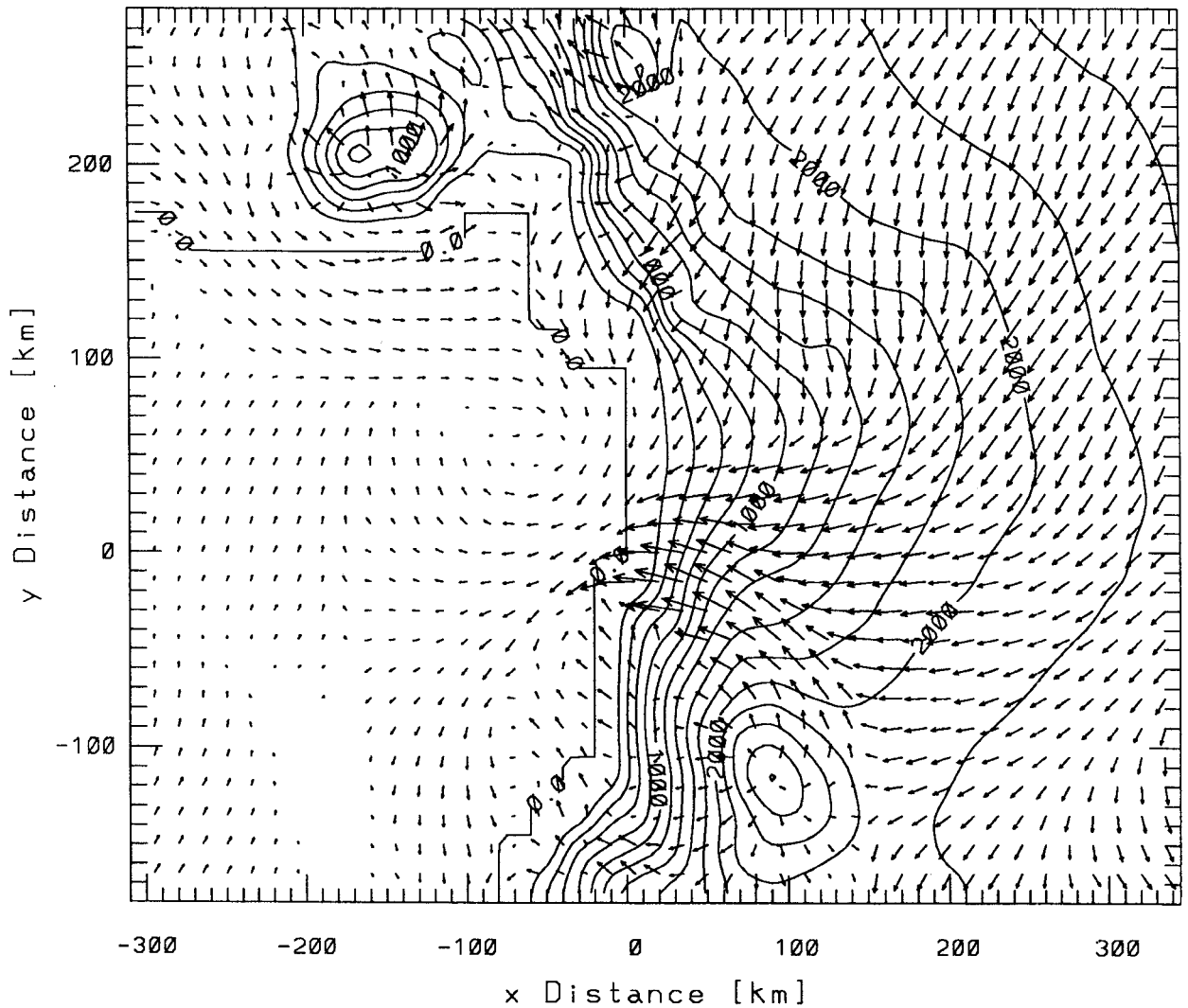
Because in a confluence zone, negatively buoyant air converges from a large interior section of the ice sheet, the supply of cold air to sustain katabatic winds blowing down the coastal marginal ice slopes is considerably enhanced [*Parish*, 1984]. It is why the katabatic wind speed in the area of Terra Nova Bay may be very large. In the present Section we describe a simulation of this atmospheric circulation which has been done with a meso-γ atmospheric model. To the author knowlege, it is the first time that such simulation is achieved using a high resolution. It will allow to have more insight in the processes governing the katabatic wind evolution in the Terra Nova Bay itself. The total coverage of the model is up to the 50 hPa pressure level in the vertical and 650×510 km in the horizontal. The terrain topography is taken from the [*Drewry*, 1983] map and is shown on Figure 4. One can see the important confluence zone extending over the whole integration domain, and which is limited by mountains in the coastal area.

The simulation is performed for polar night conditions. The initial vertical temperature profile is that observed by *Schwerdtfeger* [1984, his Fig. 6.9 p. 225, the Vostok sounding of July], with temperatures in the lowest level extrapolated downward from the temperature profile above the inversion. Because of computational costs, the horizontal grid size is chosen to be as large as 5 km. Geostrophic wind vector is chosen to be $\vec{V_g} = (0,0)$.

The wind regime is obtained after 36 hours simulation time. It is shown on Figure 5 for the lowest level of the model (10 m above the surface). Over the continent, the wind direction compares well with that inferred from observations and from previous modeling studies [e.g. *Bromwich et al.*, 1990]. Over the plateau the wind is deflected to the left because of the Coriolis force and blows nearly parallel to the topography isolines. Convergence is simulated in the lower part of the valley, with enhanced wind speed. In this area the wind direction is accross the topography isolines.

Figure 6: *Model katabatic wind isotachs after 36-hour time integration for the lowest level of the model (10 m above the surface). Contour interval of 3 m s⁻¹. Ice sheet elevation contours in meters (dashed) are also plotted. Contour interval is 200 m.*
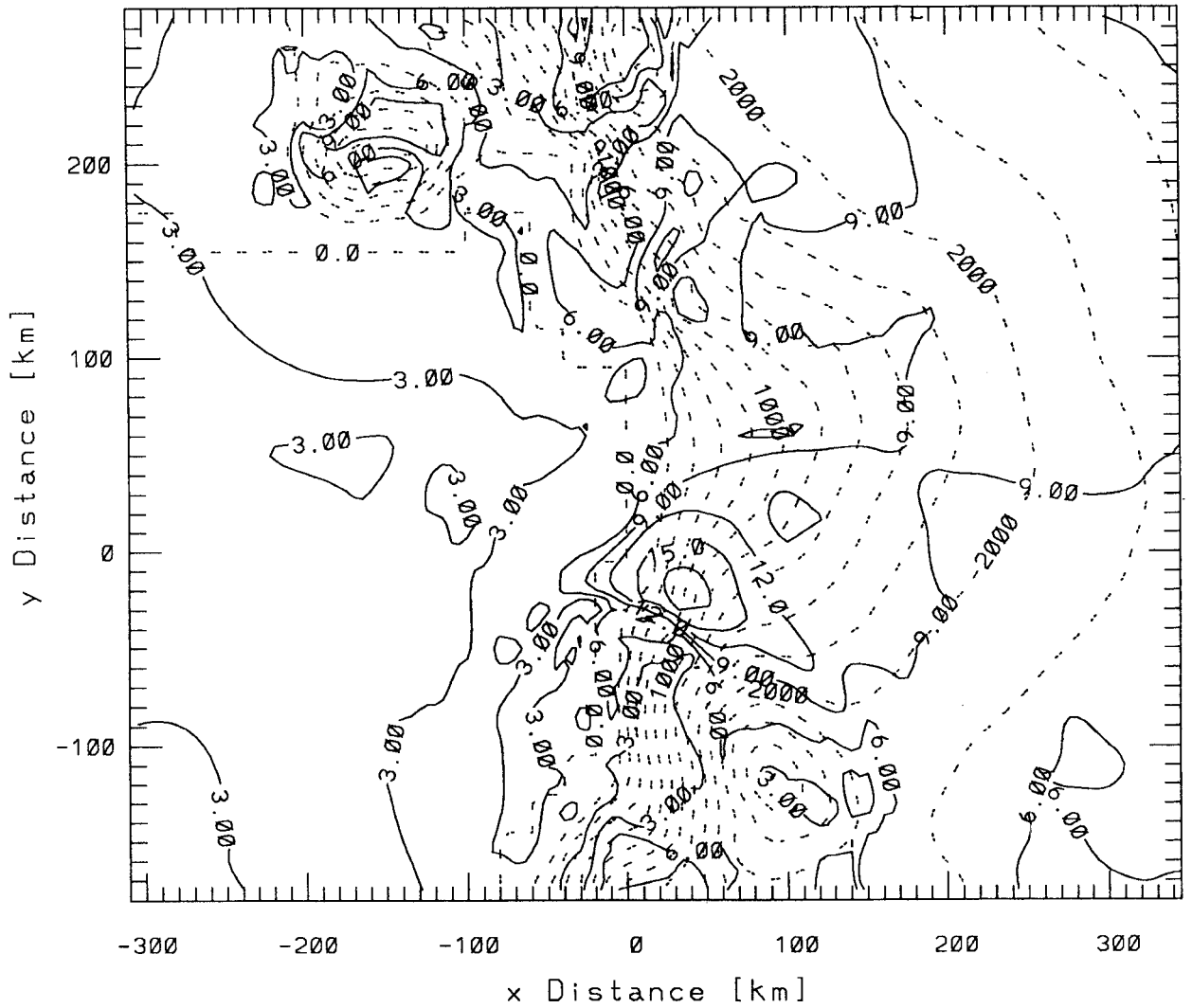
The simulated wind over the ocean is generally small, except that an intense katabatic jet is simulated in the area of the bay itself (in the Figure this may be found in the area of the axis origin). This jet is consistent with the observation of a polynya (open water area surrounded by ice) in Terra Nova Bay during the winter months, which has been found to be forced by katabatic winds [*Bromwich and Kurtz*, 1984]. Cyclonic rotation is also simulated over the ocean. The center of the vortex is located in $(x, y) = (-60\text{km}, +50\text{km})$ and is associated to boundary layer fronts. Such phenomenon has already been observed in this area and impacts the snow mass balance of the Antarctic ice sheet. For more details, see *Gallée and Schayes* [1993].

The wind speed distribution at the lowest level of the model is shown on Figure 6. It is found that the maximum wind speed (18 m s^{-1}) occurs at the 800 m surface level, rather than in the lowest part of the slope. The wind speed decrease before the coastline was also simulated with the two-dimensional version of the model and is due mainly to a decrease of the katabatic force [*Gallée and Schayes*, 1991]. It should also be mentioned that the wind speed is underestimated, when compared to the observations [*Bromwich*, 1989]. This is probably due to the crude representation of vertical turbulent processes in the model. In particular, entrainment of upper warm air into the katabatic layer plays a key role in the evolution of katabatic wind. When it is overestimated, it could cause the inhibition of the katabatic force.

Another reason could be that blowing snow, which becomes significant for wind speeds larger than 12 m s^{-1} (e.g. Périard and Pettré, 1991) and which contribute substantially to the sloped-inversion force (Kodama et al., 1985) for wind speeds larger than 28 m s^{-1} (Gosink, 1989) is not represented in the model.

Figure 7: *Model potential temperature contours after 36-hour time integration for the lowest level of the model (10m above the surface). Contour interval of 3K. Ice sheet elevation contours in meters (dashed) are also plotted. Contour interval is 200m.*
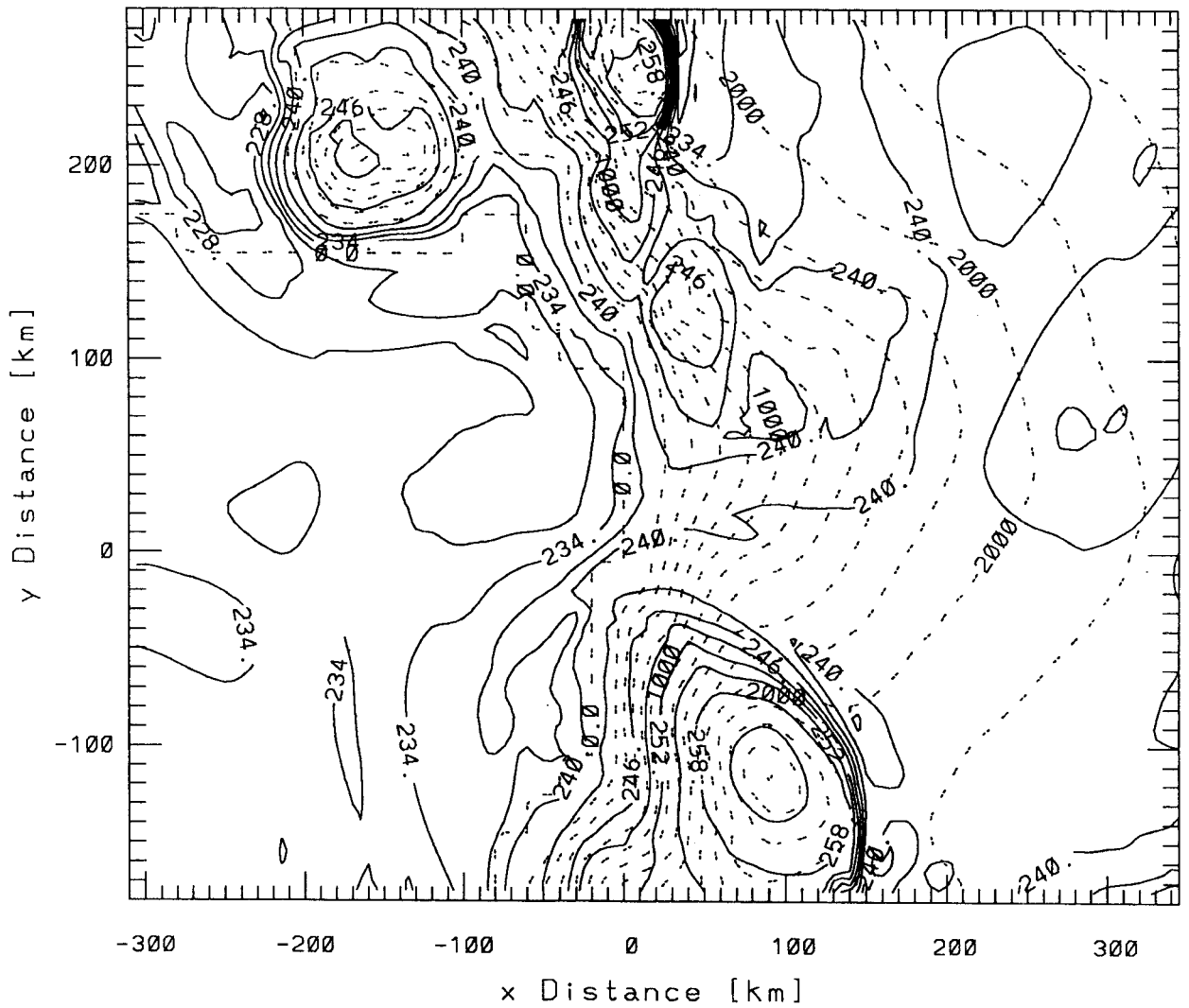
The potential temperature distribution at the lowest level of the model is shown on Figure 7. The large region with small temperature variation in the center of the Figure reveals the presence of katabatic air coming from the plateau. This is due to the fact that the katabatic air conserves the potential temperature when if flows down towards the coast. Another consequence of the adiabatic nature of the katabatic circulation is that the isentropics are nearly parallel to the streamlines.

Figure 7 also reveals the warm signature of the katabatic jet which could be due to the intense turbulent mixing associated with strong winds. This intense turbulent mixing is clearly shown by a local temperature maximum near the 2000 m elevation contour, for $x = 140$ km and $y = -80$ km. It is also found that the katabatic jet is bounded to its left side (when looking downslope) by a potential temperature discontinuity, mainly in the vincinity of the mountain. This temperature discontinuity is due to weaker winds in conjunction with higher surface elevations, and thus higher near-surface potential temperatures. Over the ocean, the katabatic jet signature may be found by examining the 237K potential temperature contour. Such thermal katabatic wind signatures have also been observed in the Terra Nova area, using thermal infrared satellite images (Kurtz and Bromwich, 1985, their Figure 3, Symbol E).

The temperature discontinuity simulated near the Ross Ice Shelf (for $x = 20$ km and $y = 250$ km) is associated to two different katabatic circulations separated by a mountain in this area (see Figure 5).

Finally it is found that the katabatic air coming from the Ross Ice Shelf is colder (potential temperature amounting to roughly 228 K) than that coming from Terra Nova (potential temperature amounting to roughly 237 K). This may be explained by weaker winds and thus a weaker turbulent mixing occuring in this area.

ANTAR
II/03

Figure 8: *The u component of the wind field in the plane y = −15km after 36-hour time integration, as a function of distance to the coast (positive distances are on the continent) and height above the surface, Positive values indicate downslope wind and are represented by solid lines. Contour interval of 1 m s⁻¹.*
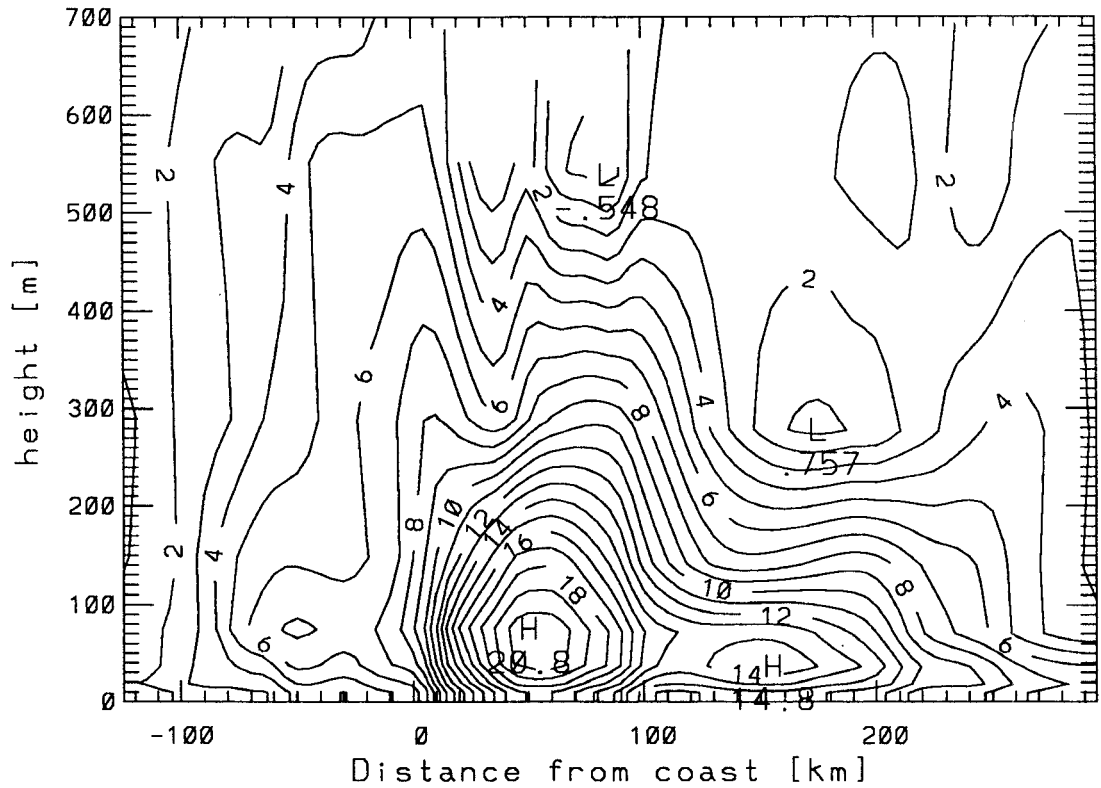
On Figure 8 is shown the x component of the wind in the vertical plane $y =$ -15km. A rapid decay of the wind is simulated on sea at 30 km from the ice-sheet foot. It corresponds to a change in the wind direction (see Figure 5). This decay happens not sufficiently far from the coast and could be due at least for two reasons: (i) turbulent entrainment at the top of the katabatic layer is overestimated; consequently the katabatic flow looses its identity too rapidly; (ii) the Terra Nova Bay polynya is not represented in the model. Indeed, strong winds blowing offshore could force the opening of a polynya so that surface temperature would be considerably higher there (271.2 K, sea water freezing temperature).

Previous simulations with the two-dimensional version of the model have shown that the katabatic air blows farer over the ocean when it is free of ice [*Gallée et al.*, 1989]. Further research has to be done in order to discuss the potential impact of the Terra Nova Bay polynya on katabatic winds.

ANTAR
II/03

Another possible reason is that because blowing snow processes are not taken into account in the model, the katabatic force is too low in the lower part of the slope.

The potential temperature distribution in the vertical plane $y = -15$ km is shown on Figure 9. In the steeper part of the slope, the katabatic layer stratification is in agreement with the observations [see *Pettré and André*, 1991] and consists, from the surface upwards, in a cold-air surface-layer, followed by a very stable capping inversion layer, an unstable layer thickening downslope, and a stable transition layer to the overlying free atmosphere. Over the ocean, the potential temperature field exhibits a vertically propagating hydrostatic gravity wave. Cold katabatic air piled up near the ice sheet foot could be responsible of this phenomenon.

Figure 9: *The potential temperature field in the plane y = −15km after 36-hour time integration, as a function of distance to the coast (positive distances are on the continent) and altitude. Contour interval of 1 K.*
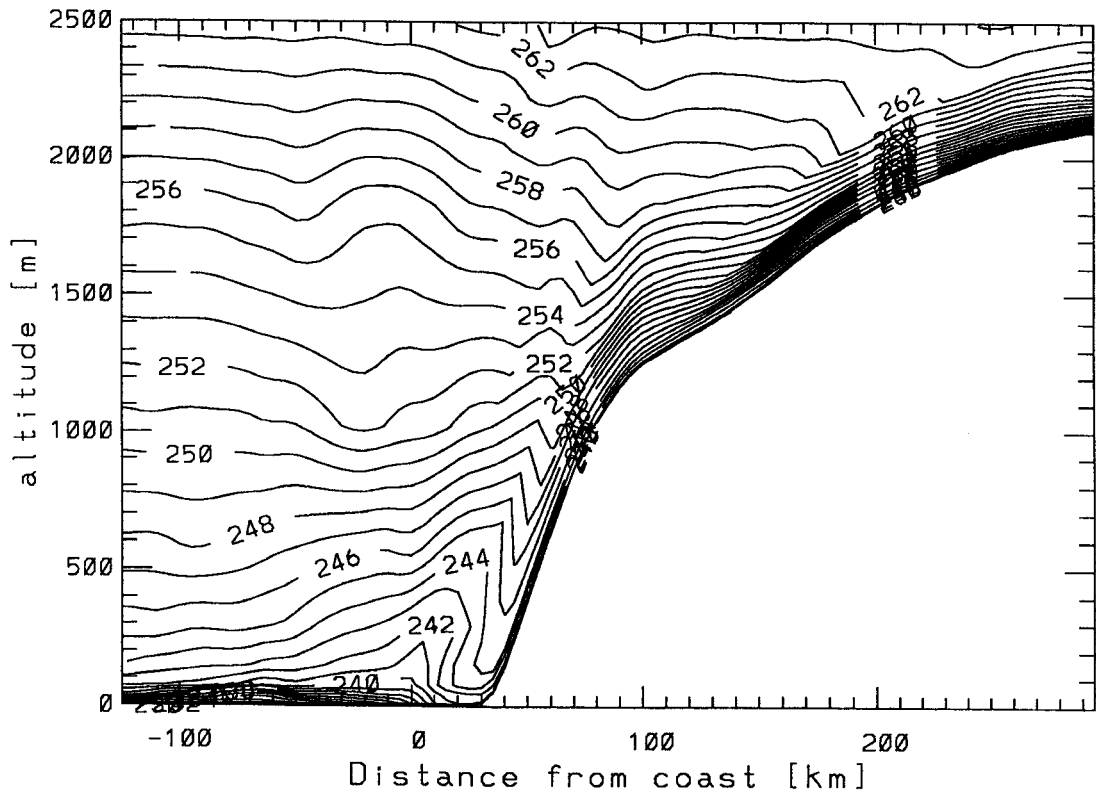
On Figure 10 is shown the x component of the wind in the vertical plane $y = -45$ km. This area is located to the left of the katabatic jet, when looking downslope. Katabatic wind speed maximum is 21 m s^{-1} and a sudden decay occurs before it reaches the coast. Such behaviour is comparable to an hydraulic jump [*Gallée and Schayes*, 1991] and is probably due to the horizontal divergence of the surface wind in this area (see Figure 5).

Figure 10: *The u component of the wind field in the plane $y = -45$ km after 36-hour time integration, as a function of distance to the coast (positive distances are on the continent) and altitude, Positive values indicate downslope wind and are represented by solid lines. Contour interval of 2 m s^{-1}.*
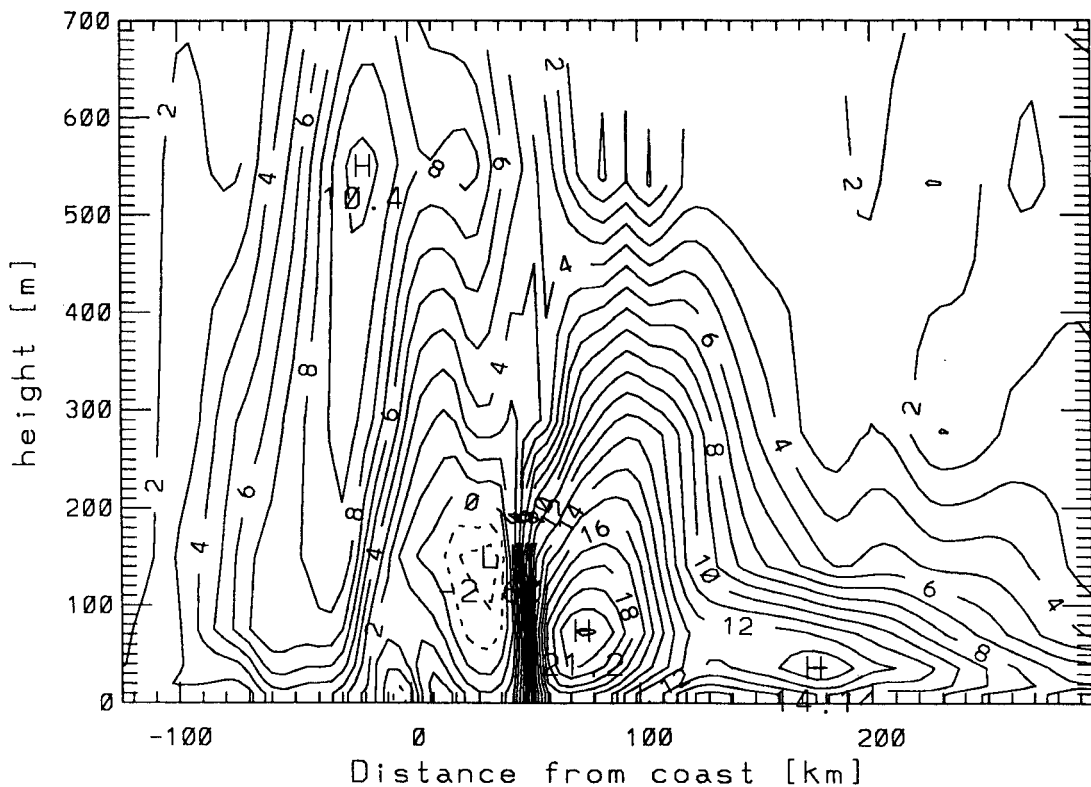
In conclusion, the results of this high resolution three-dimensional simulation of katabatic wind in the area of Terra Nova Bay compare favorably with those of previous modeling studies. In particular, a katabatic jet is simulated over the bay. Nevertheless, because the vertical turbulent mixing is crudely represented and possibly because the polynya opening and blowing snow processes are not included, katabatic air is not enought negatively buoyant to generate the strong wind speeds which could reach 30 m s^{-1} in this area, nor to allow the katabatic winds to blow more than over a few tens of kilometers over the Bay.

5 Conclusions

The aim of the present work was to develop a three-dimensional mesoscale atmospheric model in order to simulate katabatic flow in highly complex terrain. In particular, it must be a useful tool for the study of the processes governing the katabatic wind evolution in Antarctic coastal zones, like in the Terra Nova Bay area. The primitive equations were used, including the full continuity equation. The horizontal resolution was chosen to be 5 km. The model may be classified as a meso-γ atmospheric model and to the author knowlege, it is the first model of this class which is used to simulate Antarctic katabatic winds.

The model is validated by performing the classical linear and non-linear mountain wave experiments. The simulated linear waves are similar to those found in the analytical solution of the equations. The linear response of the model is numerically very stable, which is of particular importance for the simulation of drainage flows, because excessive numerical damping is prohibited. The simulated non-linear waves are very comparable to those simulated by other published models.

Then a simulation of katabatic wind is performed for polar night conditions in the area of Terra Nova Bay. The simulated fields reproduce many characteristics of the observed katabatic flow in this area. A katabatic jet is simulated, and its location is in agreement with the observations. Nevertheless, it is not yet sufficiently strong, and could be improved by using a higher order closure for the parameterization of vertical turbulence and including additional processes like the opening of a polynya forced by the wind and the increase of the negative buoyancy of the katabatic layer due to the presence of blowing snow.

Acknowledgments

ANTAR
II/03

References

[1] **Alpert P. and Neumann J.**, On the Enhanced Smoothing over Topography in some Mesometeorological Models, *Boundary Layer Meteorol.* **30**, 293–312, 1984.

[2] **Bornstein R.D.**, The Two-Dimensional URBMET Urban Boundary Layer Model, *J Appl Meteor* **14**, 1459–1477, 1975.

[3] **Bromwich, D.H.**, Satellite analyses of Antarctic katabatic wind behavior, *Bull Amer Meteor Soc, 70*, 738–749, 1989a.

[4] **Bromwich, D.H.**, An extraordinary katabatic wind regime at Terra Nova bay, Antarctica, *Mon Wea Rev* **117**, 688–695, 1989b.

[5] **Bromwich, D.H., and Kurtz, D.D.**, Katabatic Wind Forcing of the Terra Nova Bay Polynia, *J. Geophys. Res.*, **89**, 3561–3572, 1984.

[6] **Bromwich, D.H., Parish, T.R., and Zorman, C.A.**, The confluence zone of the intense katabatic winds at Terra Nova Bay, Antarctica, as derived from airborne sastrugi surveys and mesoscale numerical modeling, *J. Geophys. Res.*, **95**, 5495–5509, 1990.

[7] **Businger J.A.**, Turbulent Transfer in the Atmospheric Surface Layer, *Workshop on Micrometeorology. American Meteorological Society*, 67–100, 1973.

[8] **Deardorff J.W.**, Efficient Prediction of Ground Surface Temperature and Moisture with Inclusion of a Layer of Vegetation, *J Geophys Res* **83**, 1889–1903, 1978.

[9] Drewry, D.J., The surface of the Antarctic ice sheet, in *Antarctica: Glaciological and Geophysical Folio*, sheet 2, edited by D.J. Drewry, Scott Polar Research Institute, University of Cambridge, England, 1983.

[10] **Gallée, H., Berger, A., Schayes, G., Fichefet, Th., Marsiat, I., Tricot, C., and van Ypersele, J.-P.**, Numerical study of the air sea interactions in the Antarctic coastal zone and their implications on deep sea formation in the case of katabatic winds, in *Belgian Scientific Research Programme on Antarctica, Scientific results of phase one (oct 85–jan 89), vol. III*, S. Caschetto (ed.), Prime Minister's Services, Science Policy Office, Brussels, III-1–III-40, 1989.

[11] **Gallée, H., and Schayes, G.**, Development of a Three-Dimensional Meso-γ Primitive Equations Model, Katabatic Winds Simulation in the area of Terra Nova Bay, Antarctica, *Monthly Weather Review*, in press, 1993.

[12] **Gallée, H., and Schayes, G.**, Dynamical aspects of katabatic winds evolution in the Antarctic Coastal Zone, *Bound. Lay. Meteor.*, **59**, 141–161, 1992.

[13] **Gordon, A.L.**, The southern ocean and global climate, *Oceanus, 31, 2*, 39–46, 1988.

[14] **Heinemann, G.**, Mesoscale vorices in the Weddel Sea Region (Antarctica) *Mon Wea Rev* **118**, 779–793, 1990.

[15] **Klemp, J.B., and Lilly, D.K.**, Numerical simulation of hydrostatic waves, *J.Atmos.Sci.* **35**, 78–107, 1978.

[16] **Kodama Y., Wendler G. and Gosink J.**, The Effect of Blowing Snow on Katabatic Winds in Antarctica, *Annals of Glaciology* 6, 59–62, 1985.

[17] **Kurtz D.D. and Bromwich D.H.**, A Recurring, Atmospherically Forced Polynia in Terra Nova Bay, *Oceanology of the Antarctic Continental Shelf, Antarctic Research Series* 43, 177–201., 1985.

[18] **Long, P.E., Shaffer, W.A., Kemper, J.E., and Hicks, F.J.**, The state of the techniques development Laboratory's Boundary Layer Model, *NOAA Technical Memorandum NWS TDL66*, Silver Spring, Md., 1978.

[19] **Louis J.-F.**, A Parametric Model of Vertical Eddy Fluxes in the Atmosphere, *Boundary Layer Meteorology* 17, 187–202, 1979.

[20] **Mahrer, Y., and Pielke, R.A.**, A test of an upstream spline interpolation technique for the advective terms in a numerical mesoscale model, *Mon Wea Rev* 106, 818–830, 1978.

[21] **Mather K.B. and Miller G.S.**, Notes on Topographic Factors Affecting the Surface Wind in Antarctica, with Special Reference to Katabatic Winds, and Bibliography, *Technical Report of the University of Alaska*, 63 pp, 1967.

[22] **Miller M.J. and Thorpe A.J.**, Radiation Conditions for the Lateral Boundaries of Limited Area Numerical Models, *Quart.J.R.Met.Soc.* 107, 615–628, 1981.

[23] **Orlanski I.**, A Simple Boundary Condition for Unbounded Hyperbolic Flows, *J Computational Phys* 21, 251–269, 1976.

[24] **Parish T.R.**, A Numerical Study of Strong Katabatic Winds over Antarctica, *Mon Wea Rev* **112**, 545–554, 1984.

[25] **Parish T.R.**, Surface winds over the Antarctic continent: a review, *Rev. of Geophys.* **26**, 169–180, 1988.

[26] **Parish, T.R., and Bromwich, D.H.**, The surface wind field over the Antarctic ice sheets, *Nature* **328**, 51–54, 1987.

[27] **Parish, T.R., and Bromwich, D.H.**, Continental-scale simulation of the Antarctic katabatic wind regime. *J of Climate, 4*, 135–145, 1991.

[28] **Pease, C.H.**, The size of wind-driven coastal polynyas, *J Geophys Res* **92**, 7049–7059, 1987.

[29] **Périard, Ch., and Pettré, P.**, Climatologie de Dumont d'Urville, Terre Adélie, Antarctique, *Volume d'Actes de l'Atelier de Modélisation de l'Atmosphère, Météo-France/C.N.R.M./P.A.D., Toulouse*, 99–109, 1991.

[30] **Pettré, P., and André, J.-Cl.**, Surface-pressure change through Loewe's phenomena and katabatic flow jumps: study of two cases in Adélie Land, Antarctica, *J.Atmos.Sci.* **48**, 557–571, 1991.

[31] **Pielke R.A.**, Mesoscale Meteorological Modeling, *Acad Press*, 612 pp, 1984.

[32] **Queney, P.**, The problem of airflows over mountains: a summary of theoretical studies, *Bull. Am. Meteor. Soc.*, 29, 16–26, 1948.

[33] **Raymond, W.H., and Garder, A.**, A spatial filter for use in finite area calculations, *Mon Wea Rev* **116**, 209–222, 1988.

ANTAR
II/03

[34] **Sasamori, T.**, The radiative calculation for application to general circulations experiments, *J. Appl. Meteorol.* **7**, 721–729, 1968.

[35] **Schwerdtfeger W.**, Weather and Climate of the Antarctic, *Developments in Atmospheric Sciences*, **15**, Elsevier, 261 pp, 1984.

[36] **Seibert, P., and Morariu, B.** Improvements of upstream, semi-lagrangian numerical advection schemes, *J. Appl. Meteorol.* **30**, 117–125, 1991.

[37] **Smagorinsky, J.S.**, General circulation experiments with the primitive equations: I. The basic experiment, *Mon Wea Rev* **91**, 99–164, 1963.

[38] **Tag, P.M., Murray, F.W., and Koenig, R.**, A comparison of several forms of eddy viscosity parameterization in a two-dimensional cloud model, *J. Appl. Meteorol.* **18**, 1429–1441, 1979.

[39] **Wendler, G., Kodama, Y., and Poggi, A.**, Katabatic wind in Adélie Land, *Antarctic J. U.S.*, **18**, 236–238, 1983.

[40] **Yan, H., and Anthes, R.A.**, The efect of latitude on the sea breeze, *Mon Wea Rev* **115**, 937–956, 1987.

[41] **Zwally H.J., Comiso J.C. and Gordon A.L.**, Antarctic Offshore Leads and Polynias and Oceanographic Effects, *Oceanology of the Antarctic Continental Shelf, Antarctic Research Series* **43**, 203–226, 1985.

A NUMERICAL STUDY ON THE RESPONSE OF THE ANTARCTIC ICE SHEET TO CHANGES IN ENVIRONMENTAL CONDITIONS

Ph. Huybrechts

TABLE OF CONTENTS

ABSTRACT

Changes in the elevation and extent of the Antarctic ice sheet have an important role in modulating global atmospheric and oceanographic processes, and contribute significantly to world-wide sea levels. This report summarizes results of a numerical study on the response of the Antarctic ice sheet to changes in environmental conditions, both on the longer palaeoclimatic time scale (10^4-10^5 y) as on the shorter time scale (10^2 y) associated with future greenhouse warming.

The ice sheet model developed to this aim is three-dimensional and time-dependent. It incorporates a coupled ice shelf, grounding-line dynamics, basal sliding and isostatic bed adjustment. Ice flow is calculated on a fine mesh (40 km horizontal grid size and 10 layers in the vertical) for grounded and floating ice and a stress transition zone in between, where all stress components contribute in the effective stress of the flow law. The model has a full coupling between thermal field and ice flow and the ice sheet geometry is freely generated in response to changes in sea level, surface temperature and mass balance.

The mass-balance model consists of two parts: the accumulation rate is derived from present observed values and is consequently perturbed in proportion to the saturated vapour pressure at the temperature above the inversion layer. The ablation-and-runoff model required for warmer climates is based on the degree-day method. It accounts for the daily temperature cycle, uses a different degree-day factor for snow and ice melting and treats refreezing of melt water in a simple way.

A simulation of the present ice sheet reveals that the model is able to yield realistic results. An attempt is then made to simulate the ice sheet through the last glacial-interglacial cycle. To do this, the Vostok temperature record is used to force changes of both surface temperature and accumulation rate and sea level is prescribed by a piecewise linear sawtooth function. In line with glacial-geological evidence, the most pronounced changes occur in the West Antarctic ice sheet configuration. These fluctuations are essentially controlled by variations in eustatic sea level, whereas typical glacial- interglacial changes in temperature and ice deposition rates tend to balance one another. These findings support the hypothesis that the Antarctic ice sheet basically follows glacial episodes in the northern hemisphere by means of sea-level teleconnections.

On the shorter greenhouse warming time scale, the model's response is determined by changes in the mass balance. It is found that as long as the temperature rise is below 5°C, the Antarctic ice sheet is likely to grow, because melting at the ice sheet edge can still be offset by higher deposition rates on the plateau. These model results do not support the hypothesis of a catastrophic collapse of the West Antarctic ice sheet, not even when a uniform melting rate of 1 m/year is imposed below the ice shelves.

1. INTRODUCTION

The Antarctic ice sheet is one of the most prominent physical features on our planet. Together, the large continental East Antarctic ice sheet, the smaller marine-based West Antarctic ice sheet with flanking, floating ice shelves in the Ross and Weddell Seas, and the Antarctic Peninsula comprise an area of nearly 14 million km^2, or about twice the size of Australia. In total, the ice sheet contains around 30 million km^3 of ice and has an average thickness of 2100 m (Drewry et al., 1982). There can be little doubt of the strong impact of this huge mass of ice on the climate of the southern hemisphere and even on that of the globe as a whole. One can distinguish four main effects. The first is related to the impact of the ice sheet on the global radiation budget, since the amount of solar energy absorbed depends on the planetary albedo. In this respect, the onset of Antarctic glaciation and the occurrence of an area of high surface albedo has probably been a major factor in cooling the global climate on a geological time scale. Today, the effect is particularly evident in a high southern hemisphere equator-to-pole temperature gradient which drives more intense atmospheric and oceanic circulations than those observed in the north. Second, the prevailing winds blowing off the ice sheet result in an equatorward advection of cold air, thereby significantly influencing the sea-ice extent and sea-surface temperatures. Third, melting of ice bergs, which account for over 99% of the total mass loss of the ice sheet, keep the surrounding waters close to freezing. Fourth, there is the climatic effect resulting from the formation of deep Antarctic bottom water, which owes its high density to salt rejection both during the formation of sea-ice and the process of accretion under ice shelves. The cold saline water masses formed in this way compose most of the deep water of the world oceans and play a fundamental role in its circulation pattern.

Because of the interaction of the ice cap with the atmosphere and the oceans and because it stores more than 70% of the earth's fresh water resources, it is thus fundamental to better understand the ice sheet's basic behaviour. This is evident on several time scales. With regard to palaeoclimatic conditions during the Pleistocene, it is of crucial importance to determine the history and extent of the ice sheet's fluctuations and to find out how they are related to changes in environmental conditions. Glacial and marine geologists have spent many years in the field trying to reconstruct the ice sheet's former extent. The picture emerging from their studies seems to point to a relatively stable East Antarctic ice sheet, however flanked by an oscillating West Antarctic ice sheet, which may on several occasions have extended all the way to the edge of the continental shelf (Denton and Hughes, 1981). It has been widely speculated that eustatic sea-level changes were the primary cause of these fluctuations (e.g. Hollin, 1962), but other factors such as changes in mass balance and ice temperature may also be of major importance.

A correct understanding of the ice sheet's past behaviour is also a necessary precursor to

investigating its possible response to future climatic trends. Since the industrial revolution, the atmospheric concentration of CO_2 has risen by 25% and it is generally believed that this will lead to a warmer climate in the future (Houghton et al., 1990). Model predictions on the magnitude of this warming, in space as well in time, still differ to a wide extent, but according to the IPCC 'business-as-usual' scenario, there is a 65% chance that in the year 2100 the global mean temperature will be between 2.7°C and 5.7°C higher than the pre-industrial level, with a higher value more likely in the polar latitudes. If such a warming were to take place and initiate the melting of the Antarctic ice sheet, the consequences could be disastrous for low-lying coastal areas. For instance, a 1% change in Antarctic ice volume would result in a world-wide sea-level change of some 70 m. In particular the West Antarctic ice sheet has drawn a lot of attention. Mercer (1978) has pointed out the fact that this ice sheet, with its bed so far below sea level, may be unherently unstable in such a way that a moderate warming may lead to a runaway situation in which the major part of West Antarctica disintegrates. This would raise sea level by as much as 5 m in a few centuries time. Later modelling studies, however, suggest that this view is probably too dramatic and that a sudden collapse on these time scales is unlikely to happen (Van der Veen, 1985). Nevertheless, recent observations and modelling work have demonstrated the potential of the subshelf water circulation to induce large basal melting rates (Jenkins and Doake, 1990)

ANTAR II/04 A

In this report, the Antarctic ice sheet is investigated using a newly developed numerical model. In the model, both grounded ice and ice shelves are treated simultaneously on a fine mesh, by solving the full set of thermomechanical equations for ice flow in three dimensions. The primary difference between this model and those used in earlier studies, however, is a rigorous treatment of the flow, not only in the ice sheet, but also across the grounding line and in the ice shelf, so that the position of the grounding line can be traced during the calculations by means of a flotation criterion. This is done by allowing for different velocity solutions in grounded and floating ice and by defining a stress transition zone in between at the grounding line. The basic idea here is to incorporate in each subdomain all relevant stresses in the stress equilibrium equations and in the flow law, from which the velocities are calculated. This means that there is free interaction between grounded and floating ice, and that the entire geometry is internally generated in response to specified environmental conditions. In addition, more efficient numerical techniques have been employed that allow for a finer grid and more accurate solutions in the basal shear layers. Furthermore, the model includes basal sliding, which is restricted to regions that are at the pressure melting point, and considers the response of the underlying bedrock to changing ice loading, by taking into account both the rigidity of the lithosphere and the viscosity of the asthenosphere and including a temperature calculation.

Chapter 2 presents a description of the equations and numerical techniques governing the 3-D

model. The third section explains how the mass balance is treated and which methods are used to specify environmental conditions in different climates. Results of the numerical experiments, involving a steady state sensitivity test and a simulation of the last glacial cycle, follows in chapter 4. Chapter 5 deals with the response to future greenhouse warming.

2. THE ICE SHEET MODEL

The model formulated here essentially predicts ice thickness in space and time as well as the three dimensional flow and temperature distribution in response to specified atmospheric and environmental conditions. Defining a right-handed Cartesian coordinate system x,y,z, with the x,y plane parallel to the geoid and the z-axis pointing vertically upwards (z = 0 at sea level), the basic equation to be solved in the model is a continuity equation for ice thickness H:

$$\frac{\partial H}{\partial t} = -\nabla \cdot (\vec{v}H) + M \tag{1}$$

where $\vec{v}$ is the depth-averaged horizontal velocity vector, M the mass balance, t time (in y) and the ∇- operator is understood to be two-dimensional (in the x-y plane). Basically, the solution of eq. 1 follows from reformulating the velocity field in terms of the ice sheet geometry (ice thickness and surface gradient), so that only one unknown remains. The resulting equation is a partial differential equation of parabolic type, but nonlinear, and has to be solved by numerical methods. The model geometry is shown in fig.1.

2.1. General force balance and flow law

In order to arrive at equations describing the velocity distribution, we start with the fundamental force balance acting on an element of ice:

$$\frac{\partial \tau_{xx}}{\partial x} + \frac{\partial \tau_{xy}}{\partial y} + \frac{\partial \tau_{xz}}{\partial z} = 0 \tag{2}$$

$$\frac{\partial \tau_{yx}}{\partial x} + \frac{\partial \tau_{yy}}{\partial y} + \frac{\partial \tau_{yz}}{\partial z} = 0 \tag{3}$$

$$\frac{\partial \tau_{zx}}{\partial x} + \frac{\partial \tau_{zy}}{\partial y} + \frac{\partial \tau_{zz}}{\partial z} = \rho g \tag{4}$$
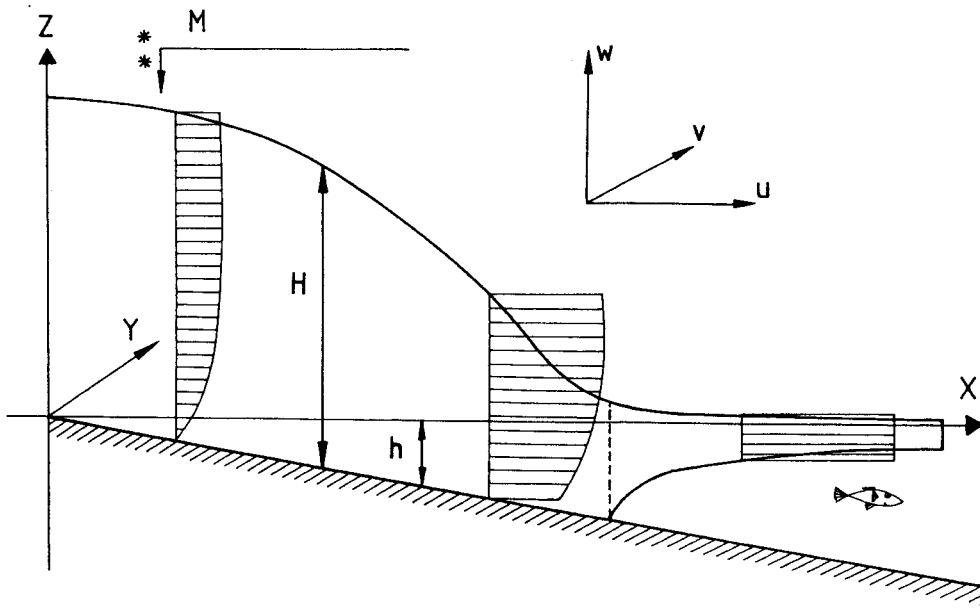
fig. 1: Model geometry. The flow is calculated separately in the grounded ice region, the ice shelf and a stress transition zone in between. For explanation of variables, see text.

and the flow law for polycrystalline ice, which is of Glen-type and exponent n = 3 (Paterson, 1981):

$$\dot{\varepsilon}_{ij} = A(T^*) \, \tau_*^2 \, \tau'_{ij}$$

$$\text{and} \quad \tau_*^2 = \tau'^2_{xx} + \tau'^2_{yy} + \tau'_{xx} \tau'_{yy} + \tau^2_{xz} + \tau^2_{yz} + \tau^2_{xy} \tag{5}$$

In these expressions τ_{ij} are the stress tensor components, with i≠j the shear stresses, i=j the normal stresses and where an accent denotes stress deviators (defined as the full stress minus the hydrostatic component: $\tau'_{ii} = \tau_{ii} - (\tau_{xx} + \tau_{yy} + \tau_{zz})/3$). ρ is ice density [910 kgm^{-3}], assumed to be constant, and g the acceleration of gravity. ε_{ij} are strain rate components related to velocity gradients by definition $(\dot{\varepsilon}_{ij} = [\partial u_i/\partial x_j + \partial u_j/\partial x_i]/2)$, τ_* the effective stress (where τ'_{zz} has been substituted employing the incompressibility condition : $\tau'_{xx}+\tau'_{yy}+\tau'_{zz}=0$) and A(T*) is a temperature-dependent flow law parameter [Pa^{-3}year^{-1}], with T* ice temperature corrected for the dependence of the melting point on pressure : $T^* = T + 8.7 \; 10^{-4} \; H$.

In ice, the vertical stress can generally be taken to equal the weight of the overlying ice ($\tau_{zz}(z)$ = -ρg(H+h-z), with h bed elevation), allowing us to rewrite the stress equilibrium in a more convenient form for the analysis below. This is equivalent to the assumption that horizontal

gradients in the vertical shear stresses are small compared to ρg in (4). After substituting for stress deviators and rearranging the terms, this gives:

$$\frac{\partial \tau_{xz}}{\partial z} = \rho g \frac{\partial (H+h)}{\partial x} - 2\frac{\partial \tau'_{xx}}{\partial x} - \frac{\partial \tau'_{yy}}{\partial x} - \frac{\partial \tau_{xy}}{\partial y} \tag{6}$$

$$\frac{\partial \tau_{yz}}{\partial z} = \rho g \frac{\partial (H+h)}{\partial y} - 2\frac{\partial \tau'_{yy}}{\partial y} - \frac{\partial \tau'_{xx}}{\partial y} - \frac{\partial \tau_{xy}}{\partial x} \tag{7}$$

These equations are in principle valid over the whole ice sheet domain, but are further simplified below by setting appropriate assumptions for the three separate flow regimes considered, namely grounded ice, floating ice and a transition zone in between at the grounding zone.

2.2. Ice flow

2.2.1. grounded ice

In the case of grounded ice, variations in the longitudinal directions are small as compared to the vertical (small aspect ratio), so that simplifications can be made according to the 'shallow ice approximation' (Hutter, 1983). This implies the normal stress tensor to be isotropic, in effect ignoring longitudinal deviatoric stresses and lateral shearing. These are the usual assumptions, that are valid as long as gridpoint spacings are an order of magnitude larger than ice thickness and sufficiently small bedrock and surface slopes are considered (Nye, 1969). These limitations are generally satisfied on a numerical grid, so that the stress balance in grounded ice is between the horizontal shear stresses τ_{xz} and τ_{yz} and surface-slope induced pressure gradients. Ignoring atmospheric pressure, resulting expressions for the shear stress distribution can then be integrated to give:

$$\tau_{xz}(z) = -\rho g(H+h-z)\, \partial(H+h)/\partial x \qquad \tau_{yz}(z) = -\rho g(H+h-z)\, \partial(H+h)/\partial y \tag{8}$$

Substituting these equations in the flow law (eq.5) and integrating the resulting equation with respect to the vertical yields expressions for the horizontal velocity components:

$$\vec{v}(z) - \vec{v}(h) = -2(\rho g)^3 \left[\nabla (H+h).\nabla (H+h) \right] \nabla (H+h) \int_{h}^{z} A(T^*)\,(H+h-z)^3\, dz \tag{9}$$

with basal boundary condition $\vec{v}(h)$. Since the flow parameter $A(T^*)$ depends on temperature (and therefore on position), equation (9) has to be evaluated numerically, given the temperature distribution.

When the temperature of the basal layers reach the melting point, bottom water is formed and basal sliding may occur. Views on how this should be modelled, however, differ widely. Here, we follow an analysis by Bindschadler (1983), and consider basal sliding to be of Weertman-type (Weertman, 1964), corrected for the effect of subglacial water pressure and restricted to regions that are at the pressure melting point:

$$\vec{v}(h) = -A_s (\rho g H)^3 \left[\nabla(H+h) \cdot \nabla(H+h) \right] \nabla(H+h) / Z^* \qquad (10)$$

where $A_s = 1.8 \ 10^{-10} \ N^{-3} yr^{-1} m^8$ and Z^* is the height above buoyancy:

$$Z^* = H + \rho_w (h - H_{sl}) / \rho \qquad (11)$$

where ρ_w is water density [1028 kgm^{-3}] and H_{sl} the sea level stand with respect to present conditions. This empirical relation seemed to fit data from West Antarctic ice streams quite well and expresses the view that pressurized subglacial water reduces basal friction in case the grounding line is approached, in turn leading to high sliding velocities.

A second integration with respect to the vertical then yields the mean horizontal ice mass flux:

$$\vec{\bar{v}}H = \int\limits_{h}^{H+h} \vec{v}(z) \ dz \qquad (12)$$

where vertical motion, which occurs as a result of accumulation and vertical strain, is calculated from the incompressibility condition:

$$w(z) - w(h) = -\int\limits_{h}^{z} \nabla \cdot \vec{v}(z) \ dz \qquad (13)$$

The kinematic boundary condition at the upper surface is given by:

$$w(H+h) = \partial(H+h)/\partial t + \vec{v}(H+h) \cdot \nabla(H+h) - M \qquad (14)$$

and M is positive in the case of accumulation. Equations (9) and (13) now fully describe the three-dimensional velocity field $\vec{V}$, with the only limitation that $\vec{v}$ is not allowed to change direction with depth, its direction being solely determined by the local surface slope.

2.2.2. ice shelf

By definition, ice shelves are in hydrostatic equilibrium with the ocean water. In contrast with the stress equilibrium conditions in grounded ice, however, the stress balance is now between the pressure gradient force arising from the surface slope, opposed by longitudinal gradients in normal deviatoric stresses (that cause ice shelf stretching) and lateral shearing induced by side-walls and ice rises (Thomas, 1973). The base of the ice shelf experiences negligible friction, so there is no shearing in horizontal planes and strain rates and velocities are independent of depth. This would be perfectly true if the surface were horizontal, but is a good approximation because ice shelves have very small surface slopes.

With these simplifications in mind, equations describing the velocity distribution can be derived from eqs. 6-7 by substituting for the flow law (eq.5) and making use of the flow law in its second-order invariant form ($\dot{\varepsilon} = A(T^*) \tau^n$). After some algebraic manipulation, details of which are omitted for the sake of brevity, the following expressions can be shown to result (for a more rigorous derivation, the interested reader is referred to Herterich (1987), where a similar 2-D derivation is performed):

$$2\frac{\partial}{\partial x}\left[f\frac{\partial u}{\partial x} \right] + \frac{\partial}{\partial x}\left[f\frac{\partial v}{\partial y} \right] + \frac{1}{2}\frac{\partial}{\partial y}f\left[\frac{\partial u}{\partial y} + \frac{\partial v}{\partial x} \right] = \rho g A(T^*)^{\frac{1}{3}}\frac{\partial(H+h)}{\partial x} \qquad (a)$$

$$2\frac{\partial}{\partial y}\left[f\frac{\partial v}{\partial y} \right] + \frac{\partial}{\partial y}\left[f\frac{\partial u}{\partial x} \right] + \frac{1}{2}\frac{\partial}{\partial x}f\left[\frac{\partial u}{\partial y} + \frac{\partial v}{\partial x} \right] = \rho g A(T^*)^{\frac{1}{3}}\frac{\partial(H+h)}{\partial y} \qquad (b)$$

$$\text{with } f = \left[\left(\frac{\partial u}{\partial x}\right)^2 + \left(\frac{\partial v}{\partial y}\right)^2 + \left(\frac{\partial u}{\partial x}\right)\left(\frac{\partial v}{\partial y}\right) + \left[\frac{1}{2}\left(\frac{\partial u}{\partial y} + \frac{\partial v}{\partial x}\right) \right]^2 \right]^{\frac{-1}{3}} \qquad (15)$$

Equations 15 (a-b) are a set of second-order partial differential equations of elliptic type, but nonlinear, and are most easily solved by point relaxation. In this way, an initial velocity distribution (u,v) is introduced and computed residuals are made zero locally in an iterative

way until the maximum error on the grid is below a certain level, in this case 1 m/year. In general, convergence is rather slow, but once an equilibrium solution was obtained, only a few iterations proved to be necessary.

In reality, a thinning ice shelf will break off at its seaward margin once a critical thickness is reached (usually around 250 m). In the model, however, calving physics are not considered explicitly, and the ice shelf is actually made to extend all the way to the edge of the numerical grid. Testing indicates that this does not present a serious problem. Model runs, in which the ice shelf was 'cut off' closer to the coast (but still outside the main embayments) did not have appreciably different ice thickness distributions or grounding line positions.

Boundary conditions at the seaward margin are then applied for unconfined, freely floating and uniformly spreading (complete stress and strain-rate symmetry in the x- and y-directions) ice shelves. Velocity components follow from the flow law and the condition that the net total force on the ice shelf front must be balanced by the horizontal force exerted by the sea water:

$$\dot{\varepsilon}_{xx} = \partial u / \partial x = 3 A(T) \tau_{xx}'^3 \qquad \dot{\varepsilon}_{yy} = \partial v / \partial y = 3 A(T) \tau_{yy}'^3$$

$$\tau_{xx}' = \tau_{yy}' = \rho g H (1 - \rho/\rho_w) / 6$$

$$\partial u / \partial y + \partial v / \partial x = 0 = \dot{\varepsilon}_{xy} \qquad (16)$$

ANTAR
II/04
A

At the grounding zone, boundary conditions are not velocity gradients, but follow from the vertically integrated velocity components.

2.2.3. grounding zone

In view of the basically different nature of the stress balance in grounded and floating ice, there must be a stress transition zone located somewhere in between near the grounding line. Here, a change should take place from shear-dominated flow to a situation where longitudinal stresses prevail, so that all stress components could be potentially important. Because the thickness at the grounding line results from a subtle balance between a whole number of competing mechanisms and feedback-loops, modelling the transition zone is a delicate matter and requires careful consideration of the various terms in the force balance. Of interest in this respect are studies by Van der Veen (1985, 1987) and Herterich (1987), who addressed the flow at the grounding line in a 2-D (vertical plane) approach. In order to deal with the ice sheet - ice shelf interaction at the grounding line in a proper way, Van der Veen (1987) advocated to include the longitudinal deviatoric stress in the effective stress term of the flow law. The

present 3-D approach incorporates this fundamental idea.

Two assumptions are made as follows. First, it is taken for granted that the width of the stress transition zone is smaller than typical gridsizes in large scale numerical models. The validity of this assumption appears to be corroborated by the two-dimensional studies of Herterich (1987) and Van der Veen (1987), although the length of the zone over which longitudinal stresses are important may be larger where basal sliding is the dominant flow mechanism. Consequently, the grounding zone in the model has a width of one gridpoint and includes all grounded grid points that border the floating ice region. The second simplification assumes that deviatoric stress *gradients* can be neglected as a contribution to the shear stresses in the stress equilibrium (eqs. 6-7). This may represent a somewhat more dubious approximation, in particular in fast-flowing outlet glaciers and ice streams, where longitudinal stretching may support part of the weight (e.g. McMeeking and Johnson, 1985). In spite of this, however, one could simply argue that this is probably the only option, because to do otherwise would imply complicated and time-consuming stress integrations along the x- and y-axes respectively. On the other hand, in Van der Veen (1987), this assumption did not appear to be crucial to the model outcome and as far as the ice sheet profile was concerned, the only thing that really mattered was the longitudinal deviatoric stress (and much less its gradient) at the grounding line only. A scale analysis of eqs. 6-7 for typical grid spacings in numerical models seems to support this. Moreover, in a recent detailed calculation of the stress distribution near the grounding zone of Byrd Glacier (an outlet of the East Antarctic ice sheet), Whillans et al.(1989) found a close correlation between the driving stress and basal drag. These points seem to indicate that, as far as large-scale numerical models are concerned, the ice sheet approximation may still be valid, so that the shear stresses follow from the usual equations (eq. 8). Other assumptions in Van der Veen's analysis are also used here, such as replacing the deviatoric stresses by their vertical mean, because information on their vertical profile is lacking.

In view of this, the vertically integrated mass flux at the grounding line (that is of final interest) can also be found by integrating expressions for the shear strain rates $\dot{\varepsilon}_{xz}$ and $\dot{\varepsilon}_{yz}$ twice along the vertical, however incorporating all stress components in the effective stress term of the flow law:

$$\ddot{v}H = -2(\rho g)^3 \left[\nabla (H+h).\nabla (H+h)\right] \nabla (H+h) \int_h^{H+h} \int_h^z A(H+h-z)^3 \, dz \, dz'$$

$$-2 \rho g \left[\overline{\tau'^2_{xx}} + \overline{\tau'^2_{yy}} + \overline{\tau'_{xx}\tau'_{yy}} + \overline{\tau^2_{xy}} \right] \nabla (H+h) \int_h^{H+h} \int_h^z A(T)(H+h-z) \, dz + \vec{v}(h) \, H \qquad (17)$$

where $\overline{\tau'_{xx}}, \overline{\tau'_{yy}}, \overline{\tau'_{xy}}$ in the transition zone cannot be specified directly, but have to be obtained by invoking the constitutive relation (5). The procedure relies on the fact that the stress field can be calculated from the flow law, given the ice sheet geometry, strain rates and the rate factor. Integrating expression for $\dot{\varepsilon}_{xx}, \dot{\varepsilon}_{yy}, \dot{\varepsilon}_{xy}$ along the vertical and dividing by ice thickness to obtain vertical mean values yields:

$$\frac{1}{H} \int_h^{H+h} \dot{\varepsilon}_{ij} \, dz = \frac{1}{H} \int_h^{H+h} \left[A(T^*) . (\tau'^2_{xx} + \tau'^2_{yy} + \tau'_{xx}\tau'_{yy} + \tau^2_{xy} + \tau^2_{xz} + \tau^2_{yz}) . \tau'_{ij} \right] dz$$

$$\text{for } \dot{\varepsilon}_{xx}, \dot{\varepsilon}_{yy}, \dot{\varepsilon}_{xy} \qquad (18)$$

Since τ'_{xz}, τ'_{yz} follow from eq. 8 and all strain rates can be calculated from the velocities that result on the grid, this represents a (non-linear) system of three equations in the three unknowns $(\overline{\tau'_{xx}}, \overline{\tau'_{yy}}, \overline{\tau'_{xy}})$ which is most easily solved by an iterative Newton-Raphson method. Only a few iterations are needed to obtain an acceptable solution.

The main effect of treating the transition zone in this way is that the ice is apparently softened there (the depth-averaged deviatoric longitudinal stresses may be up to 3 times larger than shear stresses), so that lower shear stresses are needed to produce the same ice flux. Also, this treatment fully couples ice shelf flow to the inland flow regime. This is because longitudinal stresses reflect the dynamic state of the ice shelf as well. The deformational velocity at the grounding line (and indirectly also the basal sliding velocity through changes in the ice sheet geometry) is therefore able to react to changes in the ice shelf geometry. For instance, restraining forces in the ice shelf that inhibit free spreading will reduce the velocity at the grounding line, whereafter the flux divergence decreases, in turn leading to thicker ice and smaller surface slopes. Of course, the shear stresses may react to this and increase, causing a thinning, and so forth.... The important thing is that this approach is able to represent a number of potentially effective feedback mechanisms in the flow. The adopted coupling scheme seems to work well, because it allows the grounding line to move in both directions. As such, this certainly represents an improvement over previous Antarctic models.

2.3 Thermodynamics

To close the set of equations specifying ice deformation, the temperature distribution needs to be known simultaneously in order to adjust the ice stiffness parameter. This is necessary, since A(T*) changes by three orders of magnitude for the temperature range encountered in polar ice sheets (-50°C - 0°C; Paterson, 1981). Laboratory experiments suggest an Arrhenius relationship:

$$A(T^*) = m \cdot a \exp\left\{ \frac{-Q}{RT^*} \right\} \tag{19}$$

where a $=1.14 \cdot 10^{-5} Pa^{-3} year^{-1}$ and Q$-=60 kJmol^{-1}$ for T*<263.15K, a$=5.47 10^{10} Pa^{-3} year^{-1}$ and Q$=139 kJmol^{-1}$ for T*$\geq$263.15K, R the gas constant [8.314 $Jmol^{-1}K^{-1}$] and T* [K] pressure-corrected absolute ice temperature. The enhancement factor m serves a 'tuning purpose', in this way implicitly including the softening effects due to impurity content and crystal fabric. In the model runs discussed here, its value is set at 5 for grounded ice and 1 for the ice shelf.

The temperature distribution within the ice sheet is obtained from the thermodynamic equation:

$$\frac{\partial T}{\partial t} = \frac{k}{\rho c_p} \nabla^2 T - \vec{V} \cdot \nabla T + \frac{\Phi}{\rho c_p} \tag{20}$$

Here T is temperature, and k and c_p (temperature dependent) thermal conductivity [$Jm^{-1}K^{-1}year^{-1}$] and specific heat capacity [$Jkg^{-1}K^{-1}$] respectively. In this equation, heat transfer is considered to result from vertical diffusion (first term), three-dimensional advection (second term), and deformational layer heating $\Phi = 2\dot{\varepsilon}_{xz}\tau_{xz}+2\dot{\varepsilon}_{yz}\tau_{yz}$. Boundary conditions follow from the mean annual air temperature at the upper surface. At the base, geothermal heating and dissipation due to sliding are incorporated in the basal temperature gradient. A value of 54.6 mW/m^2 is taken for the geothermal heat flux (Sclater et al., 1980).

In the ice shelf, the effects of basal melting and/or basal accretion and of spatially varying density and ice stiffness were ignored. Instead, a steady state linear vertical temperature distribution was assumed, with a surface temperature of -18 °C (representing present day ice shelf conditions and allowed to vary with climatic change) and a fixed basal temperature of -2 °C. The flow parameter is then taken to represent mean ice shelf temperature conditions.

2.4. Isostatic bed adjustment

Finally, bed adjustments are calculated with a two-layer earth deformation model that consists of a viscous fluid asthenosphere enclosed by a uniform, thin and elastic lithospheric shell, which is in floating equilibrium with the underlying substratum of the asthenosphere. The elastic properties of the rigid lithosphere determine the deflection, which gives the ultimate shape of the bedrock depression. The rate of bedrock adjustment, on the other hand, is governed by the rate of outflow in the asthenosphere and thus by its viscous properties.

The time-dependent response of the underlying substratum may be modelled by a diffusion equation for bedrock elevation h (e.g. Oerlemans and Van der Veen, 1984,chap.7):

$$\frac{\partial h}{\partial t} = D_a \nabla^2 (h - h_0 + w) \tag{21}$$

where $D_a = 0.5 \ 10^8 \ m^2 year^{-1}$ is the asthenosphere diffusivity, h_0 the undisturbed bed topography in the absence of loading and w the deflection, taken positive downwards.

ANTAR
II/04
A

The flexural stiffness of the crust causes the effect of a point load to be spread out beyond the boundary of the load itself. The lithosphere will not only bend downward under the load, but deflect upward in more remote areas, thereby creating a weak forebulge. These rheological properties give rise to deviations from *local* isostatic equilibrium, which become especially marked near the ice sheet edge, where grounding-line migration takes place (order of magnitude: 30 m). The thin-plate equation for flexural deformation may be written in its two-dimensional form as (Brotchie and Sylvester,1969; Turcotte and Schubert,1983):

$$D \nabla^4 w = q - \rho_m g w \tag{22}$$

$$q = \rho_i g H \qquad \text{if} \qquad -\rho_i / \rho_w H + H_{sl} \leq h$$

$$q = \rho_w g (H_{sl} - h) \qquad \text{if} \qquad -\rho_i / \rho_w H + H_{sl} > h$$

where D is lithospheric flexural rigidity [$10^{25}Nm$] and ρ_m mantle rock density [3300 kgm^{-3}]. The right-hand side gives the applied load q minus the upward buoyancy force arising when the lithospere bends downwards into the astenosphere; the left-hand side represents the bending resistance opposing lithospheric flexure. Since bending of a rigid plate is a linear process, isostatic displacements on gridpoints due to varying ice and water loading have been superimposed in a square with sides of 800 km.

14

2.5. Numerical scheme

The model equations are performed on a square grid that is laid out over a polar stereographic projection with standard parallel at 71°S. The grid is centred at the pole and comprises a 141 x 141 gridpoint matrix (fig. 2). Small distortions in distance arising from the sphericity of the earth have been disregarded.

Since it is rather inconvenient to integrate the thermodynamic equation in the computational phase on a grid fixed in space, as the upper and lower ice boundaries will generally not coincide with grid-points, a new vertical coordinate ζ, scaled to local ice thickness, has been introduced. Following Jenssen (1977), this stretched dimensionless vertical coordinate is
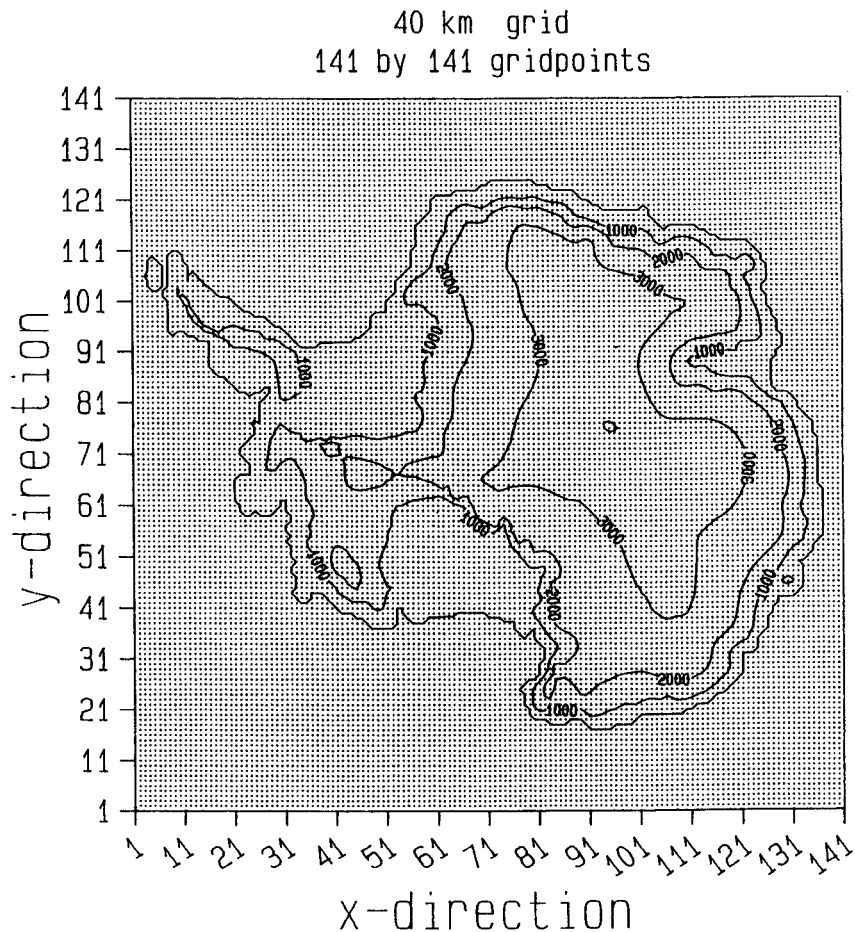
fig. 2: Numerical grid on which the calculations are performed. The model domain is covered by 141 x 141 = 19881 gridpoints. Every point in turn represents a vertical, which is subdivided into 10 layers. This adds up to a total of over 200000 gridpoints. Contour lines are for surface elevation; the lowest contour represents the ice shelf edge.

defined by:

$$\zeta = (H + h - z) / H \qquad (23)$$

such that $\zeta=0$ at the surface and $\zeta=1$ at the base. The resulting equations in this non-orthogonal system will not be shown here, but more details on the relevant transformations can be found in Huybrechts (1986). In this approach, velocity and temperature fields are computed at levels of constant ζ (the layer interfaces). In the present model, the vertical domain was subdivided into ten layers concentrated towards the base, with an uppermost layer thickness of $\Delta\zeta=0.15$ and a lowermost grid spacing of $\Delta\zeta=0.02$, which proved to be sufficient to capture the essential characteristics of the model variables.

In order to solve the continuity equation numerically, we opted for a finite-difference approach. A staggered grid in space was employed, so that mass fluxes are calculated in between grid points. Having replaced the derivatives by finite differences, the resulting finite-difference equations are usually quite readily solved by an explicit integration scheme. However, such a scheme has the important drawback that in order to preserve stability, time steps necessarily have to be taken small. Alternatively, the Alternating-Direction-Implicit (ADI) method turned out to perform satisfactorily (Mitchell and Griffiths, 1980). This is a two-step method involving the solution of sets of equations along lines parallel to the x- and y-axes at the first and second step respectively. Although not unconditionally stable, due to the non-linearity of the flow law, this scheme allows time steps to be taken an order of magnitude larger than an explicit approach. The resulting tri-diagonal systems are easily solved by some form of Gaussian elimination.

ANTAR
II/04
A

A comparable approach was applied to the solution of the thermodynamic equation. Here, the terms involving ζ-derivatives were made implicit, leading once more to a set of tri-diagonal equations that have to be solved at every gridpoint. We used an "upwind" differencing scheme to avoid the generation of oscillations common in diffusion-convection equations with a high Peclet number (i.e. a constant proportional to the ratio of advective velocity and diffusivity. Although this scheme can be shown to introduce an artificial horizontal diffusivity equal to $v\Delta r/2$, where v is the velocity and Δr the gridspacing, such an approach keeps the integration stable and influences results only marginally. In most most cases, the associated artificial heat transfer turns out to be an order of magnitude smaller than the horizontal heat advection. In the model, spatial resolution is 40 km, allowing time steps up to 40 years. The complete model is running on a CRAY-2 computer, and takes around 18 min. CPU time for a 10000 year integration.

2.6. Input data

Model inputs are bed topography, surface temperature, mass balance, thermal parameters and an initial state (that may be a thin slab of ice of equal thickness). The external forcing is made up by both prescribing eustatic sea level stand and imposing a uniform background temperature change. The latter climatic forcing drives changes both in the accumulation and surface temperature distributions. The model then outputs the time-dependent three-dimensional ice sheet geometry and the fully coupled velocity and temperature fields, as well as a number of derived physical characteristics.

Geometric input data such as bedrock elevation, surface elevation and ice thickness for the present ice sheet have been interpolated from an original 20 km-digitalisation by the Australian group (Budd et al, 1984) of the Drewry (1983) map folio series and have been locally complemented beneath ice shelf areas with data from bathymetric charts (GEBCO, Canadian Hydrographic Service) and more recent sources (Herrod, 1986). A contoured representation of the resulting initial bed topography is shown in fig. 3. The undisturbed bedrock heights, needed in the bed adjustment calculations, have been reconstructed assuming present isostatic
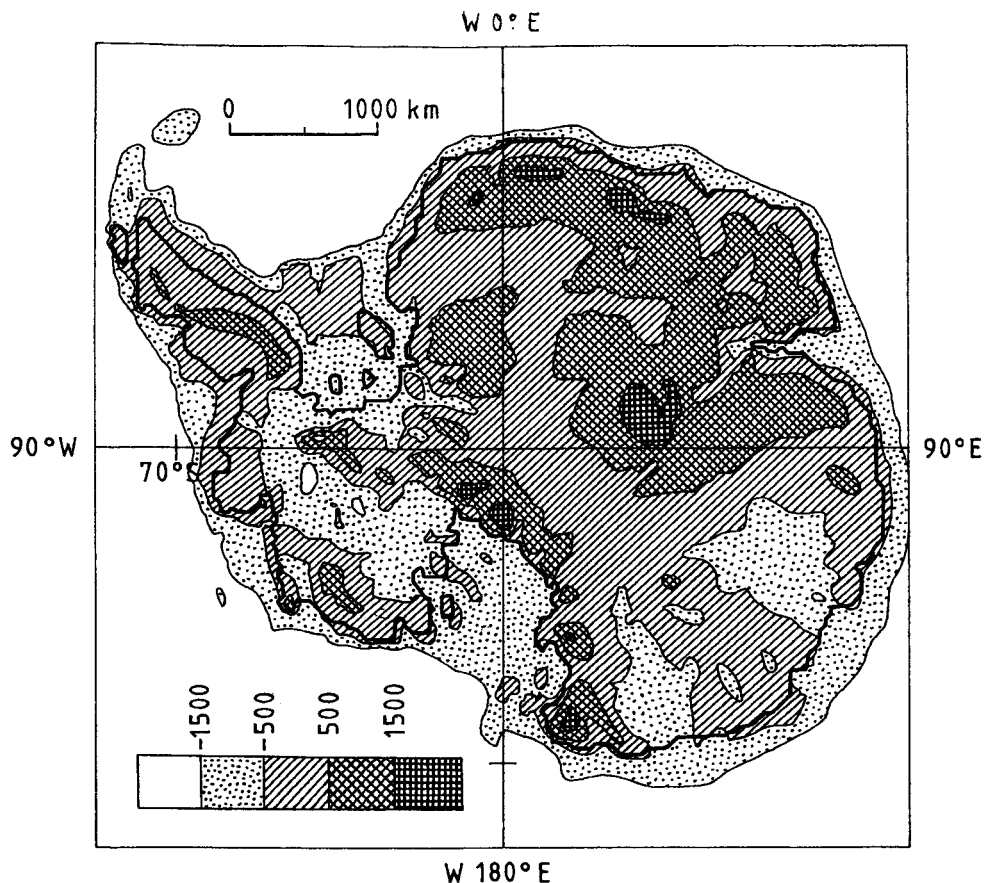
fig.3: Measured bedrock elevation used as input to the model. The *thick line* is the present grounding line. Units are in m above contemporary sea level.

equilibrium. This may introduce an error, because uplift following the last glacial-interglacial transition some 15000 years ago is probably still in progress (Greishar and Bentley, 1980), but a sound alternative is not readily available.

3. TREATMENT OF THE MASS BALANCE

In the model, the components of the mass balance (accumulation and runoff) and its perturbations are parameterized in terms of temperature, which is the principal forcing parameter. Although accumulation and runoff result from quite complex processes, involving the circulation pattern in the atmosphere and the energy balance at the ice sheet surface, such an approach is necessary to keep calculation times within reasonable bounds. Also, accumulation rates produced by General Circulation Models are too uncertain to justify application in the type of sensitivity experiments described here. A similar remark applies to thermodynamic models for the melting/refreezing processes in the upper firn layers. Model runs involving past climatic conditions do not consider ice ablation. Such a process may however become important in warmer climates, such as those associated with future greenhouse warming.

ANTAR
II/04
A

3.1 Accumulation

The spatial distribution of the accumulation rate on the Antarctic ice sheet appears to be strongly related to air temperature, which controls the amount of vapour that can be advected inland. Such a relationship seems to be particularly strong over the inland plateau, where year-round temperatures are far below freezing, and snow deposition results from an almost continuous fallout of ice crystals and also some surface sublimation. Robin (1977) proposed that accumulation could be set proporional to the saturation vapour pressure of the air circulating above the inversion layer. In Lorius et al. (1985) it was argued that the rate of change with temperature of the saturation vapour pressure is the relevant quantity from a physical point of view. Indeed, the relation thus obtained between accumulation and temperature appeared to be consistent with accumulation rates deduced from the ^{10}Be content in the Vostok ice core (Yiou et al, 1985).

Based on these observations, the following procedure was adopted to calculate accumulation rates. As a first step, basic data sets for accumulation rate and surface temperature were obtained by quadratically interpolating and smoothing raw data, as compiled at the Scott Polar Research Institute (Cambridge, U.K.), on the 40 km model grid. The resulting distributions are shown in figs. 4-5. The mean annual surface temperature *change* δT occurring at the grid points during the integration then consists of two parts: one associated with the imposed
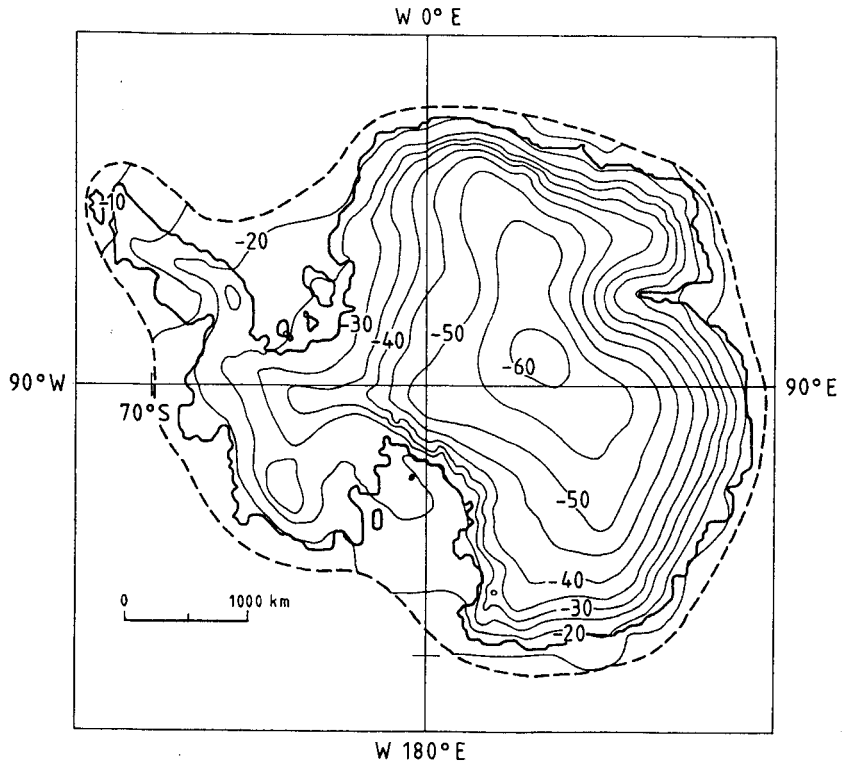
fig. 4: Upper boundary condition for the temperature calculations. Values are in °C.
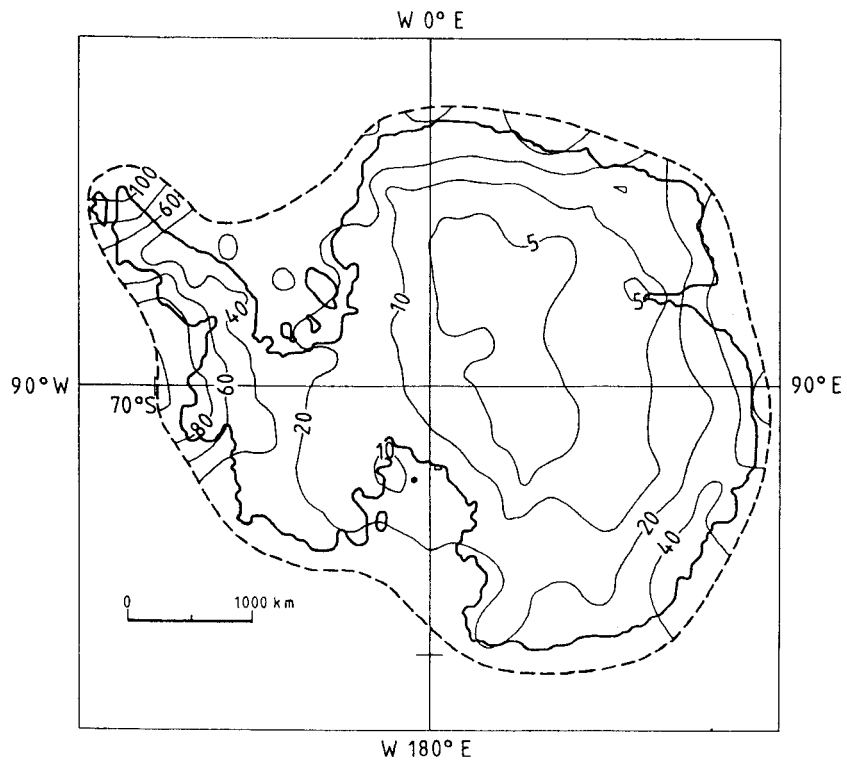
fig. 5: Accumulation rate data [in cm/year ice equivalent] corresponding to the present topography. The above fields are perturbed in the experiments to include the effects of both different climates and ice sheet geometries. Data outside the stippled area are not shown, because they do not influence the model outcome.

climatic warming $\Theta(t)$ and one with the change in surface elevation:

$$\delta T = \gamma\, \delta H + \Theta(t) \text{ , where}$$
$$\gamma = 5.1\ ^\circ C/km \quad \text{if} \quad H \leq 1500\ m$$
$$\gamma = 14.3\ ^\circ C/km \quad \text{if} \quad H > 1500\ m \tag{24}$$

Lapse rates are suggested by a linear multiple regression study by Fortuin and Oerlemans (1990). It is assumed that the temperature of formation of precipitation T_f is close to the temperature prevailing at the top of the inversion layer. The following linear relation between T_s (the surface temperature) and T_f is suggested by Jouzel and Merlivat (1984):

$$T_f\, [K] = 0.67\ T_s\, [K] + 88.9 \tag{25}$$

If the accumulation rate is governed by the amount of water vapour in the air, it should be proportional to $\partial P/\partial t$, where P is the water-vapour pressure at the condensation temperature T. The accumulation rate for any perturbed climatic state is therefore obtained from the product of its reference (present) value, times the ratio of the derivatives of the saturation vapour pressure over a plane surface of ice for the reference and perturbed states. This gives (Lorius et al., 1985) :

ANTAR
II/04
A

$$M\,[T_f(t)] = M\,[T_f(present)] \cdot \exp\left\{ 22.47\left[\frac{T_0}{T_f(present)} - \frac{T_0}{T_f(t)}\right] \right\} \cdot \left\{ \frac{T_f(present)}{T_f(t)} \right\}^2 \tag{26}$$

$T_0 = 273.16$ K is the triple point of water. For surface temperatures prevailing over Antarctica, resulting accumulation rates typically differ by a factor 2 for a 10°C temperature shift.

This approach implies that the precipitation pattern does not follow changes in either ice sheet geometry or different patterns of air circulation and their associated storm tracks. This may be questionnable, in particular at the ice sheet margin, however Fortuin and Oerlemans (1990) did not find significant correlations with such factors as distance to open water and surface slope (related to orographic effects). In addition, net accumulation depends on such factors as snowdrift and evaporation, and changes in these factors could differ from the change in precipitation alone. Also here, a more sophisticated treatment would be far beyond the scope of the present study and is probably not justified in the light of the other approximations used.

3.2. Runoff

At present, there is little or no surface melting in Antarctica. If temperatures go up, however, summer melting may occur in the lower regions of the continent, and ultimately runoff towards the ocean may result. To estimate the importance of these effects, we have to rely on measurements taken in the ablation zone of the Greenland ice sheet. In the event of a substantial warming, melting conditions on the Antarctic ice sheet are then likely to resemble those of present-day Greenland.

The annual melt rate will be calculated by means of a degree-day model. As shown by Braithwaite and Olesen (1989), there is a high correlation between positive degree days and melt rates at the ice margin in West Greenland. The annual number of positive degree-days is parameterized in several steps. Data from 16 Antarctic coastal stations (Orvig, 1970) were used to relate summer temperature (mean of December and January) and annual temperature amplitude (both in °C) to geographical latitude ϕ (in °S):

$$T_{sum} = 25.11 - 0.39 \, \phi + \gamma H \qquad (r = 0.84) \qquad (27)$$

$$A_{ann} = -30.74 + 0.59 \, \phi \qquad (r = 0.91) \qquad (28)$$

The correlation coefficients appear to be sufficiently large to justify this approach. In the calculations the daily cycle during the summer months (NDJF) was set to 3.02 °C (mean value of the 16 coastal stations with a standard deviation of 0.16 °C) and temperature during the summer season was fitted by a sinusoidal function with a half-period of 5 months and peaking on January 1st. This is necessary because the yearly temperature march has a rather flat profile in winter, because insolation is zero. By integrating the parameterized annual and daily temperature cycle through the year (with a 30 min. time step), the number of positive degree days (PDD) is easily obtained. The result can be approximated quite accurately by a fourth-order polynomial:

$$\begin{aligned} PDD \; [\text{°C day}] = \; & (58.259 - 2.201 \; A_{ann} + 0.038 \; A_{ann}^2) + \\ & + (50.263 - 2.265 \; A_{ann} + 0.045 \; A_{ann}^2) \; T_{sum} + \\ & + (12.326 - 0.788 \; A_{ann} + 0.019 \; A_{ann}^2) \; T_{sum}^2 \end{aligned} \qquad (29)$$

This is subject to the conditions that the summer temperature is between -3 and +10°C, and that the annual amplitude is between 7 and 22°C.

PDD represents the potential energy for melting. This potential energy is used for melting snow and/or ice according to the following two-step scheme:

Step 1. Snow is melted with a degree-day factor of 0.003 m ice equivalent per unit of PDD, and the meltwater percolates into the snowcover and refreezes. Runoff occurs when enough latent heat is released by the refreezing process to raise the uppermost 2 m from the mean annual temperature to the melting point:

$$RM = \frac{\Delta T \times 2m \times c_p}{L} \approx 0.012 \times \Delta T \tag{30}$$

where RM is the maximum amount of refrozen meltwater [m/year], ΔT the temperature difference between the mean annual temperature and the melting point, L the latent heat of fusion [3.35 x 10^5 Jkg^{-1}] and c_p specific heat capacity [2009 Jkg^{-1}°C^{-1}].

Step 2. Refrozen melt water ('superimposed ice') and in a later stage glacier ice are melted with a higher degree-day factor of 0.008 m ice equivalent per unit of PDD. This higher value is essentially related to a lower albedo for bare ice as compared to snow. Degree-day factors are from Braithwaite and Olesen (1989).

This process may stop at either of the stages 1 or 2, depending on the magnitude of PDD.

ANTAR
II/04
A

On the ice shelf, all melting is assumed to refreeze into superimposed ice and no runoff takes place. In view of the very small surface slope, this is to be expected for a long time to come.

The treatment of the refreezing process sketched above is admittedly rather crude. However, an alternative technique seems difficult to construct with our present knowledge. Some theoretical model studies on wetting-front propagation into cold snow exist (Pfeffer et al., 1990), but these results are not readily transferable to the present problem. Also field studies of the energy transfers involved in the formation of ice lenses and superimposed ice have been very limited. Useful data were obtained from field campaigns on the Laika ice cap in arctic Canada (Blatter and Kappenberger, 1988) and on the Greenland ice sheet (Ambach, 1963, 1968). Analysis of Ambach's results suggests that taking a 2 m thick (ice equivalent) layer to heat up annually by refreezing gives the correct order of magnitude.

3.3 Sensitivity of the surface mass balance

With the mass-balance model described above it is possible to study how the total ice budget gained (or lost) at the surface depends on temperature. Fig. 6 displays the surface mass balance and its components integrated over the entire ice sheet. Only grounded ice has been considered as ice mass changes in the floating shelves do not affect global sea level. The surface elevation of the ice sheet, which is a necessary input parameter for the mass-balance

model, was taken from the 'interglacial steady-state reference run' (see also further under 4.1). For present conditions, it is found that an amount of 24.06 x 10^{11} m^3 of ice equivalent is deposited on the ice sheet surface every year. This amount of ice would lower global sea level by 6 mm/year, were it not that each year a same amount is discharged across the grounding line to form an ice shelf and, ultimately, ice-bergs (assuming a stationary state).

For a 1°C temperature rise with respect to present conditions, the mass balance increases by an amount of 1.43 x 10^{11} m^3 of ice, i.e. by 5.9%. This corresponds to an additional mean accumulation rate spread out over the entire grounded ice sheet of 10.3 mm/year water equivalent. Since the area of the world oceans is about 29 times larger than the area of the Antarctic ice sheet, this would imply a rate of sea-level lowering of 0.36 mm/year.

Runoff is negligible for the present climate, but it is found to increase progressively with temperature. This higher-order dependence occurs because a warming climate will not only increase melting rates, but also the length of the ablation season.

While the temperature increase is below 5.3 °C, the mass balance increases, because the increase in accumulation outweighs the increase in runoff. At this stage, the total accumulation amounts to 32.75 x 10^{11} m^3, of which 8.7 % runs off in summer. This would extract an

Antarctic mass balance
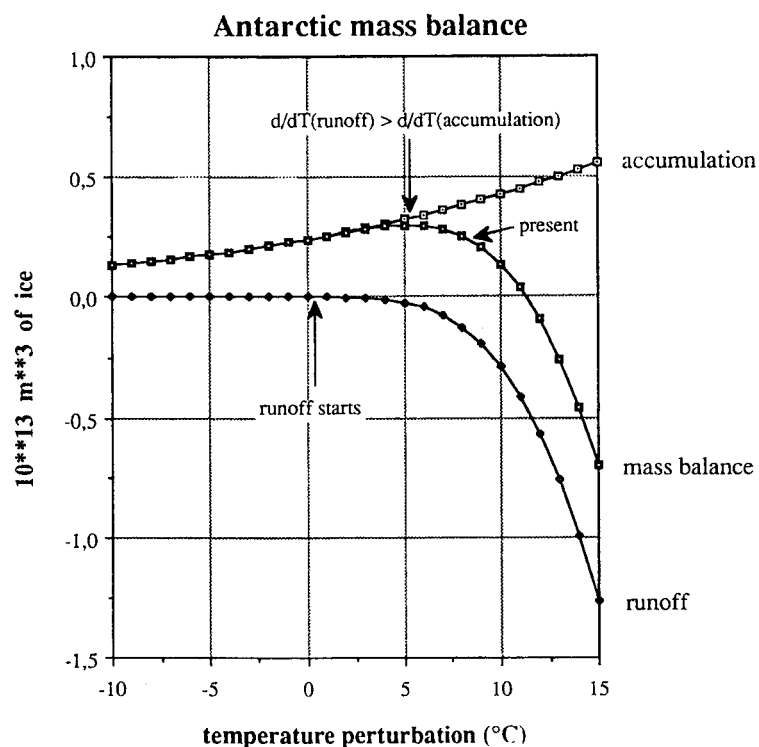
fig. 6: Dependence of Antarctic mass balance components on temperature relative to present. For a temperature rise below 5.3°C, the mass balance would still be larger than today.

annual amount of 1.46 mm from the world's oceans, if ice sheet dynamics were to remain unchanged. This applies to the total surface balance, but the spatial pattern of change of course depends on altitude.

Temperature has to rise by 8.3 °C to match the present mass balance, and an increase of 11.4 °C leads to a negative total surface balance. If this situation were to last over a long time (say thousand of years) ice shelves could not be sustained and a large ice-free strip would develop on the Antarctic continent.

In climates colder than today, changes of the surface mass balance follow the changes of the accumulation rate. According to the treatment adopted in this study the mean accumulation rate changes by 6.4 % for every degree at a temperature perturbation of -10°C and by 6.1 % for present conditions. The result is a monotonous increase with temperature that is nearly linear over the interval of practical interest.

4. MODELLING THE LAST GLACIAL CYCLE

As mentioned in the introduction, the Antarctic ice sheet seems to have undergone important changes during the Pleistocene glacial cycles. In particular the ice sheet extent during the last glacial glacial cycle is fairly well documented in the environmental record and this is also the period which is best suited to validate the model. The picture emerging from the glacial-geological data indicates that the West Antarctic ice sheet may have completely filled the continental shelf during maximim glaciation. There seems to be a general consensus that this was indeed the case in the Weddell Sea, although views still differ whether the shallow Ross Sea was completely land-ice covered, or there was only a minor expansion (Denton and Hughes, 1981, who favour the maximum ice sheet hypothesis).

From a schematic point of view, four main mechanisms can be identified by which the Antarctic ice sheet reacts to changes in the climate system. First, changes in surface boundary conditions which result in lower ice temperatures in the basal shear layers will reduce deformation rates, thereby leading to a thickening. Second, changes in ice deposition rates modify the local stress field through changes in mass balance and ice sheet geometry and affect the amount of ice that is discharged into the ice shelf. Third, lower global sea level stands, induced by the glacial cycle on the continents of the northern hemisphere, reduce the thickness necessary for grounding in regions where the bed is below sea level. Fourth, isostatic bed adjustments and fluctuations in ice shelf thickness, associated with different stress conditions and climatic forcing, have a similar effect on grounding.

These mechanisms raise a number of fundamental questions regarding the ice sheet's basic behaviour, namely (i) what is the relative importance of changes in these environmental conditions; (ii) what are the response time scales associated with these changes; (iii) what is the spatial distribution of ice-sheet fluctuations; and (iv) how do all these effects interplay during a glacial-interglacial cycle? The answers to these questions are, among other things, important in the light of a better understanding of ice-sheet histories from proxy data, and the contribution of Antarctic ice-sheet volume changes in world-wide sea levels.

A steady state sensitivity study (Huybrechts, 1990b) brought to light that thermomechanical coupling and grounding-line advance introduces very long response time scales to the ice sheet system. According to this study, it took the model 30000 to 40000 years to grow to full glacial extent after sudden glacial conditions were imposed. A direct consequence is that the Antarctic ice sheet may never reach its 'maximum possible' glacial extent, suggesting that a time dependent experiment is needed to reconstruct the ice sheet's history during a glacial-interglacial cycle. As a second consideration, such an experiment is also thought to be a good test of the model: not only should the model be able to simulate a glacial buildup, but it should also reproduce a deglaciation when boundary conditions are reset. In other words, if the model can simulate past ice sheet behaviour in reasonable agreement with geomorphological field evidence, then it would have sufficient credibility to be used in predictions of future ice sheet changes, such as those associated with the expected greenhouse warming of the earth's atmosphere.

4.1. Reference states

Before performing such a model run, it is necessary to define a reference state, against which model output can be compared. Starting from the observed ice sheet and running the model forward in time with prescribed changes in environmental conditions is a less meaningful way to proceed, because it is unlikely that the input data are in full internal equilibrium with the model physics. The model ice sheet will certainly evolve from the present observed state, but it would be unclear why. Shortcomings in the description of ice mechanics, insufficient data, or the fact that the present ice sheet is just not in steady state could all play a role. As a consequence, it would be impossible afterwards to distinguish between the 'natural model evolution' and the 'real' ice sheet response. One way to circumvent this ambiguity is to define a steady state and relax the model to equilibrium. The resulting steady state interglacial run, although differing from the presently observed data in some detail, should then be used as input in a climatic change experiment.

This reference run is obtained in several steps. First, the coupled velocity and temperature fields are run forward in time for 100000 years in a quasi-diagnostic way (thus keeping ice
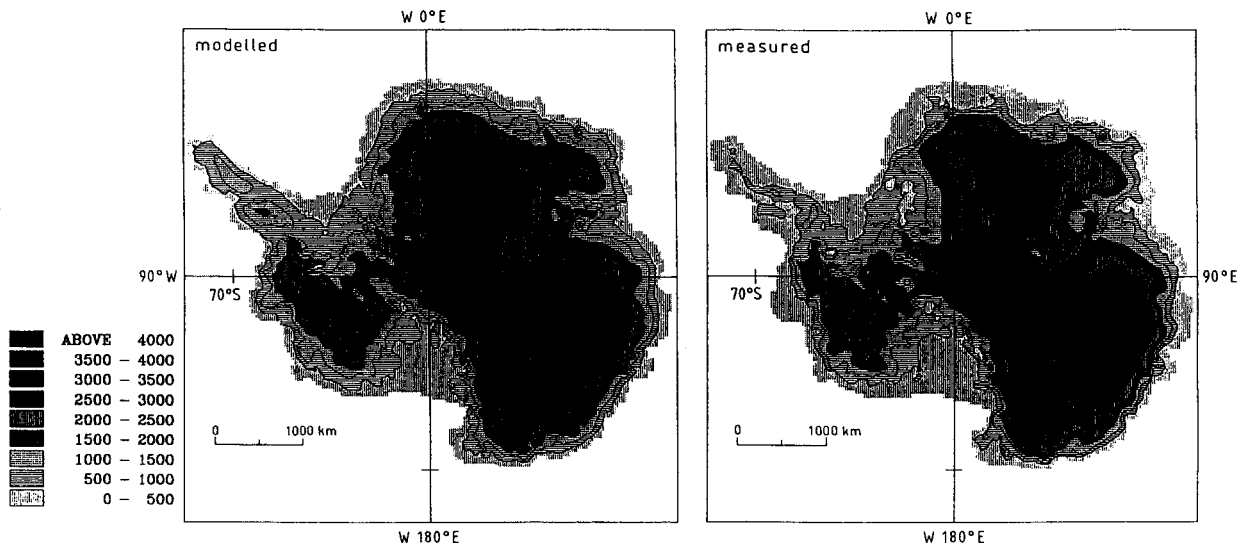
fig. 7: A comparsion between modelled and measured ice thicknesses (m). In this run, the position of the grounding line is still prescribed, but ice thickness is a free variable.

ANTAR
II/04
A

thickness and the grounding line position fixed) until an approximate steady solution settles down. In a subsequent stage, the position of the grounding line is still prescribed, but ice thickness is allowed to relax to steady state. The result is shown in fig. 7, where also a comparison is made with the observations. Modelled ice thicknesses then appear to be within 5-10% or so of these, which is certainly acceptable. Somewhat larger deviations are found in the Pine Island and Thwaites Glacier catchment areas (approx. 90°W, WAIS) and upstream the Shackleton Range in Dronning Maud Land (30-40°W, EAIS). However, this does not necessarily have to mean that the model is in error. Alternatively, insufficient bedrock data coverage in these areas and/or the fact that the ice sheet is just not in steady state there could both play a role.

Other basic variables (velocity and basal temperature fields) relevant to the present modelled state are displayed in figs. 8-9 and provide an additional check on global model performance. As far as can be judged from available data, the velocity field (fig. 8) looks quite reasonable, with very low velocities over central East Antarctica, typically around 200 m/y at the grounding line and up to 1500 m/y along central portions of the three major floating ice regions, the Ronne-Filchner, Amery and Ross ice shelves. These modelled ice shelf velocities are certainly of the right magnitude, although they tend to be somewhat higher than the observations: the Ronne and Filchner ice shelves flow at a maximum rate of ± 1500 m/year (Robin et al., 1983); the Ross ice shelf at ±1100 m/year (Thomas et al., 1984); and the Amery
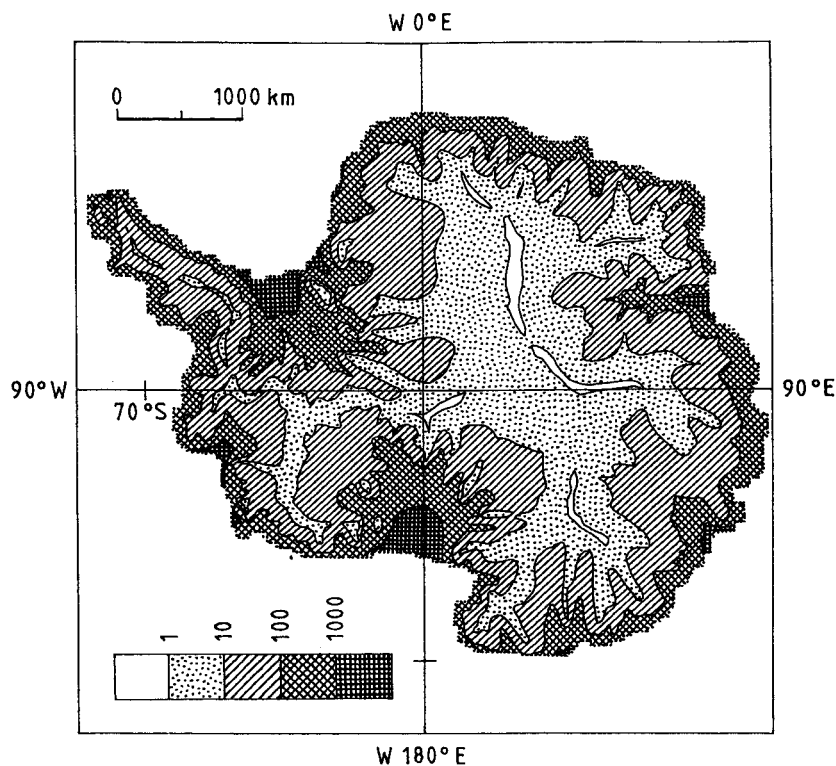
fig. 8: Calculated speed of ice flow in the interglacial reference run, prescribed grounding line. Shown are depth-averaged values [m/year]. The corresponding surface velocities in the grounded ice sheet are 5-10% larger, depending on the temperature conditions in the bottom layers and the amount of basal sliding.
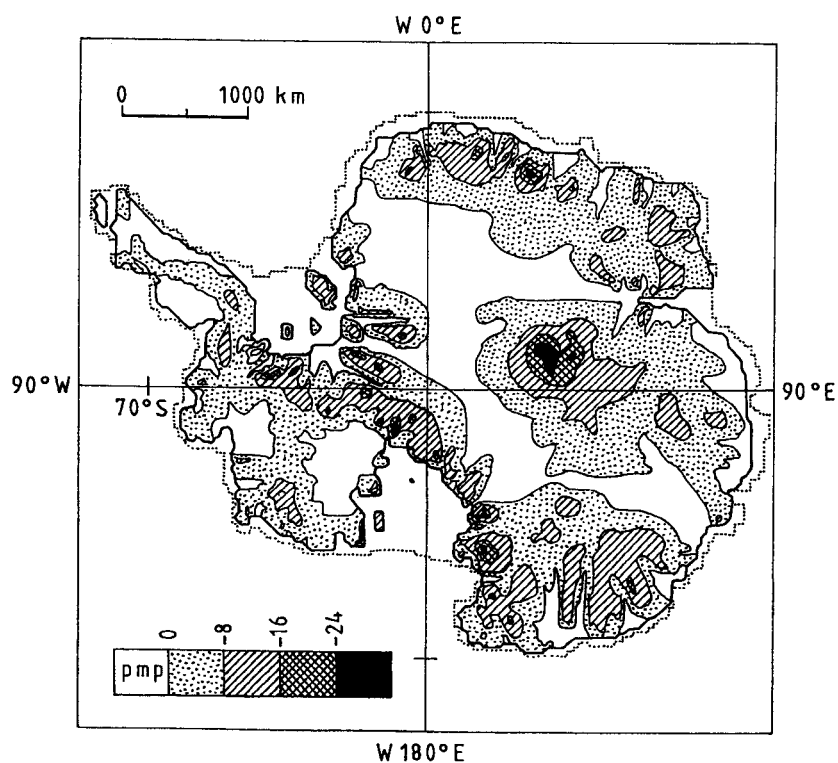
fig. 9: Bottom temperatures produced by the model for present conditions and prescribed grounding line [in °C]. They have been corrected for the dependence of temperature on pressure. White areas within the stippled line are areas where the ice is at the pressure melting point.

ice shelf at ±1300 m/year (Budd et al., 1982). This discrepancy may be due to the neglect of basal melting in the mass balance of the ice shelf. As a consequence, the model probably overpredicts the mass outflow and, since the thicknesses agree much better, this results in somewhat higher velocities.

Although ice streams and outlet glaciers (discharging an important fraction of the ice mass into the ocean) are not explicitly included in the calculations, they show up distinctly and major outlet glaciers are characterized with velocities up to 500 m/year (fig.8). This is essentially a consequence of the fine grid in use.

According to the model, bottom ice at pressure melting point appears is dominant over most of the Antarctic Peninsula and is widespread in West Antarctica. In East Antarctica, basal melting is confined to the thick interior regions (because of the insulating effect of ice) and the fast flowing regions at the margin (fig.9). This temperature field can be reconciled with independent evidence for temperate ice from radio-echo sounding, where sub-ice lakes in central areas have been found to obscure reflections (Oswald and Robin, 1973). The coolest basal layers are found above the Gamburtsev Mountains, where the ice is relatively thin (1500 -2000m) and along the fringing mountain ranges. Here, both thin ice and cold ice advecton from above play an important role.

ANTAR
II/04
A

Finally, also variations in the extent of the grounded ice sheet come into play and the grounding line is allowed to migrate for another 100000 years. The result is shown in fig. 10. Somewhat larger deviations from the present observed state include thicker ice in the Antarctic Peninsula (mainly due to poor bedrock data below the present ice shelf areas) and a slight recession at the seaward edge of the most overdeepened EAIS outlet glaciers (Totten, Ninnis and Mertz Glaciers). In West Antarctica, the model fails to resolve several narrow channels separating ice covered islands from the mainland. Also surface slopes inland of the Ross ice shelf tend to be somewhat larger than observed. Anyhow, considering the complexity of the model and the fact that the complete geometry is *internally generated*, the resulting configuration is certainly acceptable, and the model seems capable of reproducing the most important characteristics of the ice sheet.

Also shown in fig.11 is the glacial steady state run, in which sea level was stepwise lowered by 130m, background temperatures were decreased by 10°C and concomitant reduced accumulation rates were applied. This ice sheet now extends almost all the way to the continental shelf edge, corresponding with a volume gain of 7.4×10^6 km^3 of ice (32.42 against 25.02), or alternatively, an Antarctic contribution to global sea level lowering with 15.9 m (including the correction made for ice merely displacing ocean water). More details of these and other steady state experiments have been presented elsewhere (Huybrechts, 1990b,1992).
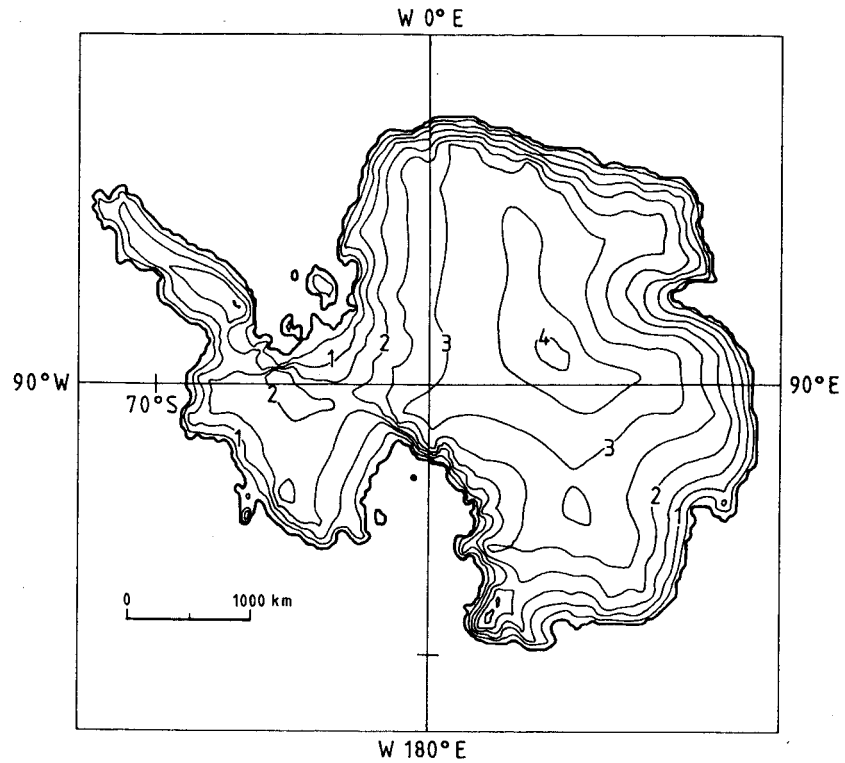
fig. 10: The 'interglacial reference state' as produced by the model, showing surface elevation (in km).
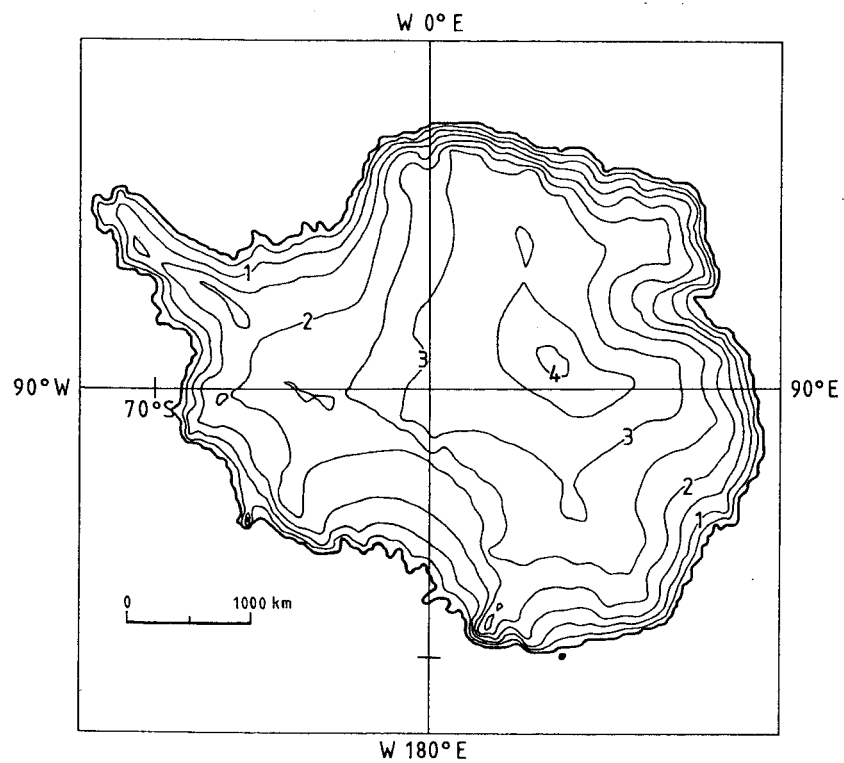
fig. 11: The glacial steady state, in which sea level was depressed by 130 m and a temperature lowering of 10°C was applied.

4.2. Experimental setup and model forcing

In order to simulate the last glacial-interglacial cycle, two forcing functions were used to drive the model. The Vostok temperature signal (Jouzel et al., 1987) was chosen to perturb the 10m - temperature and accumulation fields. This record dates back to 164000 years before present, i.e. well into the ice age preceding the last interglacial, and is assumed to be independent of latitude. A reliable forcing function for sea level, however, is more difficult to construct. $\delta^{18}O$ values in deep ocean cores have long been considered a good proxy for continental ice volume and hence, the glacio-eustatic component of sea-level change. However, Shackleton (1987) argues that this simple explanation is no longer tenable, because oxygen isotope values in benthonic foraminifera differ from the water value by an amount which is temperature dependent. According to Chappell and Shackleton (1986), this temperature effect may partially explain the discrepancy between the ice volume history that these records imply, and that derived from the altitude of dated coral terraces around the world. For these reasons, the more familiar 'saw-tooth' sea level function was chosen, piecewise linearly connecting the points (-140 ky, -130m; -125 ky, 0m; -16 ky, -130m; -6ky, 0m) respectively. The maximum deviation from either curve extreme (New Guinea terraces or oxygen isotope ice volume record) is then generally within 20-25 m.

ANTAR
II/04
A

The model calculations start at 164000 years BP, when the ice sheet has been run initially to a stationary state with a sea level depression of 130 m and a temperature perturbation of -5°C. The latter value was chosen to produce an initial temperature distribution intermediate to the glacial and interglacial states. This is justified because of the long thermodynamic response time scales involved.

4.3. Results

Figure 12 displays the Antarctic ice sheet at several stages during the last glacial cycle. The first picture is of the ice sheet during the Eem interglacial at 120 ky BP. Clearly, the ice sheet is significantly smaller than today, in particular in West Antarctica. However, this model behaviour should not necessarily be interpreted as proof for a West Antarctic ice sheet collapse at that time, and is probably also caused by the specific startup conditions used. In particular the fact that in the model the bed was fully depressed at 140 ky BP may have caused the grounding line to retreat substantially more into inland areas.

During the subsequent glacial buildup (second picture), a moderate lowering of sea level by some 35-40 m is enough to initiate grounding in the Weddell Sea, and the ice shelf runs aground on a number of high sea-banks near the present ice shelf front. This obstructs the ice flow landinwards and results in a relatively rapid thickening, so that almost instantaneous
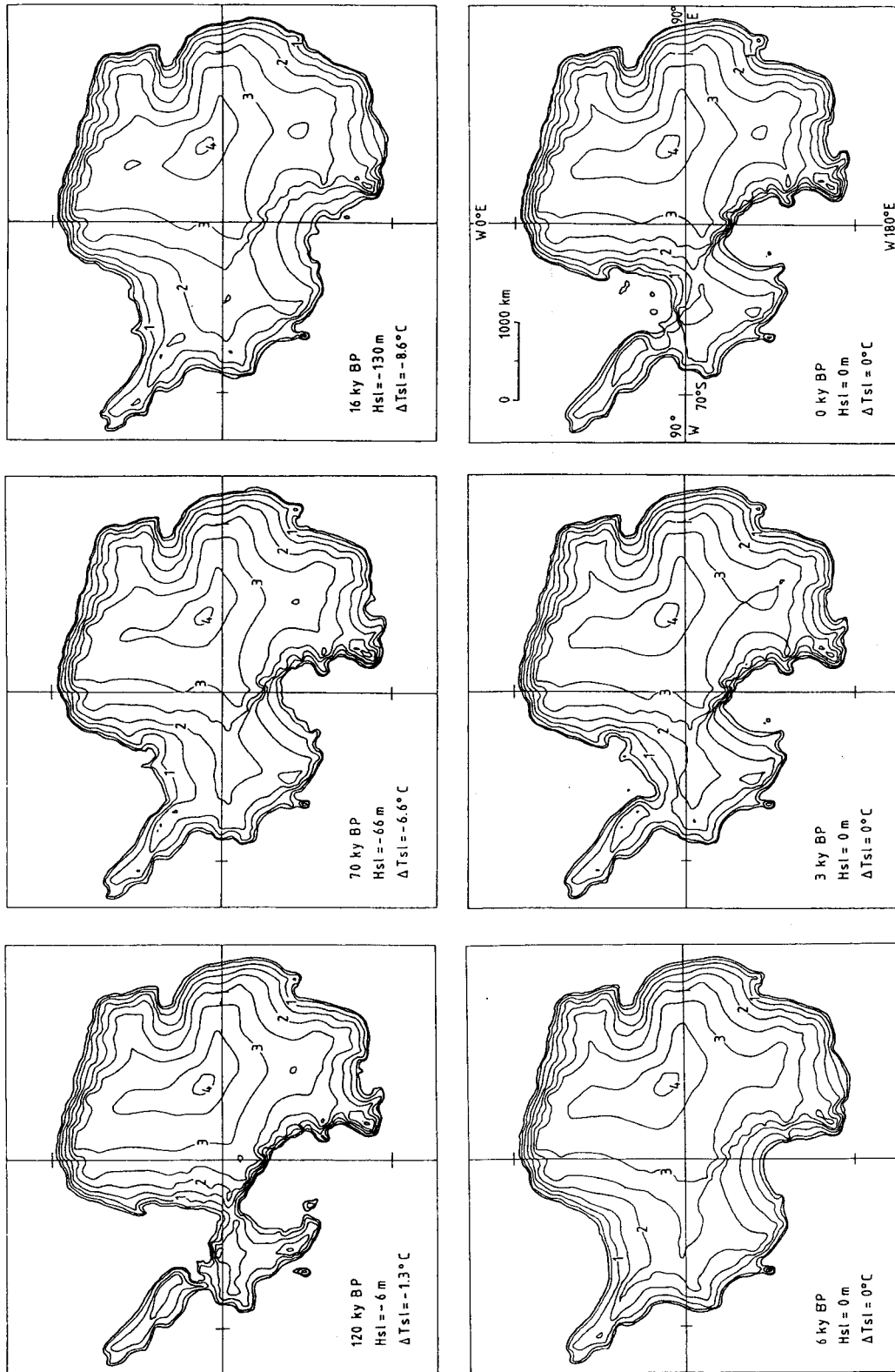
fig. 12: Stages in the modelled evolution of the Antarctic ice sheet during the last glacial-interglacial cycle. H_{sl}: world-wide sea level stand; ΔT_{sl}: temperature change. Times as indicated; contours are in m above present sea-level.

grounding occurs over a large area. The situation in the Ross Sea, on the other hand, is quite different. Here, the free water depth below the ice shelf generally *increases* towards the sea and consequently, grounding is of a more gradual nature. Also the threshold for grounding appears to be larger and widespread grounding is only produced in the later stages of a glacial period, in particular when the sea level depression exceeds 100 m (third picture).

Comparing the simulation at 16 ky BP with the stationary 'glacial' geometry in fig. 11 demonstrates that the Antarctic ice sheet has not fully reached its maximum extent, especially not in the Ross Sea. At this stage, the Antarctic ice sheet volume has grown to 31.0 x 10⁶ km³, corresponding to a global sea level lowering of 12.3 m relative to the interglacial reference run. This is less than the 16 m found for the steady state glacial run.

The concomitant deglaciation of the Antarctic ice sheet is essentially a partial desintegration of the West Antarctic ice sheet. Grounding-line retreat is triggered by a rise of world-wide sea-level, but lags behind. In the model, it begins around 8000 years BP and is nearly completed by the present time. This delay may be related to increased accumulation rates, which during the early stages of the Holocene thicken the ice and offset the retreating effect of rising sea level. The time lag between the onset of the recession and the beginning of the climatic warming is also the reason why the ice volume reaches a maximum during the early stages of the glacial-interglacial transition: at that time accumulation rates have already increased, while the ice sheet domain has not yet started to shrink and the surface warming signal has not reached basal shear layers.

ANTAR
II/04
A

Once the thresholds for grounding-line retreat are passed, overall retreat appears to take around 6000 years to complete. An important feature is that this disintegration seems to develop its own dynamics: environmental boundary conditions do not change after 6 ky BP, and the process of grounding-line retreat, once it has been initiated, then becomes entirely internally controlled. It only stops when a new equilibrium is achieved between ice thickness and sea depth. This happens when the ice shelf is able to stabilize the ice sheet and prevent excessive outflow. Stress conditions in the ice shelves then keep the grounded portions in place, and consequently, there is no collapse.

Fig. 12 also shows that the ice sheet retreats earlier in the Ross Sea than in the Weddell Sea. Like the glacial buildup, this is caused by the existence of a eustatic threshold for grounding-line migration, which is larger for the Ross Sea. A crucial role is also played by the bed adjustment process: it allows the grounding line to retreat into depressed inland areas first, but subsequent isostatic rebound slows the retreat down and eventually results in a small advance. It is interesting to note that during this evolution, ice rises in the Ronne-Filchner ice shelf (Korff Ice Rise and Berkner Island) never completely disappear. In the East Antarctic ice
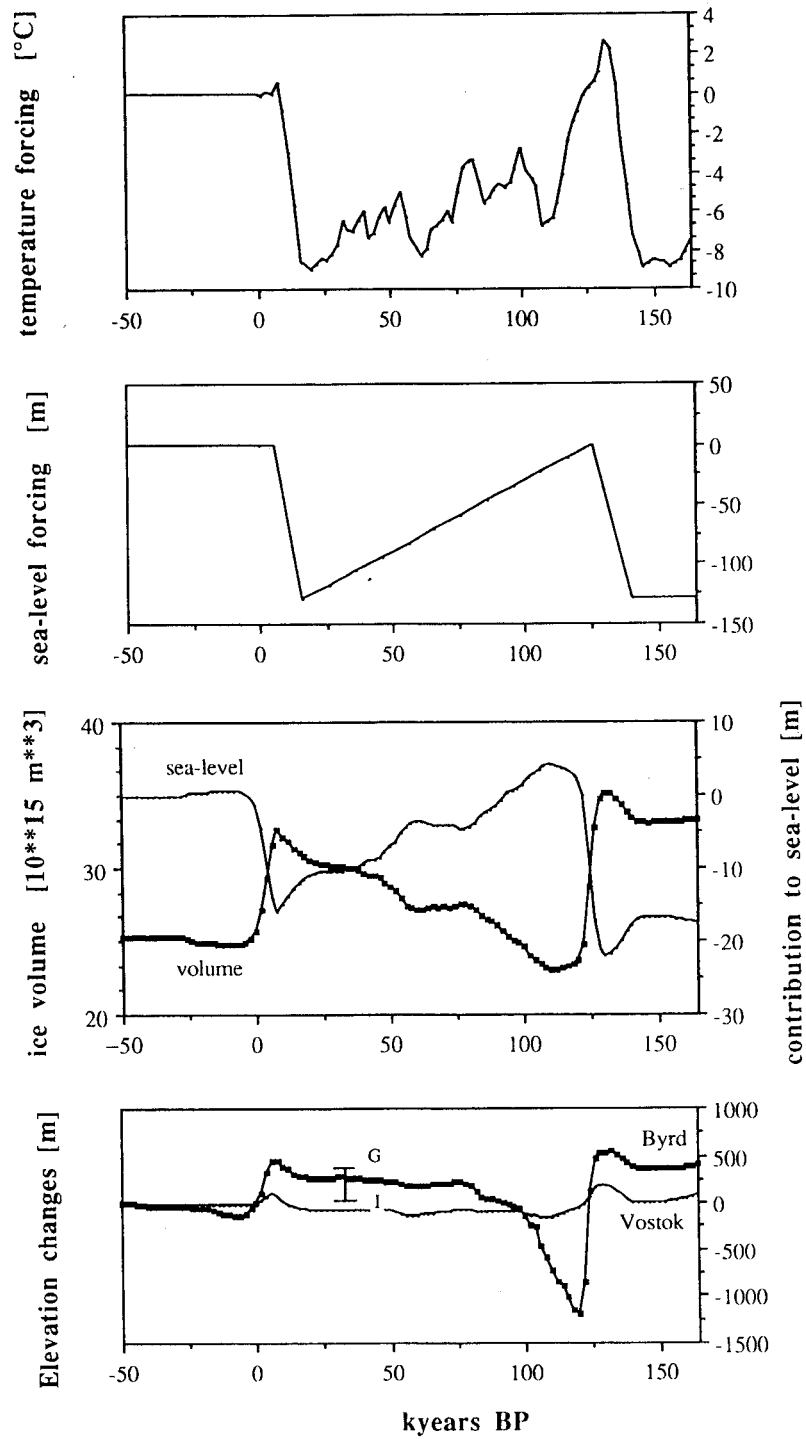
fig.13: Forcing (upper panels) and evolution of some large-scale model variables (lower panels) in the 'standard' model experiment on the last glacial cycle. The vertical bar in the lowest panel refers to the glacial (G) and interglacial (I) steady states at Byrd (80°S, 120°W). The corresponding bars for Vostok (78.5°S, 106.8°E) should be at -9 and -1m, respectively. They are not shown because they almost coincide, which is because of the counteracting effects of changes in accumulation rate and temperature, and to a lesser extent grounding-line movements. The conspicuous 'low' during the Eem should not be taken too literally and may be a model artefact for reasons discussed in the text.

sheet, on the other hand, changes in ice thickness are less pronounced and reflect the combined effects of accumulation and temperature changes much like the fixed-domain studies discussed earlier, onto which a thinning wave caused by postglacial grounding line retreat is superimposed. The thresholds for grounding-line recession are also different for each outlet system. Retreat occurs first in the Totten Glacier area at about 9 ky BP and ends at 6 ky BP. In the Ninnis/Mertz glacier system, retreat starts at 5 ky BP and is finally completed only by 3 ky BP. When the model is run for another 50000 years into the future, it produces an ice sheet virtually identical to the present interglacial reference state.

The overall response of the ice sheet in this experiment is summarized in fig. 13. Displayed are the model forcing functions and the evolution of ice volume and the equivalent sea level changes. Clearly, the dominant forcing is eustatic sea level, and the response is modulated by fluctuations in accumulation rate and ice temperature. Changes in surface altitude are of considerable interest in the interpretation of information from deep ice cores. They are shown in the lower panel for two locations. Typical elevation changes at Vostok station (East Antarctic ice sheet) are generally within 150 m, whereas the modelled fluctuations at Byrd (West Antarctic ice sheet) are substantially larger. These values should not be taken too literally, in particular during the first 50000 years or so which are needed for the model to forget its initial conditions. However, they suggest that the climatic signal recovered at Vostok is probably not biased too much by level fluctuations. The situation for Byrd, on the other hand, is likely to be a lot more complicated because of important changes in the grounded ice domain.

ANTAR
II/04
A

5. RESPONSE TO FUTURE GREENHOUSE WARMING

In a final series of experiments, the question is addressed of how the Antarctic ice sheet may respond to the anticipated greenhouse warming of the earth's atmosphere and results are presented of a tentative calculation of its contribution to world-wide sea levels. Since the inland ice covers an area of about one-thirtieth of the world's oceans, any small imbalance between the total mass accumulated over its surface and the total rate of discharge should have a marked influence. In addition, it has been stressed several times in the literature that the West Antarctic ice sheet, with its bed so far below sea level, could be so inherently unstable that a moderate climate warming may lead to a run-away situation in which the major part of West Antarctica disintegrates in a few centuries time (e.g. Mercer, 1978). Later modelling studies have suggested that this view is probably too dramatic (e.g,. Van der Veen, 1985) and that a sudden collapse in these short time scales is unlikely to happen. Nevertheless, the question of how Antarctica may contribute to changing sea levels is still frequently asked. Here, we will concentrate on the more regular effect of a change in *surface* mass balance.

Greenhouse warming scenario
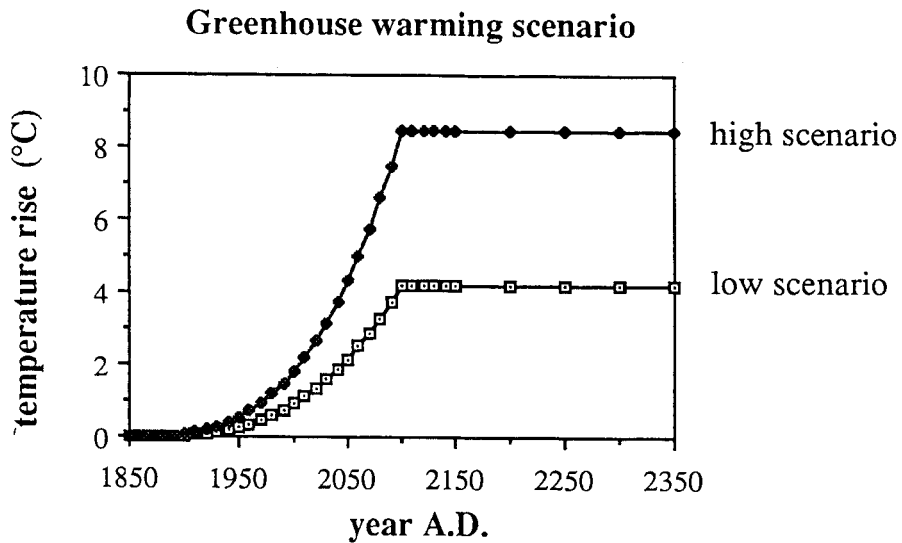
fig.14: The temperature scenario's ('high' and 'low') used to force the mass balance and ice dynamics model. The lower curve is a fit to the 'business-as-usual' scenario of IPCC, the upper curve corresponds to a temperature rise by twice as much.

In order to force the mass balance model, two temperature scenarios are prescribed based on GCM simulations and calculations of time-dependent climatic change. They are shown in fig. 14. The low scenario is simply a fit to the 'business-as-usual' temperature scenario proposed by the IPCC Working Group (Houghton et al., 1990). It predicts that temperature rises by 4.2°C by the year 2100, starting from 1850, which is considered as an undisturbed reference state. The probability that this figure is correct within 1.5°C is estimated to be 67%. The 4.2°C figure applies to the global mean surface temperature, however. In order to take into account the larger temperature rise predicted for polar latitudes, an alternative forcing function will be used in which temperature rises by twice as much (the 'high scenario'). The disagreement produced by the various GCM-simulations does not really allow us to differentiate the greenhouse warming over Antarctica according to location and season. Consequently, in the model experiments temperature perturbations are assumed to be uniform through the year and independent of latitude. Since it is not known what will happen after 2100 AD (given that such a warming occurs in the first place!), temperature forcing is held constant after this date.

In the interpretation of the results, a distinction is made between the 'static effect', which can be studied with the mass balance model solely, and the 'dynamic effect', in which also ice dynamics come into play. Although the modelling experiments on the last glacial cycle suggest that the ice sheet must still be responding to its past mass balance history, this complication is neglected and a stationary ice sheet ('the interglacial reference run') is taken as initial condition. Much of the material presented further below draws on a paper by Huybrechts and Oerlemans (1990).

5.1. Static response

In view of the long response time scales, in particular in the interior of the East Antarctic ice sheet, initially a 'static experiment' is considered, i.e. the present ice-sheet geometry is assumed to be in equilibrium with the velocity field, and changes with respect to the present mass balance are accumulated forward in time. So the velocity field remains unchanged, in effect keeping the amount of ice transported across the grounding line constant. In this calculation, changing surface elevations have been taken into account as a contribution to local temperature changes (although this contribution is very small) and the maximum amount of ice that can melt away is equal to the present ice thickness. The results in terms of equivalent sea-level rise are shown in fig. 15. Since the imposed temperature perturbations are lower or equal to the 8.3 K mark (implying that the mass balance is always larger than at present), the expected increase in ice volume occurs. This is particularly apparent for the low scenario, where the volume increase lowers global sea level by 1.2 cm by the year 2000, 9.1 cm by the year 2100 and up to 41 cm by the year 2350, i.e. 500 years after the onset of the warming. However, a somewhat more complicated response shows up in the high scenario, where the ice volume decreases somewhat around 2100, because the 8.4 °C temperature perturbation just exceeds the 8.3 °C mark a little bit. This effect disappears later because at the edge, where melting rates have gone up to a few meters per year, the total ice thickness has melted away. Obviously, at this stage the assumptions made in this static experiment break down.

ANTAR II/04 A

5.2. Dynamic response

Considering the substantial changes in ice thickness, in particular for the high scenario, the ice sheet is expected to show a dynamical response too. On the plateau this is not the case, and the increased accumulation rates lead to increased ice thicknesses of a few tens of meters at most, without a significant change in the velocity field at all. On the other hand, nearer to the coast and the grounding line the situation becomes quite different, because response times are much shorter here.

Several dynamic processes can be distinguished that result in lower grounded ice volumes compared to the corresponding static run. For the 'low' warming case, the mass balance at first increases everywhere and ice thickening is largest at low elevations. After a while, however, velocities in the lower reaches start to react to this and increase, and ice transport towards the ocean is enhanced. This leads to a thinning, which partly counteracts the thickening caused by increased accumulation. This sucking effect is mainly caused by increased ice-mass discharge on the ice shelves and is apparent along a few gridpoints inland. For a somewhat larger warming the mass balance at lower elevations decreases and eventually surface melting and runoff occur in the most northerly locations. However, the resulting

high scenario
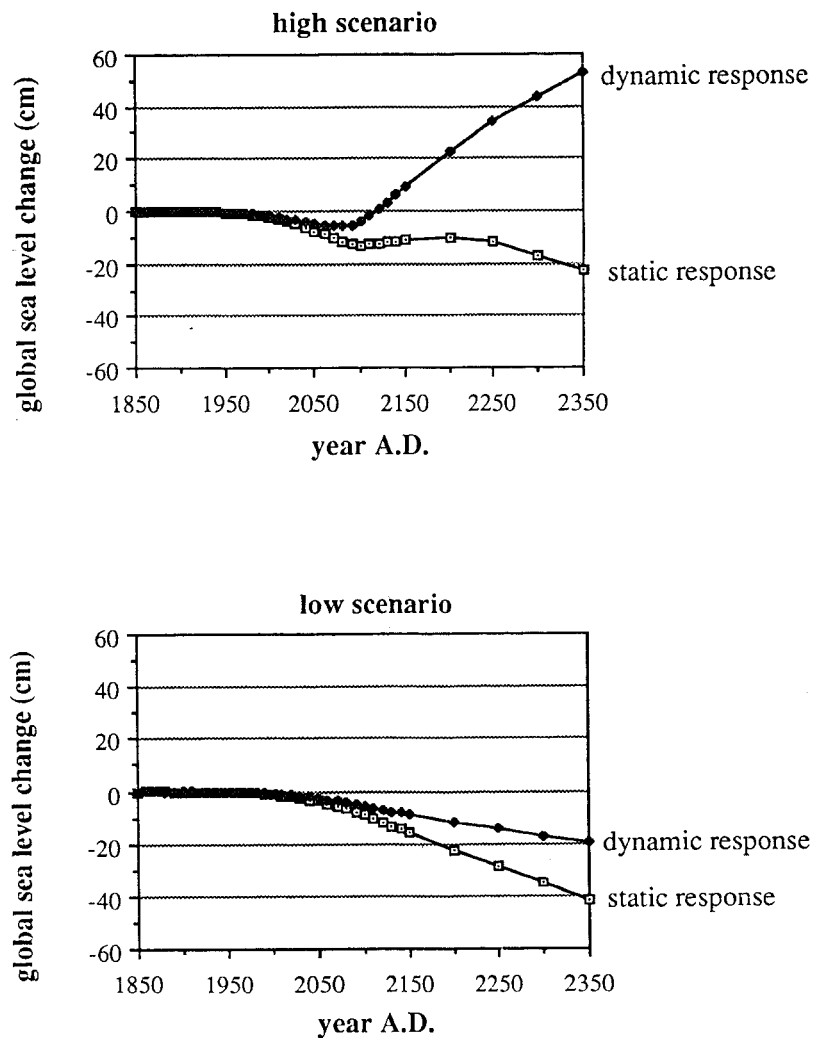
low scenario

fig. 15: Response of the ice sheet expressed in global sea-level changes for the high scenario (upper graph) and the low scenario (lower graph).

change in ice thickness near the grounding line is not large enough to produce significant grounding-line retreat. In summary, initially there is some seaward migration (if there is no melting), followed by a slight recession in some places, but overall the grounded domain does not change its dimensions much.

This is essentially the picture that applies to the low scenario. By 2350 some seaward migration of the grounding line occurs in the most poleward locations (the Ronne-Filchner and Ross ice shelf) and a slight retreat is apparent in the Antarctic Peninsula and along parts of the East-Antarctic coast, in particular between 110 and 150°E. Basically, the net static effect is partially counteracted by an increased ice-mass discharge across the grounding line, and this leads to reduced rates of global sea-level lowering. Compared to the static effect, this

reduction amounts to 18% by 2000, 36% by 2100 and 53% by 2350 (see fig. 15). This increasing fraction reflects the response time scale near and beyond the grounding line. So, from this low greenhouse warming experiment it can be concluded that, as long as the warming is below some 5°C, the Antarctic ice sheet will probably lower global sea level by some tens of centimeters after a few centuries.

As can also be seen from the results shown in fig. 15, the situation becomes quite different for a larger warming. In particular, when this warming exceeds 5-6°C, i.e. after 2060-2070 in the high scenario, thinning at the grounding line becomes larger and significant grounding-line retreat sets in. Viscous spreading of the newly-formed ice shelves then enhances ice-mass discharge from the grounded ice sheet. This has immediate consequences for global sea level and the dynamic effect now becomes dominant, leading to a global sea level *rise* of as much as 0.5 m after 500 years of simulated time. Nevertheless, grounding-line recession is still insignificant along the major ice shelves (Ronne-Filchner and Ross), because, even with a warming of 8.4°C, the number of positive degree-days at these locations is still below 50 and no runoff takes place. The areas where grounding line retreat has taken place by 2500 (when calculations end) are shown in black in fig.16.

ANTAR
II/04
A
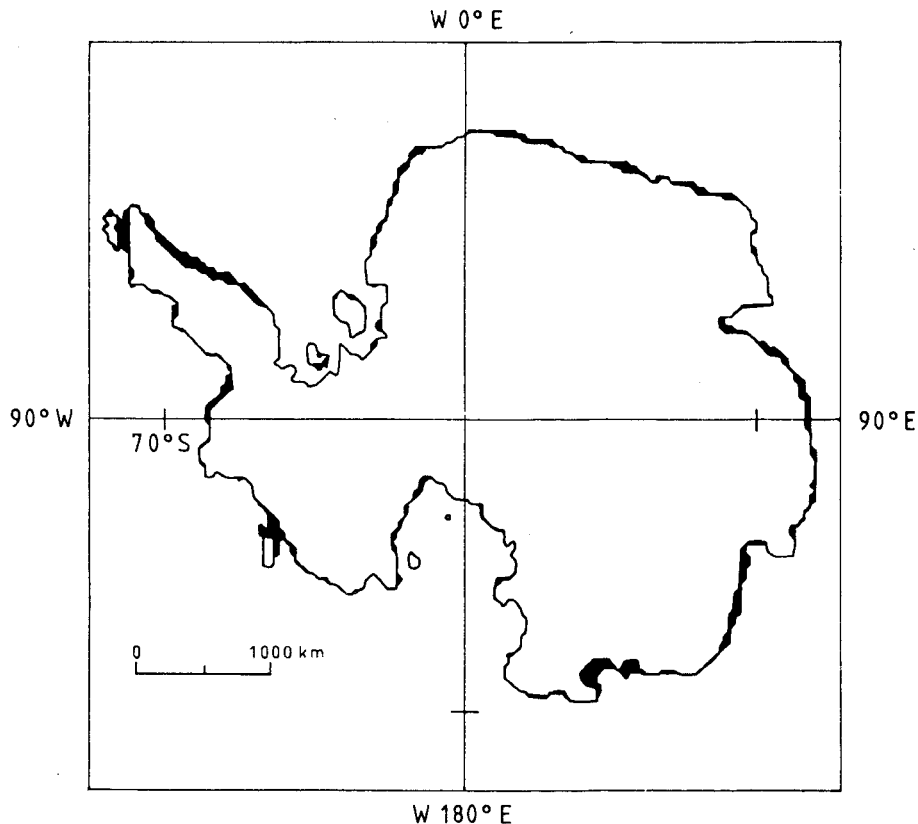
fig. 16: Grounding-line retreat for the 'high scenario' experiment. The black areas indicate where grounded ice has been replaced by ice shelf by the year 2500 (when the integration stops).

5.3. Effect of melting beneath ice shelves

In the experiments discussed above, basal melting beneath ice shelves was not considered. This is simply because it is not known how the oceanic circulation and the heat exchange with the ice shelves will react to higher ocean temperatures following a climatic warming. In the parameterization of the surface mass balance, no surface runoff occurs in the catchment areas feeding the Filchner-Ronne and Ross ice shelves, not even in the rather extreme +8.4°C warming. Thus, it is clear that no significant grounding line retreat occurred there, let alone a catastrophic collapse of the West Antarctic ice sheet (WAIS). Nevertheless, it has been
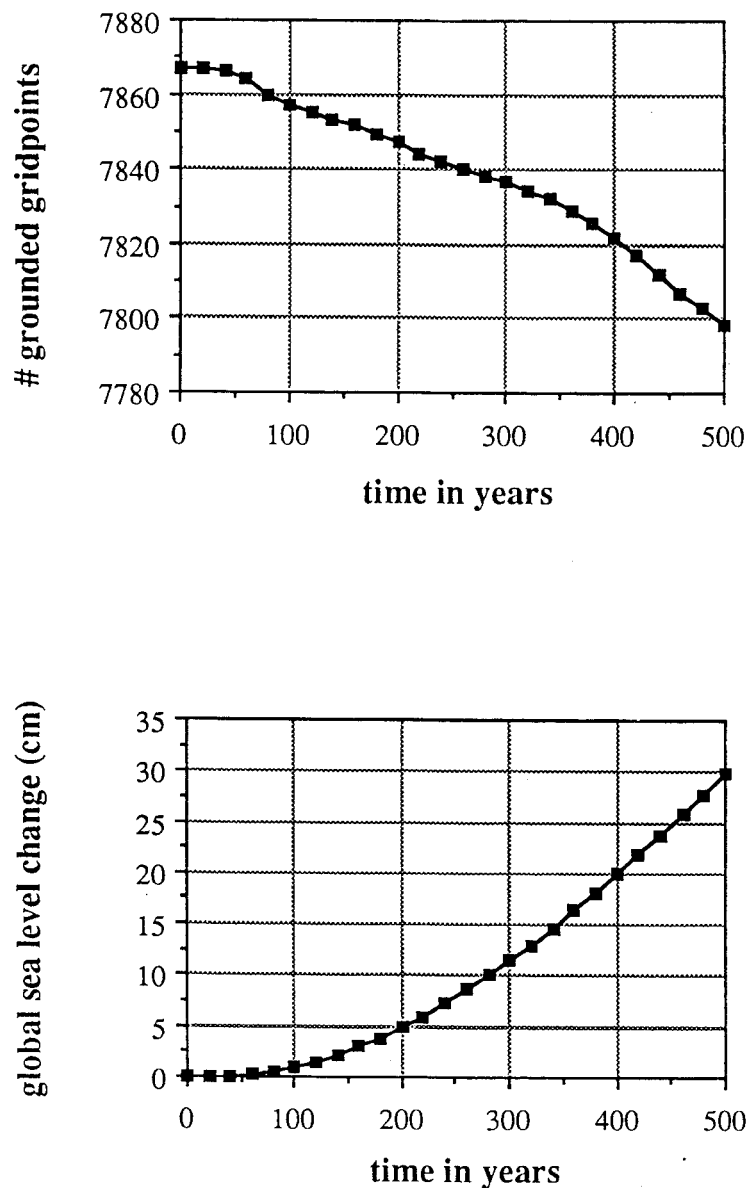
fig. 17: Response of the Antarctic ice sheet to an instantaneously imposed melting rate beneath ice shelves of 1 m/y. According to the model, the area of grounded ice would decrease by less than 1% in 500 years.

suggested by several authors that increased melting could weaken the ice shelves and reduce their buttressing effect, ultimately inducing a collapse of the entire WAIS. To investigate this point somewhat further, a final schematic experiment was performed, in which the mass balance of the ice shelf was reduced stepwise by 1m/y at time zero, while keeping the surface climate fixed. From qualitative reasoning, such an estimate appears to be of a realistic order of magnitude (cf. Bentley, 1984). In this experiment, we were mainly interested in the effect of ice shelf thinning on the grounded ice sheet, and did not consider the possibility of the ice shelf completely breaking up, so that calving could take place at the grounding line.

Results for 500 years of simulated time are summarized in fig. 17. The number of gridpoints with grounded ice and sea-level change are shown. As can be judged from this figure, ice shelf thinning does lead to grounding-line retreat, but the total effect is smaller than the direct surface mass-balance response in the high scenario. For instance, the areas denoted in black on fig.16 correspond to a decrease of the ice sheet domain by 240 gridpoints (compared to 70 in the bottom melting experiment). On the basis of these model results, it can be concluded that a West Antarctic ice sheet collapse on a time scale of half a millenium or so is unlikely to happen. It is also realized, however, that the fast ice streams presently flowing through the ice sheet are not explicitly modelled in this study, and that they could possibly speed up the response under particular circumstances.

ANTAR
II/04
A

6. CONCLUDING REMARKS

In this study, a rather detailed model for the entire Antarctic ice sheet was presented, designed for climatic change experiments. In my opinion, this model represents a well-balanced reflection of our current knowledge of the dynamics of ice sheets and ice shelves, supplemented with mass-balance treatments which are reasonable. When the model is submitted to a varying climatic input, it is then apparently able to account for major characteristics of the Antarctic ice sheet, in present as well as past environments. As such, the model can certainly be considered a useful tool for simulating the ice sheet under a wide range of environmental conditions, and therefore, can aid in our understanding of its fundamental behaviour.

Here, I examined the ice sheet during the last glacial cycle and with respect to future greenhouse warming. During the simulation of the last glacial cycle, I found the model to be most sensitive to changes in sea level, which was the most decisive factor in controlling changes of the ice sheet extent. Changes in accumulation rate and ice temperature were also of some importance, but on the longer time scales (>10 ky), their effects appeared to approximately counteract each other. The role of sea level is particularly interesting given the

difficulties in reconciling the approximate simultaneity of glacial expansion in both hemispheres with the Milankovitch forcing. Consequently, these results support the hypothesis that the Antarctic ice sheet is linked to glacial events on the northern hemisphere continents through changes in eustatic sea level.

In the model, the most pronounced fluctuations occurred in the West Antarctic ice sheet geometry and the Ronne-Filchner ice shelf appeared to be more sensitive to grounding than the Ross ice shelf. On the East Antarctic plateau, on the other hand, changes in surface elevation were found to be generally within 100-150 m. This has wider implications, as it indicates that palaeoclimatic information derived from deep ice cores (Vostok, Dome C) has probably not been biased too much by level fluctuations and, hence, is likely to be essentially of climatic origin.

However, the long response times for grounding-line advance and thermo-mechanical coupling mean that the Antarctic ice sheet did not reach its full glacial extent until 16 ky BP. At this stage, its contribution to the global sea level lowering was some 12 m. This is significantly less than the steady state value of 16 m and certainly less than the 35 m put forward by Nakada and Lambeck (1987). The latter value was obtained as a residual when subtracting equivalent ice volume from fully grown northern hemisphere ice sheets from 130 m of sea-level. This discrepancy could imply that the northern hemisphere ice sheets have contained substantially more ice than currently believed, or, alternatively, that sea level was depressed by less than 130 m.

The satisfactorily simulation of the major features of the Antarctic ice sheet during the last glacial-interglacial cycle may be considered to validate the model. In a final series of experiments, an attempt was therefore made to investigate the possible response of the ice sheet to future greenhouse warming. On the basis of prescribed changes in surface temperature and a simple model for meltwater runoff, these calculations indicate that when the temperature rise is below some 5°C, the Antarctic ice sheet is likely to grow. Moreover, the hypothesis of a catastrophic collapse of the West Antarctic ice sheet, which may lead to a 5 m sea level rise in a few centuries time, is not supported by the model results presented here, even when basal melting beneath ice shelves was taken into account. A similar lack of unstable behaviour was found during a glacial-interglacial transition. Although on the basis of model results in the initializing phase, an interglacial transition of larger amplitude than the last one (16-6 ky) could not be excluded, if the bed under the West Antarctic ice sheet is depressed deeply enough. These results confirm a recent trend in model studies on the stability of West Antarctica, in which the ice sheet-ice shelf system is investigated in an integrated way and in which rapid disintegration is progressively considered unlikely, at least on such a short time-scale.

Nevertheless, in the present study a considerable number of uncertainties remain and the results could still be refined in several ways. The late Holocene deglaciation produced by the model may indicate shortcomings in the description of the ice mechanics. A more detailed treatment of basal sliding and explicit modelling of ice streams could be such 'missing factors' which could potentially speed up the response during a warming climate. Extensive field studies are currently being carried out to study the dynamics of ice streams, and one may hope that improved understanding and modelling will result. In a future development of the model, advantage could then also be taken of numerical nesting techniques in which a denser grid is used in those areas where this is required. These improvements should then enable the model to treat the flow near the grounding line and in the ice shelves in a more accurate way.

Alternatively, also shortcomings in the isostasy model could be responsible for enhancing the delayed deglaciation. Incorporation of a discontinuous, variable rigidity plate and a more accurate treatment of asthenospheric viscous flow may lead to small changes in bed elevation. Future runs could then clarify to what extent the timing and speed of the last deglaciation are a function of the phase lag between the response to sea-level and air temperature (accumulation rate).

ANTAR
II/04
A

However, much of the uncertainty concerning the numerical results probably arises from imperfections in the environmental forcing. For instance, a better quality record for global sea level depression, especially during the final stages of the Wisconsin, may yield a somewhat different maximum glacier stand, especially in the Ross Sea. Also, the model may be used in an iterative fashion to date the Vostok temperature record more precisely and correct for shifts in surface elevation. In this respect, particle trajectories and ice age-depth profiles could easily be constructed, even in a transient situation.

With respect to a significant warming, the formulation of the melting/run-off process can certainly be improved, and here much information can be taken from energy balance/ mass balance studies in other parts of the world (Greenland in particular). Also the effects of a warming on the oceanic circulation and melting rates beneath ice shelves are not really known. A similar remark applies to changes in the accumulation distribution resulting from potential changes in the atmospheric circulation pattern and possibly, from changes in snow drift and surface sublimation. Nevertheless, in spite of the fact that our knowledge appears still inadequate in many respects, I have no firm reasons to believe that these refinements would influence the basic model outcome in the sense that the results would become entirely different.

ACKNOWLEDGEMENTS

REFERENCES

Ambach, W. (1963): Untersuchungen zum Energieumsatz in der Ablationszone des Grönlandischen Inlandeises, Meddelelser om Grønland 174(4),311p.

Ambach, W. (1968): Ein Beitrag zur Kenntnis des Wärmehaushaltes des Grönlandischen Inlandeises. Vorlaufige Ergebnisse, EGIG 1967, Polarforschung VI, 18-23.

Bentley, C.R. (1984): Some aspects of the cryosphere and its role in climatic change, in: J.E. Hansen (ed.): Climate processes and climate sensitivity, Geophys.Monogr. 29, AGU (Washington D.C.), 207-220.

Bindschadler, R. (1983): The importance of pressurized subglacial water in separation and sliding at the glacier bed, J.Glaciol. 29 (101), 3-19.

Blatter, H. and G. Kappenberger (1988): Mass balance and thermal regime of Laika ice cap, Coburg Island, N.W.T., Canada, J. Glaciol. 34, 102-110.

Braithwaite, R. and O.B. Olesen (1989): Calculation of glacier ablation from air temperature, West Greenland, in: J. Oerlemans (ed.), Glacier fluctuations and climatic change, Kluwer Academic Publishers, 219-233.

Brotchie, J.F. and R. Silvester (1969): On crustal flexure, J.Geophys.Res. 74 (22), 5240-5252.

Budd, W.F.; M.J. Corry and T.H. Jacka (1982): Results from the Amery ice shelf project, Ann.Glaciol. 3, 36-41.

Budd, W.F.; D. Jenssen and I.N. Smith (1984): A three-dimensional time-dependent model of the West Antarctic ice sheet, Ann.Glaciol. 5, 29-36.

Chapell, J. and N.J. Shackleton (1986): Oxygen isotopes and sea level, Nature 324, 137-140.

Denton, G.H. and T.J. Hughes (eds) (1981): The last great ice sheets, John Wiley (New York), 485 p.

Drewry, D.J. (ed.) (1983): Antarctic glaciological and geophysical folio, Scott Polar Research Institute (Cambridge).

Drewry, D.J.; S.R. Jordan and E. Jankowski (1982): Measured properties of the Antarctic ice sheet: surface configuration, ice thickness, volume and bedrock characteristics, Ann.Glaciol. 3, 83-91.

Fortuin, J.P.F. and J.Oerlemans (1990): Parameterization of the annual surface temperature and mass balance of Antarctica, Ann. Glaciol. 14, 78-84.

Greishar, L. and C.R. Bentley (1980): Isostatic equilibrium grounding line between the West Antarctic inland ice sheet and the Ross ice shelf, Nature 283, 651-654.

Herrod, L.D.B. (1986): Sea-bottom topography beneath Ronne ice shelf, Antarctica, Filchner Ronne Ice Shelf Program Report no. 3, Alfred Wegener Institut (Bremerhaven), 72-80.

Herterich, K. (1987): On the flow within the transition zone between ice sheet and ice shelf, in: Van der Veen, C.J. and J. Oerlemans (eds): Dynamics of the West Antarctic ice

ANTAR
II/04
A

sheet, D. Reidel (Dordrecht), 185-202.

Hollin, J.T. (1962): On the glacial history of Antarctica, J.Glaciol. 4 (32), 173-195.

Houghton, J.T.; G.J. Jenkins and J.J. Ephraums (1990): Climate change: The IPCC scientific assessment, Cambridge University Press, 365p.

Hutter, K. (1983): Theoretical glaciology, D. Reidel (Dordrecht), 510 p.

Huybrechts, Ph. (1986): A three-dimensional time-dependent numerical model for polar ice sheets: some basic testing with a stable and efficient finite difference scheme, Geografisch Instituut VUB Report 86-1, 39 p.

Huybrechts, Ph. and J. Oerlemans (1988): Evolution of the East-Antarctic ice sheet: a numerical study on thermo-mechanical response patterns with changing climate, Ann. Glaciol. 11, 52-59.

Huybrechts, Ph. (1990a): The Antarctic ice sheet during the last glacial-interglacial cycle: a three-dimensional experiment, Ann. Glaciol. 14, 115-119.

Huybrechts, Ph. (1990b): A 3-D model for the Antarctic ice sheet: a sensitivity study on the glacial-interglacial contrast, Clim. Dyn.5, 79-92.

Huybrechts, Ph. and J. Oerlemans (1990): Response of the Antarctic ice sheet to future greenhouse warming, Clim. Dyn.5, 93-102.

Huybrechts, Ph.; A. Letreguilly and N. Reeh (1991): The Greenland ice sheet and greenhouse warming, Palaeogeog. Palaeoclim. Palaeoecol.(Global and Planetary Change Section) 89, 399-412.

Huybrechts, Ph. (1992): The Antarctic ice sheet and environmental change: a three-dimensional modelling study, Berichte zur Polarforschung 99, 241p.

Jenkins, A. and C.S.M. Doake (1991): Ice-ocean interaction on Ronne Ice Shelf, Antarctica, J. Geophys. Res. 96 (C1), 791-813.

Jenssen, D. (1977): A three-dimensional polar ice sheet model, J.Glaciol. 18 (80), 373-389.

Jouzel, J. and L. Merlivat (1984): Deuterium and oxygen 18 in precipitation: modelling of the isotopic effects during snow formation, J.Geophys.Res. 89 (D7), 11749-11757.

Jouzel, J.; C. Lorius, J.R. Petit; C. Genthon; N.I. Barkov; V.M. Kotlyakov and V.M. Petrov (1987): Vostok ice core: a continuous isotope temperature record over the last climatic cycle (160.000 years), Nature 329, 403-408.

Lorius, C.; J. Jouzel; C. Ritz, L. Merlivat; N.I. Barkov; Y.S. Korotkevich and V.M. Kotlyakov (1985), A 150.000-year climatic record from Antarctic ice, Nature 316, 591-596.

McMeeking, R.M. and R.E. Johnson (1985): On the analysis of longitudinal stress in glaciers, J.Glaciol 31 (109), 293-302.

Mercer, J.H. (1978): West Antarctic ice sheet and CO_2 greenhouse effect: a threat of disaster, Nature 271, 321-325.

Mitchell, A.R. and D.F. Griffiths (1980): The finite difference method in partial differential equations, John Wiley (Chichester), 272 p.

Nakada, M. and K. Lambeck (1988): The melting history of the late Pleistocene Antarctic ice sheet, Nature 333, 36-40.

Nye, J.F. (1969): The effect of longitudinal stress on the shear stress at the base of an ice sheet, J.Glaciol. 8 (53), 207-213.

Oerlemans, J. and C.J. Van der Veen (1984): Ice sheets and climate, D.Reidel (Dordrecht), 217 p.

Orvig, S. (ed.) (1970): Climates of the polar regions, World Survey of Climatology 14, Elsevier (Amsterdam), 370 p.

Oswald, G.K.A. and G.de Q. Robin (1973): Lakes beneath the Antarctic ice sheet, Nature 245, 251-254.

Paterson, W.S.B. (1981): The physics of glaciers 2nd edition, Pergamon Press (Oxford), 380 p.

Pfeffer, W.T.; T.H. Illangasekare and M.F. Meier (1990): Analysis and modelling of meltwater refreezing in dry snow, J. Glaciol. 36 (123), 238-246.

Robin, G. de Q. (1977): Ice cores and climatic change, Phil.Trans.R.Soc.London Ser.B 280, 143-168.

Robin, G. de Q.; C.S.M. Doake; H. Kohnen; R.D. Crabtree; S.J. Jordan and D. Möller (1983): Regime of the Filchner-Ronne ice shelves, Antarctica, Nature 302, 582-586.

Sclater, J.G.; C. Jaupart and D. Galson (1980): The heat flow through oceanic and continental crust and the heat loss of the earth, Rev.Geophys. Space Phys. 18, 289-311.

Shackleton, N.J. (1987): Oxygen isotopes, ice volume and sea level, Quat.Science Rev. 6, 183-190.

Thomas, R.H. (1973): The creep of ice shelves, J.Glaciol. 12 (64), 45-53.

Thomas, R.H.; D.R. MacAyeal; D.H. Eilers and D.R. Gaylord (1984): Glaciological studies on the Ross ice shelf, Antarctica, 1973-1978, in: Bentley, C.R. and D.E. Hayes (eds): The Ross ice shelf: Glaciology and geophysics, Antarctic Research Series 42, 21-53.

Turcotte, D.L. and G. Schubert (1982): Geodynamics. John Wiley (New York) 440 p.

Van der Veen, C.J. (1985): Response of a marine ice sheet to changes at the grounding line, Quat.Res. 24, 257-267.

Van der Veen, C.J. (1987): Longitudinal stresses and basal sliding: a comparative study, in: C.J. Van der Veen and J. Oerlemans (eds): Dynamics of the West Antarctic ice sheet, D. Reidel (Dordrecht), 223-248.

Weertman, J. (1964): The theory of glacier sliding, J.Glaciol. 5(39), 287-303.

Whillans, I.M.; Y.H. Chen; C.J. Van der Veen and T.J. Hughes (1989): Force budget: III. Application to three-dimensional flow of Byrd Glacier, Antarctica, J.Glaciol. 35 (119), 68-80.

Yiou, F.; G.M. Raisbeck, D. Bowles, C. Lorius and N.I. Barkov (1985): [10]Be in ice at Vostok Antarctica during the last climatic cycle, Nature 316, 616-617.

ICE DYNAMICAL STUDIES IN THE SØR RONDANE MOUNTAINS, DRONNING MAUD LAND EAST ANTARCTICA

F. Pattyn, H. Decleir
and Ph. Huybrechts

TABLE OF CONTENTS

ABSTRACT

On the basis of field work carried out during three antarctic summer seasons, -in collaboration with the Japanese Antarctic Research Expedition (JARE)-, and by means of both Landsat TM and SPOT satellite imagery, we present a quantitative and qualitative picture of the glacier characteristics and subglacial relief of the Central Part of the Sør Rondane area, Dronning Maud Land, Antarctica. The quantitative data are then used in a model to simulate both the present and the past glacier behaviour.

For this purpose we describe first the mass balance and temperature regime of the area as a function of elevation. The mass balance is derived from previous Belgian work in the same area, while the temperature regime was taken from a parameterization of Fortuin and Oerlemans. Arguments to use this parameterization was found by studying the brightness temperatures of the snow surface (from Landsat TM thermal red band) which displays also a twofold temperature gradient as found by these authors. The map of ice surface characteristics, based on field work and on an interpretation of a colour composite, combining SPOT channels XS1, SXS2 and XS3, allows a distinction to be made between active and passive glaciers and to identify the upper region of the Sør Rondane area as en ablation island.

On the basis of movement stakes, surveyed during two consecutive seasons, the velocity field and dynamical aspects of Jenningsbreen could be determined. It was shown how this glacier is in the process of being cutoff from the main ice supply. The resulting negative divergence of the horizontal velocity field explains the vertical movement necessary for the emergence at the glacier surface of englacial debris to form the extensive supraglacial tills. Ice thickness measurements were carried out using the radio echo sounding and gravimeter technique during three field seasons. The results are presented as maps of subglacial relief, revealing the central part of the Sør Rondane as an ice covered fjord landscape. The characteristic U-shaped valley cross-profiles originated by widening and deepening of an inherited coastal mountain fluvial drainage pattern.

A flow line model was then developed to simulate the behaviour of the outletglaciers of the Sør Rondane. The nearly stagnant character of Jenningsbreen was confirmed. It is shown how the present ablational character of the Sør Rondane is in equilibrium with the glacier dynamics. A significant greater ablation is required to produce deglaciation in this area.

The simulation of the Last Glacial Maximum shows a very modest increase in elevation and advancement of the ice sheet. In the mountains this explains a 200-400 m ice surface increase. Glacio-geological findings, which refer to a higher glacier stand, must then be brought back to events prior to the LGM and witness much wetter, probably Late Cenozoic, environmental conditions.

ANTAR
II/04
B

1. INTRODUCTION

Ice free areas, form a window in the thick ice sheet cover of Antarctica through which important glacio-geological evidences can be observed with respect to the history of environmental change of this continent. Occupying 2 % of the Antarctic territory, two types of ice free areas can be recognized. The first are the low lying coastal oases (e.g. Bunger Oasis, Vestfold Hills ...) which are due to a recent (Holocene) ice sheet retreat and to related isostatical crustal rebound : they are characterized by a distinct ablation area covered with ground moraine, elevated marine terraces, fresh and saline lakes etc. ...

The second type consists of the ice free areas of the marginal mountains of Antarctica. These mountains protrude through the ice surface because of the lowering of the ice sheet near its margin and dam the ice flow from the interior. Some glaciers however manage to cut their way through the mountain range, so called outlet glaciers, dividing the range in different blocks. Due to a lowering of the ice surface of the inland ice sheet and/or uplift of the mountains, some of the valleys have become severed from the ice supply of the interior and became ice free. The waxing and waning of the Antarctic ice sheet has left both erosional and depositional features in this area and this since a very long time. The physiography is therefore polycyclic in character but it shows at present all the characteristics of a cold and arid environment.

The reconstruction of the paleogeography of these ice free areas at different moments in the past -of the glaciations and deglaciations- is clearly of importance in unravelling the history of the Antarctic ice sheet.

ANTAR II/04 B

In this paper we will report on the present glaciological conditions in the Sør Rondane Mountains, Dronning Maud Land, Antarctica and try to simulate the present and past behaviour of the outlet glaciers with respect to the geomorphological and geological findings. The work, reported here, summarizes our contribution with respect to the dynamics of the glaciers in the Sør Rondane of phase II of the Belgian Programme on Antarctic Research, organized by the Science Policy Office. It presents some new observational evidences and interpretations based on field work and remote sensing in addition to the already published work by Pattyn et al. (1992) and Pattyn and Decleir (1992).

2. THE MASS BALANCE OF THE SØR RONDANE AREA

The east-west lying Sør Rondane Mountains dam the main ice flow coming from the polar plateau (Fig.1) and reduce considerably the mass flux towards the coast.
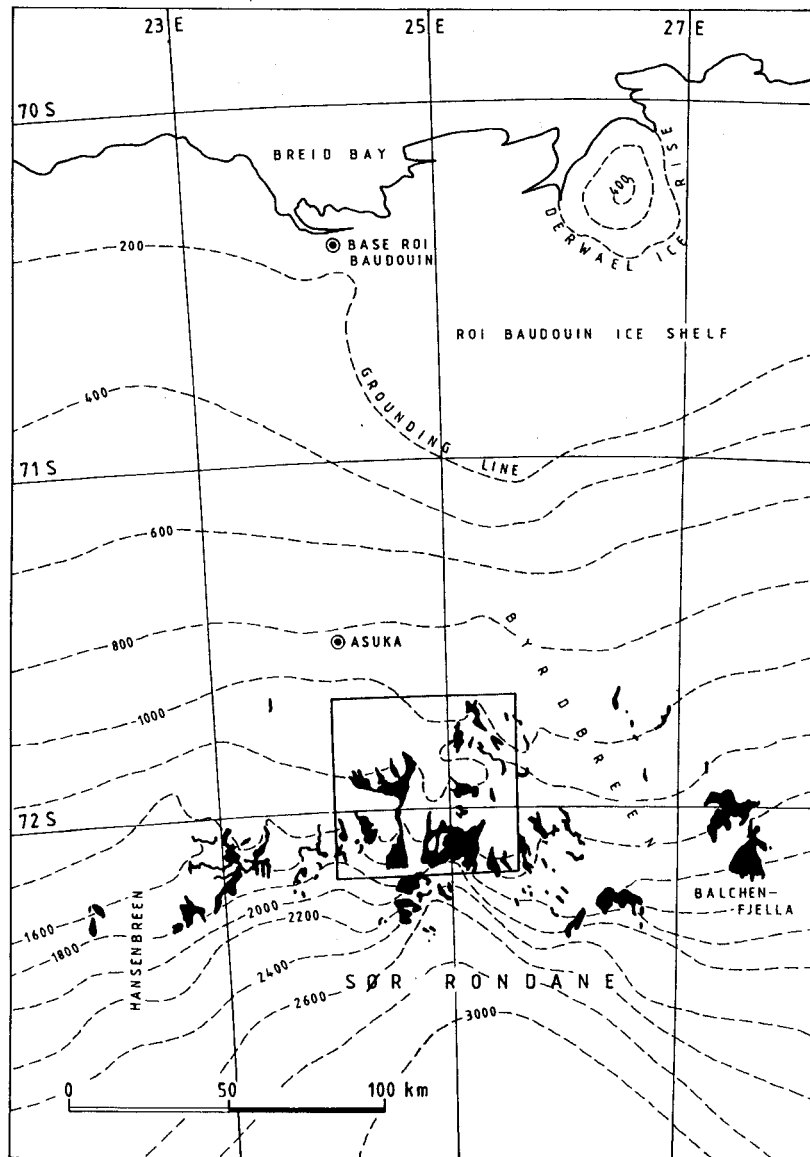
Fig.1: Situation Map of the Sør Rondane and contiguous coastal ice shelf area (Roi Baudouin ice shelf). The quadrangle shows the "Central Part" of the Sør Rondane.

The ice flow is channelled in different outlet glaciers through the range. The total ice discharge, assuming a density of 917 kg/m^3, amounts to 1.76 km^3/a (after Van Autenboer and Decleir (1974, 1978)) but corrected for a probable underestimation of 10 % (Decleir et al, 1989). This amounts to a mean mass flux (defined here as the discharge of ice per km) of 0.01 km^2/a, calculated over the 180 km long northern boundary of the range. This mass flux is very low as compared to the mean mass flux for Antarctica as a whole (0.15 km^2 /a). The mass flux of the ice shelf at the coast is much larger than the 0.01 km^2/a flux through the mountains. By comparing the coastal configurations on a 1937 and 1960 map, Van Autenboer (1964) estimated

the ice shelf velocities at about 300m/a. This value agrees with the results (velocities ranging between 250 and 300m/a) from the repeated survey (1965/67) of a geodetic network spanning the area between Base Roi Baudouin and Derwael Ice Rise (Derwael, pers. comm.).
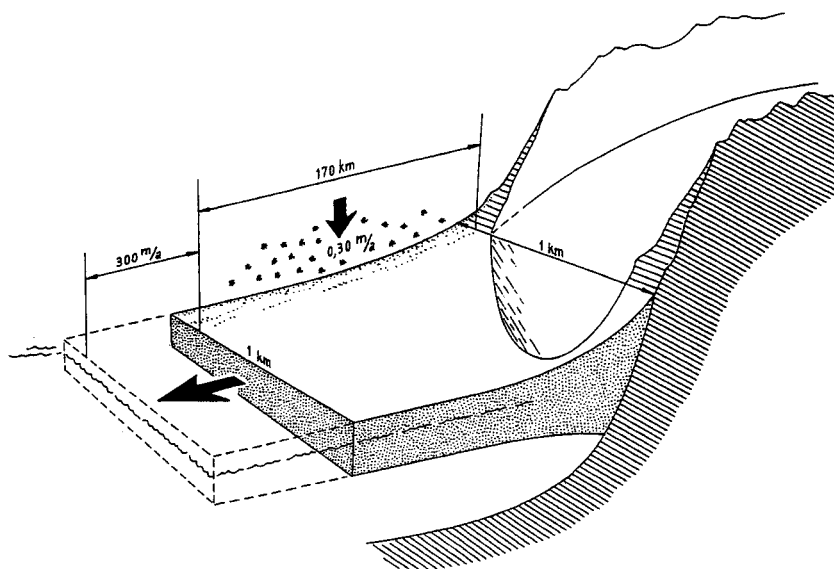
Fig.2: Schematic representation of the mass balance calculation of the Roi Baudouin ice shelf. From the right is the influx from the outlet glaciers of the Sør Rondane. The ice shelf loses mass through calving. The horizontal mass divergence is compensated by the positive accumulation over the area.

Assuming a mean frontal ice thickness of 200 m a mean mass flux of 0.06 km^2/a is inferred. This leaves us with a horizontal mass divergence of 0.06 - 0.01 = 0.05 km^2/a, which -in case of equilibrium- must be compensated by a mean net mass accumulation of 0.30 m/a of ice over the 170 km inland ice slope and ice shelf. It suggests a relatively independent existence of the ice shelf (Fig.2).

The areal distribution of the mass balance is however difficult to assess. A net accumulation of 0.43 - 0.50 m/a of ice was measured at Base Roi Baudouin (situated at an altitude of 37 m a.s.l. on the ice shelf, 12 km from the coast) by drilling (Tongiorgi et al, 1961) and from stake measurements (De Breuck, 1961). A few km further to the South, on the first slope beyond the grounding line, a higher accumulation of 0.67 m/a was measured as should be expected in this area where the snow precipitation is mainly caused by cyclonic activity. Further inland on the regular rising inland ice slope -away from the moist bringing source- both Belgian and Japanese stake measurements indicate a rapid decrease of the mass balance to reach a few cm at the foot of the Sør Rondane at an altitude of 1000 m. For the model calculations we will assume -below 1000 m- a linear decrease of the mass balance M with altitude z.

$$M = 0.50 - 0.00025 \, z \qquad z < 1000 \, m$$

which results in an average mass balance of 0.37 m/a over the 170 km inland ice slope, a figure which is to be compared with the 0.30 m/a estimated from the mass balance divergence. The discrepancy is probably due to the linear assumption, but it should also be mentioned that Nishio at al (1970) estimated, on the basis of a more recent hydrographic survey, much lower ice shelf velocities and a discharge which exceeds the one through the mountains by a factor of two only. Further inland, beyond the mountains, an exponential decrease -typical for cold polar deserts- was assumed

$$M = 0.687 \exp(-0.000106 \, z) \qquad z \geq 1000 \, m$$
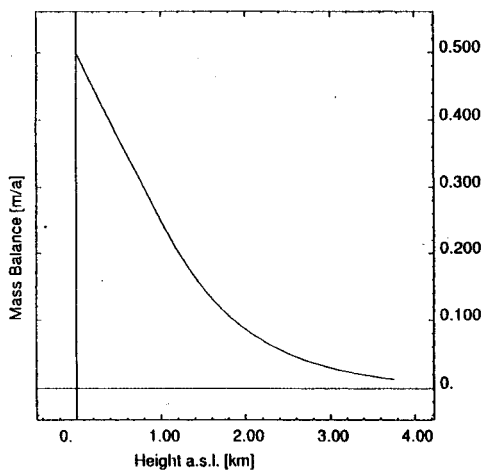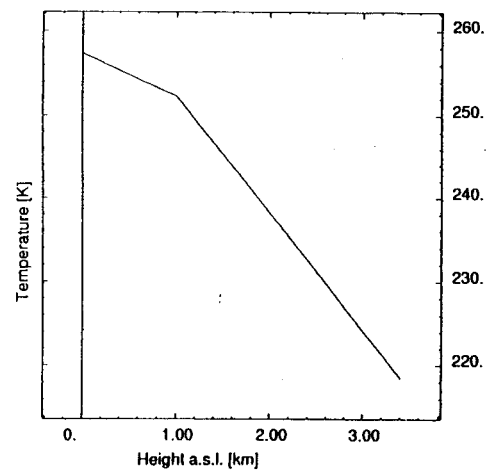
Fig.3a   Fig.3b

Fig.3: Adopted mass balance (Fig.3a) and temperature (Fig.3b) parameterization as a function of height.

producing a mass balance of 0.01 m/a at an altitude of 4000 m. Fig.3a shows the complete parameterization of the mass balance.

3. THE TEMPERATURE REGIME OF THE SØR RONDANE AREA

In Antarctica, the temperature decrease with latitude parallells the decrease with altitude resulting in a very strong correlation of temperature with elevation. Based on a multiple regression analysis, Fortuin and Oerlemans (1990) found a lapse rate "along the surface" of -14.3 K/km

for the "interior region" of Antarctica (z ≥ 1500 m) and - 5.1 K/km in the "escarpment region" (200 m ≤ z < 1500 m).

The Sør Rondane, where the glaciers descend from an altitude of 2000 m to reach 1000 m at the foot of the mountains, separates the "interior region" from the inland ice slope ("escarpment region"). Base Roi Baudouin, the Belgian station which was situated on the ice shelf, is representative for the northern margin of the inland ice slope and has a mean temperature of -15.3°C

Surface temperature from Landsat TM data

The Earth Resource satellite Landsat Thematic Mapper has the ability to image the earth at high resolution (30m) and in different wavelength regions, ranging from th visible up to the thermal infrared). In the temperature range from 0 to -25 ° C the terrestrial radiation is strongest between 9 μm and 14 μm with a maximum around 11 μm. This maximum is covered by Thematic

Mapper band 6 (TM6) (10.40 - 12.50 μm) and lies in the atmospheric window with reduced atmospheric absorption so that this band effectively records relative ground temperatures. Singh (1988) proposes an accurate algorithm for converting TM6 digital numbers into brightness temperatures. This relation is given by

$$T = \frac{b}{\ln(L\lambda) - a} \quad \text{and} \quad L\lambda = (L_{max} - L_{min})\frac{DN}{255} + L_{min}$$

where T is the brightness temperature (K) and $L\lambda$ the spectral radiance ($mWcm^{-2} sr^{-1} \mu m^{-1}$). For a radiance between 0.19968 and 0.48350 (220 ≤ T ≤ 260) values of a and b are 4.1368 and - 1264.63 respectively. At higher spectral radiances (between 0.48350 and 0.92949), values of a and b equal 4.1754 and - 1274.674 respectively (Singh, 1988). L_{max} = 1.55996 and L_{min} = 0.12378 are the maximum and minimum spectral radiance resp. and read from the header file supplied with the image on the Computer Compatible Tapes. DN is a digital number ranging from 0 to 255 and corresponding to L_{min} and L_{max}.

The algorithm was then applied to a TM image of the central part of the Sør Rondane, resulting in a map of surface brightness temperatures (Fig.4). The brightness temperatures range from - 32° C on the highest parts of the plateau (2600 m a.s.l.) up to + 8° C on the rocks and nunataks. The brightness temperatures decrease with increasing elevation and depend on both the reflectivity of the material and the incidence angle of the sun. The highest temperatures are therefore found on the low reflectance zones, such as rock outcrops and bare ice zones. The lowest temperatures are related to snow cover of the highest part of the plateau.

Fig 4. also highlights the damming effect of the Sør Rondane Mountains upon the main ice stream from the polar plateau : it shows the very high and hence cold surfaces south of the mountain range and the rapid increase in temperature as the glaciers cut through the range, which is associated with a lowering of the ice surface and a change from snow cover to bare ice due to the oasis effect.

In order to calculate real surface temperatures one should retain only thermal radiances of one textural unit defined by constant albedo. This was carried out by extracting only brightness temperatures of the snow surface by an overlay operation between a classified TM image, displaying snow and ice cover and a TM6 image of the same region. For 68 pixels on the snow surface terrain heights were extracted from a topographic map, and a relation established between surface topography and brightness temperature (Fig.5).
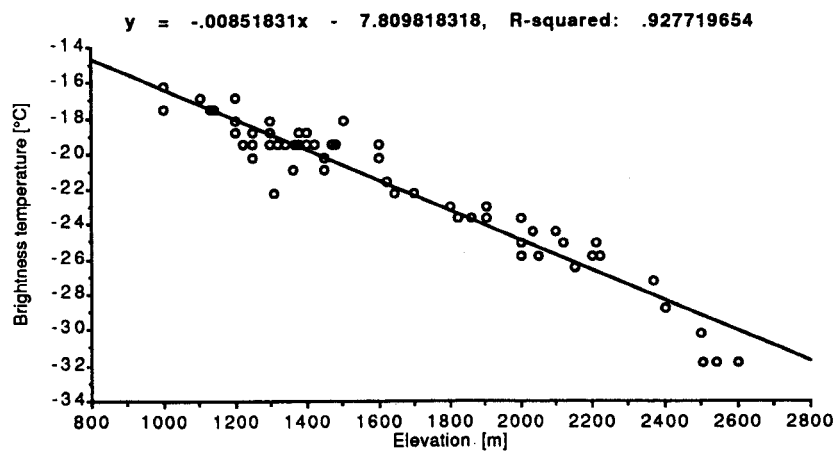
Fig.5: Linear relationship and correlation between brightness temperatures of the snow cover and elevation.

The linear regression line shows a mean temperature gradient of - 8.5° C/km with a temperature of - 7.8° C at sea level.

Two Japanese stations (one field station SS100 situated 520 km southeast of the study area at 3005 m a.s.l. and Asuka station situated 60 km north of the Sør Rondane at 965 m a.s.l.) measured at least twice daily the air temperature above the snow surface at the time the Landsat TM image was recorded (3.12.86 at 6h07m UT). Temperatures at Asuka and SS100 amounted to -8.5 and -25.0° C respectively. Relating these temperatures linearly to elevation, one obtains a temperature gradient of - 8.1° C/km, which is in accord with the TM6 brightness temperature gradient of - 8.5°C/km. We can conclude that the TM6 thermal infrared band effectively records relative ground temperatures. Nevertheless a large offset (9° C) exists between the measured surface temperatures and the TM6 brightness temperatures, probably attributed to atmospheric

conditions and illumination-angle. Applying the linear regression analysis on the TM6 data for an elevation zone of 900-1500 m (northern part of the area and covering partly the inland slope area) and the zone 1500-2600 in (southern part of the area and covering partly the interior area) we find temperatures gradients of -6.4° C/km and -10.3° C/km respectively. Although one cannot conclude to the correctness of the results of Fortuin and Oerlemans (-5.1 K/km and -14.3K/km) from our measurements which strictly apply to a particular time at a particular day, the satellite measurements underscore the existence of two different temperature regimes, as pointed out by Fortuin and Oerlemans (1990).

Adopted Temperature Regime

For the model calculation is this paper we will assume, below 1000 m

$$T = 257.4 - 0.0051 \qquad \text{for } z < 1000 \text{ m}$$

with z in m, T in K where the lapse rate is taken from Fortuin and Oerlemans (1990) and the sealevel temperature adapted to the mean temperature at Base Roi Baudouin, which results in an acceptable temperate regime for the Asuka Station (t = -20.5° C)

Further inland, the linear decrease in temperature is much reduced and, again taking the lapse rate from Fortuin and Oerlemans (1990), we find

$$T = 266.4 - 0.0143 \, z \qquad \text{for } z \geq 1000 \text{ m}$$

ANTAR
II/04
B

The adapted temperate profile is shown in Fig.3b.

4. THE SURFACE CHARACTERISTICS OF THE CENTRAL PART OF THE SØR RONDANE

It has already been said that the Sør Rondane impede the ice discharge from the polar plateau, imposing a divergent flow pattern south of the range. This is also apparent from the fact that the two large glaciers which traverse the Sør Rondane (Byrdbreen and Hansenbreen) are also situated at the eastern and western margin resp. of the range (Fig.1), underscoring the damming effect of the Central Part. We will now concentrate on the glacial characteristics of this Central Part.
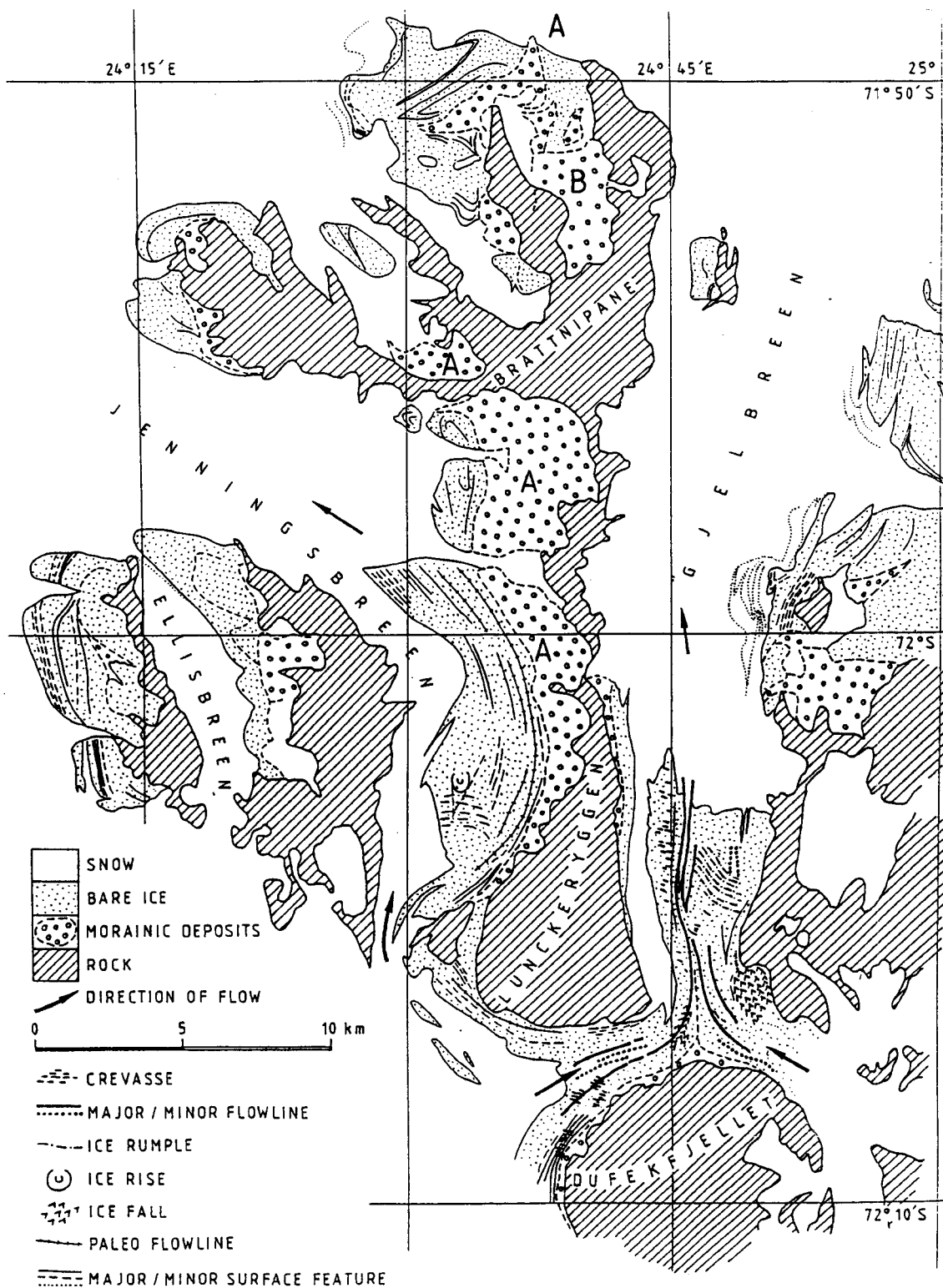
Fig.6: Map of surface characteristics of the ice and snow derived from SPOT imagery. Note the large surface covered by bare ice un Upper Jennings- and Gjelbreen. A and B indicate where the moraine deposits occur on ice or on bedrock resp.

Ice Surface characteristics from Satellite Imagery

The Central part is characterized by steep topographic slopes, dry valleys, local glaciers, and two outlet glaciers,Gjelbreen and Jenningsbreen.

Although the European SPOT satellite lacks, as compared to the Landsat -5 Thematic Mapper, the infrared emissive bands, it reveals, due to the larger pixel resolution (20 m in multispectral mode ; 10 m in panchromatic mode) much information on the glacier surface and bare ice areas. The reflections on the bare ice surface reveal details not visible on aerial photographs nor in multispectral composition of Landsat TM images. On the basis of a visual interpretation of a colour composite combining SPOT multispectral channels XS1, XS2 and XS3, a glaciological map of the Sør Rondane was created (Fig.6), displaying the surface characteristics of the Jennings- and Gjel-Glacier. Four main classes were identified on the visual image : snow, bare rock, bare ice and morainic deposits.

The **bare rock** consists of steep slopes, flat topped ridges -at intermediate level (a few hundred meters above the ice surface)- pyramidal peaks and sharp ridges at higher level and a few north-south trending dry valleys. The **moraine deposits** consist of supraglacial deposits (marked "A" on the map, Fig.6) on the one hand and tills covering the slopes adjacent to the present glacier (marked "B") on the other hand.

The **supraglacial tills** exist mainly as lateral moraines and occur extensively on the eastern side of Jenningsbreen. The ridges at the outer margin (the "glacier side") of these moraine fields cover approximately 500 m thick ice and are well aligned according to the flow lines. Very often they can be traced back glacier-upwards to well marked spurs, where the debris originate supraglacially from slope erosion.

ANTAR
II/04
B

: Shear zone   : Englacial debris
   : Hummocky moraine   : Active glacier
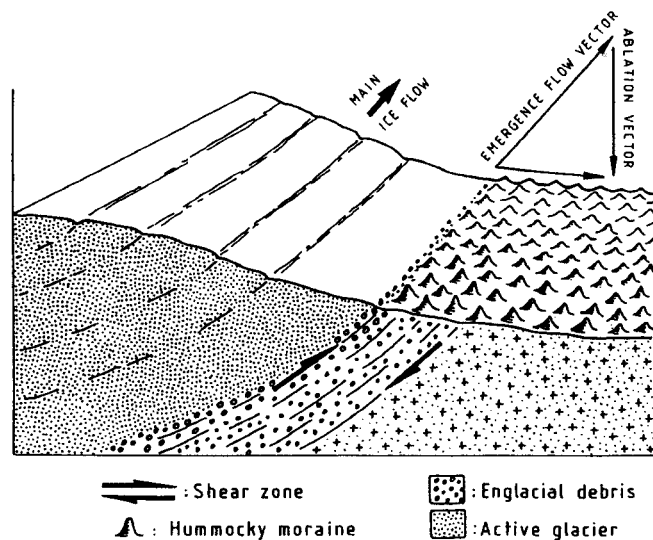
Fig.7: Emergence of englacial debris at the ice surface due to shear ("shear moraine") and extension of the till over a large surface due to lateral creep (after Chinn, 1991).

Further inwards they merge into a chaotic hummocky moraine field. Here, the debris derived from slope erosion are mixed with the englacial debris, emerging at the surface as a shear moraine (Fig.7).

The wide area, covered by the hummocky moraine, is explained by lateral creep which follows from the resultant component "along the glacier surface" of the emergence flow vector. The ice cored hillocks are protected from further ablation due to a thin veneer of rock fragments. These particles are derived from the glacier sole further inland (Souchez, 1966). According to Chinn (1991), the transition from a wet based glacier sole to a dry based zone has the potential to entrain such vast quantities of debris from the bed due to plucking. We will show later (§7) that this is indeed be the case for Upper Jenningsbreen.

Moreover the polycyclic origin of the landscape will further increase the debris supply. The micro-relief of the moraine field is also characterized by snow drift deposits and repeated melting-refreezing.

The **bare ice** (or blue ice) is snow free ice characteristic for ablation areas in Antarctica. The extensive occurrence of blue ice in the Sør Rondane shows that this marginal mountain range can be considered as an ablation island within the continental sized accumulation area of the East Antarctic ice sheet. These blue ice areas occur clearly on the western side (i.e. leeward side) of the ridges where wind scouring due to turbulence behind the nunataks is greater than the reduced snow drift deposition. The ablation of the ice is further increased by higher air temperatures caused by the naked, often steep, rock surfaces and the adiabatic heating of the down flowing air stream.

Two different types of surface features on the bare ice could be identified on the SPOT image, i.e. topographical and spectral :

(i) **topographic features** are the result of strain rates in the glacier or of aeolian activity. Both actions result in height changes on the surface. Such topographic features are mainly found on Gjelbreen, which can be considered as the only real active outlet glacier in the Central Part of the Sør Rondane. Extensive flow-lines (longitudinal ridges) are due to strain rates caused by the confluence of two ice streams near Dufekfjellet while the ice rumples and crevasses are due to strain downstream from the ice fall. These crevasses are smoothly molded by both wind deposition and erosion.

(ii) **Spectral features** on the other hand are not materialized by relief disturbance, but are characterized by differences in spectral response measured by satellite. These patterns are mainly found on nearly stagnant glaciers such as Jenningsbreen. The conspicuous textural lines on the latter, suggesting flow lines, can therefore be interpreted as paleo-flowlines. Also, a peculiar kind of banding in the ice was detected in the bare ice field, which is especially conspicuous in the Brattnipane area (Fig.8).

Plate 1. Top : Supra-glacial till originating from local spur on Gjelbreen (view from south to north). Bottom : extensive hummocky moraine field covering 500 m thick ice near the east side of Jenningsbreen (view from south to north)

The ice field there is characterized by a steep slope descending towards an area covered with supraglacial till. These bands can be interpreted as the outcropping of different sub-horizontal ice layers. The white ice contains many air bubbles and might be formed by firnification at the surface. The blue ice contains less air bubbles while the dark superimposed ice was formed by refreezing at the surface and is very poor in ice bubbles.

Concluding, the surface characteristics of the Central Part of the Sør Rondane, as studied by satellite imagery, underscores the ablation character of the Sør Rondane and allow to distinguish between active glaciers (Gjelbreen) and inactive glaciers (Jenningsbreen).

5. GLACIER DYNAMICS

By measuring ice velocities and ice thicknesses in the exit area of the outlet glaciers of the Sør Rondane, Van Autenboer and Decleir (1978) were able to calculate the ice discharge through each of these glaciers. Hansenbreen in the west and Byrdbreen in the east discharge about 73 % of the total ice transport through the mountains. In the Central Part of the Sør Rondane, the total ice transport is much reduced : Gjelbreen discharges approximately 4,7 % and one notices ice velocities of 9-10 m/a. For Jenningsbreen, extremely low values were found : 0.2 % of the total ice discharge and ice velocity values below 1 m/a, although the ice thickness amounts to more than 1000 m at certain places. In view of these findings, a more accurate and more extensive network was established to study the glacier dynamics of Jenningsbreen.

Ice Velocity Measurements on Jenningsbreen

An accurate and -at the same time- rapid survey of movement markers (bamboe stakes) was carried out during JARE 31 and JARE 32 (JARE: Japanese Antarctic Research Expedition). Bamboe stakes were drilled in the ice, at approximately 1 km interval, along four traverse lines crossing the glacier (J1, J2, J3 and J4 on the map, fig.9) in January 1990 (JARE 31) and remeasured during January 1991 (JARE 32). The end points on rock of the traverse lines were marked with paint and provided with a cairn. The traverse lines were surveyed with a total station and 3 reflectors (4 tripods) minimizing the error made when interchanging theodolite and reflecting prisms. From the different measuring stations all possible angles and distances were measured. The distances were measured in both directions, the maximum distance, employing a reflector consisting of 3 prisms, proved to be 3.5 km. The altitude a.s.l. of the stations was measured by trigonometric heighting and from barometric altimetry at the end points. All electronic distance measurements were corrected for the atmospheric effect using the estimated air pressure and temperature at the station (from the altitude of the station and the pressure and temperature recording at nearby Asuka Station).
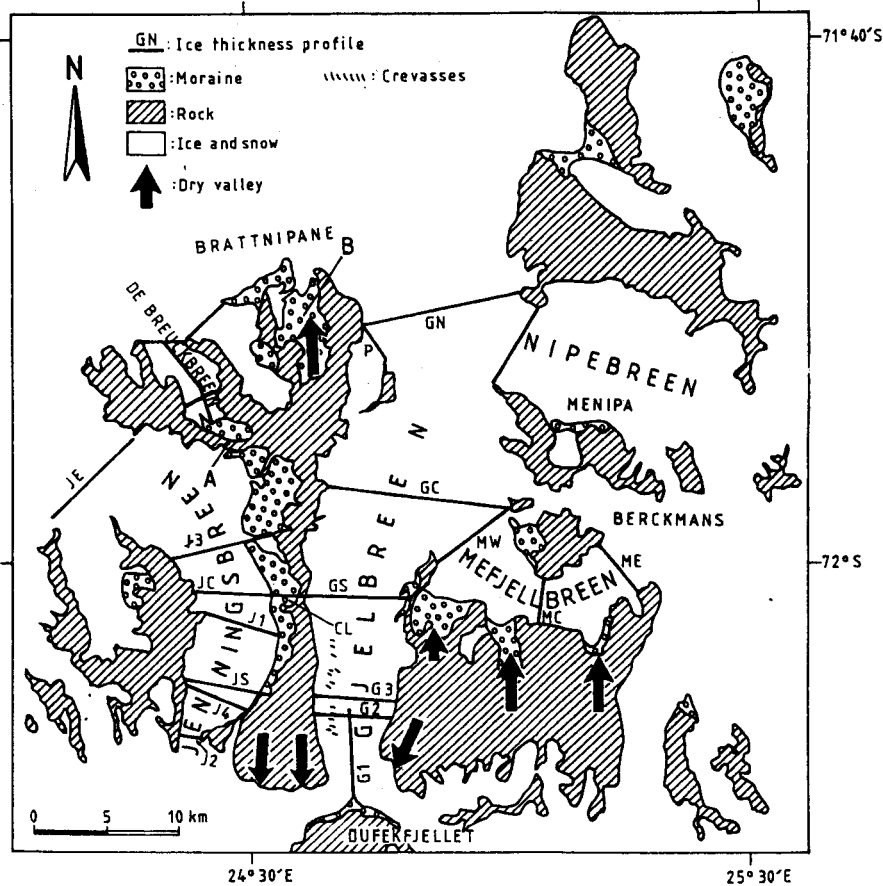
Fig.9: Map of the Central Part of the Sør Rondane (see also situation map Fig.1) showing the survey lines (ice thickness, altimetry, ice velocities...) carried out during Japanese Antarctic Research Expedition (JARE) Summer Field Seasons 1986-1987 (JARE28), 1989-1990 (JARE31) and 1990-1991 (JARE32).

The atmospheric correction factor (for both field seasons) varied between 27-42 mm/km. Generally, the distances measured in both directions were equal within 1-2 mm except between stations with a significant altitude difference. The horizontal distance H between A and B was always taken as the mean of $H_{AB} = S_{AB} \sin z_{AB}$ and $H_{BA} = S_{BA} \sin z_{BA}$, where H and S stand for the horizontal and oblique one way distance resp. and z is the zenithal angle. No further correction due to refraction of the zenithal angle proved necessary as the correction factor $\Delta H = \frac{1 - k/2}{R} S^2 \sin z \cos z$ (with k = 0.13 the refraction factor and R = 6371 the earth's radius) was equal and opposite for reciprocal sightings. All distance measurements are thought to be correct within 1 cm.

ANTAR
II/04
B

The horizontal angles were measured as the mean of two series, each consisting of face left and face right sightings. Angle measurements were less reliable than the distance measurement due to the instability of the tripod in the firm and ice layers and due to weather conditions (refraction, snow drift, wind vibration). Angle measurements are thought to have an accuracy within 5" but a few exceptions of 10" could not be avoided. Since the traverses crossed the glacier more or less perpendicular to the flow lines, starting and ending on firm ground, the traverse points and the end points were chosen in function of safety and easy access. End bearings at both sides of the traverse were therefore not always possible. Another control, available on all traverses, was the total distance which was taken as the average distance calculated for both field seasons.

From the least squares analysis and taking into account the above mentioned conditions (total distance, one or two end bearings) the calculated velocity vectors are plotted on a Landsat TM image of Jenningsbreen (Fig.10).

Discussion

The map (Fig.10) shows the rapid decrease of the velocities from about 12 m/a near the icefall to 0.3 m/a in the exit area. It confirms the low velocities measured by Van Autenboer and Decleir (1978) and suggests that Jenningsbreen is a nearly stagnant glacier in the process of being cutoff from the main ice supply of the polar plateau. An abraded rock surface with striae marks in the icefall area points also in this direction. Glacier ice thickness cross-sections were determined (see §6) along the same 4 lines and in the same points where the velocity measurements were carried out. These 4 lines divide Jenningsbreen in 4 sections (Fig.11).
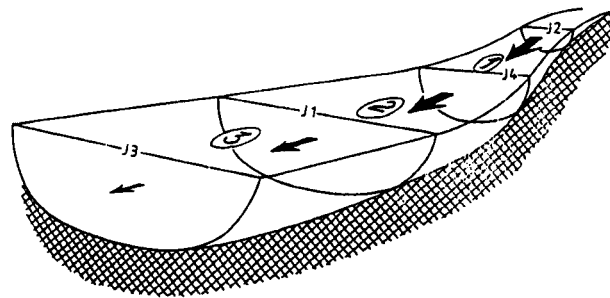
Fig.11: Schematic represention of the three sectors on Jenningsbreen, bounded by the traverse lines J2, J4, J1 and J3, to calculate the necessary ablation in case of equilibrium requirements.

For each section, mass input and output could be calculated and from this the horizontal mass divergence inferred (Table 1) and the corresponding vertical change in height due to the conservation of mass. In steady state conditions this vertical increase in

**Table 1:** Elements of the mass balance of each sector of Jenningsbreen, cfr. Fig.11

	input	output	Divergence	Areal Surface	Vertical Change in height
Section 1	$5.64 \ 10^6 \ m^3$	$4.22 \ 10^6 \ m^3$	$- 1.42 \ 10^6 \ m^3$	$11.86 \ 10^6 \ m^2$	$+ 0.12 \ ^m/a$
Section 2	$4.22 \ 10^6 \ m^3$	$2.36 \ 10^6 \ m^3$	$- 1.86 \ 10^6 \ m^3$	$25.18 \ 10^6 \ m^2$	$+ 0.07 \ ^m/a$
Section 3	$2.36 \ 10^6 \ m^3$	$1.07 \ 10^6 \ m^3$	$- 1.30 \ 10^6 \ m^3$	$37.01 \ 10^6 \ m^2$	$+ 0.04 \ ^m/a$

ice thickness is compensated by ablation at the ice surface varying from $0.04 \ ^m/a$ in the north to 0.12 m/a near the icefall in the south. The measured accumulation/ablation values were taken along the same lines (although irregularly spaced) as the ice thicknesss measurements. Averaging one finds a negative mass balance or an ablation ranging from 0.01 m/a in the north (sector 3) to 0.2 m/a in the south (sector 1). Thus the visual picture from the satellite image, characterizing the upper region of the Central Sør Rondane as an ablation area (Fig.6), is largely confirmed. Our numerical results indicate that this ablation might well be in balance with the glacier dynamics (table 1). In any case a very significant ablation is required in order to produce deglaciation in the area! The measured accumulation/ablation values are very irregular, with snow accumulation in the west (windward side) and most of the ablation in the east (leeside).

ANTAR
II/04
B

6. SUBGLACIAL MORPHOLOGY

The subglacial morphology was reconstructed from ice thickness measurements by radio echo sounding and by the gravimetric technique. The radio echo sounder, developed at Scott Polar Research Institute (SPRI, Cambridge, UK) was a light-weight instrument, mounted on a wooden Nansen sledge. Both transmitter and receiver, power supply and recording equipment were fitted in one aluminium case, allowing room for both instrumentation (including two antennas) and operator on the small sledge. The performances of the sounder was limited to 1000 m. For the deeper parts of the glacier the gravimetric technique was used. Previous experiments (Decleir et al, 1990) showed that the latter technique, employed with a suitable interpretation model, resulted in reliable ice thickness profiles. The gravimetric technique is also successful on moraine covered ice surfaces, where the electromagnetic method fails and which are inaccessible for snow sledge or snow scooter.
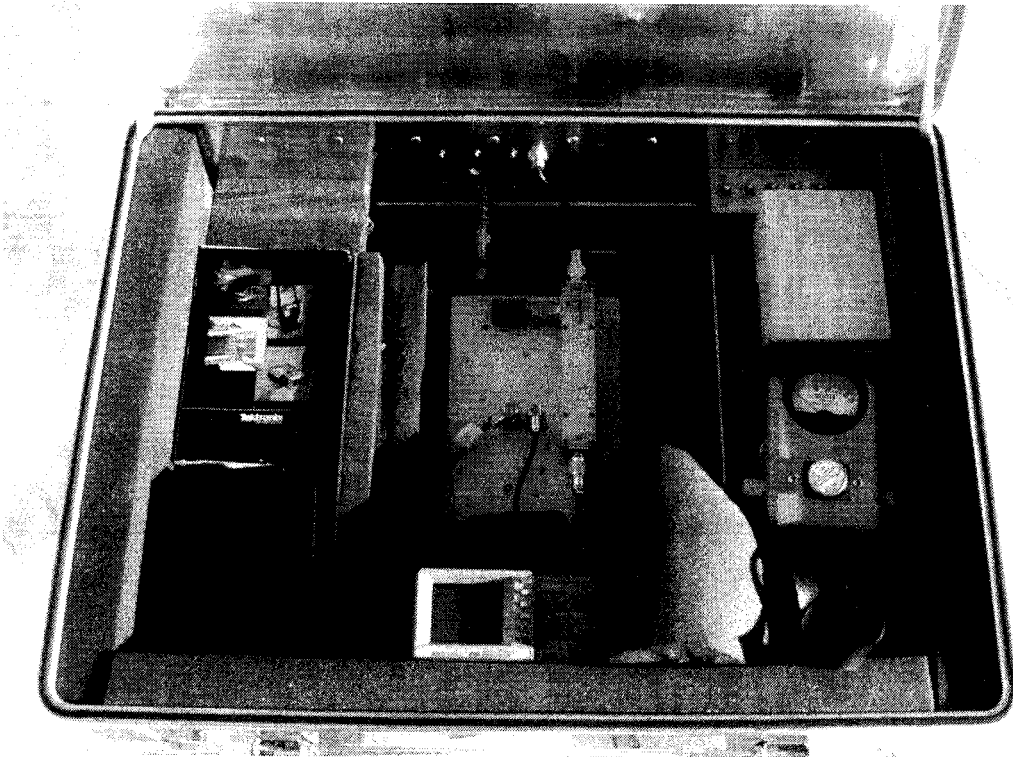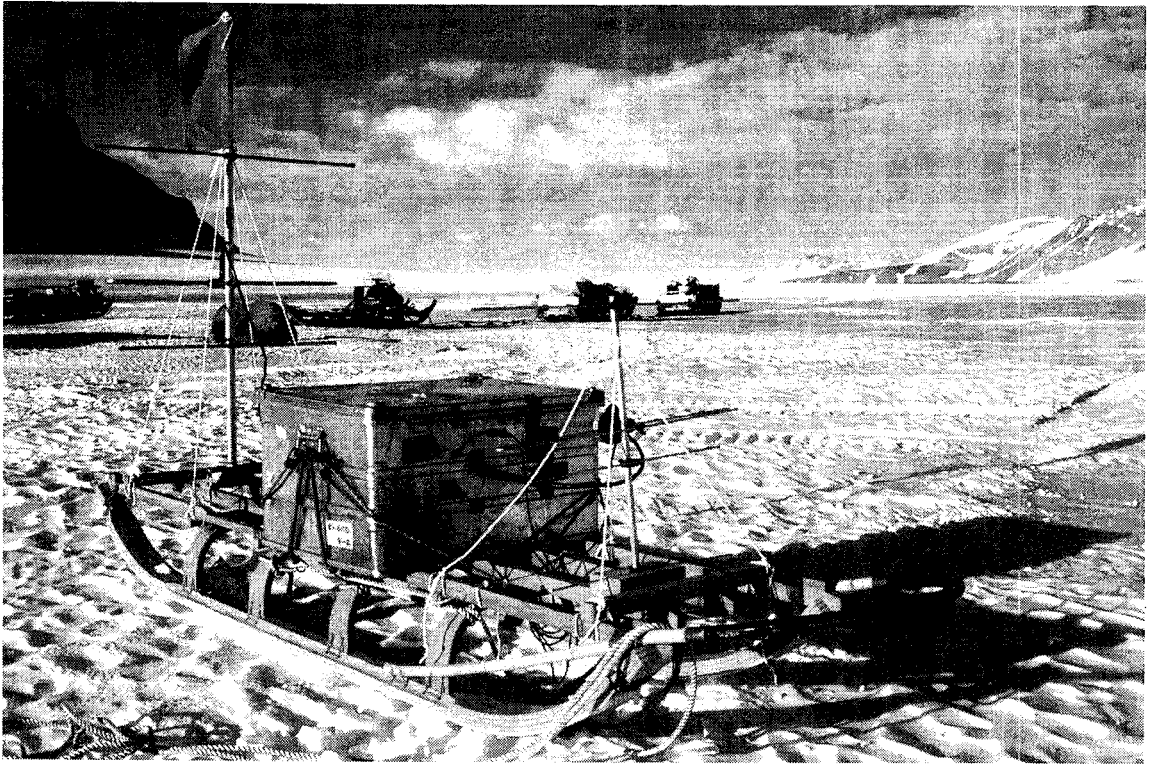
Place 5. Top : radio echo sounding sledge with aluminium box containing the sounder and two antennas. Bottom : Inside the aluminium box (batteries at the bottom) showing the transmitter (receiver unit, oscilloscope and other equipment
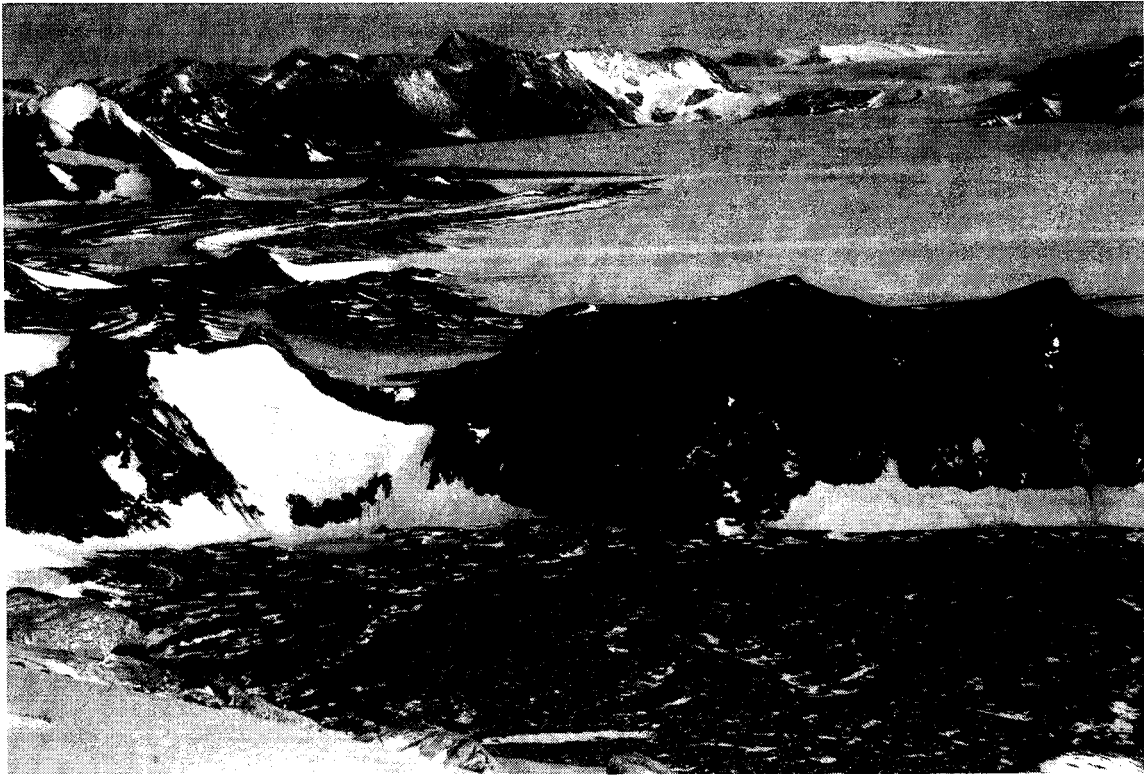
Plate 6. View from north to south on Jenningsbreen. In front is the ablation moraine of De Breuckbreen. Through the small col on the ridge separating Jennings- from De Breuckbreen one sees the higher glacier stand of Jenningsbreen. In the past the latter flowed northwards crossing the ridge and feeding De Breuckbreen. Note also the extensive supra-glacial till at the west side of Jenningsbreen (compare Fig. 12)

ANTAR
II/04
B
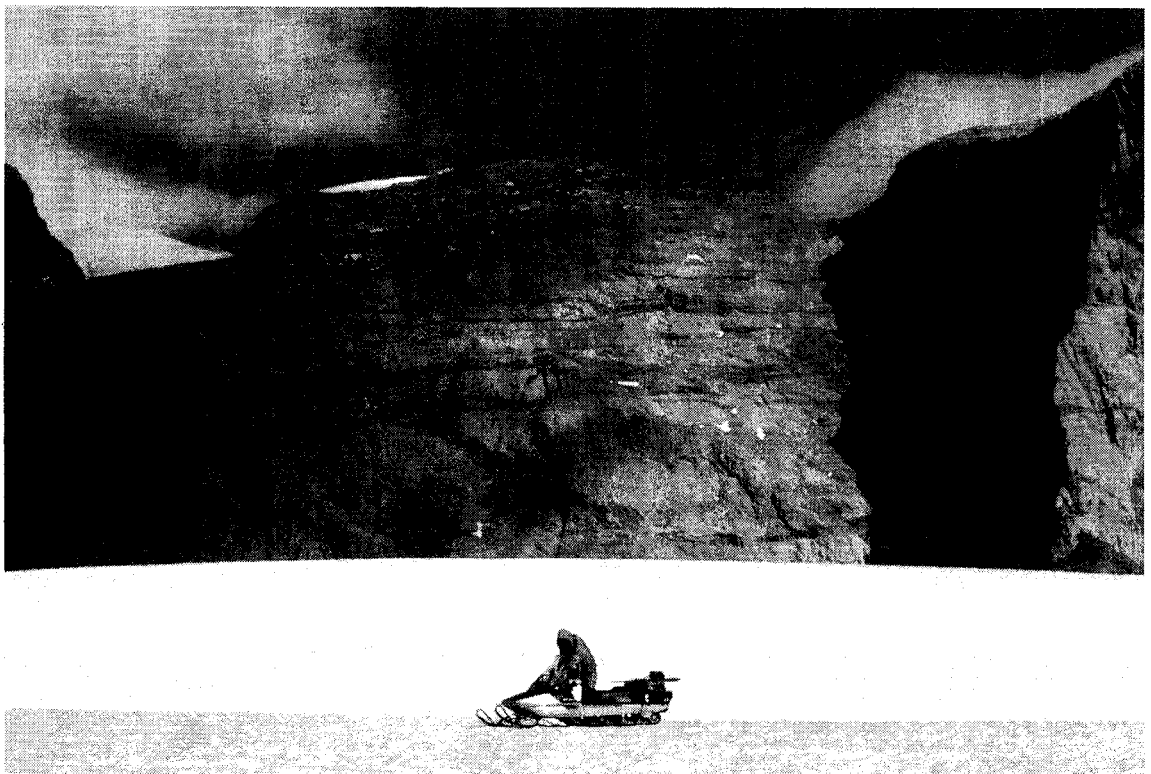
Plate 7. Top : view from north to south on Gjelbreen. A series of crevasses can be seen in the central part of the glacier. Bottom : longitudinal ridges on Gjelbreen. These ridges are accentuated by the alternation of naked and firn covered ice (see also Fig. 13.)

Most of the ice thickness profiles were glacier cross profiles, but a few longitudinal lines were also run (Fig.9). The map of the subglacial relief is shown in Figs. 12 and 13.

In the Central Part of the Sør Rondane, Gjelbreen and Jenningsbreen have cut a 40 km long U-shaped valley through the mountains. At the southern entrance, the ice is funnelled through a fairly narrow gorge (3 km wide), spilling over and cascading down the trough head to flow northwards in a widening valley (10-12 km wide in the exit area).

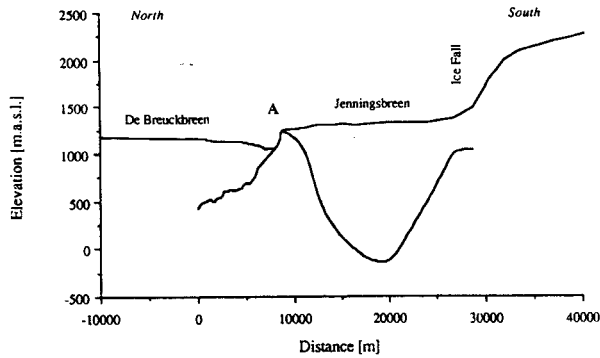The south-north longitudinal profiles of Gjelbreen and Jenningsbreen are given in Fig.14.
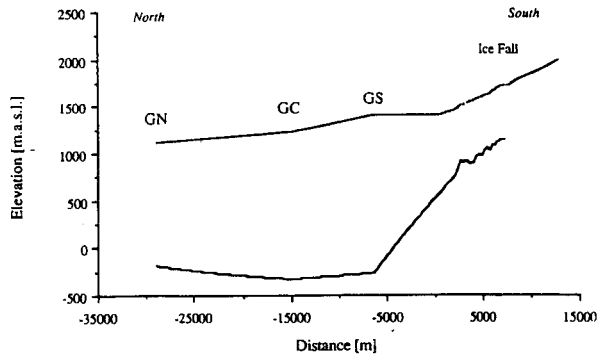

Fig. 14a   Fig.14b

Fig.14: South-north meridional profiles along De Breuckbreen-Jenningsbreen (Fig.14a) and Gjelbreen (Fig.14b).

For Jenningsbreen we have drawn the profile along a meridian following De Breuckbreen, across a small ridge A and then continuing the middle and upperpart of Jenningsbreen. Both Gjelbreen and Jenningsbreen display in their upperpart (near the icefall), proceeding northwards, a rapid thickening of the ice characterized by a steep bedrock slope of 120 m/km (the "troughhead"), with the bedrock dipping below sealevel some 10-20 km north of the icefall.

The maps (Figs.12 and 13) show the subglacial relief as an ice covered fjordlandscape. A selection of cross profiles (Fig.15) displays the characteristic U-shape of the ice filled valleys often with a slope break separating the region with present subaerial weathering from the area with glacial erosion. Such breaks are also observed in the dry valleys adjacent to Jenningsbreen and Gjelbreen revealing a former higher glacier stand (e.g. Hirakawa and Moriwaki, 1990). By calculating Graf's form ratio $F_R = D/2W$, where D is the depth and W the half width of the valley we were able to show that F_R is fairly constant along the glacier, although the valley depth's vary between 400-1700 m (Pattyn et al, 1992). This suggests that the deepening of the glacial trough is proportional to the widening is such a way that the form of the cross-profile is preserved.
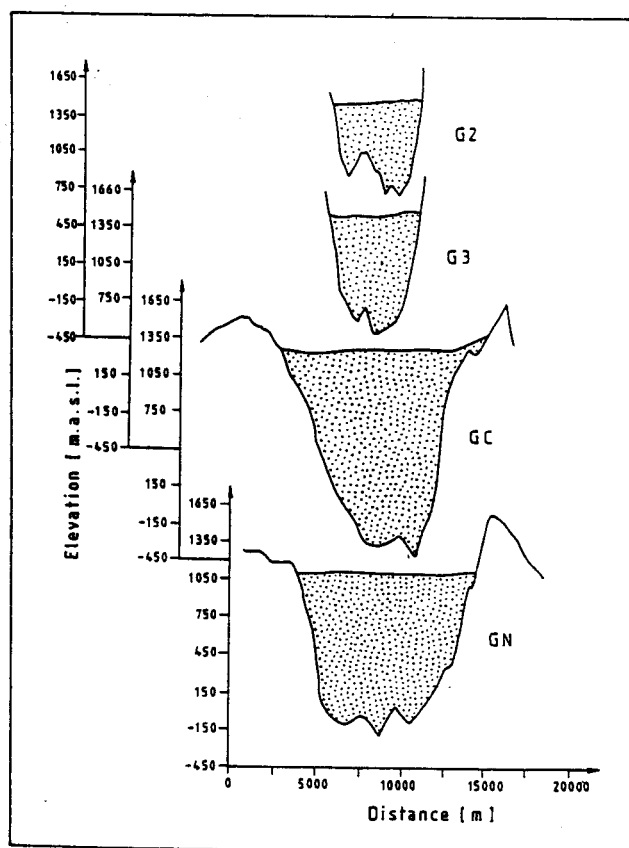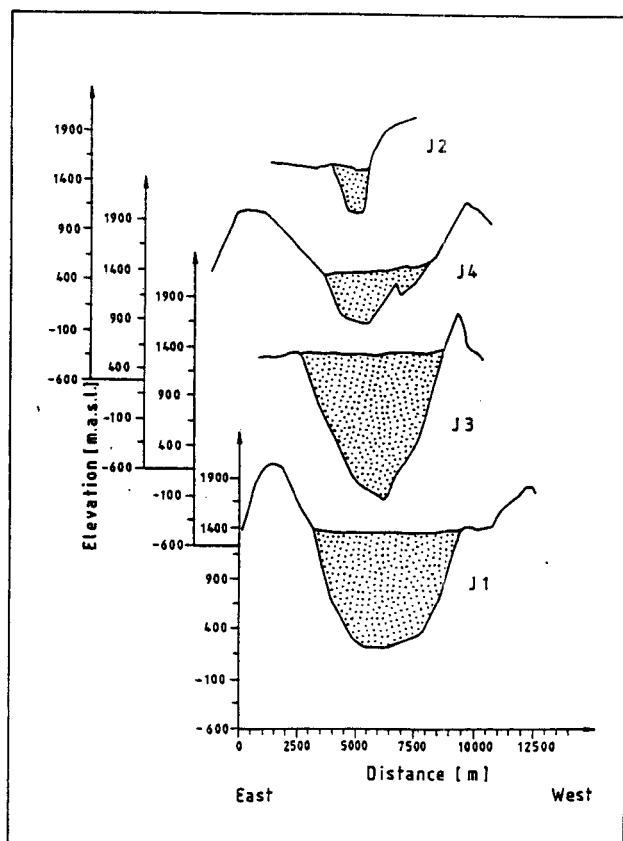
ANTAR
II/04
B

Fig.15a

Fig.15b

Fig.15: Glacier cross profiles along the traverse lines on Gjelbreen (Fig.15a) and Jenningsbreen (Fig.15b). For the situation of the traverse lines, see Fig.9.

The Sør Rondane are thus divided in a number of massifs, seperated by the U-shaped valleys, creating a complex landscape, characterized in the first place by selective linear erosion.

The intervening massifs on the other hand are marked by cold based small valley glaciers and local ice caps probably exerting little erosion. Yet, a number of other features testify here of a former higher and much more active glacier stand, of which the above mentioned south-north tending valleys are the most prominent. These features includes the full scale of alpine morphology (arêtes, horns, cirques ...) witnessing in fact of former wetter and warmer glacial conditions probably preceding the present dry and cold based conditions. These arid (and cold) conditions preclude significant geomorphological change by frost action owing to the extremely low water content of the ground (Matsuoka et al., 1988, 1990, 1992). Yet, the morphological forms caused by physical weathering and salt action are omnipresent (slope forms, honeycomb weathering, desert pavement...) witnessing very long ice free conditions.

23

The head of these dry valleys, the steep south-facing cirques lie on one line with the ice fall or through head of the outletglaciers. All these morphological features characterize an east-west running ice divide situated near the southern rim of the Sør Rondane Mountains. It was probably inherited from a preglacial watershed seperating the short energetic northward flowing rivers to the coast from the southward flowing rivers towards the interior of the continent.

The dominance of this south-north trending preglacial flow is highlighted by the study of the subglacial relief of the at present east-west flowing Mefjellbreen, a tributary of Gjelbreen. Fig.13 and the cross-sections (Fig.16) clearly reveal in the central part of Mefjellbreen a south-north tending subglacial ridge, linking the high grounds of Mefjell with the Berckmans and Menipa area.

Thus the glacial age inherited a rectangular fluvial grid which underwent significant valley widening and deepening and this for both the subsequent (south-north) and (short) east-west river valleys.

ANTAR II/04 B

Fig.16: Glacier cross profiles along the traverse lines on Mefjellbreen. For the situation of the traverse lines, see Fig. 9.

7. GLACIER SIMULATION

Model formulation

With the construction of the longitudinal and cross profiles and the map of the subglacial morphology we have set the scene for an experiment in which we will try to simulate the present behaviour of the outlet glaciers in this part of the Sør Rondane. A flow line was constructed perpendicular to the surface contours from the ice divide towards the coast, along the glaciers. Bedrock topography in the mountains was obtained from the cross-sectional and longitudinal glacier profiles. Based on airborne radio echo sounding profiles, flown by

Japanese scientists (Nishio and Uratsuka, 1991), we were able to prolong the bedrock topography northwards and southwards of the range. Given thus the subglacial and surface topography, as well as the data for surface temperature and mass balance (Fig.3), along a complete flow line it is possible to apply a numerical ice flow model similar to the one used by Oerlemans and Van der Veen (1984).

This model was first applied to preliminary data in the Sør Rondane by Pattyn *et al.* (1989), where a complete overview of the employed modelling technique can be found. The results obtained here may differ somewhat from Pattyn *et al.* (1989), but new input (subglacial topography) and reference material (present ice thickness and surface velocities), and a better mass balance distribution function account for these. A fixed grid in space is used, with 120 grid points along the x- axis and grid spacing of 5 km. The first grid point is situated on the polar plateau at an elevation of 3500 m a.s.l. The last grid point 50 km north from the present ice shelf front near the border of the continental shelf, so that the grounding line can move freely over the shelf. Sensitivity experiments (Pattyn *et al.*, 1989) already pointed out that a shift of the plateau ice divide further inland did not alter the model results, but imposed larger demands on the computation time. The continuity equation, defining conservation of the mass, relates the local rate of change of ice thickness with the flow field. The latter is found by substituting the basic stress equilibrium in a Glen-type flow law. In the mountain range, where the ice sheet transforms into a valley glacier a shape factor is introduced to account for the effect of the side drag on the valley walls (Paterson, 1981). Since the cross sections of the valleys in the Sør Rondane have a parabolic shape, this factor is found to vary between 0.6 and 1.0, depending upon the form ratio of the valley profiles (a higher form ratio implies more side drag and thus lower velocities). The model also allows for the temperature dependence of the flow properties of ice. This is important since a 10°C temperature shift implies an order of magnitude change in strain rates. The thermodynamics were incorporated using a method described by Oerlemans and Van der Veen (1984) by expanding the vertical temperature profile as a second degree polynomial in terms of z, the height above the bedrock. The coefficients are then obtained from the lower (geothermal heat flux) and upper (surface temperature) boundary condition and the vertically integrated heat equation (Oerlemans and Van der Veen, 1984).

Simulation of the present-day glaciation (Jenningsbreen and Gjelbreen)

Figs. 17a and 17b show the reference run for Jenningsbreen and Gjelbreen where the model has been allowed to relax to a stationary state and where the model tuning parameters (one for the ice sheet, one for the ice shelf ; Pattyn *et al.*, 1989) have been adjusted to obtain the present ice thickness distribution. It can be seen that a reasonable fit has been obtained between the modelled and actual ice surface in accordance with a realistic mass balance and temperature regime as prescribed, and taking into account an ablation value of 0.10 m/a in the upper regions of the mountain valleys.

SOLID LINE - MODELLED PROFILE

DASHED LINE - PRESENT PROFILE

Fig.17a

SOLID LINE - MODELLED PROFILE

DASHED LINE - PRESENT PROFILE

ANTAR
II/04
B
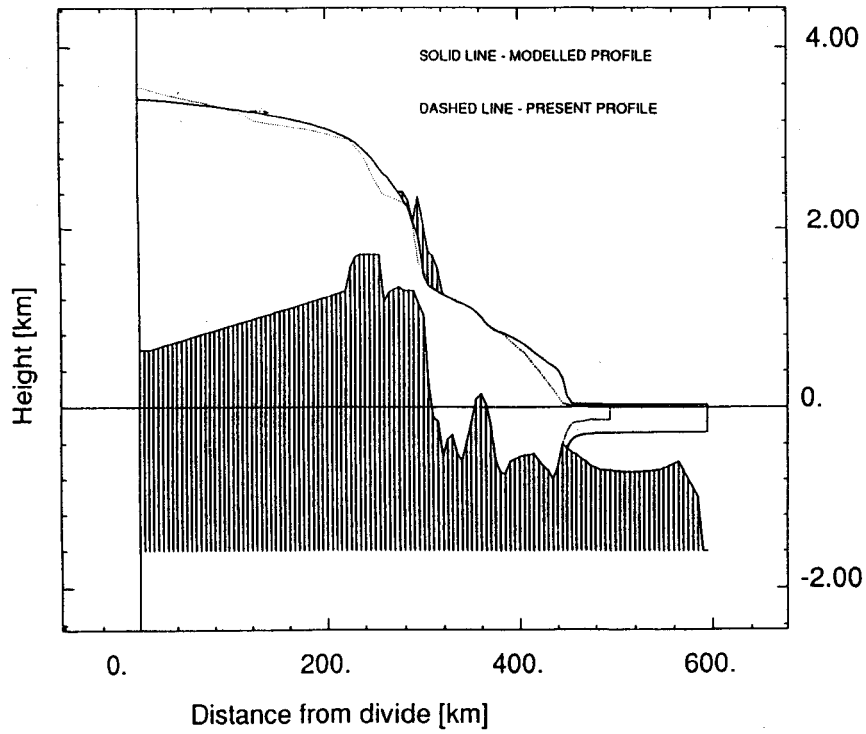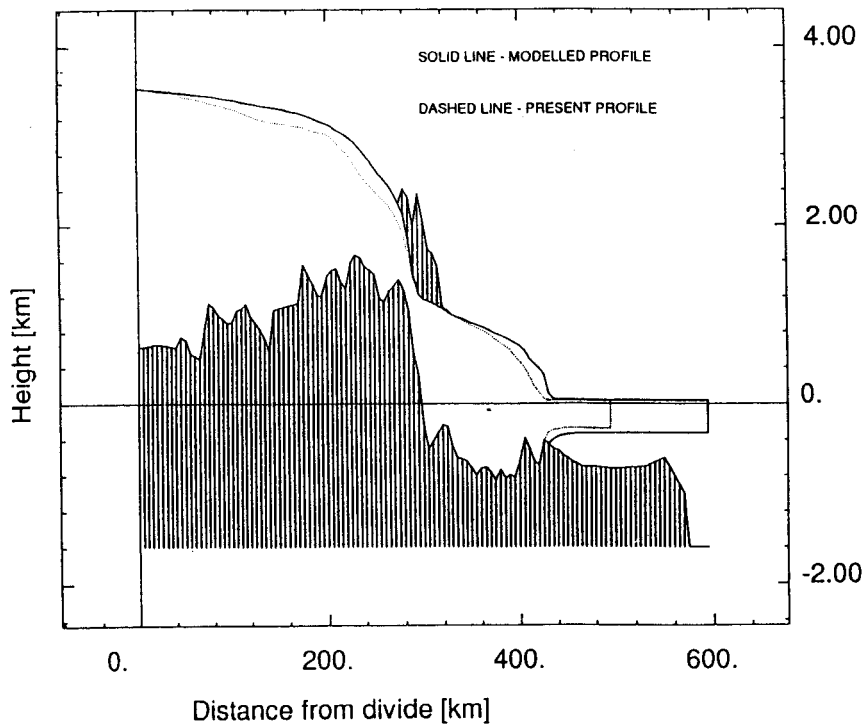
Fig. 17b

Fig.17: Reference run of the flow line model under the present environmental conditions for Jenningsbreen (Fig.17a) and for Gjelbreen (Fig.17b).
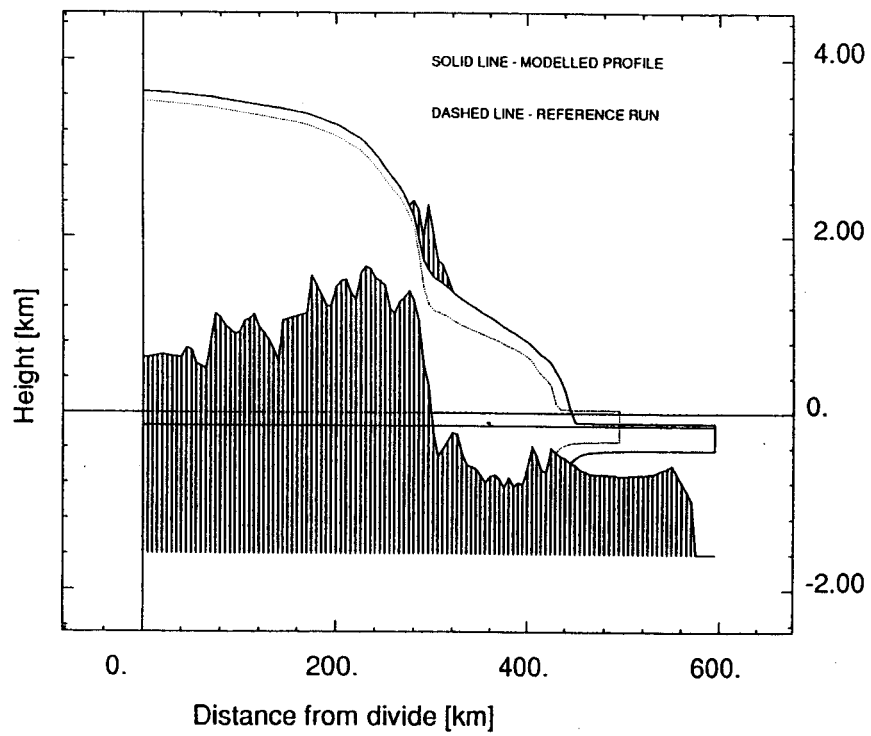
Fig.18a
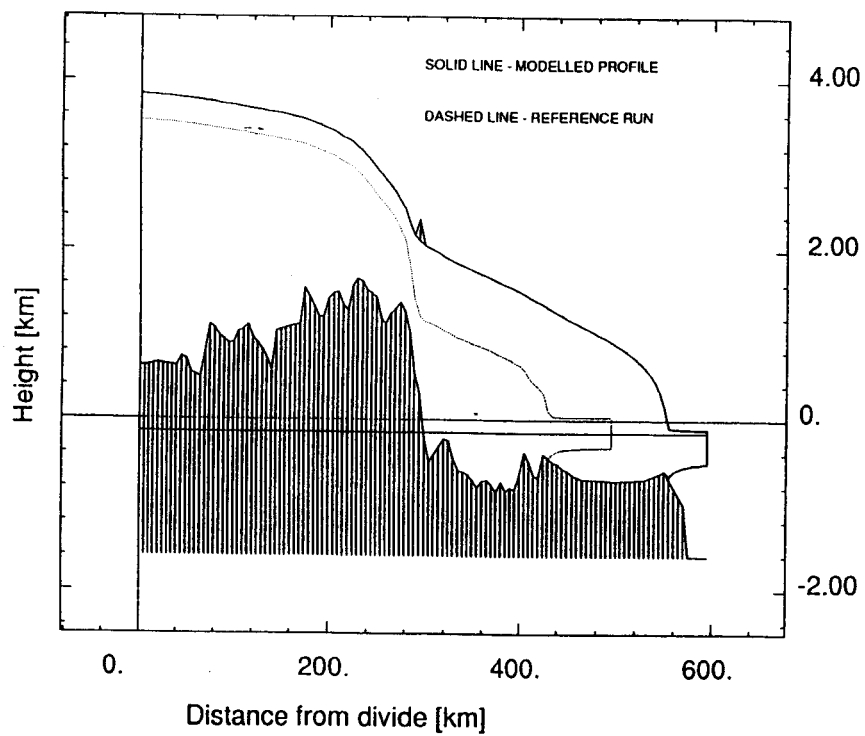
Fig. 18b

Fig.18: Two different ice-age experiments for Gjelbreen : Fig. 18a shows the results for a temperature decrease of 11°C, a 50% decrease in accumulation and a sealevel lowering of 150m. In fig. 18b the model is forced by a sealevel drop of 150m and a temperature decrease of 11°C but with the present mass balance.
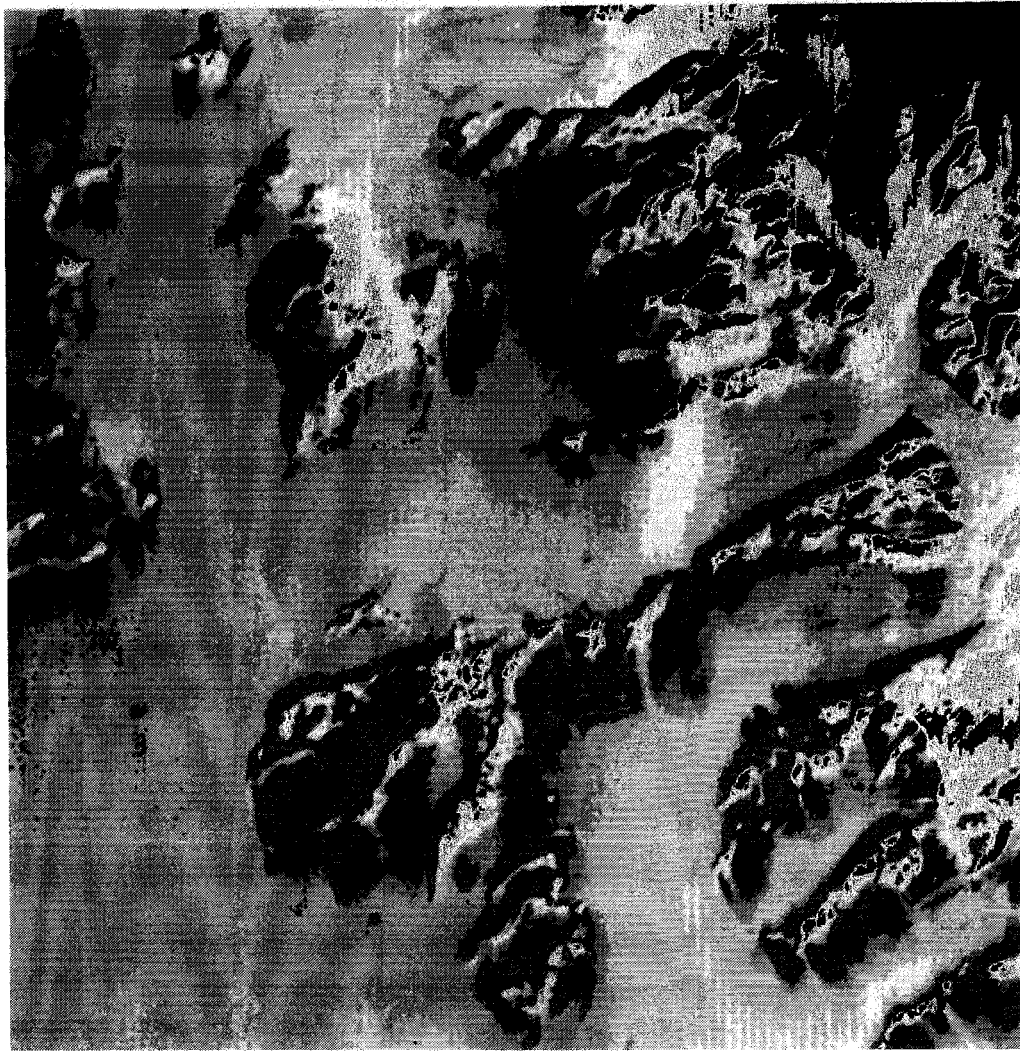
LEGEND

	T < -33 C
	-33 <= T < -31 C
	-31 <= T < -29 C
	-29 <= T < -27 C
	-27 <= T < -25 C
	-25 <= T < -23 C
	-23 <= T < -21 C
	-21 <= T < -19 C
	-19 <= T < -17 C
	-17 <= T < -15 C
	-15 <= T < -13 C
	T >= -13 C

Fig. 4: Color coded brightness temperatures determined from Landsat TM6 (ID 5100706072) on 03.12.1986 at 6h07m UT. Brightness temperatures range from -32°C (bottom right) tot +8°C on rock outcrops.

ANTAR
II/04
B

Fig.8: Infrared composite map (SPOT image 153-690 bands 1, 2 and 3) of the Brattnipane area, enhancing the glacier surface characteristics. The enhancement is apparent by comparing this image with the TM-map of Fig.12 or Fig. 13.

ANTAR
II/04
B

Plate 2. Top : theodolite station on ridge at western side of Gjelbreen. Bottom : reference point on firn ground, later provided with a cairn
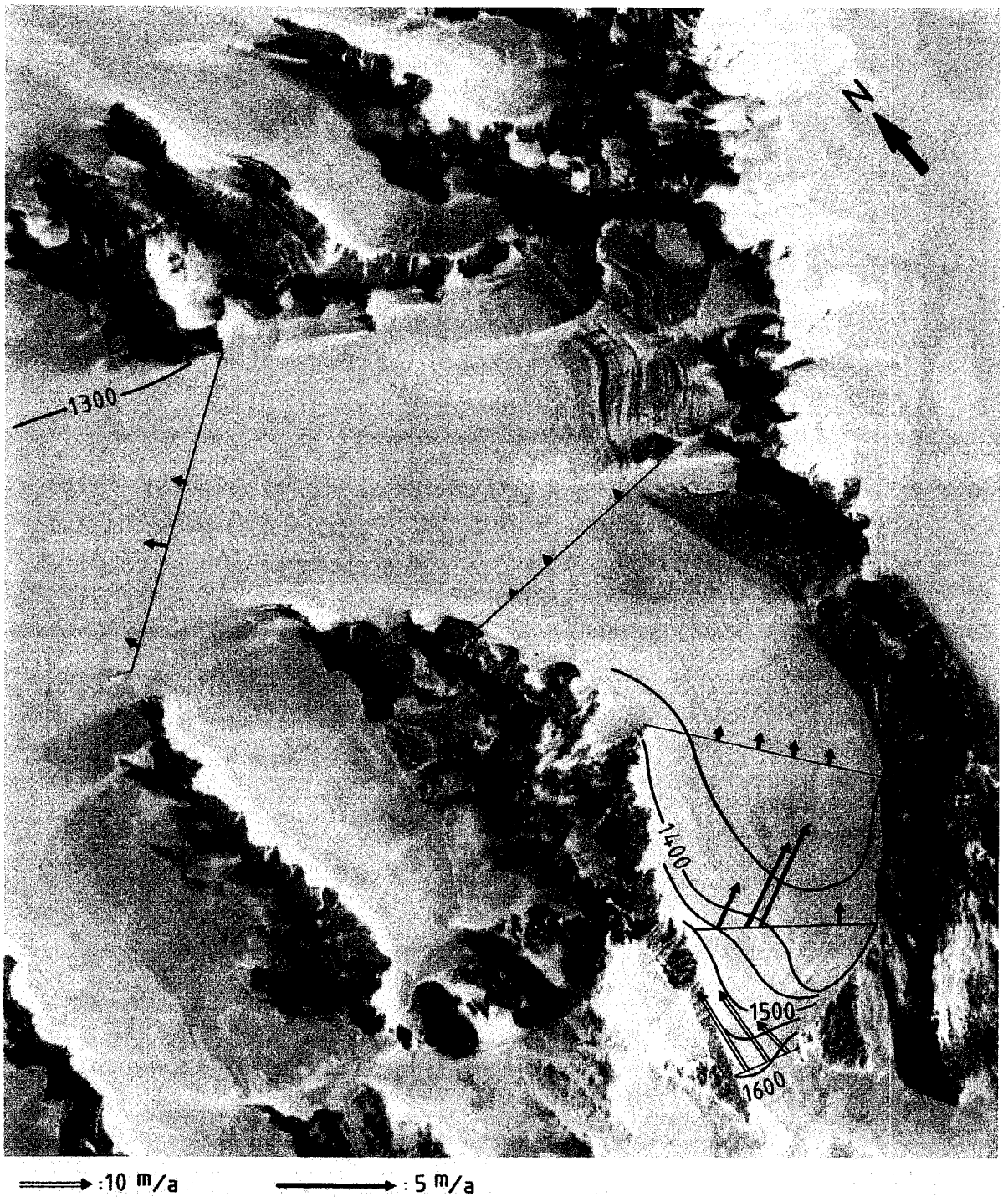
Fig.10: Landsat TM-map of Jenningsbreen showing surface height contours in m and the velocity vectors in m/a. The northern most survey line is taken from Van Autenboer and Decleir (1974). Note the high velocities in the ice fall area and the stagnant character of the glacier further downstream.
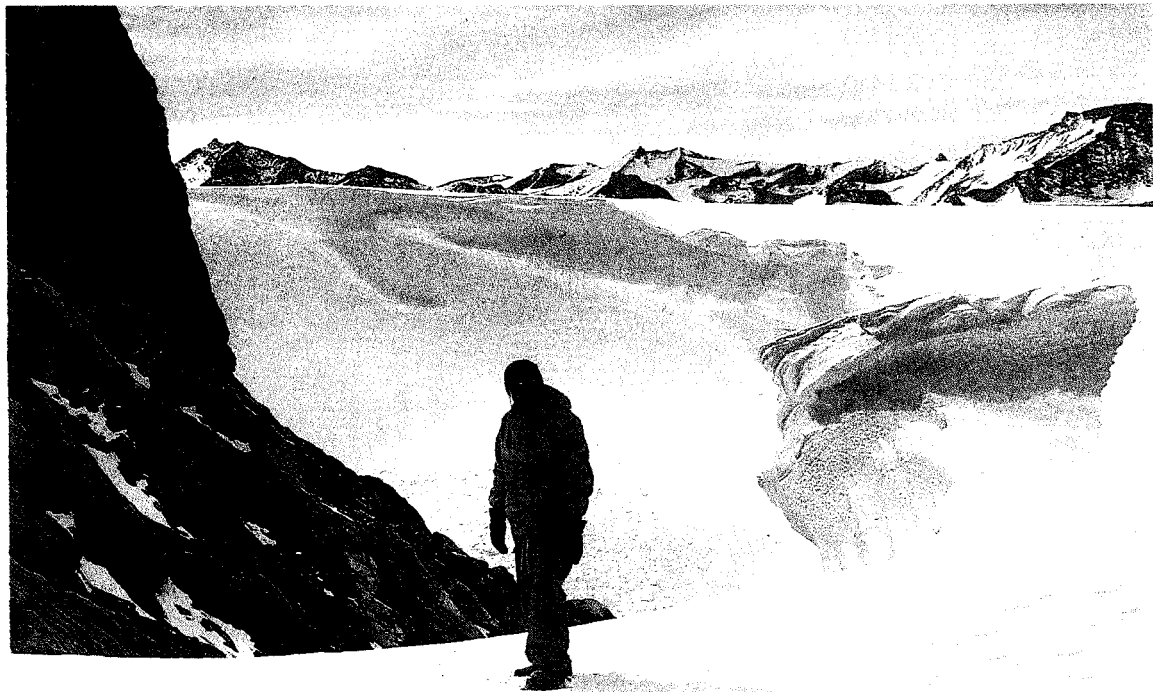
Plate 3. Top : steep sloping west side of Jenningsbreen covered with firn. Sastrugis witness of wind erosion from katabatic wind descending from ice fall and plateau. Bottom : windscoops mark the aeolian character of snow drift accumulation at west side of Jenningsbreen
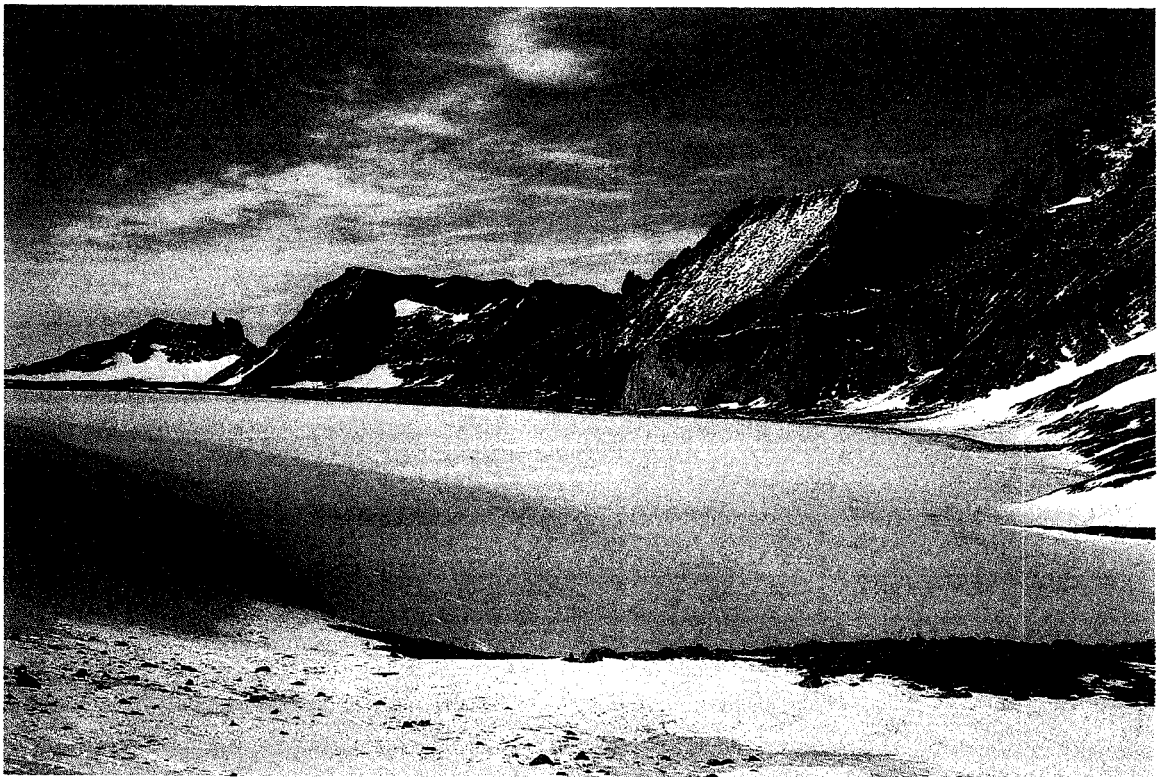
Plate 4. Top : low lying east side of Jennignsbreen characterized by blue ice (view from the south). Bottom : view from east to west on Jenningsbreen showing blue ice in front (east) and snow covered west side. A local ice cap covers the range west of Jenningsbreen. The hanging glaciers mark the disconnection of this ice cap from Jenningsbreen
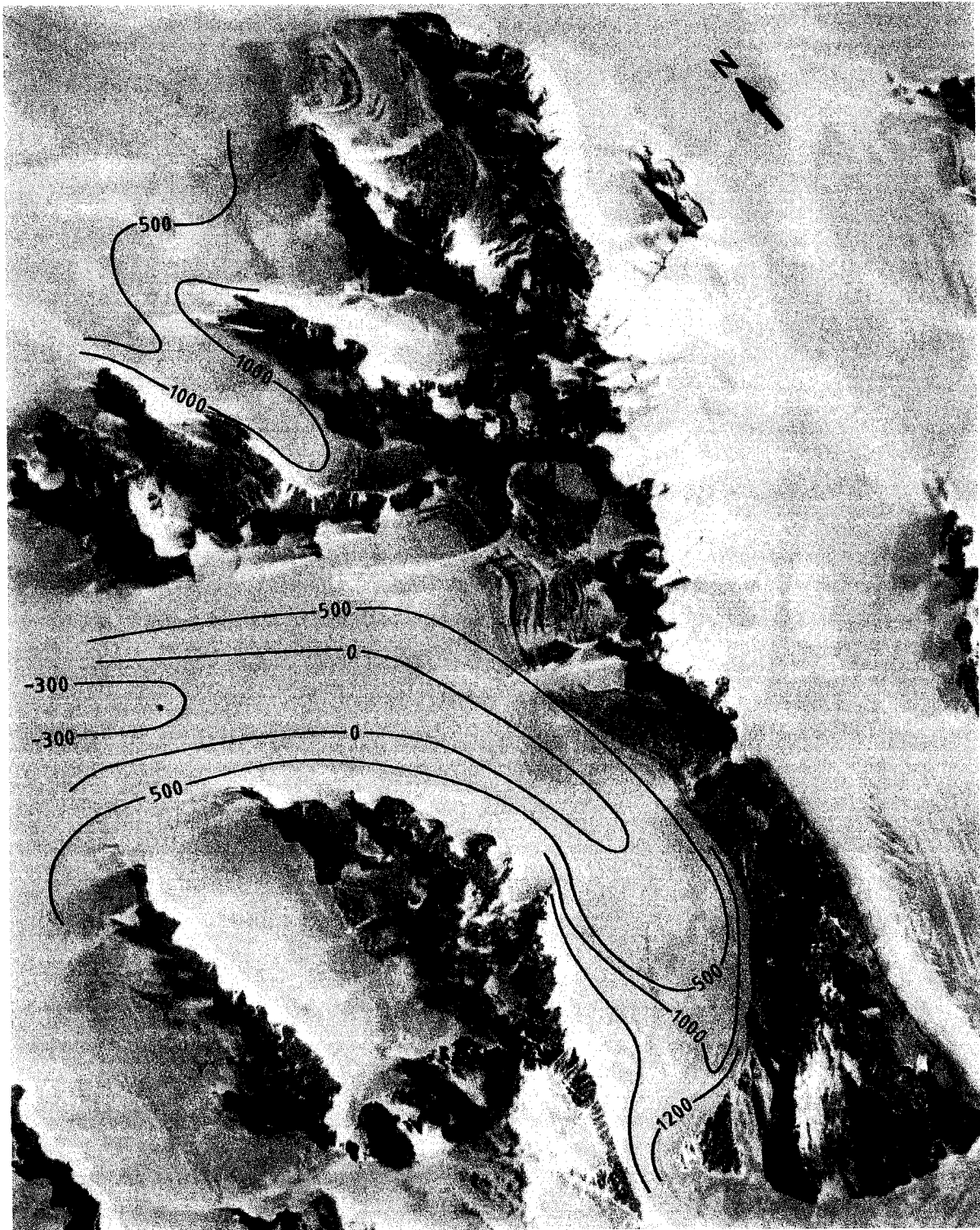
Fig.12: Landsat TM-map of Jenningsbreen and De Breuckbreen showing subglacial bedrock contours in m.
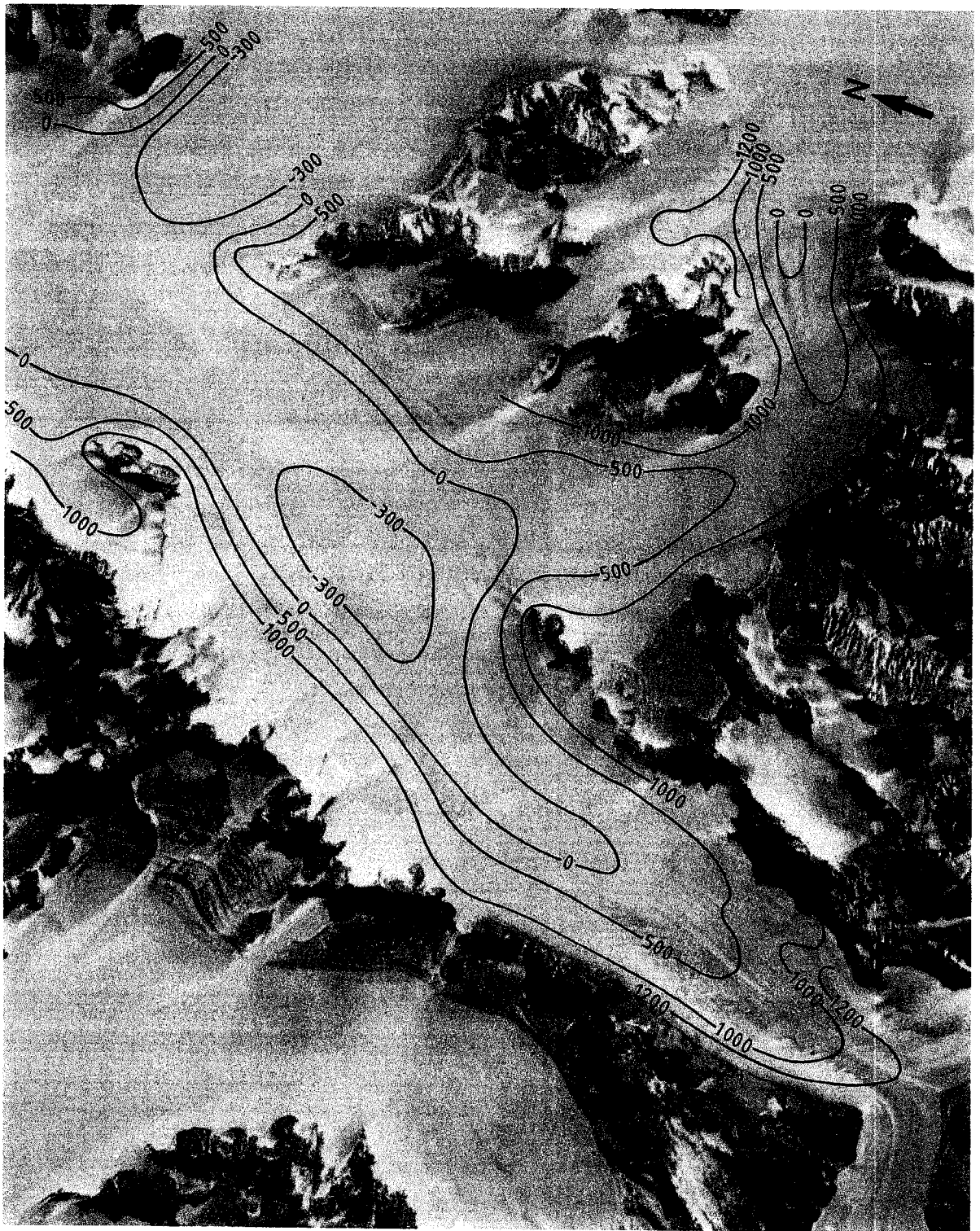
Fig.13: Landsat TM-map of Gjelbreen and Mefjellbreen showing subglacial bedrock contours in m.

The ice surface profile of the outlet glaciers show a marked concavity in the otherwise convex topography of the East Antarctic ice sheet and reflects the effect of the mountains. The concavity is due to (i) the stiffening and piling up of cold ice behind the mountains, (ii) the softening and increased velocity above and beyond the rock threshold where the ice channels into the outlet valleys, (iii) the decreasing velocities in the northern and overdeepened part of the fjordlike inlets and (iv) the increased mass balance on the inland ice slope. The softening of the ice is due to the drastic lowering of the ice sheet over the mountains and the related increase in surface temperature and ice velocities. In the ice fall area the pressure melting point is reached so that basal sliding and active erosion might be held responsible for the cutting of the gorge and the entrainment of debris from the glacier bed (see §4).

Table 2: Comparison of calculated and measured ice velocities (m/a) at different points of the glacier

| | Gjelbreen | | Jenningsbreen | | |
	calc.	observed	outlet (calc)	observed	local (calc)
Max Slope	69	-	102	12	28
Middle glacier	33	-	40	1	9
Exit area	13	10	20	1	5
Ice shelf	286	300	366	300	306

An independent check on these simulations is feasible by comparing the computed with the measured surface velocities of the glaciers (Table 2). For Gjelbreen, the measurements in the exit area are in agreement with the simulated values. The calculated velocities for Jenningsbreen ("outlet" in Table 2) are however much too high. As explained by Pattyn *et al.* (1989) this can be overcome by modelling Jenningsbreen as a "local" glacier (Table 2), where the lower velocities are in accord with the reduced ice discharge. This is accomplished by situating the origin of Jenningsbreen not on the plateau ice divide but on a small ice dome just behind the mountain range. Evidences for the reduction in the ice supply can be observed in the icefall region where a low and flat lying ridge, forming part of the trough head has come ice free. An abraded (tinted) rock surface with striae testifies among other things of the glacial activity but the severely weathered surface also points to a significant period since the deglaciation commenced.

We can thus conclude that, in addition to creating a concave ice topography, the damming effect of the Sør Rondane results in a very reduced ice flow (Gjelbreen) and even in a glacier which is at present in the process of being cut off from the main ice supply (Jenningsbreen).

ANTAR II/04 B

Simulation of the last glacial maximum

Although we ignore at present the precise environmental conditions reigning in the Sør Rondane during the last glacial maximum, the proximity to the central ice divide suggests the use of the climatic forcing similar to the one found for the Vostok ice core. In the model, surface temperature is perturbed to changes in background temperature (assumed uniform over the ice sheet) and local changes in surface elevation. Changes in surface temperature also affect accumulation rates in different climates. Following Lorius *et al.* (1985) the accumulation rate M(t) in the past is calculated from its present value M(0) times the ratio of the derivatives of the saturation vapour pressure with respect to $T_f(t)$ and with respect to $T_f(0)$, where T_f is the temperature of formation of precipitation :

$$M(t) = M(0) \exp\left[22.47 \left[\frac{T_0}{T_f(0)} - \frac{T_0}{T_f(t)} \right] \right] \cdot \left[\frac{T_f(0)}{T_f(t)} \right]^2$$

with $T_f(t) = 0.67\ T_s(t) + 88.9$, where $T_s(t)$ is the surface temperature and $T_0 = 273.15$ K (see also Huybrechts, 1992). Applying this formula for a temperature decrease of 11°C during the last glacial maximum (Jouzel *et al.*, 1987), we find for each point of the glacier profile (assuming that the temperature decrease with altitude, Fig.3b) an accumulation rate which is roughly 50% of the present one.

Imposing these climatic conditions, together with an estimated 150 m sea level drop, the glacier topography of Jenningsbreen and Gjelbreen was again simulated and compared with the reference run for the present climate. Table 3 gives the difference in altitude at some key points of the profiles, Fig. 18a shows the result for Gjelbreen.

Table 3: Increase in surface altitude (height in m) for the ice age experiment as compared to the present altitude for Gjelbreen and Jenningsbreen

	Gjelbreen	Jenningsbreen (outlet)
Plateau	+ 110	+ 115
Dufek Massif	+ 128	+ 126
Ice slope	+ 390	+ 232
Middle glacier	+ 348	+ 225
Exit area	+ 207	+ 214
Piedmont area	+ 215	+ 147

The discrepancies between the differences for Gjelbreen and Jenningsbreen (Table 3) might be due to the different methods employed to obtain them. For comparison of the glacial simulation with the present one we were forced to treat Jenningsbreen as an outlet glacier. As pointed out in the above section, although the resulting topography is an acceptable one, a physical inconsistency arises generating exaggerated velocities. The results for Gjelbreen seem therefore a better basis for comparison with paleo-glacial reconstructions based on field evidence as well as for general discussion.

Fig.18b shows for Gjelbreen another ice age experiment forced only by a drop of 150 m in sea level and -11°C in sea level temperature (preserving thus the present mass balance). A substantial increase in ice thickness is noted on the plateau due to the reduced deformation of the colder ice, while a very large (>1000 m) increase is observed north of the mountains due to the grounding of the ice sheet and the advance of the grounding line until the edge of the continental shelf. This increase in thickness due to the shift in grounding line is apparently dammed by the mountain range. The resulting profile still contains the conspicuous concavity notwithstanding the appreciable ice cover over the mountains. This continued existence of the concavity characterizing the profile of outlet glaciers seriously undermines older results based on the use of parabolic and elliptical profiles for reconstructing the paleo-surface of outlet glaciers (e.g. Denton and Hughes, 1981; Mayewski and Goldthwait, 1985).

Coming back to the more realistic ice age simulation of Fig. 18a (Table 3), where the reduced accumulation rate due to the lower temperatures is taken into account, we notice an advance of the grounding line of 20 km and an increase in altitude of the polar plateau of some 100 m. In the mountain range the glacial simulation produces north of the icefall a steeper glacier surface as compared to the present reference run (Fig.6c and Table 3) with an increase in elevation varying from 390 m in the south to 215 m in the north, reducing the concavity. The resultant higher velocities diminish the negative divergence at the same time as the associated vertical ice and debris movement in the valleys. In this ice age model, based on physical grounds, there is no room for a drastic increase in surface elevation at the foot of the ice fall (> 1000 m) as obtained by Hirakawa and Moriwaki (1990) in their reconstruction of the paleo ice surface. These authors also report in their study, which is completely based on geomorphological and glacio-geological evidence, an average increase in ice thickness of 400 m. As this is of the same order of magnitude as our findings, the morphology and glacial sediments point to a 200-400 m higher glacial stand characterizing glacial maximum. In our opinion, the evidence for a higher ice surface is witness for an environment predating the last glacial maximum and characterizing much wetter environmental conditions (confer but not necessary equal to Fig.18b). However, the timing of this glacial maximum remains an unsolved question. Our modelling specifically relates to the Last Glacial Maximum (LGM, 18000 BP) and is driven by the environmental conditions as prescribed by the Vostok ice core record. The obtained relatively moderate steady state response of the Antarctic ice sheet during this LGM is in accord with more advanced 3-dimensional modelling for Antarctica as a whole (Huybrechts, 1990a, 1990b, 1992).

ANTAR
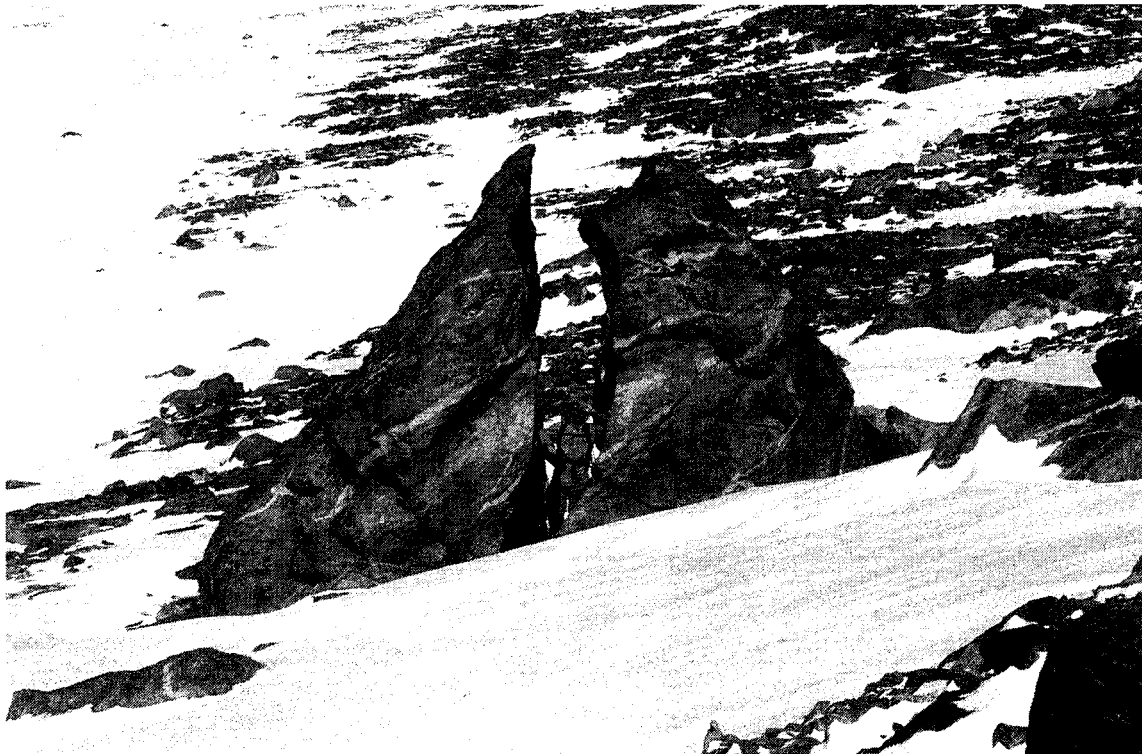II/04
B

Aspects of deglaciation

The polycyclic origin of the present glacial morphology in East Antarctica urges us to think about the role of the frequent and undoubtedly long-duration periods of deglaciation (at least compared to the last glacial maximum, see Porter, 1989). The Sør Rondane forms a small ablation island within the continental-sized accumulation area of the East Antarctic ice sheet. A lowering of the ice sheet topography results in reduced mass transport to the glaciers traversing the mountains. Both the modelling experiment as well as the small ice discharge values indicate that such is the case for Jenningsbreen. Speculating then on the future behaviour of this glacier, it is quite possible that, once completely severed from the ice supply coming from the south, the substantial ablation in the upper part of the valley will cause a continued lowering of the ice surface of Upper Jenningsbreen. In the end, the ice flow will reverse (north to south), the glacier being fed from the north by ice, circumventing the central part of the mountains. In our opinion, several small scale examples of such scenario can actually be observed in the Sør Rondane.

In the Brattnipene area for instance, De Breuckbreen lies in the northward extension of Jenningsbreen and was previously fed by this glacier, the ice flowing over the low col A (Fig. 6) on the ridge separating the two glaciers (Van Autenboer, 1964, Hirakawa *et al.*, 1988). Once cut off from the Jenningsbreen supply, the surface of De Breuckbreen lowered by some 200 m, reversing the flow as can actually be observed. The inverted moraines both on the ice and in the dry valley of Brattnipene (Pierrebotnen on the Norwegian map, near B on Fig. 6) are another witness (but now the final phase) of this deglaciation process of which many other examples can be found in the Sør Rondane.

8. DISCUSSION

We have shown that the Sør Rondane forms a small ablation island within the continental sized positive mass balance area of East Antarctica. Lowering of the inland ice sheet resulted then in an extension of the ice free surfaces and in a reduction of the ice supply towards the outlet glaciers traversing the range. Jenningsbreen became in this way a nearly stagnant glacier with abundance of supraglacial till, largely derived from the glacier bed due to upward movement which is associated with the rapid decrease of the ice velocities within the mountain range. Other, more protected, valleys became completely ice free and inverted moraine arcs testify here of incursion of ice lobes coming from the north after circumventing the Sør Rondane. Thus it is tempting to conclude that we are witnessing today a continuation of a deglaciation process.

However, our mass balance calculations show that the present ablation values might well be in

ANTAR
II/04
B

Plate 8. Top : man-sized honey comb weathering in granite massif near Menipa. They underscore the long duration of arid conditions. Bottom : frost shattering in dry valley area near Mefjell

balance with the glacier dynamics. Hence, a considerable greater ablation or smaller ice supply is required in order to produce such deglaciation. In addition the omnipresent geomorphological features caused by physical and chemical weathering on the one hand, and the extreme low morphological activity of these processes due to the low water content of the soil on the other hand, point to a very long existence of the present arid and ice free conditions. This is also suggested by Nishiizumi et al. (1991) who presented for the first time an absolute time scale on when the rocks in the Sør Rondane became ice free, by measurements of cosmic ray bombardment products ($^{26}Al/^{10}Be$ ratios vs the ^{10}Be concentrations in quartz). They found ages of deglaciation starting from 36 Ka to 4 Ma ago. Moriwaki et al. (1992) tried to correlate the relative age of tills, determined by degree of weathering, with the height of the tills and the absolute ages as given by Nishiizumi et al. (1991). They concluded that most of the Sør Rondane was once overridden by the ice sheet prior to 4 Ma in the Late Cenozoic. Since then the ice sheet has retreated intermittently. Tills of of the lowest stage are then related to the LGM a few ten thousand years ago and occur a few meter above the present ice surface. This however is difficult to reconcile with our findings. Our results, which point already to a very moderate response to the environmental forcing as compared with previous modelling still suggests a change in elevation of a few hundred meters for the outlet glaciers. Tills or glacial-morphological features occurring more than 400m high must predate the last glacial maximum, maybe related to a more extensive ice sheet during the Late Cenozoic, characterized by more humid environmental conditions. A wet environment is in any case required to explain the many alpine morphological features observed in the mountain range.

ACKNOWLEDGEMENTS

REFERENCES

Campbell, I.B. and Claridge, G.G.C. (1987): Antarctica : Soils, Weathering Processes and Environment. Elsevier, Amsterdam, 368p.

Chinn, T.J. (1991): Polar glacier margin and debris features. In Memorie della società geologica

Italiana, **XLVI**, 25-44.

De Breuck, W. (1961): Glaciology in Eastern Queen Maud Land, Preliminary report third Belgian Antarctic Expedition 1960. Mededelingen van de Koninklijke Vlaamse Academie voor Wetenschappen, Letteren en Schone Kunsten van België, Klasse der Wetenschappen, **XXIII** (6), 15p.

Decleir, H., Nishio, F. and Ohmae, H. (1989): A comparative study on ice thickness determination in valley glaciers of the Sør Rondane, Antarctica : Radio Echo Sounding and gravimetric method. Proceedings of the NIPR Symposium on Polar Meteorology and Glaciology, **2**, 133-141.

Denton, G.H. and Hughes, T.J. (Eds.) (1981): The last great ice sheets. New York, J. Wiley, 485p.

Fortuin J. and Oerlemans, J. (1990): Parameterization of the annual surface temperature and mass balance of Antarctica. Annals of Glaciology, **14**, 78-84.

Hayashi, M. and Miura, K. (1989): Glacial landforms and weathering processes in the Balchenfjella region, eastern part of the Sør Rondane Mountains, East Antarctica. Proceedings of the NIPR Symposium on Antarctic Geosciences, **3**, 65-80.

Hirakawa, K. and Moriwaki, K. (1990): Former ice sheet based on the newly observed glacial landforms and erratics in the central Sør Rondane Mountains, East Antarctica. Proceedings of the NIPR Symposium on Antarctic Geosciences, **4**, 41-54.

Hirakawa, K., Matsuoka, N. and Moriwaki, K. (1988): Reconstruction of maximum glacial extent in the central Sør Rondane Mountains, East Antarctica. Proceedings of the NIPR Symposium on Antarctic Geosciences, **2**, 146-161.

Hirano, M. and Aniya, M. (1988): A rational explanation of cross-profile morphology for glacial valleys and of glacial valley development. Earth Surface Processes and Landforms, **13**, 707-716.

Huybrechts, P. (1990a): The Antarctic ice sheet during the last glacial-interglacial cycle: a three-dimensional experiment. Annals of Glaciology, **14**, 115-119.

Huybrechts, P. (1990b): A 3-D model for the Antarctic ice sheet: a sensitivity study on the glacial-interglacial contrast. Climate Dynamics, **5**, 79-92.

Huybrechts, P. (1992): The Antarctic ice sheet and environmental change : a three-dimensional modeling study. Berichte zur Polarforschung, **99**, 1-241.

Iwata, S. (1987): Debris-mantled rectilinear slopes in the western Sør Rondane Mountains, East Antarctica. Proceedings of the NIPR Symposium on Antarctic Geosciences, **1**, 178-192.

Jouzel, J., Lorius, C., Petit, J.R., Genthon, C., Barkov, N.I., Kotlyakov, V.M. and Petrov, V.M. (1987): Vostok ice core: a continuous isotope temperature over the last climatic cycle (160.000 years). Nature, **329**, 403-408.

Lorius, C., Jouzel, J., Ritz, C., Merlivat, L., Barkov, N.I., Korotkevich, Y.S. and Kotlyakov, V.M. (1985): A 150.000-year climatic record from Antarctic ice. Nature, **316**, 591-596.

Matsuoka, N. (1991): Rock weathering processes in the Sør Rondane mountains, East

ANTAR
II/04
B

Antarctica. In Abstracts Sixth International Symposium on Antarctic Earth Sciences, NIPR, Tokyo, 397-401.

Matsuoka, N., Moriwaki, K. and Hirakawa, K. (1988): Diurnal frost-heave activity in the Sør Rondane mountains, Antarctica. In Arctic and Alpine Research, 20 (4), 422-428.

Mayewsky, P.A. and Goldthwait, R.P. (1985): Glacial events in the Transantarctic Mountains: a record of the East Antarctic ice sheet. In Geology of the Central Transantarctic Mountains, Antarctic Research Series, 36, ed. M.D. Turner and J.F. Splettstoesser, Washington DC, Americam Geophysical Union, 275-324.

Moriwaki, K., Hirakawa, K. and Matsuoka, N. (1991): Weathering stage of till and glacial history of the central Sør Rondane mountains, East Antarctica. In Proceedings of the NIPR Symposium on Antarctic Geosciences, 5, NIPR, Tokyo, 99-111.

Nishiizumi, K., Kohl, C.P., Arnold, J.R., Klein, J., Fink, D. and Middleton, R. (1991) Cosmic ray produced ^{10}Be and ^{26}Al in Antarctic rocks: exposure and erosion history, Earth and Planetary Science Letters, 104, 440-454.

Nishio, F. and Uratsuka, S. (1991): Subglacial water layer and grounding line derived from backscattering coefficients of radio echo sounding in the Shirase Glacier and Roi Baudouin Ice Shelf, East Antarctica. Proceedings of the NIPR Symposium on Polar Meteorology and Glaciology, 4, 93-102.

Nishio, F., Isjikawa, M., Ohmae, H., Takashi, S. and Katsushima, T. (1984): A preliminary study of glacial geomorphology in area between Breid Bay and the Sør Rondane Mountains in Queen Maud Land, East Antarctica. Antarctic Record, 83, 11-28.

Oerlemans, J. and Van der Veen, C.J. (1984): Ice sheets and climate. Dordrecht, D. Reidel Publishing Company, 217p.

Paterson, W.S.B. (1981): The physics of glaciers. Oxford, Pergamon Press, 380p.

Pattyn, F., and Decleir, H. (1992): Satellite monitoring of ice and snow conditions in the Sør Rondane, Antarctica. Annals of Glaciology, in print.

Pattyn, F., Huybrechts, P. and Decleir, H. (1989): Modeling glacier fluctuations in the Sør Rondane, Dronning Maud Land, Antarctica. Zeitschrift für Gletscherkunde und Glazialgeologie, 25, 33-47.

Pattyn, F., Decleir, H. and Huybrechts, P. (1992): Glaciation of the Central Part of the Sør Rondane, Antarctica: Glaciological Evidence. In Recent Progress in Antarctic Earth Science, ed. National Institute of Polar Research, in print.

Porter, S.C. (1989): Some geological implications of average Quaternary glacial conditions. Quaternary Research, 32, 245-261.

Souchez, R. (1966): The origin of moraine deposits and the characteristics of glacial erosion in the Western Sør Rondane, Antarctica. Journal of Glaciology, 6, 249-259.

Tongiorgi, E., Picciotto, E., De Breuck, W., Norling, T., Giot, J. and Pantanetti, F. (1961): Deep drilling at Base Roi Baudouin, Dronning Maud Land, Antarctica. Journal of Glaciology, 4, 101-110.

Van Autenboer, T. (1964): The geomorphology and glacial geology of the Sør Rondane, Dronning Maud Land, Antarctica. <u>Mededelingen van de Koninklijke Vlaamse Academie voor Wetenschappen, Letteren en Schone Kunsten van België, Klasse de Wetenschappen</u>, **XXVI** (8), 89p.

Van Autenboer, T. and Decleir, H. (1974): Mass transport measurements in the Sør Rondane, Dronning Maud Land, Antarctica, Preliminary Report. <u>Professional Paper, 1974 (6)</u>, Ministerie van Economische Zaken en Energie van België, 25p.

Van Autenboer, T. and Decleir, H. (1978): Glacier discharge in the Sør Rondane, a contribution to the mass balance of Dronning Maud Land, Antarctica. <u>Zeitschrift für Gletscherkunde und Glazialgeologie</u>, **14**, 1-16.

ANTAR
II/04
B

SEA ICE AND CIRCULATION IN THE WEDDELL SEA

B. Petit* and C. Demuth**

INSTITUTE OF HYGIENE
AND EPIDEMIOLOGY

* Management Unit of the
Mathematical Model (MUMM)

Gulledelle, 100
B-1200 Brussels, Belgium

** Air Section

Rue J. Wytsman, 14
B-1050 Brussels, Belgium

Contents

Abstract

The model of sea ice formation developed during the first phase of the Belgian Scientific Research Programme on Antarctica is the base of the present work. The thermodynamic features have been completely checked to improve the behaviour of the mixed layer.

The improvement of ice motion has been studied by developing circulations models. At first, a 2.5D vertical plane model is applied in antarctic conditions to point out the problems encountered in the Southern Ocean. This model is then extended in the third direction of space to obtain a 3D oceanic model. This three-dimensional model is used to compute the currents in the Weddell Sea for each month in a year. It reproduces the clockwise circulation of the Weddell Sea and the strong north-east currents in the northern part of the Drake Passage. These results are then introduced in the SEAICE model to calculate the ice dynamics. They yield satisfying ice thicknesses and ice extent.

1 Introduction

The purpose of this report is to describe the research done at MUMM (Management Unit of the Mathematical Model of the North Sea and the Scheldt Estuary) within the framework of the Belgian Scientific Research Programme on Antarctica.

The SEAICE model was already presented at the end of the first phase of the scientific programme (Demuth and van Ypersele, 1989). Within the frame of the preparatory phase of the coupling between SEAICE and a 3D ocean circulation model, various aspects of SEAICE have been reviewed. The major improvements brought in the model are presented in Section 2. In this section, the results of a set of experiments, including a preliminary study of the impact of a warming of the atmosphere, performed with the new version of the model are presented and discussed. Briefly stated, the model variables, especially the depth of the mixed layer, evolve now more regularly. The averaged quantities (*e.g.*, sea ice extent, oceanic fluxes) remain consistant with the results previously obtained and in a satisfying agreement with the observations. The warming of the atmosphere tends to reduce the sea area covered by ice and to increase the oceanic fluxes.

The development of the three-dimensional oceanic model has been made in two steps. In a first step, the development of a vertical plane model, named hereafter the 2.5D model, which includes the three components of the velocity vector has been pursued. A description of the model is given in Section 3. Several numerical experiments have been performed to test and verify the 2.5D model (Demuth, 1990). The 2.5D model has also been used within the frame of an intercomparison exercise with a similar model developed by Fettweis *et al.* (1991). A brief overview of this experiment, which deals with the computation of the circulation induced by a katabatic wind, is also given in the Section 3.

In a second stage, the full 3D hydrodynamic model has been developed by extending the 2.5D model in the third direction of space (the horizontal y-direction). The numerical procedure of the 3D model is very similar to that used in the 2.5D model. The main difference lies in the computation of the pressure field. In the 3D model, a two-dimensional elliptic equation of Poisson type is solved to compute the value of the pressure at the next time level.

In the last part of Section 3, the results of the preliminary applications of the 3D model to the Weddell sea are presented and discussed. At this stage, it suffices to say that some features

of the wind-induced circulation in the area of interest are fairly well reproduced. The computed currents are then used to simulate the ice dynamics in the SEAICE model.

Some conclusions are given in the Section 4.

2 SEAICE model

2.1 Introduction

In the first phase of the Belgian Scientific Research Programme on Antarctica, a sea ice model, referred to as SEAICE, has been developed (Demuth and van Ypersele, 1989) and applied to a sector of the Southern Ocean including the Weddell Sea and the Drake Passage. The results obtained with the model driven by the available climatological data showed that the integrated values like the amplitude of the ice extent and the mean oceanic heat fluxes exchanged between ice and ocean were in good agreement with the glaciological data observed by satellite. However, for certain parameters, like the mixed layer depth, the time evolution displayed spurious oscillations even when the so-called robust-diagnostic method was used to force the calculated fields to remain more or less close to the observations.

As an attempt to determine the origin (errors into the coding of the computer program and/or loss of precision in the discretization of the conservation laws) of this spurious behaviour of some model variables, a complete review of the whole aspects of the modelisation has been made during the course of the phase II. This review has yielded important improvements of the model which are described in this section.

Without going into a complete description of the SEAICE model, it is necessary to recall that this model is divided into two major parts according to the processes which constrain the ice and determine its thickness and movement :

i) a thermodynamic component which computes the thickness and the temperature of the ice deduced from the heat exchanged vertically through the ice-air and ice-ocean interfaces and horizontally through the channels of open water called leads. The heat flux balances are estimated from three specific models : an ice model based on the "zero–layer" model suggested by Semtner (1976), a model for the leads and an oceanic mixed layer model proposed by Fichefet and Gaspar (1988). The latter calculates the value of the temperature and of the salinity in the upper ocean layer whose thickness is also computed.

ii) a dynamical component which takes into account the ice motion under the influence of the wind and the ocean currents. The ice velocity, deduced from the balance between wind and water drag, is taken as a linear function of the geostrophic wind obtained from meteorological data and the upper ocean current. In the applications described hereafter, the upper ocean

current is provided by the 3D ocean general circulation model developed by van Ypersele (1986).

2.2 Improvements of the SEAICE model

2.2.1 Thermodynamic component

a) Zero–layer ice model

The ice which can be covered by snow, is assumed to be a uniform flat slab floating at the surface of the oceanic mixed layer. The time evolution of the ice thickness is computed on the basis of the energetic exchanges with the atmosphere and the ocean.

At the ice or snow-air interface, the variation of the ice or snow thickness depends on the difference between the surface temperature and the melting temperature (0°C for snow, −0.1°C for ice). If this difference is positive, there is melting at the surface. Otherwise, the ice grows. The surface temperature is deduced from the balance between the solar radiation $F_{sol,i}$ (including the surface albedo), the non-solar heat flux $F_{nsol,i}$ and the conductive flux F_c.

At the ice-sea interface, where the temperature is assumed to be always at the freezing point $T_f(S_m)$ of the seawater (variable with the salinity S_m of the mixed layer), the variations of the ice thickness depend on the competition between the heat flux from the ocean to the ice F_b and the conductive flux F_c.

The analysis of the coding of the computer program of the SEAICE model has shown that the sign of the solar radiation absorbed at the surface $F_{sol,i}$ was not compatible with the coordinate system used in the equation of temperature below the mixed layer (z-axis pointing downwards). However, this correction does not change significantly the results. This term is multiplied by the z derivative of the solar radiation transmission which decreases rapidly with the depth and influences only slightly the behaviour of temperature in the rest of the water column.

The continuity in the time evolution of the albedo influences the variations of the ice temperature and thickness. The albedo is the fraction of solar radiation reflected by a given surface (in our case, snow, ice or water). This parameter appears in the thermal equilibrium at the surface through a non linear equation describing the balance of fluxes at the same surface. An iterative procedure is required to determine the surface temperature from the balances of fluxes. The method of Newton-Raphson is used. This technique is efficient if the start root is not too far from the solution of the next step and if the studied function (*i.e.*, here, the balance of

fluxes at the surface) is continuous. However, as it can be seen on Figure 1, the albedo formula's proposed by Fichefet and Gaspar (1988) and used in SEAICE do not meet this requirement : the ice albedo depends on the ice thickness and on the type of ice (melting, forming, frozen, ...) and it is defined by a piecewise continuous function. It is not simpler for the snow albedo because it is determined, of course, by the snow parameters and moreover by the ice parameters. With these formulations for the albedo, the convergence of the iterative procedure cannot be guarantee. The ice albedo can be easily rendered continuous : it suffices to suppress the jump. For the snow albedo, no simple approximation has yet been found to make it continuous.
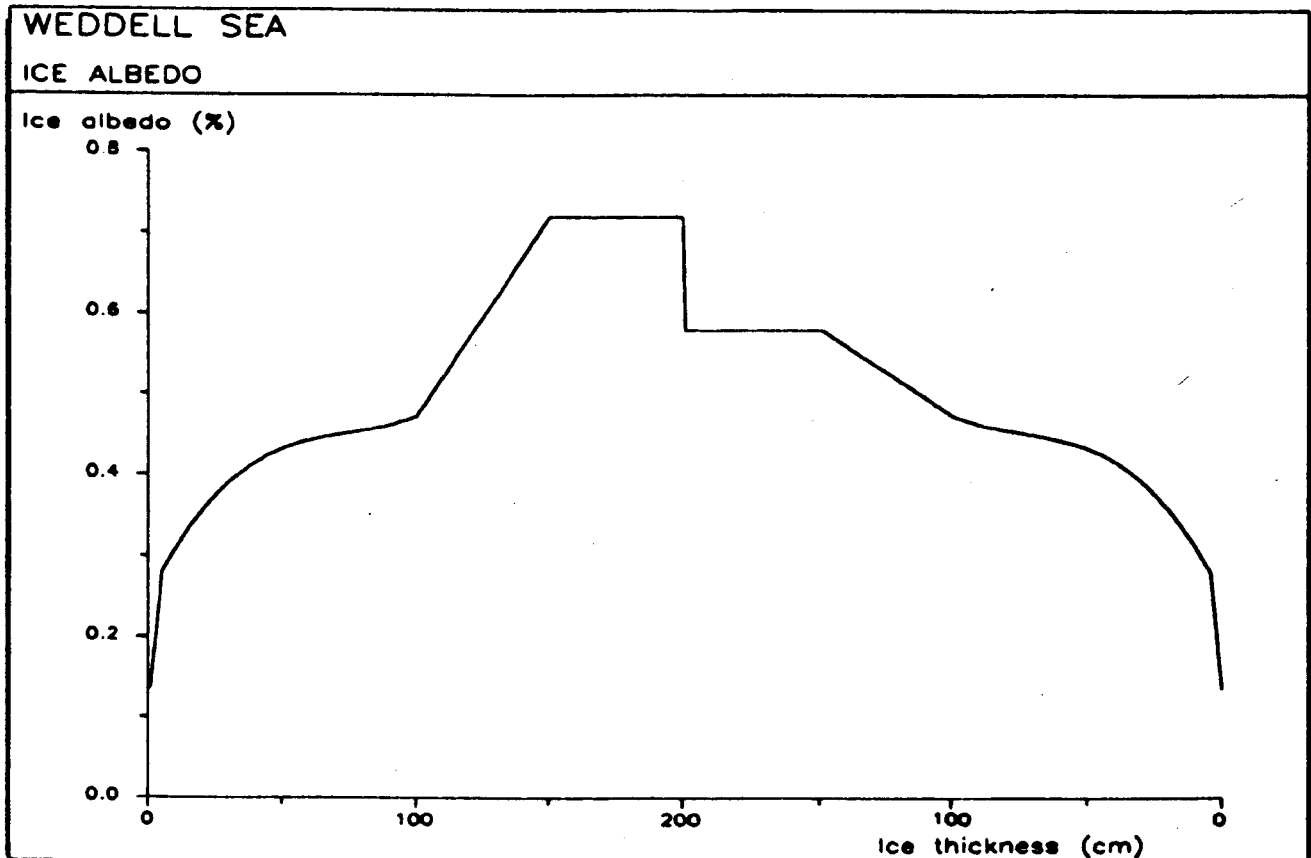

Figure 1: Ice albedo evolution (%) (the ice thickness
increases from 0 to 2 m and then, melts completely).

b) Oceanic mixed layer model

With or without ice, the upper layer of the ocean is assumed to be well mixed under the influence of the surface stresses, the heat fluxes and, if the seawater is freezing or the ice is melting, the salt fluxes. The temperature T_m and the salinity S_m are computed from the conservation laws integrated along the depth. The mixed layer depth h_m is the solution of a non linear equation proposed by Gaspar (1988). In this equation, the main turbulent structures of the oceanic mixed layer are taken into account.

The modifications introduced in this important component of SEAICE deal mainly with the vertical distribution of temperature and salinity during the shallowing of the mixed layer and with the computation of the salt exchanges between the ice and the mixed layer.

Concerning the vertical distribution of temperature and salinity, a peculiar attention has been paid to improve the conservation of heat and potential energy and the influence of the discontinuity between the mixed layer and the deep ocean.

At the ice-ocean interface, several MUMM experiments have clearly shown that the finite difference analog used to compute the salt flux was not enough accurate and that a second order approximation was necessary to ensure a better conservation of the total salt. In the new version of the model, the salt exchange is computed implicitly according to :

$$F_{salt}^{t+\Delta t} = \left(S_m^{t+\Delta t} - S_i \right) \frac{\partial M_i}{\partial t} \qquad (2.1)$$

where M_i is the mass of ice per unit area (*i.e* the product of the ice thickness h_i, the fractional ice cover A and the density $\rho_i = 900$ kg m^{-3}); S_m, the mixed layer salinity; S_i, the ice salinity and Δt, the time step.

All these modifications have significantly improved the model results. The range of variation of the mixed layer depth has been reduced. The mixed layer reaches no longer the sea bottom. The fields of the variables (surface temperature, mixed layer depth, ice thickness, ...) appear as being more smooth than with the previous version of the model.

Finally, the model can be run in a pure prognostic way without an excessive loss of heat and salt. Even if the so-called robust-diagnostic method is not used, the model results remain realistic. Recall that, in the robust-diagnostic method, a newtonian forcing term (proportional to the difference between computed and observed values and inversely proportional to a characteristic "damping" time) is added in the diffusion equations of salinity and temperature below the mixed

layer mostly to keep the solution as close as possible to the observations and to palliate the lack of horizontal effects.

2.2.2 Dynamic component

The ice velocity redistributes the ice mass created at the ocean surface. During this process, the ice mass per unit area M_i must be conserved according to the equation

$$\frac{\partial M_i}{\partial t} + \nabla \cdot \left(\underline{v_i}\, M_i \right) = 0 \qquad (2.2)$$

where $\underline{v_i}$ denotes the ice velocity.

This equation is divided into conservation laws for the ice thickness and the fractional ice cover. A similar conservation equation is used to compute the snow thickness.

The ice velocity $\underline{v_i}$ is deduced from the balance between wind and water drag and is expressed as a linear function of the geostrophic wind $\underline{v_a}$ and the ocean current $\underline{v_w}$:

$$\underline{v_i} = \alpha \exp\left(-i\beta \right) \underline{v_a} + \underline{v_w} \qquad (2.3)$$

where α is a scaling factor equal to 0.008 and β a rotation angle equal to 8 °(van Ypersele, 1986).

The weakness of the equation (2.3) is the ice velocity divergence which must be relatively small as long as the effects of internal ice resistance are not included. Indeed, the divergence of the wind speed must be nearly equal to zero and, except in the areas where strong up or downwellings occur, the divergence of the ocean current in the upper layer is also very small.

An analysis of the wind field and ocean current field used in SEAICE has shown that the divergence of the ice velocity could be too large in some parts of the computational domain.

To avoid artificial appearance or disappearance of ice due to unrealistic ice velocity divergence, the ice mass conservation law (2.2) is solved following the divergence-corrected approach proposed by Kitada (1987).

2.2.3 Sea-ice experiments

a) Statement of the problem

A set of experiments has been carried out with the modified SEAICE model. As in the first phase of the Belgian Scientific Research Programme on Antarctica, the area of interest is a sector of the Southern Ocean centered on the Weddell Sea and the Drake Passage. This area will be further described in the section 3.3.4 (applications of the 3D model to the Weddell Sea).

These experiments are similar to those discussed in Demuth and van Ypersele (1989). The model is forced with climatological atmospheric fields. The ice motion is induced by the surface current field obtained from the model of van Ypersele (1986) and by the wind velocity deduced from meteorological data. The results of the SEAICE model are compared to observations (Zwally *et al.*, 1983).

b) Experimental setup

A set of four experiments able to underline the different phenomena responsible for the sea ice formation has been performed. The following processes are taken into account :

1. the thermodynamics only,

2. the thermodynamics and the ice transport by wind,

3. the thermodynamics and the ice transport by wind and currents,

4. the same as "3" with a uniform atmospheric warming of 4K (this might be caused by a too high quantity of atmospheric CO_2).

The model uses a spherical grid of 1° latitude by 2° longitude. The time evolution of the salinity is constrained by a robust-diagnostic method, *i.e.*, a Newtonian forcing term in the diffusion equation for S. The damping time is constant and equals to 10 days to stay coherent with the results presented in Demuth and van Ypersele (1989). The temperature is left fully prognostic because of the dependence of the freezing point on salinity.

ANTAR
II/10

The snow fall is not taken into account in these simulations. As already mentioned, no sufficiently continuous formulation has been found for the snow albedo.

c) Results and conclusions

The main characteristics of the annual cycle of the effective ice area for the four simulations as well as the observations (Zwally *et al.*, 1983) are presented in Table I. The simplified dynamics improve the amplitude of seasonal cycle of sea ice extent by allowing ice expansion through transport. The hypothetical atmospheric warming diminishes the amplitude of the cycle. The annual cycle of the effective ice area during the fifth year of simulation is displayed on figure 2.

Table I: Comparison of sea-ice five-year simulations with observations (Zwally *et al.*, 1983).

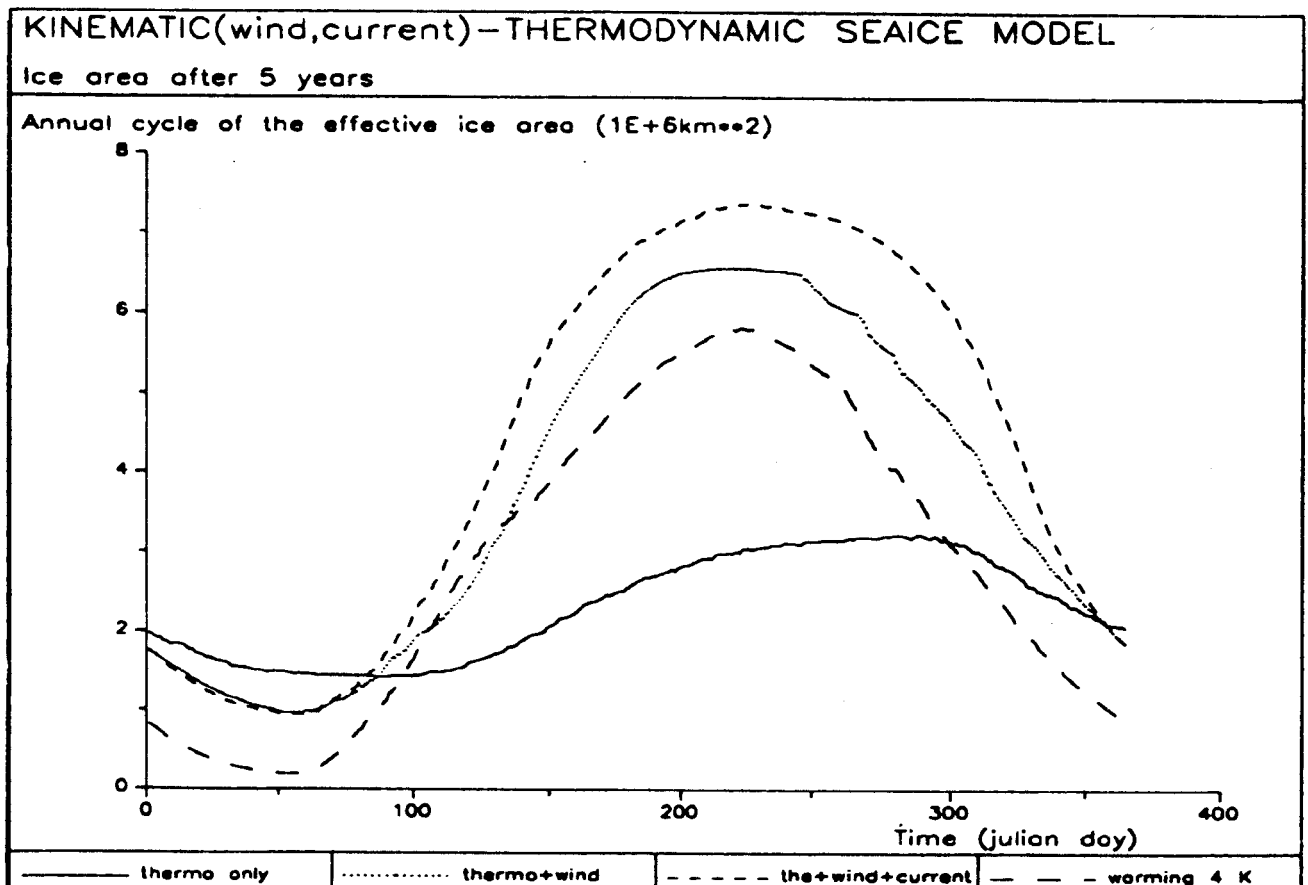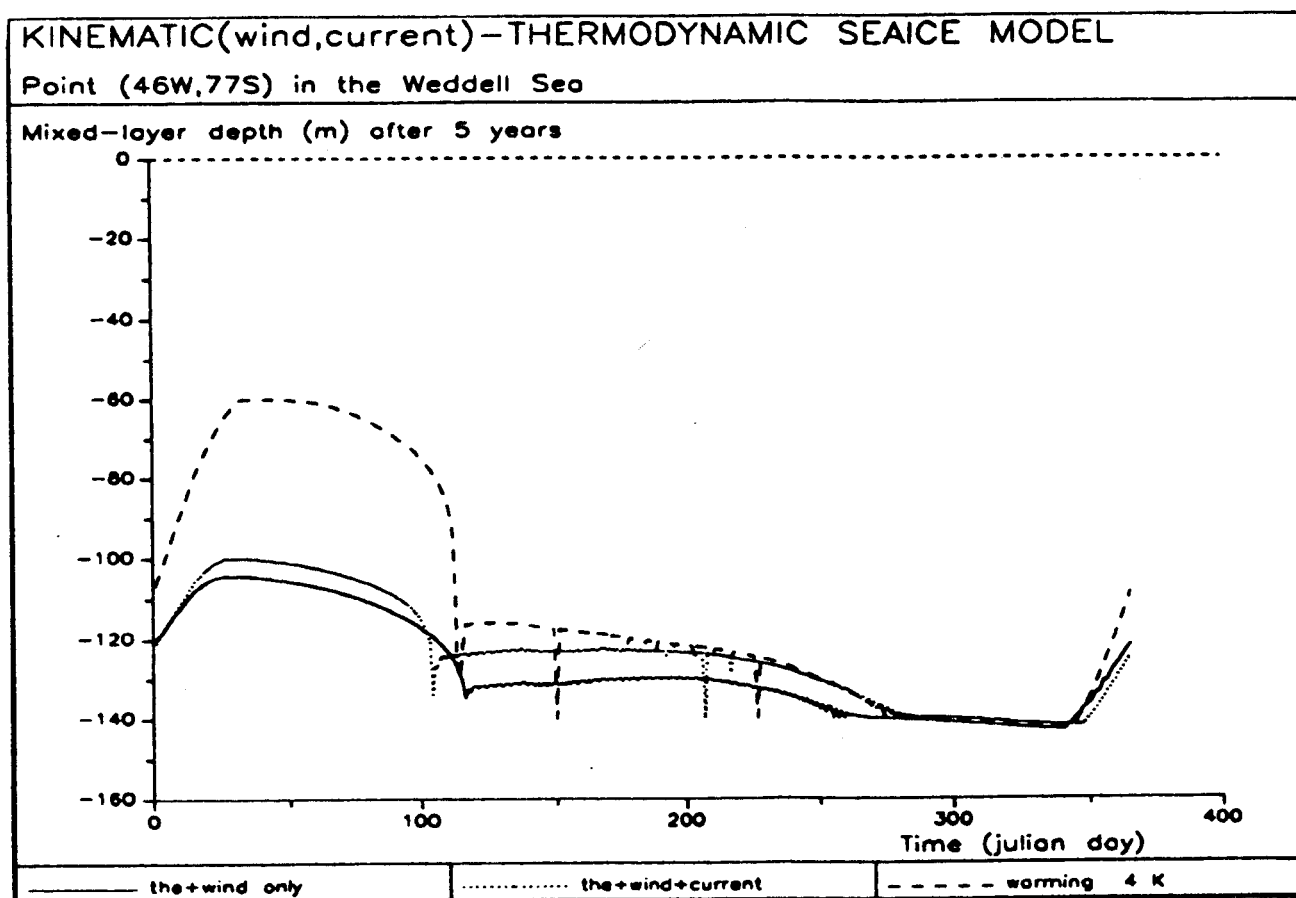|	Date$_{min}$	Area$_{min}$ (10^6 km^2)	Grow (days)	Date$_{max}$	Area$_{max}$ (10^6 km^2)	Decay (days)
Observations	Feb.15	0.8	210	Sep.15	5.2	155
Thermodynamics only	Mar.28	1.426	194	Oct.8	3.210	171
Thermodynamics + wind	Feb.26	0.947	163	Aug.8	6.547	202
Thermodynamics + wind + current	Feb.28	0.935	169	Aug.16	7.376	196
Thermodynamics + wind + current + 4K	Feb.24	0.190	169	Aug.14	5.820	196

Figure 2: Comparison of annual cycles of the effective ice area computed by the SEAICE model for the four proposed simulations after 5 years.

The time evolution of the mixed layer depth at two points of the Weddell Sea, coastal and offshore respectively are displayed on Figures 3 and 4. It is noticeable on these figures that the mixed layer depth evolves continuously and that it reaches no longer the sea bottom. The behaviour of the mixed layer depth can be summarized as follows :

1. a deepening : the ice formation rejects salt in the mixed layer which becomes heavier and deepens in the water column;

2. a shallowing corresponding to the spring ice melting.

KINEMATIC(wind,current)–THERMODYNAMIC SEAICE MODEL

Point (46W,77S) in the Weddell Sea

Mixed–layer depth (m) after 5 years

ANTAR
II/10

Time (julian day)

the+wind only   the+wind+current   warming 4 K

Figure 3: Comparison of annual mixed layer depth (m) cycles computed at the coastal point (46°W, 77°S) for the three proposed simulations.

12

KINEMATIC(wind,current)—THERMODYNAMIC SEAICE MODEL

Point (28W,66S) in the Weddell Sea

Mixed-layer depth (m) after 5 years
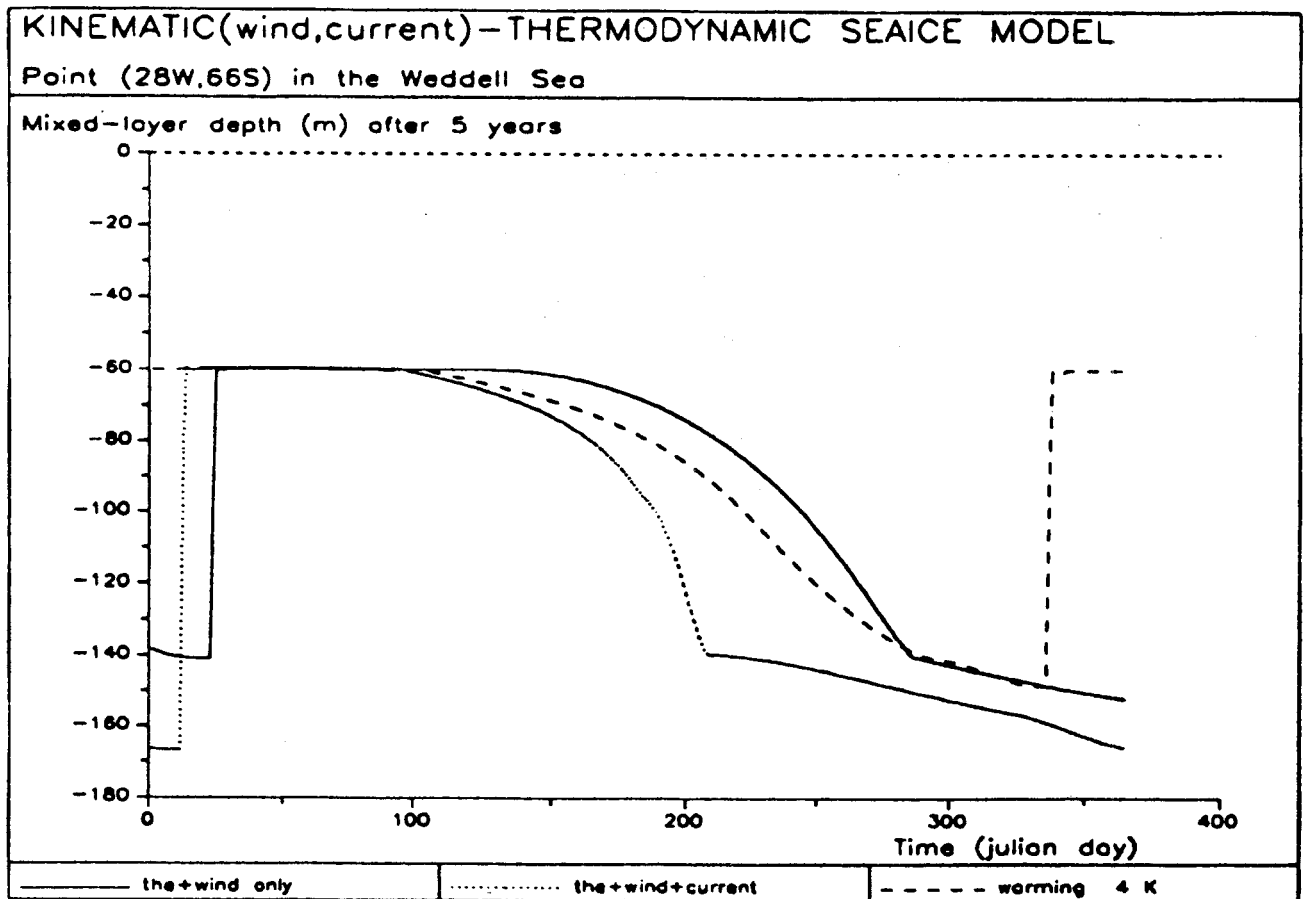
Figure 4: Comparison of annual mixed layer depth (m) cycles computed
at the offshore point (28°W, 66°S) for the three proposed simulations.

The figures (5, 6, 7 and 8) depict the surface repartition of representative variables (surface temperature, ice thickness, fractional ice cover, mixed layer depth) computed by the model at the end of September during the fifth year of a complete simulation, *i.e.*, forced by wind and current. The smooth and continuous distribution of the values of these variables is coherent with the averaged inputs used for the SEAICE model.

Table II summarizes the oceanic heat flux over the ice covered Weddell sector. The values are close to the estimated heat flux, which ranges from 9 to 16 Wm^{-2} (Gordon *et al.*, 1984).

Table II: Averaged oceanic heat flux (Wm^{-2}) for each year of simulation.

	1st year	2nd year	3rd year	4th year	5th year
Thermodynamics only	19.942	21.226	15.620	27.672	19.417
Thermodynamics + wind	24.344	14.260	13.672	12.920	17.382
Thermodynamics + wind + current	25.310	18.236	16.447	20.661	15.216
Thermodynamics + wind + current + 4K	20.064	19.596	21.626	18.015	17.888

The Antarctic sea ice cannot be modelled properly with thermodynamics only. The ice dynamics play an important role. Due to the wind and oceanic currents, the ice can be transported far from its point of formation.

The model is very sensitive to the amount of salt rejected by the ice. This aspect had already been underlined in the beginning of this paper with the correction of the salt exchanges. In the applications discussed in this section, the ice salinity has been set equal to 4 $^0/_{00}$. Numerical experiments have been performed using other values. These applications have underlined that a reduction of the ice salinity tends to decrease the ice thickness and that, a contrario, ice thickness grows if a higher ice salinity is chosen. A possible explanation of this process could be : when a low value is chosen for the ice salinity, the salinity of the mixed layer tends to remain higher and, as a consequence, the freezing temperature decreases, which slows down ice formation.

ANTAR
II/10

Consequently, since the salt distribution plays a so significant role, it can be argued that the horizontal diffusion and advection in the conservation equation of salt are necessary to improve the accuracy of the model : this kind of study must evolve to a sea ice model fully coupled to a 3D hydrodynamic model. It is the purpose of the following part of this paper. Anyway, if the ocean polynya are really caused by convection moving, a complete model is a way to understand the formation of these ice free areas.

3 Circulation models

3.1 Introduction

As explained above, the SEAICE model gathers the thermodynamic processes related to the freezing and the melting of ice with only one dynamic process, corresponding to the movement of the ice under the combined action of wind and oceanic surface current. Associated to this dynamic process, the heat and salt transfers from the sea surface to the bottom, through the ice and the mixed layer, are vertically modelled at each point of the ocean, when this one is considered at rest and described by temperature and salt fields known from the climatological data. The model does not take into account the horizontal exchanges of heat and salt inside the ocean. The only horizontal connection is made by the ice motion at the sea surface. The state of each water column changes independently of the closest columns, except if the sea surface is covered by the ice.

The necessity of a 3D model is quite obvious to understand, following the improvements brought in the SEAICE model. We have shown that the ice dynamics need very accurate ocean currents to represent the ice transport in a proper way.

The temperature and the salinity in and below the mixed layer evolve according to equations limited to the vertical terms. However, several tests and simulations with the SEAICE model have proved the very high sensitivity of the ice thickness and mixed layer evolutions to the salinity. For the purpose of obtaining better results, we must include the horizontal diffusion and advection in the salt equation.

From the energetic point of view, the weakness of an equation of temperature reduced to vertical terms appears near the ice pack limit. Indeed, under the ice, the mixed layer temperature equals the freezing temperature of water (about 2°C below zero) whereas in the free ice area, the sea surface temperature is higher than this value (sometimes largely). This discontinuity is not acceptable because the ice free meshes along the ice pack limit are likely to receive ice by dynamic effects. However, this ice does not transport its sea ice interface temperature because of the lack of horizontal terms in the temperature equation. At certain points, the ice thickness and the sea temperature are thus not thermodynamically compatible. To preserve the consistency of these two variables, an artifice is used to correct the sea temperature along the ice pack limit before computing the ice thermodynamics. The temperature is approximated by the average

of the sea ice interface temperatures of the nearest meshes covered by ice. The only "proper" method to take all these phenomena into account is a fully 3D model.

3.2 2.5D model

3.2.1 Preliminaries

The development of a numerical code capable of modelling the oceanic circulation in the Weddell Sea has been divided into two phases. At first, a model, named 2.5D model, has been developed. It is able to simulate the circulation in a vertical plane, defined by the depth (z) and one horizontal direction, while retaining the three components of the velocity vector and the Coriolis parametre. The obtained current field is the hydrodynamic response of the ocean either to the wind forcing (barotropic circulation) or/and to variations of the temperature and salinity (baroclinic circulation). The introduction of the third dimension in the numerical code, second part of the modelling, has led, after major adaptations, to a fully 3D model. In this study, the circulation driven by the wind will only be considered so as not to mix all numerical problems.

The 2.5D and the 3D model are built on the same equations. Therefore, the numerical method will be presented in details for the 2.5D vertical plane model only. This 2.5D model will be used to obtain the barotropic circulation in a coastal zone of the Adélie Land, the wind over the sea being deduced from the katabatic wind model developed by Gallée *et al.* (1989). On this occasion, the 2.5D vertical plane model (MUMM model) will be compared to a similar model developed by Fettweis *et al.* (1991) (KUL model) in the framework of the Belgian Scientific Research Programme on Antarctica. The results obtained by these models will be also compared when the katabatic wind is blowing across a coastal basin with a flat bottom. Other results can be found in Fettweis *et al.* (1991) when the bottom is variable.

3.2.2 Governing equations

The local hydrodynamic and thermodynamic state at any point in the fluid flow field can be determined by the solution of the three-dimensional, time-dependent, non linear Navier-Stokes equations describing the conservation of mass, momentum, temperature and salinity. In order to simplify the set of equations, several assumptions are made for the 2.5D and 3D models :

1. The flow is studied within the approximation of the tangent plane. This assumption means that the ocean is described by a half space Oxyz, where the z-coordinate is in the downward vertical direction (z=0 at the surface, z=h at the bottom).

2. The pressure is hydrostatic.

3. The Boussinesq approximation, meaning that density variations can be neglected except in the gravitational acceleration term, is made.

4. The zero[th]-order turbulent closure has been chosen by using the eddy coefficient concept, which is analogous to a laminar fluid description with respect to the diffusion terms. The horizontal eddy coefficient is taken as constant and isotropic, and the vertical eddy coefficient can be made a function of time, vertical coordinate and/or flow variables.

5. The Coriolis parametre is taken as constant.

In addition, in the 2.5D model, all the variables, except the pressure, are assumed to be uniform in one of the horizontal direction, taken as being the y-axis. Hence, the domain of interest reduces to a vertical plane perpendicular to this direction. The model, however, does not reduce to a conventional standard "x-z" model. The three components of the velocity vector are calculated and the Coriolis acceleration is included in the momentum equations. The pressure gradient in the direction perpendicular to the plane can be set equal to zero, computed by means of an additional assumption (e.g., zero net flux in the y-direction) or prescribed on the basis of available observations or other model results.

With the above assumptions, in a right-handed coordinate system with the z-axis pointing downwards, the governing equations are :

$$\frac{\partial u}{\partial t} + \frac{\partial u^2}{\partial x} + \frac{\partial wu}{\partial z} + fv = -\frac{1}{\rho_0}\frac{\partial p}{\partial x} + \frac{\partial}{\partial x}\left(A_h\frac{\partial u}{\partial x}\right) + \frac{\partial}{\partial z}\left(A_v\frac{\partial u}{\partial z}\right) \tag{3.1}$$

$$\frac{\partial v}{\partial t} + \frac{\partial uv}{\partial x} + \frac{\partial wv}{\partial z} - fu = -\frac{1}{\rho_0}\frac{\partial p}{\partial y} + \frac{\partial}{\partial x}\left(A_h\frac{\partial v}{\partial x}\right) + \frac{\partial}{\partial z}\left(A_v\frac{\partial v}{\partial z}\right) \tag{3.2}$$

$$\frac{1}{\rho}\frac{\partial p}{\partial z} = g \tag{3.3}$$

$$\frac{\partial u}{\partial x} + \frac{\partial w}{\partial z} = 0 \tag{3.4}$$

$$\frac{\partial T}{\partial t} + \frac{\partial uT}{\partial x} + \frac{\partial wT}{\partial z} = \frac{\partial}{\partial x}\left(K_{Th}\frac{\partial T}{\partial x}\right) + \frac{\partial}{\partial z}\left(K_{Tv}\frac{\partial T}{\partial z}\right) \tag{3.5}$$

$$\frac{\partial S}{\partial t} + \frac{\partial uS}{\partial x} + \frac{\partial wS}{\partial z} = \frac{\partial}{\partial x}\left(K_{Sh}\frac{\partial S}{\partial x}\right) + \frac{\partial}{\partial z}\left(K_{Sv}\frac{\partial S}{\partial z}\right) \tag{3.6}$$

To close the system, we add a state equation of the type

$$\rho = \rho(T, S, p) \tag{3.7}$$

where t denotes the time; u, v and w, the $x-$, $y-$ and $z-$components of the velocity vector; f, the Coriolis parametre; g, the acceleration due to gravity; p, the pressure; ρ, the density; A_h and A_v, the horizontal and vertical eddy viscosity coefficients for the velocity, respectively; T and S, the temperature and the salinity; $K_{T,S\ h}$ and $K_{T,S\ v}$, the horizontal and vertical eddy viscosity coefficients for the temperature and the salinity, respectively.

The seven dependent variables of this model, *i.e.*, u, v, w, T, S, p and ρ are to be calculated as functions of x, z and t only. The one term in the equations which involves a derivative with respect to y, *i.e.*, $\partial p / \partial y$, can be a forcing for this model or deduced from special conditions. The thermodynamic aspect of the circulation (T, S) is not envisaged in this paper.

For the horizontal components of the velocity vector, the following boundary conditions are used :

1. along the lateral solid boundaries,

$$u = v = 0 \ ; \tag{3.8}$$

2. at the bottom, we can impose the same condition as for the lateral solid boundaries (no-slip condition)

$$u = v = 0 \tag{3.9}$$

or specify the tangential stress exerted by the current on the bottom by a linear or quadratic law of the bottom current (slip condition);

3. at the surface, the tangential force exerted by the wind on the water is specified :

$$-A_v \frac{\partial u}{\partial z} = \frac{\tau_x}{\rho_0} \tag{3.10}$$

$$-A_v \frac{\partial v}{\partial z} = \frac{\tau_y}{\rho_0} \tag{3.11}$$

where τ_x, τ_y are the components of the wind stress.

For the vertical component of the velocity which is determined from equation (3.4), no lateral boundary conditions are required. The top and bottom conditions are :

1. at the bottom

$$w = 0 ; \qquad (3.12)$$

2. at the surface

$$\text{either } w = 0 \text{ for the rigid lid assumption} \qquad (3.13)$$

$$\text{or } w = \frac{\partial \eta}{\partial t} \text{ for the free surface condition,} \qquad (3.14)$$

where η denotes the sea surface elevation below the mean sea level.

3.2.3 The vertical equilibrium

The equation (3.3) can be integrated along the z-coordinate :

$$p = p_s + g \int_0^z \rho \, dz \qquad (3.15)$$

where $p_s(x, y, t)$ is the surface pressure depending on the horizontal coordinates and the time.

The nature of the surface conditions better specifies p_s. With the "rigid lid" assumption, the pressure p_s represents the pressure exerted by the ocean on the lid. In case of "free surface" assumption, p_s is the sum of the atmospheric pressure and the pressure due to the elevation, $-\rho_0 g \eta$.

3.2.4 The sigma (stretched vertical) coordinate system

The original equations are first transformed from a Cartesian coordinate system into a sigma coordinate system. The (x, y, z) coordinate system is transformed into the (α, β, σ) coordinate system where

$$\alpha = x , \qquad (3.16)$$

$$\beta = y \qquad (3.17)$$

and

$$\sigma = \frac{z}{h(x)} \; .$$

(3.18)

By renaming α and β , x and y again for the sake of clarity, the transformed momentum and continuity equations can be written as :

$$\frac{\partial u}{\partial t} + \frac{\partial \Omega u}{\partial \sigma} + fv = -\frac{1}{\rho_o}\frac{\partial p}{\partial x} + \frac{1}{h}\frac{\partial}{\partial \sigma}\left(\frac{A_{eff}}{h}\frac{\partial u}{\partial \sigma}\right) + F_x$$

(3.19)

$$\frac{\partial v}{\partial t} + \frac{\partial \Omega v}{\partial \sigma} - fu = -\frac{1}{\rho_o}\frac{\partial p}{\partial y} + \frac{1}{h}\frac{\partial}{\partial \sigma}\left(\frac{A_{eff}}{h}\frac{\partial v}{\partial \sigma}\right) + F_y$$

(3.20)

where

$$F_x = -\frac{1}{h}\frac{\partial hu^2}{\partial x} + \frac{1}{h}\frac{\partial}{\partial x}\left[A_h\frac{\partial hu}{\partial x} - A_h h'\frac{\partial \sigma u}{\partial \sigma}\right] - \frac{1}{h}\frac{\partial}{\partial \sigma}\left[A_h h'\frac{\partial \sigma u}{\partial x}\right]$$

(3.21)

$$F_y = -\frac{1}{h}\frac{\partial huv}{\partial x} + \frac{1}{h}\frac{\partial}{\partial x}\left[A_h\frac{\partial hv}{\partial x} - A_h h'\frac{\partial \sigma v}{\partial \sigma}\right] - \frac{1}{h}\frac{\partial}{\partial \sigma}\left[A_h h'\frac{\partial \sigma v}{\partial x}\right]$$

(3.22)

$$\frac{\partial p}{\partial \sigma} = \rho g h$$

(3.23)

$$\frac{1}{h}\frac{\partial hu}{\partial x} + \frac{\partial \Omega}{\partial \sigma} = 0$$

(3.24)

with

$$h' = \frac{\partial h}{\partial x} \; ,$$

(3.25)

$$A_{eff} = A_v + A_h\left(h'\sigma\right)^2$$

(3.26)

and

$$\Omega = \frac{1}{h}\left[w - \sigma u h'\right].$$

(3.27)

3.2.5 Numerical procedure

The numerical procedure for the solution of the set of equations 3.19 to 3.24 is based on the work of Paul and co-workers (e.g., Paul and Lick, 1981; Jamart *et al.*, 1982). In the following development, the handling of the momentum equations and the pressure equation will be discussed after a presentation of the numerical grid.

The time derivatives are approximated by forward finite differences. The spatial derivatives are approximated by central finite differences except at the upper and lower boundaries where a second-order accurate finite difference analog is used to compute the vertical derivatives.

a) Numerical grid

The arrangement of the grid lattice used is presented in Figure 9. The grid points are staggered on a lattice of type B (Arakawa, 1972). Each mesh is limited by a continuous line. The horizontal components of the velocity, u and v, are located at the mesh corners (white square on the Figure 9) and the vertical component w is located at the centre (black square) but with a supplementary point at the middle of the horizontal face at the surface level. It is also at this surface point that the pressure and the elevation are computed. The temperature and the salinity are located at the centre of a each rectangle mesh.
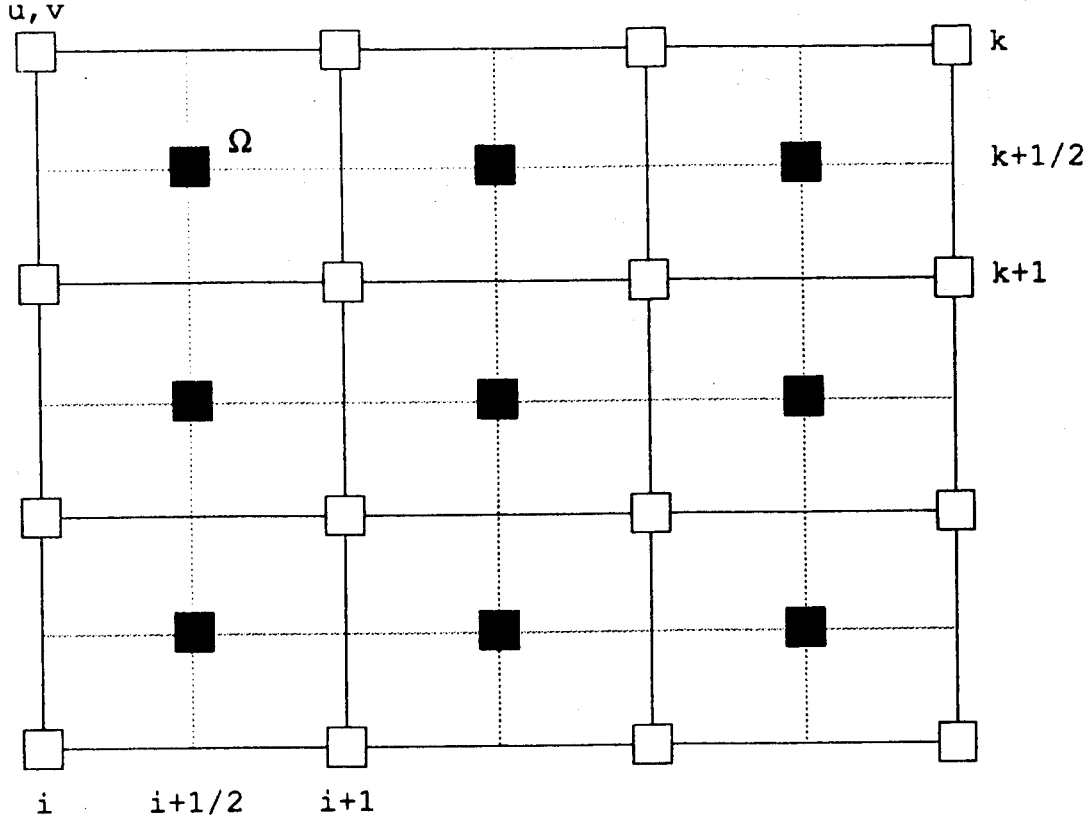
Figure 9: Numerical grid.

b) Momentum equations

Away from the boundaries, with k, i and L indexing the σ, x and t coordinates, respectively, and without spelling out the discrete representations of the explicit terms and of the pressure gradient, the finite difference approximations to equations (3.19) and (3.20) are

$$
\frac{u_{k,i}^{L+1} - u_{k,i}^L}{\Delta t} + \Theta_A \frac{1}{2\Delta\sigma} \left[\bar{\Omega}_{k+1/2,i}^L \left[u_{k+1,i}^{L+1} + u_{k,i}^{L+1} \right] - \bar{\Omega}_{k-1/2,i}^L \left[u_{k,i}^{L+1} + u_{k-1,i}^{L+1} \right] \right]
$$

$$
+ \Theta_x f v_{k,i}^{L+1} + \Theta_{Px} \frac{1}{\rho_o} \left[\frac{\partial p}{\partial x} \right]_i^{L+1}
$$

$$
- \Theta_D \frac{1}{(h_i \Delta\sigma)^2} \left[A_{eff_{k+1/2,i}} \left[u_{k+1,i}^{L+1} - u_{k,i}^{L+1} \right] - A_{eff_{k-1/2,i}} \left[u_{k,i}^{L+1} - u_{k-1,i}^{L+1} \right] \right]
$$

$$
= -(1 - \Theta_A) \frac{1}{2\Delta\sigma} \left[\bar{\Omega}_{k+1/2,i}^L \left[u_{k+1,i}^L + u_{k,i}^L \right] - \bar{\Omega}_{k-1/2,i}^L \left[u_{k,i}^L + u_{k-1,i}^L \right] \right]
$$

$$
- (1 - \Theta_x) f v_{k,i}^L - (1 - \Theta_{Px}) \frac{1}{\rho_0} \left[\frac{\partial p}{\partial x} \right]_i^L
$$

$$
+ (1 - \Theta_D) \frac{1}{(h_i \Delta\sigma)^2} \left[A_{eff_{k+1/2,i}} \left[u_{k+1,i}^L - u_{k,i}^L \right] - A_{eff_{k-1/2,i}} \left[u_{k,i}^L - u_{k-1,i}^L \right] \right]
$$

$$
+ [F_x]_{k,i}^L \tag{3.28}
$$

$$
\frac{v_{k,i}^{L+1} - v_{k,i}^L}{\Delta t} + \Theta_A \frac{1}{2\Delta\sigma} \left[\bar{\Omega}_{k+1/2,i}^L \left[v_{k+1,i}^{L+1} + v_{k,i}^{L+1} \right] - \bar{\Omega}_{k-1/2,i}^L \left[v_{k,i}^{L+1} + v_{k-1,i}^{L+1} \right] \right]
$$

$$- \Theta_y f u_{k,i}^{L+1} + \Theta_{Py} \frac{1}{\rho_0} \left[\frac{\partial p}{\partial y} \right]_i^{L+1}$$

$$- \Theta_D \frac{1}{(h_i \Delta \sigma)^2} \left[A_{eff_{k+1/2,i}} \left[v_{k+1,i}^{L+1} - v_{k,i}^{L+1} \right] - A_{eff_{k-1/2,i}} \left[v_{k,i}^{L+1} - v_{k-1,i}^{L+1} \right] \right]$$

$$= -(1 - \Theta_A) \frac{1}{2\Delta \sigma} \left[\bar{\Omega}_{k+1/2,i}^{L} \left[v_{k+1,i}^{L} + v_{k,i}^{L} \right] - \bar{\Omega}_{k-1/2,i}^{L} \left[v_{k,i}^{L} + v_{k-1,i}^{L} \right] \right]$$

$$+ (1 - \Theta_y) f u_{k,i}^{L} - \left(1 - \Theta_{Py} \right) \frac{1}{\rho_0} \left[\frac{\partial p}{\partial y} \right]_i^{L}$$

$$+ (1 - \Theta_D) \frac{1}{(h_i \Delta \sigma)^2} \left[A_{eff_{k+1/2,i}} \left[v_{k+1,i}^{L} - v_{k,i}^{L} \right] - A_{eff_{k-1/2,i}} \left[v_{k,i}^{L} - v_{k-1,i}^{L} \right] \right]$$

$$+ [F_y]_{k,i}^{L} \tag{3.29}$$

The overbar denotes a linear interpolation in the horizontal direction and the various Θ_S' are the parametres which determine the degree of implicitness with which different terms are evaluated. At the upper and the lower boundaries, the derivatives with respect to σ are approximated by second-order accurate, one-sided expressions.

A simple representation of the set discretized momentum equations at point x_i, in matrix form, is (kl and nl are the total numbers of discrete $u - v$ points respectively in the $\sigma-$ and the x–direction.) :

$$A\vec{u} + \Theta_x f\vec{v} = \vec{U} + \vec{G} - \Theta_{Px} \frac{1}{\rho_0} \left[\frac{\partial p}{\partial x} \right]^{L+1} \vec{I} \tag{3.30}$$

$$A\vec{v} - \Theta_y f\vec{u} = \vec{V} + \vec{F} - \Theta_{Py} \frac{1}{\rho_0} \left[\frac{\partial p}{\partial y} \right]^{L+1} \vec{I} \tag{3.31}$$

where

$$\vec{u} = \begin{bmatrix} u_{1,i}^{L+1} \\ u_{2,i}^{L+1} \\ \cdot \\ \cdot \\ \cdot \\ u_{kl-1,i}^{L+1} \end{bmatrix} \qquad \vec{v} = \begin{bmatrix} v_{1,i}^{L+1} \\ v_{2,i}^{L+1} \\ \cdot \\ \cdot \\ \cdot \\ v_{kl-1,i}^{L+1} \end{bmatrix} \tag{3.32}$$

$$\vec{U} = \frac{1}{\Delta t} \begin{bmatrix} u_{1,i}^{L} \\ u_{2,i}^{L} \\ \cdot \\ \cdot \\ \cdot \\ u_{kl-1,i}^{L} \end{bmatrix} \qquad \vec{V} = \frac{1}{\Delta t} \begin{bmatrix} v_{1,i}^{L} \\ v_{2,i}^{L} \\ \cdot \\ \cdot \\ \cdot \\ v_{kl-1,i}^{L} \end{bmatrix} \tag{3.33}$$

$$\vec{G} = \begin{bmatrix} g_{1,i}^L + [F_x]_{1,i}^L \\ g_{2,i}^L + [F_x]_{2,i}^L \\ \cdot \\ \cdot \\ \cdot \\ g_{kl-1,i}^L + [F_x]_{kl-1,i}^L \end{bmatrix} \qquad \vec{F} = \begin{bmatrix} f_{1,i}^L + [F_y]_{1,i}^L \\ f_{2,i}^L + [F_y]_{2,i}^L \\ \cdot \\ \cdot \\ \cdot \\ f_{kl-1,i}^L + [F_y]_{kl-1,i}^L \end{bmatrix} \tag{3.34}$$

$$A = \begin{bmatrix} \tilde{b}_1 & \tilde{c}_1 & \tilde{e}_1 & & & & \\ a_2 & b_2 & c_2 & & & & \\ \cdot & \cdot & \cdot & & & \\ & \cdot & \cdot & \cdot & & \\ & & a_k & b_k & c_k & & \\ & & & \cdot & \cdot & \cdot & \\ & & & & \cdot & \cdot & \\ & & & & & a_{kl-1} & b_{kl-1} \end{bmatrix} \qquad \vec{I} = \begin{bmatrix} 1 \\ 1 \\ \cdot \\ \cdot \\ \cdot \\ 1 \end{bmatrix}. \tag{3.35}$$

The coefficients which have been introduced are given by

$$\tilde{b}_1 = \frac{1}{\Delta t} + \Theta_A \frac{1}{\Delta\sigma}\left[\frac{3}{2}\bar{\Omega}_{3/2,i}^L - \frac{8}{3}\bar{\Omega}_{1,i}^L\right] + \Theta_D \frac{3}{(h_i\Delta\sigma)^2}A_{eff_{3/2,i}} \tag{3.36}$$

$$\tilde{c}_1 = \Theta_A \frac{1}{\Delta\sigma}\left[\frac{3}{2}\bar{\Omega}_{3/2,i}^L - \frac{1}{6}\bar{\Omega}_{5/2,i}^L\right] - \Theta_D \frac{1}{(h_i\Delta\sigma)^2}\left[3A_{eff_{3/2,i}} + \frac{1}{3}A_{eff_{5/2,i}}\right] \tag{3.37}$$

$$e_1 = -\Theta_A \frac{1}{6\Delta\sigma}\bar{\Omega}_{5/2,i}^L + \Theta_D \frac{1}{3(h_i\Delta\sigma)^2}A_{eff_{5/2,i}} \tag{3.38}$$

$$a_k = -\Theta_A \frac{1}{2\Delta\sigma}\bar{\Omega}_{k-1/2,i}^L - \Theta_D \frac{1}{(h_i\Delta\sigma)^2}A_{eff_{k-1/2,i}} \tag{3.39}$$

$$b_k = \frac{1}{\Delta t} + \Theta_A \frac{1}{2\Delta\sigma}\left[\bar{\Omega}_{k+1/2,i}^L - \bar{\Omega}_{k-1/2,i}^L\right]$$
$$+ \Theta_D \frac{1}{(h_i\Delta\sigma)^2}\left[A_{eff_{k+1/2,i}} + A_{eff_{k-1/2,i}}\right] \tag{3.40}$$

$$c_k = \Theta_A \frac{1}{\Delta\sigma}\bar{\Omega}_{k+1/2,i}^L - \Theta_D \frac{1}{(h_i\Delta\sigma)^2}A_{eff_{k+1/2,i}} \tag{3.41}$$

$$g_{1,i}^L = -(1-\Theta_A)\frac{1}{\Delta\sigma}\{\frac{3}{2}\bar{\Omega}_{3/2,i}^L\left(u_{2,i}^L+u_{1,i}^L\right)$$

$$-\frac{8}{3}\bar{\Omega}_{1,i}^L u_{1,i}^L - \frac{1}{6}\bar{\Omega}_{5/2,i}^L\left(u_{3,i}^L+u_{2,i}^L\right)\}$$

$$-(1-\Theta_x)fv_{1,i}^L - (1-\Theta_{Px})\frac{1}{\rho_0}\left[\frac{\partial p}{\partial x}\right]_i^L$$

$$+(1-\Theta_D)\frac{1}{h_i\Delta\sigma}\{\frac{3}{h_i\Delta\sigma}A_{eff_{3/2,i}}\left(u_{2,i}^L-u_{1,i}^L\right)$$

$$+\frac{8}{3}\frac{1}{\rho_0}\tau_{w_i}^{xL} - \frac{1}{3h_i\Delta\sigma}A_{eff_{5/2,i}}\left(u_{3,i}^L-u_{2,i}^L\right)\}$$

$$+\Theta_D\frac{1}{h_i\Delta\sigma}\frac{8}{3}\frac{1}{\rho_0}\tau_{w_i}^{xL+1} \qquad (3.42)$$

$$g_{k,i}^L = -(1-\Theta_A)\frac{1}{2\Delta\sigma}\left[\bar{\Omega}_{k+1/2,i}^L\left(u_{k+1,i}^L+u_{k,i}^L\right) - \bar{\Omega}_{k-1/2,i}^L\left(u_{k,i}^L+u_{k-1,i}^L\right)\right]$$

$$-(1-\Theta_x)fv_{k,i}^L - (1-\Theta_{Px})\frac{1}{\rho_0}\left[\frac{\partial p}{\partial x}\right]_i^L$$

$$+(1-\Theta_D)\frac{1}{(h_i\Delta\sigma)^2}[A_{eff_{k+1/2,i}}\left(u_{k+1,i}^L-u_{k,i}^L\right)$$

$$-A_{eff_{k-1/2,i}}\left(u_{k,i}^L-u_{k-1,i}^L\right)] \qquad (3.43)$$

$$f_{1,i}^L = -(1-\Theta_A)\frac{1}{\Delta\sigma}\{\frac{3}{2}\bar{\Omega}_{3/2,i}^L\left(v_{2,i}^L+v_{1,i}^L\right)$$

$$-\frac{8}{3}\bar{\Omega}_{1,i}^L v_{1,i}^L - \frac{1}{6}\bar{\Omega}_{5/2,i}^L\left(v_{3,i}^L+v_{2,i}^L\right)\}$$

$$+(1-\Theta_y)fu_{1,i}^L - (1-\Theta_{Py})\frac{1}{\rho_0}\left[\frac{\partial p}{\partial y}\right]_i^L$$

$$+(1-\Theta_D)\frac{1}{h_i\Delta\sigma}\{\frac{3}{h_i\Delta\sigma}A_{eff_{3/2,i}}\left(v_{2,i}^L-v_{1,i}^L\right)$$

$$+\frac{8}{3}\frac{1}{\rho_0}\tau_{w_i}^{yL} - \frac{1}{3h_i\Delta\sigma}A_{eff_{5/2,i}}\left(v_{3,i}^L-v_{2,i}^L\right)\}$$

$$+\Theta_D\frac{1}{h_i\Delta\sigma}\frac{8}{3}\frac{1}{\rho_0}\tau_{w_i}^{yL+1} \qquad (3.44)$$

$$f_{k,i}^L = -(1-\Theta_A)\frac{1}{2\Delta\sigma}\left[\bar{\Omega}_{k+1/2,i}^L\left(v_{k+1,i}^L+v_{k,i}^L\right) - \bar{\Omega}_{k-1/2,i}^L\left(v_{k,i}^L+v_{k-1,i}^L\right)\right]$$

$$+(1-\Theta_y)fu_{k,i}^L - (1-\Theta_{Py})\frac{1}{\rho_0}\left[\frac{\partial p}{\partial y}\right]_i^L$$

$$+(1-\Theta_D)\frac{1}{(h_i\Delta\sigma)^2}[A_{eff_{k-1/2,i}}\left(v_{k+1,i}^L-v_{k,i}^L\right)$$

$$-A_{eff_{k-1/2,i}}\left(v_{k,i}^L-v_{k-1,i}^L\right)] \qquad (3.45)$$

Since the discretized equations are linear in $\vec{u}$ and $\vec{v}$, the horizontal velocities at the new time level can be decomposed into a component (*) which does not depend on the unknown pressure gradient and a component (') which depends on the unknown pressure gradient :

$$\vec{u} = \vec{u}^* + \vec{u}' \tag{3.46}$$

$$\vec{v} = \vec{v}^* + \vec{v}' \tag{3.47}$$

where the individual components satisfy

$$A\vec{u}^* + \Theta_x f \vec{v}^* = \vec{U} + \vec{G} \tag{3.48}$$

$$A\vec{v}^* - \Theta_y f \vec{u}^* = \vec{V} + \vec{F} \tag{3.49}$$

$$A\vec{u}' + \Theta_x f \vec{v}' = -\Theta_{Px} \frac{1}{\rho_0} \left[\frac{\partial p}{\partial x}\right]^{L+1} \vec{I} \tag{3.50}$$

$$A\vec{v}' - \Theta_y f \vec{u}' = -\Theta_{Py} \frac{1}{\rho_0} \left[\frac{\partial p}{\partial y}\right]^{L+1} \vec{I} \tag{3.51}$$

The computation of $\vec{u}^*$ and $\vec{v}^*$ requires the solutions of a pair of pentadiagonal systems.

c) **Pressure gradient**

The next step is to derive an equation for the pressure. Formally, the solution $\vec{u}'$ and $\vec{v}'$ of equations (3.50) and (3.51) can be written as

$$\vec{u}' = \Theta_x f \Theta_{Py} \frac{1}{\rho_0} \left[\frac{\partial p}{\partial y}\right]^{L+1} \vec{\lambda}^A - \Theta_{Px} \frac{1}{\rho_0} \left[\frac{\partial p}{\partial x}\right]^{L+1} \vec{\lambda}^B \tag{3.52}$$

$$\vec{v}' = -\Theta_y f \Theta_{Px} \frac{1}{\rho_0} \left[\frac{\partial p}{\partial x}\right]^{L+1} \vec{\lambda}^A - \Theta_{Py} \frac{1}{\rho_0} \left[\frac{\partial p}{\partial y}\right]^{L+1} \vec{\lambda}^B \tag{3.53}$$

where $\vec{\lambda}^A$ and $\vec{\lambda}^B$ satisfy

$$[AA + \Theta_x \Theta_y f^2 I]\vec{\lambda}^A = \vec{I} \tag{3.54}$$

$$[AA + \Theta_x \Theta_y f^2 I]\vec{\lambda}^B = A\vec{I} \tag{3.55}$$

With the rigid lid assumption and as long as at least one of the lateral boundaries consists of a wall, the transport in the x-direction vanishes everywhere

$$\sum_{k=1}^{kl-1} W_k u_{k,j}^{L+1} = 0 \qquad j = 2, ..., nl-1 \qquad (3.56)$$

where W_k are the weights used for the numerical integration along the vertical. In this summation, we take into account the no slip condition at the bottom. The combination of (3.56), (3.46) and (3.52) yields an equation for the pressure gradient along x

$$\Theta_{Px} \frac{1}{\rho_0} \left[\frac{\partial p}{\partial x} \right]_i^{L+1} = \frac{1}{\sum_{k=1}^{kl-1} W_k \lambda_{k,i}^B} [\sum_{k=1}^{kl-1} W_k u_{k,i}^{*\,L+1}$$

$$+ \Theta_x f \Theta_{Py} \frac{1}{\rho_0} \left[\frac{\partial P}{\partial y} \right]_i^{L+1} \sum_{k=1}^{kl-1} W_k \lambda_{k,i}^A] \qquad (3.57)$$

d) Solution scheme

- Calculate the forcing terms $\vec{G}$, $\vec{F}$ and the matrix A of equations (3.48) and (3.49).

- Solve for $\vec{u}^*$ and $\vec{v}^*$ from equations (3.48) and (3.49).

- Solve for $\vec{\lambda}^A$ and $\vec{\lambda}^B$ from equations (3.54) and (3.55).

- Calculate the pressure gradient from equations (3.57).

- Calculate $\vec{u}'$ and $\vec{v}'$ from equations (3.52) and (3.53).

- Calculate the new velocities from equations (3.46) and (3.47).

- Finally, the vertical velocity is obtained by integrating the continuity equation.

3.2.6 Ekman's solution

For the discussion of the following simulations, the Ekman solution (1905) corresponding to a simplified version of the model equations is introduced.

We can simplify the general equations to obtain an analytical solution for u and v. Dropping the horizontal diffusion and advection terms, the momentum equations become for a stationary state (Ekman, 1905) :

$$fv = A_v \frac{\partial^2 u}{\partial z^2} - \frac{1}{\rho_0} \frac{\partial p}{\partial x} \qquad (3.58)$$

$$-fu = A_v \frac{\partial^2 v}{\partial z^2} - \frac{1}{\rho_0} \frac{\partial p}{\partial y} \qquad (3.59)$$

with the boundary conditions :

1. at the top, the tangential force exerted by the wind on the water is specified by the equations (3.10) and (3.11),

2. at the bottom, the no-slip condition (3.9) is used,

3. we need two more conditions to calculate $\partial p/\partial x$ and $\partial p/\partial y$. For the pressure gradient along x, we impose

$$\overline{u} = \int_0^h u \, dz = 0 \qquad (3.60)$$

where h is the height of water column. The pressure gradient along y is assumed to be zero.

Introducing a complex velocity and a complex wind stress

$$U = u + iv \qquad (3.61)$$

$$\tau = \tau_x + i\tau_y \qquad (3.62)$$

where $i^2 = -1$ and combining equations (3.58) and (3.59), we obtain

$$\frac{\partial^2 U}{\partial z^2} - \alpha^2 U = \frac{1}{A_v \rho_0} \frac{\partial p}{\partial x} \qquad (3.63)$$

where

$$\alpha = \sqrt{\frac{if}{A_v}} \qquad (3.64)$$

with the boundary conditions :

1. at the top :

$$-A_v \frac{\partial U}{\partial z} = \frac{\tau}{\rho_0} \qquad (3.65)$$

2. at the bottom :

$$U = 0 \qquad (3.66)$$

The solution of the problem is then readily calculated :

$$U = \frac{\tau}{\rho_0 A_v \alpha} \left[\frac{sh\ \alpha(h-z)}{ch\ \alpha h} \right] - \frac{i}{f\rho_0} \frac{\partial p}{\partial x} \left[1 - \frac{ch\ \alpha z}{ch\ \alpha h} \right] \tag{3.67}$$

3.2.7 Simulation of the currents driven by katabatic winds

The purpose of this partial study is to compare the numerical solutions of two 2.5D models, the MUMM and the KUL models, on a specific problem of the oceanic circulation in the Southern Ocean. Some differences exist between the two models. The ways to discretize equations are different. Essentially, the KUL model is basically explicit and has a fixed grid size in the vertical plane, whereas the MUMM model is semi-implicit using σ coordinates for the vertical discretization but both models use staggered B-grid. A complete description of the KUL model has been made in Fettweis *et al.* (1991). The Table III summarizes the main characteristics of the two models.

	KUL	MUMM
Grid	B-grid	B-grid
Vertical coordinate	fixed	σ
Horizontal advection	explicit, first order upwind	explicit, second order central
Horizontal diffusion	explicit, second order central	explicit, second order central
Vertical advection	explicit, first order upwind	semi-implicit, second order central
Vertical diffusion	explicit, second order central but first order at the top and the bottom	semi-implicit, second order central

Table III: Comparison of the two numerical approaches.

The area of Adélie coast has been chosen as example for the comparison study. The vertical plane is 500 km long. The horizontal eddy viscosity coefficient A_h is 200 m^2 s^{-1}; the vertical one A_v is 0.01 m^2 s^{-1}; g is 9.81 m s^{-2}. The Coriolis parameter f has been taken at 67.5 degrees South and the horizontal grid size is 4 km. A katabatic wind computed by the UCL model (Gallée *et al.*, 1989) is blowing over the water surface. It is decreasing to zero at 200

km from the coast and is then blowing in the opposite direction, i.e, eastward. The wind stress deduced from these data is shown in the Figure 10. The sea is initially at rest.
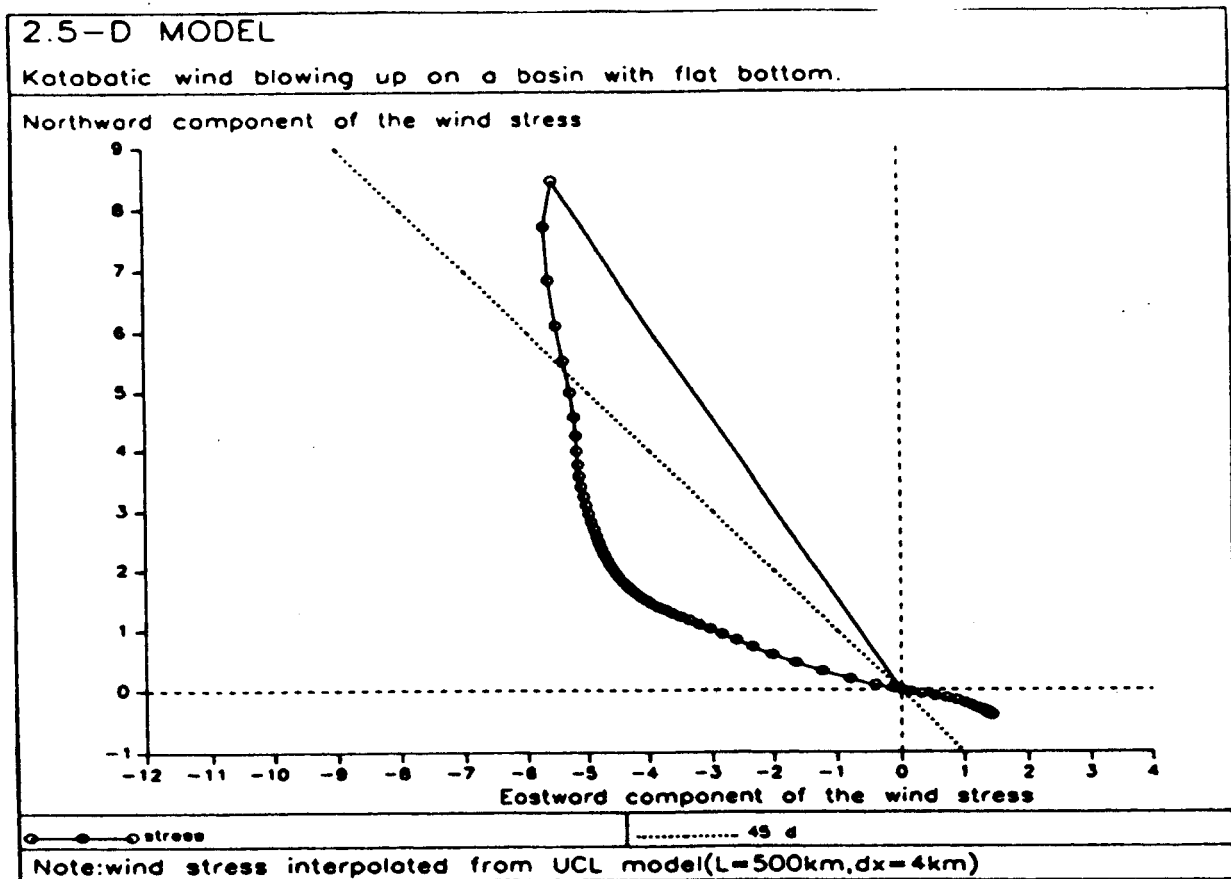

Figure 10: Wind stress (Nm^{-2}) deduced from the UCL data.

Different bathymetries have been used to compare the two models :

1. a constant depth of 400 m;

2. a bottom composed of two parts at a constant depth of 400 m and 4000 m, separated by a linear shelf break with a 5 percent slope placed in three different positions.

The most interesting results have been obtained with the flat bottom, this is the reason why we just present here this case. The other simulations have been described completely in Fettweis *et al.* (1991).

For a flat bottom, both models have the same vertical discretization : the vertical grid size is constant and equal to 10 m. The results reach nearly the steady state after 50 days of simulation.

The main advantage of this simple topography is that we can compare the results of the two models with the analytical solution of Ekman presented above.

The Figure 11 shows the flow pattern consisting of two cells. In the first 200 km, the flow is directed onshore in the top layer, except close to the continent, with downwelling at

the continental margin, offshore flow at the bottom and upwelling around 200 km. At about 50 m depth and close to the continent a vertical eddy exists. For the second cell (from 200 to 500 km), the flow is in opposite direction, offshore at the top and onshore at the bottom. The behaviour of the seaward flow in the first 10 km may look surprising but it is in agreement with the Ekman's theory. It would be interesting to check in a further study if this result is related to the formation of coastal polynyas. This would need a system of fully coupled models (atmospheric, sea-ice, ocean circulation).

Differences between the two solutions can be observed at the continental boundary. The horizontal extension of the offshore directed flow in the surface layer close to the continent is shorter for the KUL than for the MUMM model. The layer at the continental margin where downwellings occurs is thinner for the KUL model, this results also in a different shape and placement of the vertical eddy between the two models.
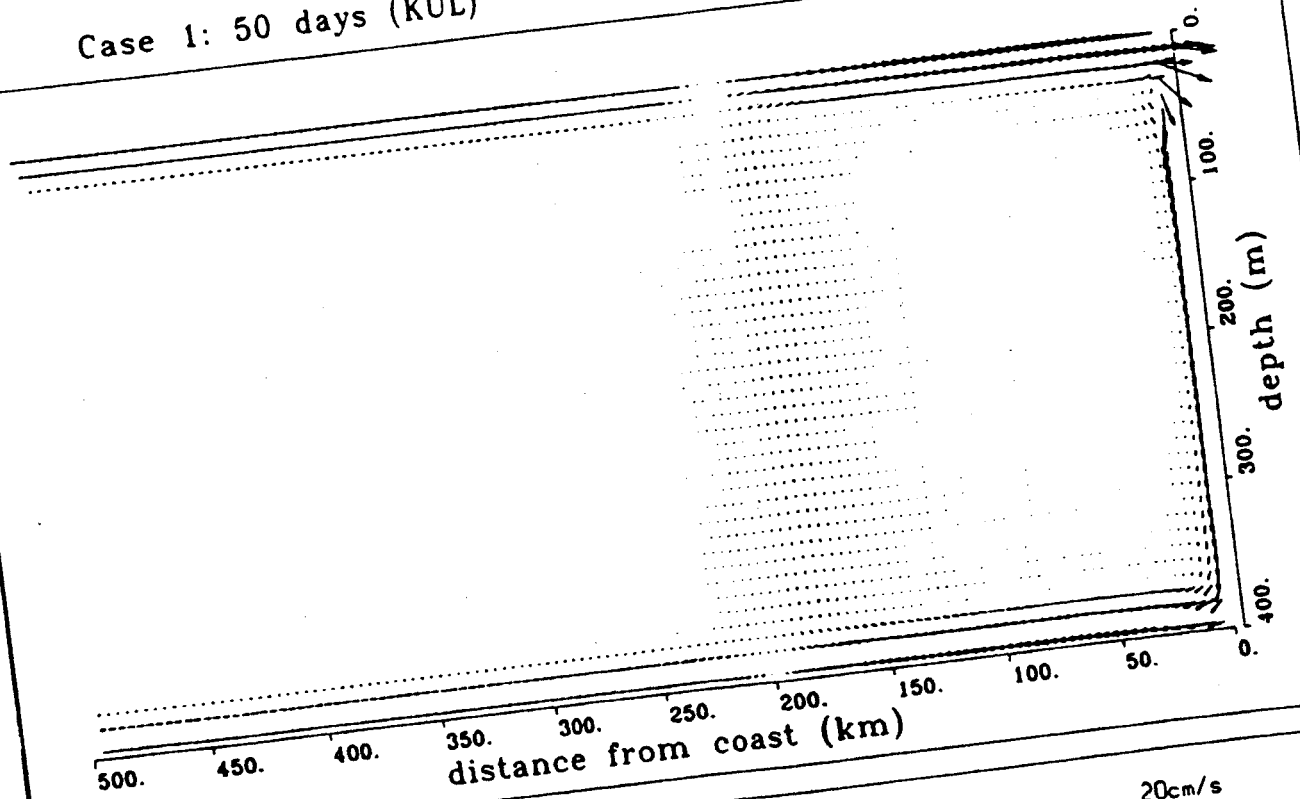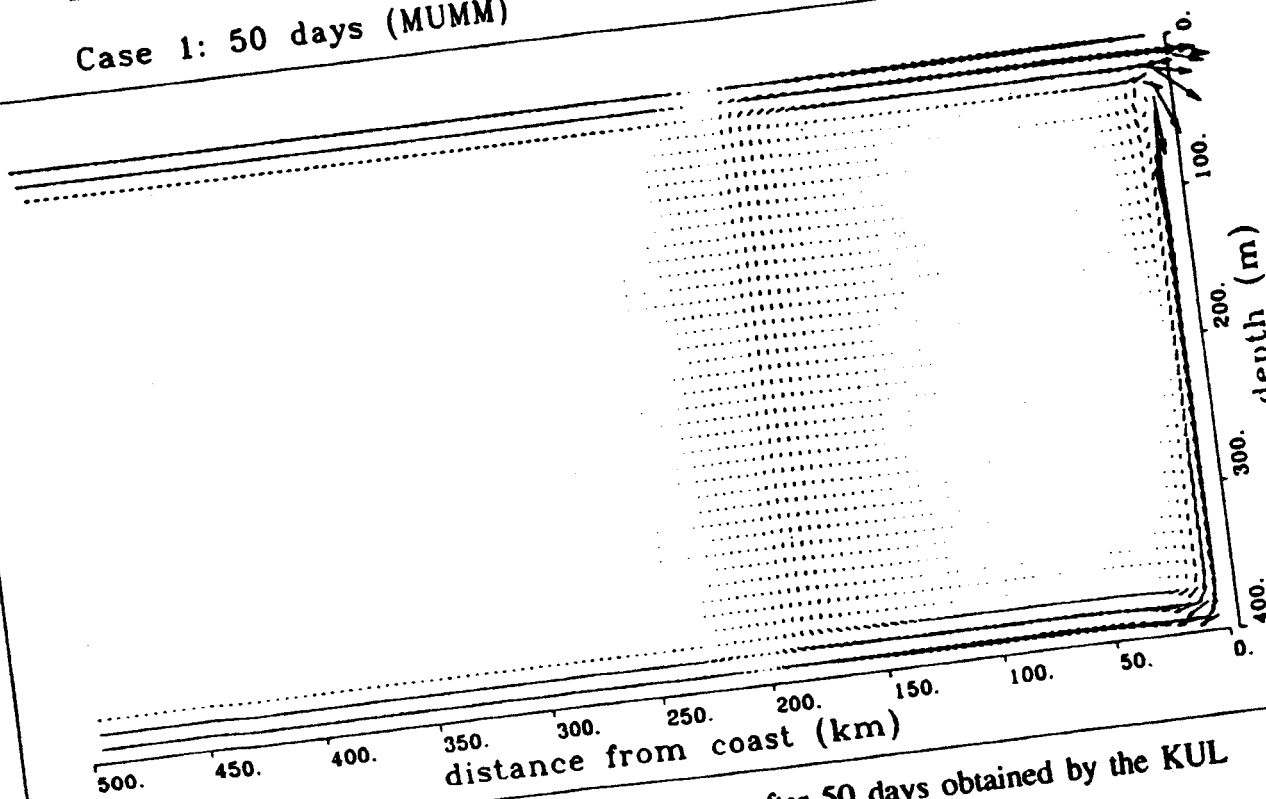
Figure 11: Flow field in the vertical plane after 50 days obtained by the KUL model (top) and the MUMM model (bottom) with a vertical grid size of 10 m.

The northward velocity component profiles are presented in Figure 12. The results of the two models are nearly identical except at the surface and at the bottom where the MUMM results are closer to the Ekman solution.
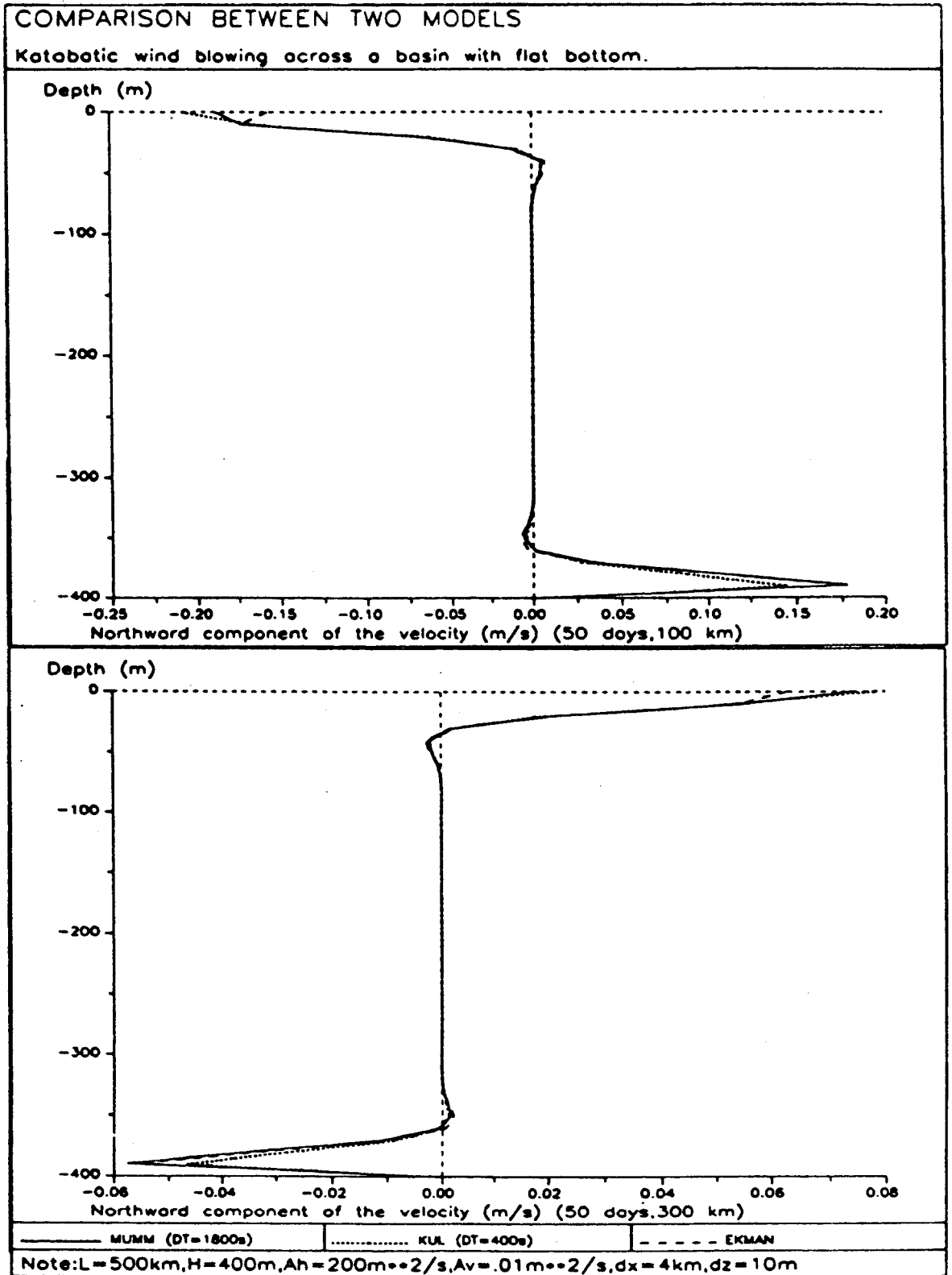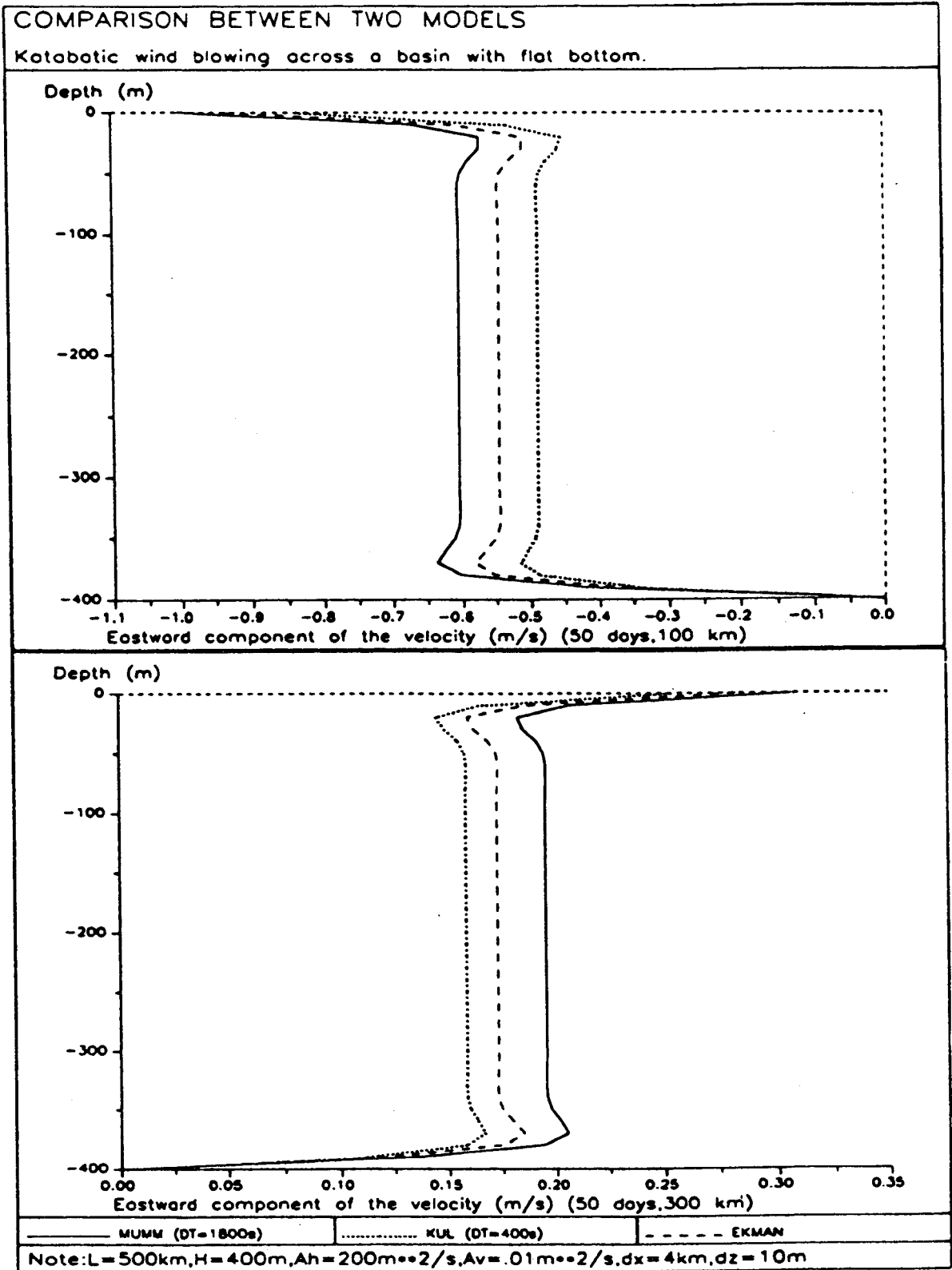

Figure 12: Northward velocity profiles (ms⁻¹) after 50 days at 100 km (top) and 300 km (bottom) from the coast with a vertical grid size of 10 m.

The eastward velocity component profiles are presented in Figure 13. The two results enclose the Ekman solution but the accuracy is not good.

Figure 13: Eastward velocity profiles (ms^{-1}) after 50 days at 100 km (top) and 300 km (bottom) from the coast with a vertical grid size of 10 m.

The pressure gradient evolution with the distance from the coast is shown in Figure 14. The value of the pressure gradient for the three proposed solutions is different. Its absolute value is on the whole lower for the KUL model than for the MUMM model. The Ekman solution is, except in the region around 200 km and near the closed boundary where the horizontal diffusion plays a significant role, between the solutions of the KUL and the MUMM model.
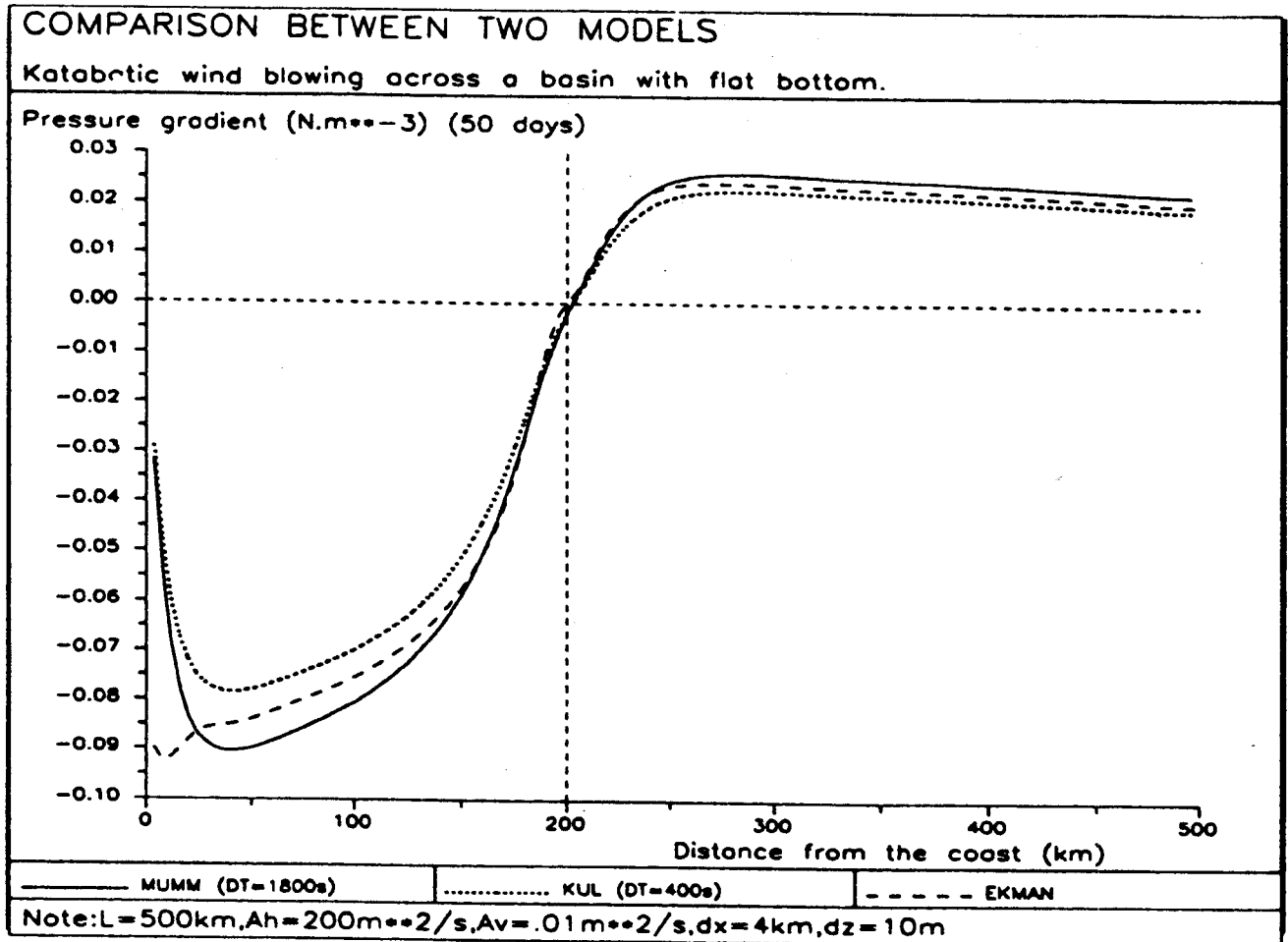
Figure 14: Northward component of the pressure gradient (Nm^{-3}) depending on the distance from the coast after 50 days with a vertical grid size of 10 m.

The different numerical approaches are responsible for the discrepancies between the results of the two models. Consequently, the KUL has used a second order vertical advection scheme without obtaining significant improvements. To change the first order vertical scheme to a second one at the surface has just an influence on the northward component of the velocity : the KUL solution approaches the MUMM solution.

In order to test the influence of the vertical discretization, the vertical grid size has been decreased from 10 to 5 m. The figures 15, 16 and 17 underline the better agreement between the model results and the Ekman solution. This improvement should be expected. Indeed, the
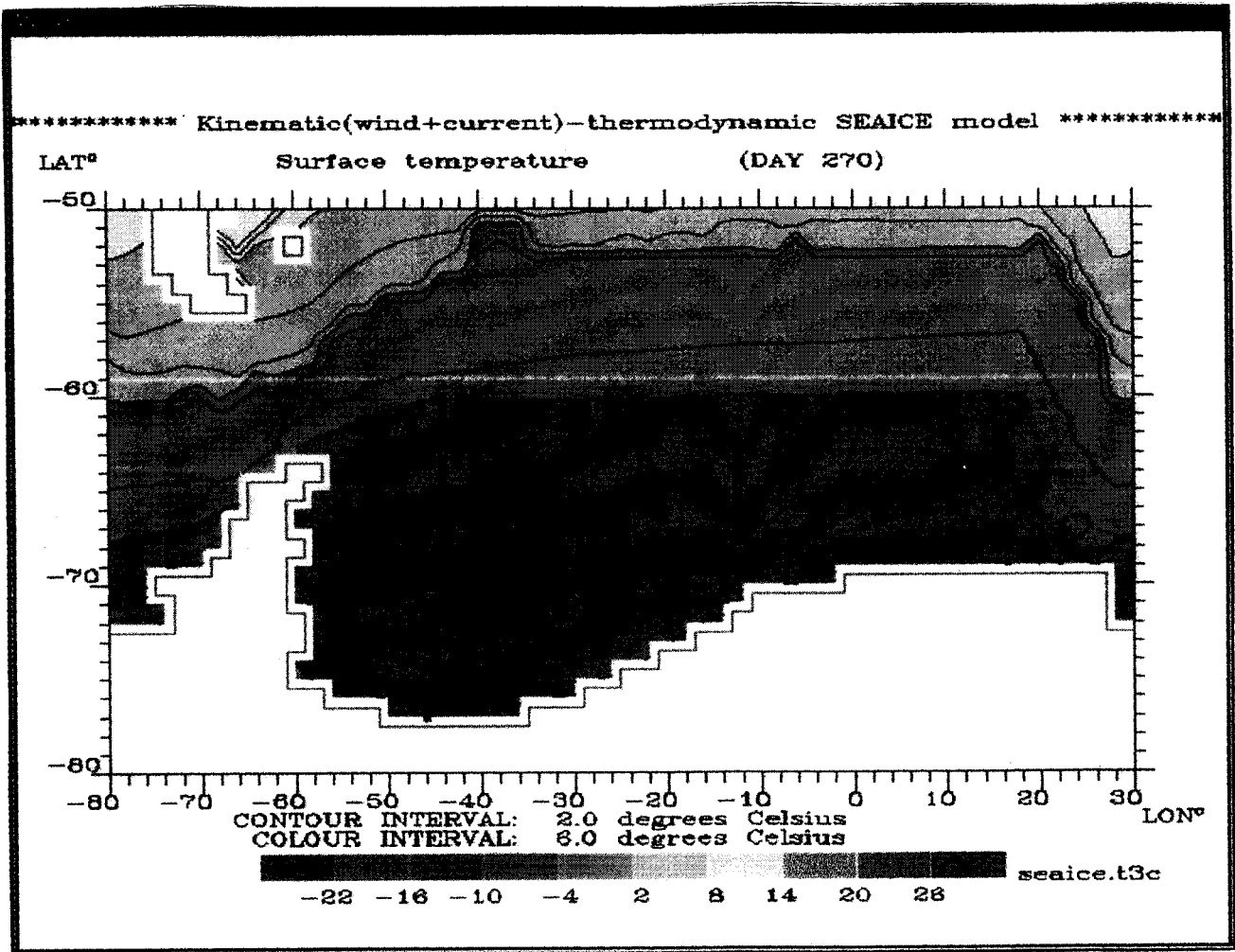
Figure 5: Surface temperature (°C) on Julian day 270 (27 September) of the fifth year of simulation. The southern part of this picture presents the ice surface temperature and the rest, the sea surface temperature. This figure can be compared with the position of the ice cover on Figure 6.
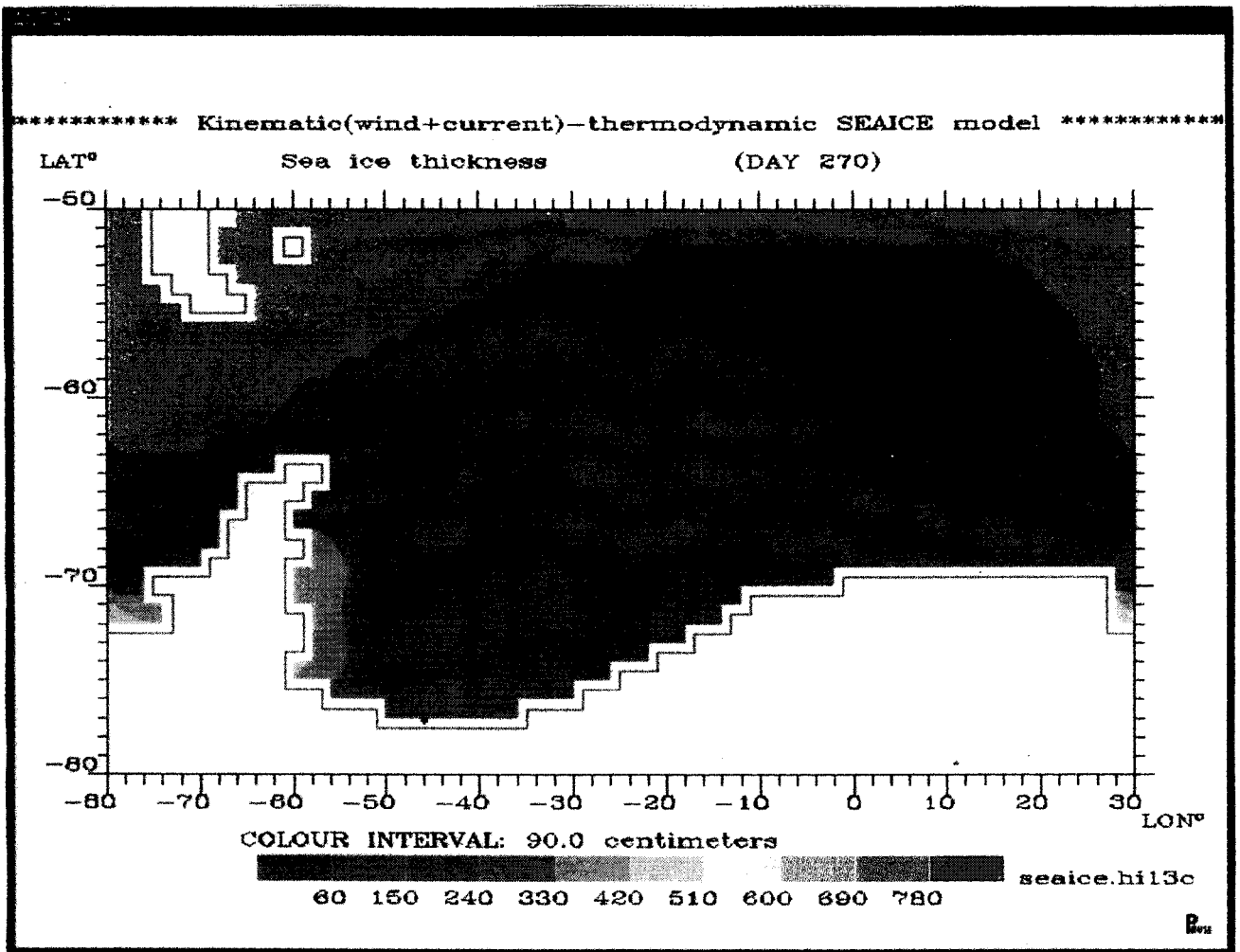
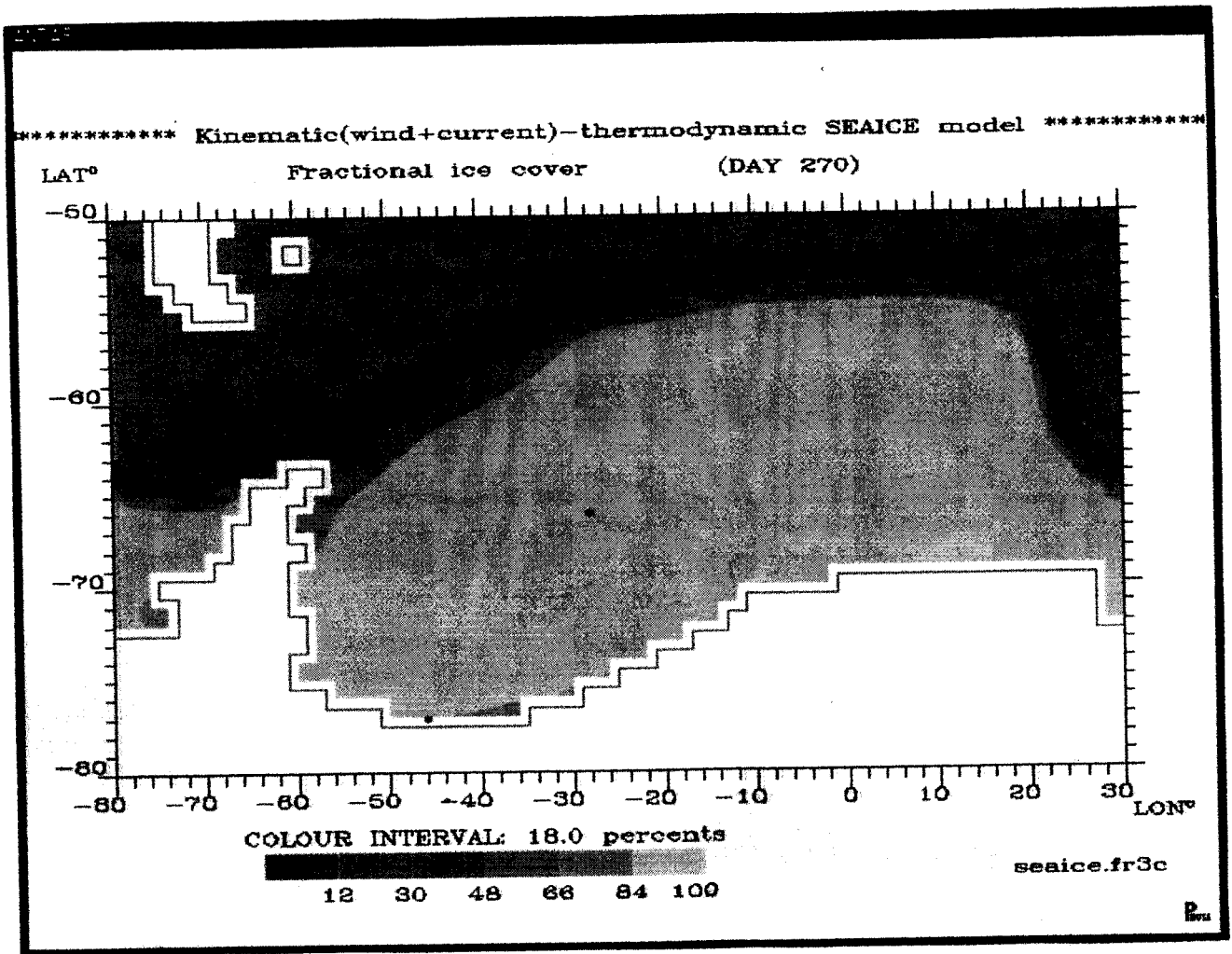Figure 6: Ice thickness (cm) on Julian day 270 (27 September) of the fifth year of simulation.

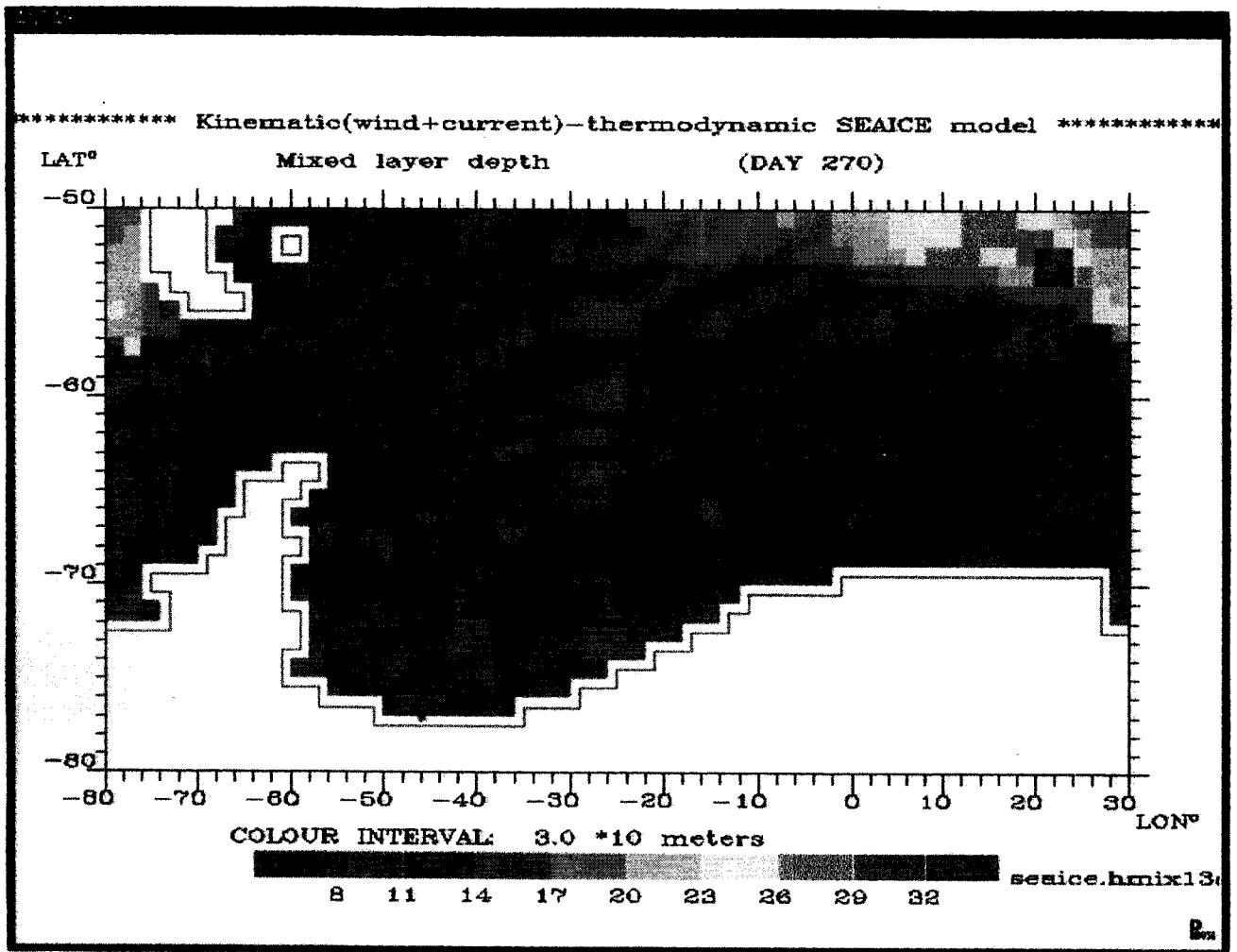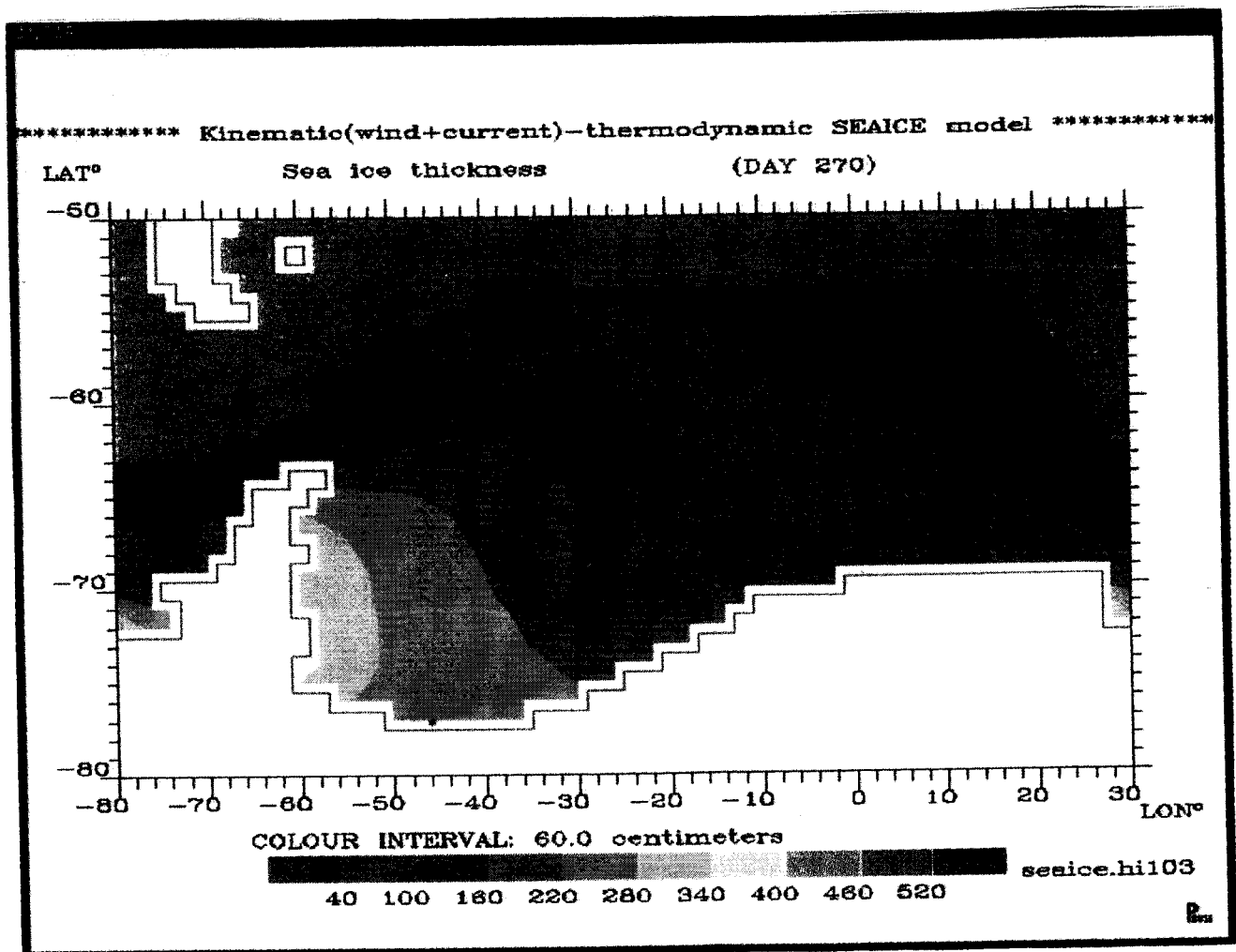Figure 7: Fractional ice cover (%) on Julian day 270 (27 September) of the fifth year of simulation.

Figure 8: Mixed layer depth (m) on Julian day 270 (27 September) of the fifth year of simulation.

We can compare these two last figures with this one obtained in the same conditions, but with the UCL currents (figure 6). On average, the MUMM currents diminish the ice extent and yield smaller ice thicknesses. Moreover, the ice thickness distribution is smoother and the transition between the area nearly fully covered by ice (until 98 %) and the area free of ice is more continuous.

Figure 22: Ice thickness (cm) on Julian day 270 (27 September) of the fifth year of simulation with wind corrections along the Peninsula.
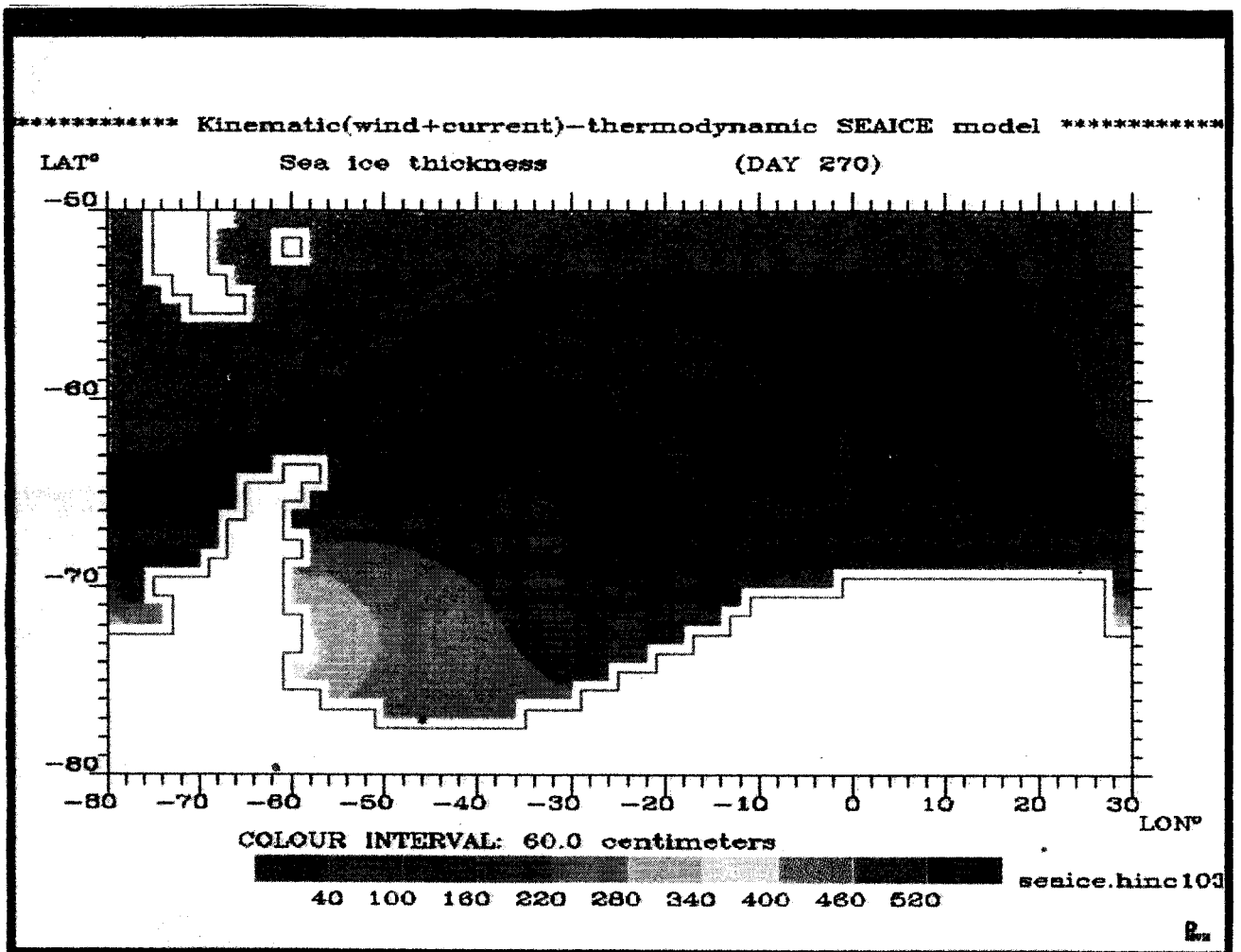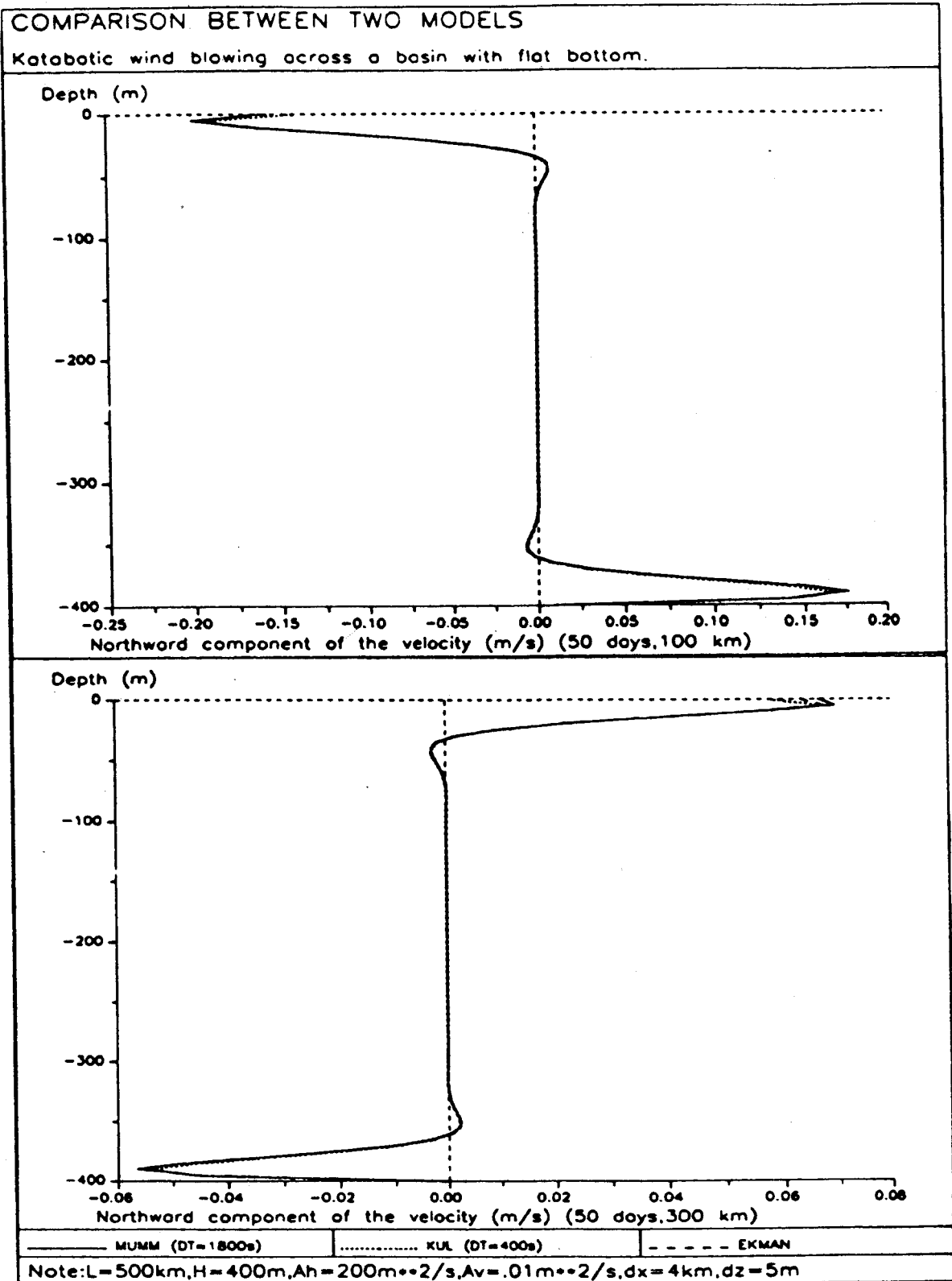
Figure 23: Ice thickness (cm) on Julian day 270 (27 September) of the fifth year of simulation without wind corrections along the Peninsula.

thickness of the Ekman surface layer is relatively small (20 m) and a high resolution is required to resolve this layer.

Figure 15: Northward velocity profiles (ms^{-1}) after 50 days at 100 km (top) and 300 km (bottom) from the coast with a vertical grid size of 5 m.
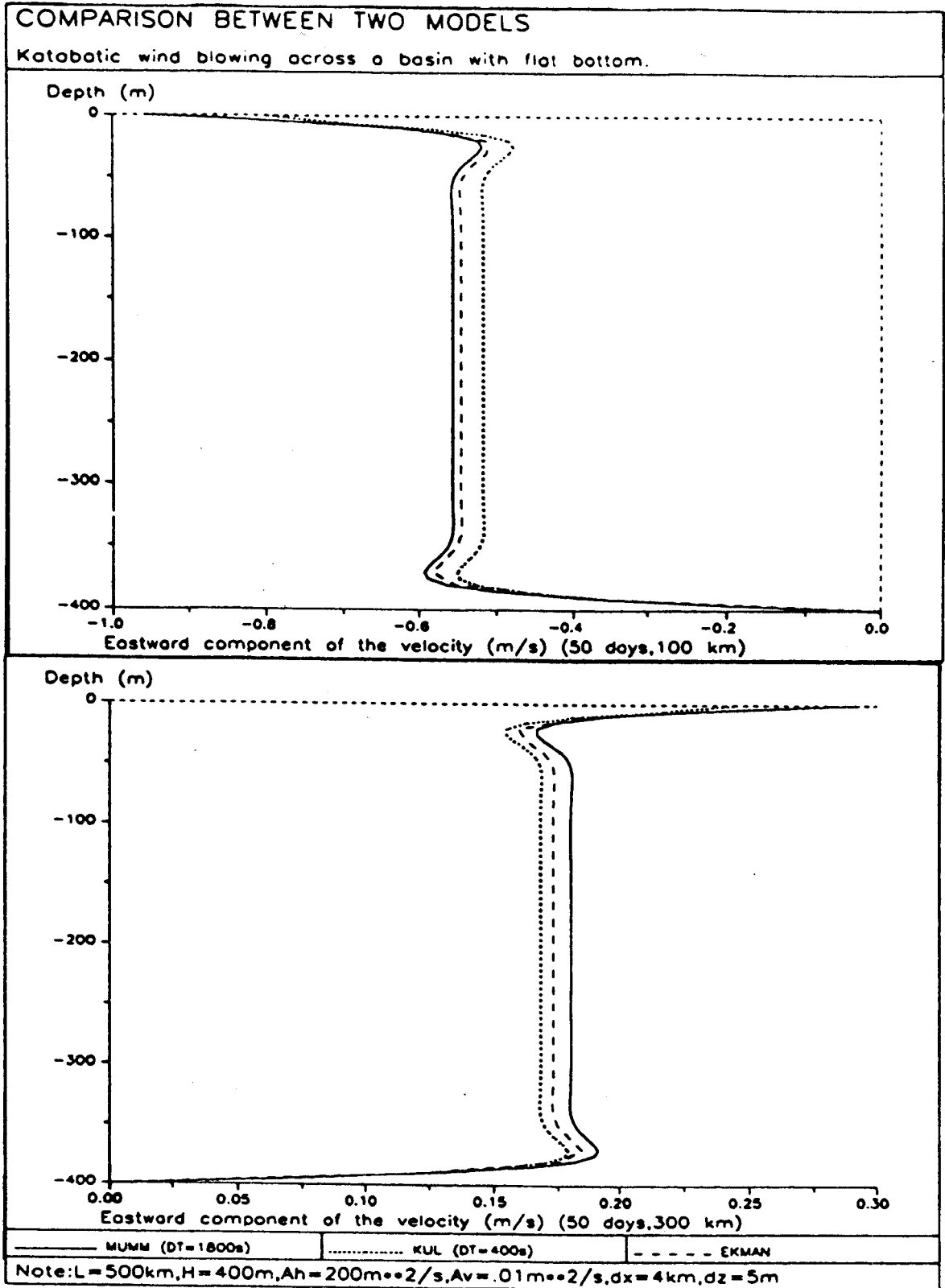
COMPARISON BETWEEN TWO MODELS
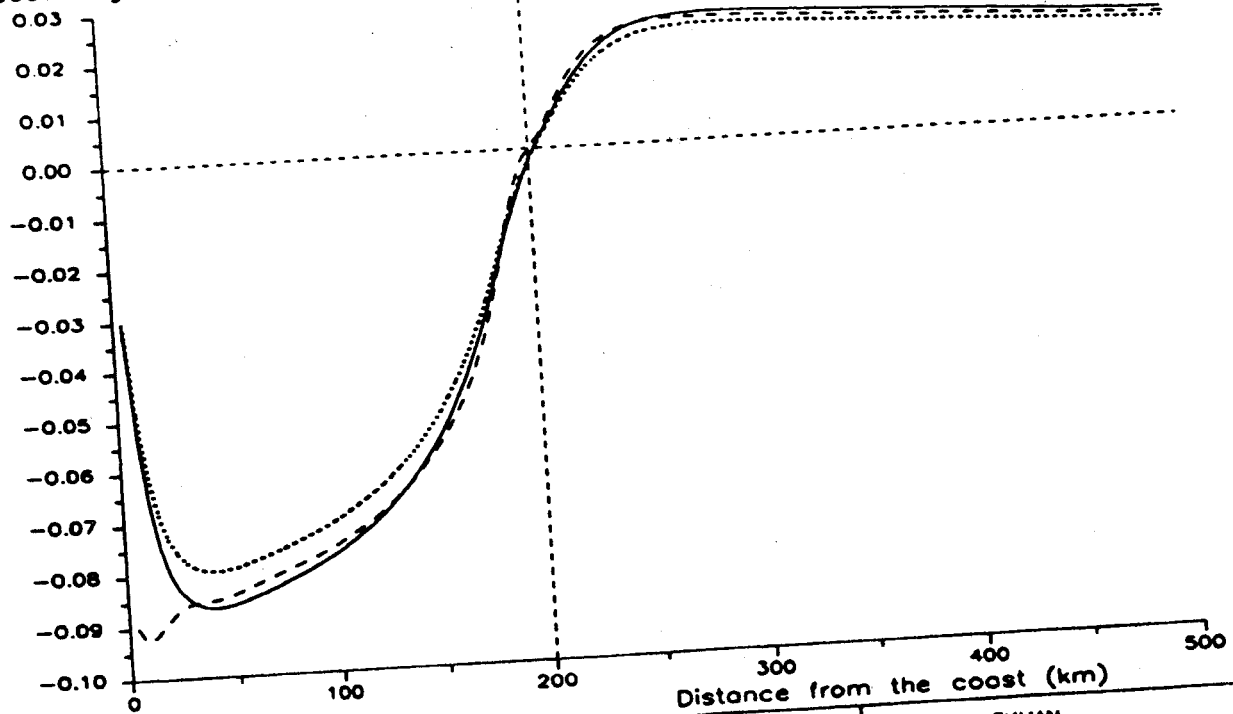
Katabatic wind blowing across a basin with flat bottom.

Figure 16: Eastward velocity profiles (ms^{-1}) after 50 days at 100 km (top) and 300 km (bottom) from the coast with a vertical grid size of 5 m.

Figure 17: Northward component of the pressure gradient (Nm^{-3}) depending on the distance from the coast after 50 days with a vertical grid size of 5 m.

3.3 3D model

3.3.1 Introduction

The development of a three dimensional oceanic model has been made up step by step from the 2.5D plane model previously explained. This progressive evolution is quite easy to understand. The 3D model is an extension of the 2.5D one in a third direction : it is thus obvious that the 3D model presents, at least, the same difficulties as the 2.5D one. The most of numerical problems have been studied with the 2.5D model because it provides two-dimensional matrices of results easier to interpret and to plot. So, each improvement was applied immediately to the 3D model. Finally, this parallel evolution of the two models has allowed us to perform preliminary applications of the three-dimensional model to our area of interest, the Weddell Sea.

3.3.2 Governing equations

Of course, the 3D model uses the complete hydrodynamic equations : all the variables can evolve in the three directions of space. In a simple way, the governing equations become :

$$\frac{\partial u}{\partial t} + \frac{\partial uu}{\partial x} + \frac{\partial vu}{\partial y} + \frac{\partial wu}{\partial z} + \frac{1}{\rho_0}\frac{\partial p}{\partial x} + fv$$
$$= \frac{\partial}{\partial x}\left(A_h\frac{\partial u}{\partial x}\right) + \frac{\partial}{\partial y}\left(A_h\frac{\partial u}{\partial y}\right) + \frac{\partial}{\partial z}\left(A_v\frac{\partial u}{\partial z}\right) \tag{3.68}$$

$$\frac{\partial v}{\partial t} + \frac{\partial uv}{\partial x} + \frac{\partial vv}{\partial y} + \frac{\partial wv}{\partial z} + \frac{1}{\rho_0}\frac{\partial p}{\partial y} - fu$$
$$= \frac{\partial}{\partial x}\left(A_h\frac{\partial v}{\partial x}\right) + \frac{\partial}{\partial y}\left(A_h\frac{\partial v}{\partial y}\right) + \frac{\partial}{\partial z}\left(A_v\frac{\partial v}{\partial z}\right) \tag{3.69}$$

$$\frac{1}{\rho}\frac{\partial p}{\partial z} = g \tag{3.70}$$

$$\frac{\partial u}{\partial x} + \frac{\partial v}{\partial y} + \frac{\partial w}{\partial z} = 0 \tag{3.71}$$

For the sake of clarity, we keep the same formalism as for the 2.5D equations. To point out the differences between the two models, the additional terms are underlined.

3.3.3 Numerical procedure

The procedure used in the 3D model is similar to that of the 2.5D model, so that the discussion (see 3.2) can be viewed as general description of both models. We must just keep in mind that most of the variables are now function of x. y, z and t. The terms depending on y are treated following the same method as the corresponding terms depending on x : we just need to replace the variables by analogy. The generalization may seem easy but, in fact, it is a little bit more complex.

The big difference compared with the 2.5D model is that the pressure gradient in the y-direction does not depend on an external condition : the pressure, function of x and y, is completely defined by the equations of the motion. The horizontal discretization of the two

pressure gradient terms allows to compute the pressure by a two-dimensional elliptic equation of the Poisson type.

More explicitly, the integration of the continuity makes appear the pressure gradients at the four corners of the horizontal cell by taking account of the decomposition of the horizontal velocity into a known part independent on the pressure but with a non zero divergence and an unknown part dependent on the pressure (equations (3.46) and (3.47)). The discretization of these gradients on each cell of the domain generates a linear algebraic system which is time dependent in case of free surface.

The solution of this algebraic equation is provided by the Successive Over-Relaxation (SOR) algorithm. This method is analog to the Newton-Raphson one, except that it uses an extra parameter ω weighting the correction term. The method converges if the over-relaxation parameter ω is chosen between 1 and 2. For a complex problem, the optimum value of ω can be determined empirically on the basis of the number of iterations necessary to reduce the initial error to a certain tolerance. The convergence of the SOR method is responsible for an important increase of the calculation time. The solution of the pressure equation in case of the rigid lid requires the pressure to be fixed at one sea point in the domain.

Once the pressure determined, the barotropic part of the velocity is known and the sum of the two velocities defines the new velocity. Then, the continuity equation is used to determine the vertical velocity.

3.3.4 Wind driven circulation in the Weddell Sea

a) Set-up

The 3D model will be used to simulate the wind driven circulation in the Weddell Sea sector, the same sector considered in the applications of the SEAICE model. This geographical area, extending from latitude 50°S to 80°S and from longitude 80°W to 30°E, includes the Southern tip of South America, the Drake Passage, the Weddell Sea and the Falkland Islands.

The model domain is horizontally gridded, in spherical coordinate system, by elements of 2 degrees in longitude and 1 degree in latitude (56 grid points in longitude and 31 in latitude). The choice of this grid results from the work performed by Gordon and Baker (1982) to provide a better data set to study the Southern Ocean. This allows to use the temperature and the salinity data without interpolation and, in a first approach, to define the depth at each horizontal grid

point at the level where the last temperature and salinity values are known. The maximum depth is 4960 meters in the retained sector.

For the sake of the modelling, the northern open sea boundary at 50°S is considered closed so that along the continental and insular boundaries which are schematized by stepwise boundaries. The cyclic continuity is established between western (80°W) and eastern (30°E) open sea boundaries : what flows out of the domain through one side flows back into the domain through the other side. Following van Ypersele (1986), this condition requires, to ensure a smooth connection, a linear interpolation of the meteorological and oceanological data over the five grid points close to the eastern boundary. This restricts the interpretation of the results to the sector located between the longitudes 80°W and 20°E.

The geostrophic wind, $\underline{v_a}$, extracted by van Ypersele (1986) from the climatological data compiled by Taljaard *et al.* (1969), exerts on the ocean a tangential stress, $\underline{\tau}$, calculated using the drag law as follows :

$$\underline{\tau} = C_d \rho_a \|\underline{v_a}\| \underline{v_a} \tag{3.72}$$

where C_d (nondimensional) is the drag coefficient appropriate for the type of surface at each point, and, ρ_a, the air density. C_d is set equal to 0.8×10^{-3} over water.

b) Simulation

The 3D model is applied to simulate the wind driven hydrodynamic circulation in the Weddell Sea sector horizontally described, in a first approach, by a uniform Cartesian grid with a bathymetry deduced from the level where the last temperature and salinity are known. However, as this bottom has sharp slopes, the depths $h_{i,j}$ at each sea point (x_i, y_j) will be filtered by an explicit spatial filter (Raymond and Garder, 1988) given by

$$16 \, \overline{h_{i,j}} = \Lambda_i^0 \Lambda_j^0 h_{i,j} \tag{3.73}$$

where $\overline{h_{i,j}}$ is the smoothed field and the operators Λ_i^0 and Λ_j^0 such that

$$\Lambda_i^0 h_{i,j} = h_{i-1,j} + 4h_{i,j} + h_{i+1,j} \tag{3.74}$$

$$\Lambda_j^0 h_{i,j} = h_{i,j-1} + 4h_{i,j} + h_{i,j+1} \tag{3.75}$$

The bathymetry used in the simulations is presented in Figure 18 where the filter applied and the cyclic continuity is imposed laterally. Most of the parameters of the model used in the calculations are chosen to stay coherent with van Ypersele (1986) :

1. horizontal eddy viscosity : $A_h = 5000$ m^{2}s^{-1},

2. vertical eddy viscosity : $A_v = 0.005$ m^{2}s^{-1}.

3. latitude for the Coriolis parameter : $\lambda = 65$ degrees South

4. horizontal grid size : $\Delta x = \Delta y = 100$ km,

5. levels along the water column : 180 in σ–coordinate.

   The number of meshes along the depth is chosen so that the Ekman layer is included, at least, in one mesh. With the used parameters, the Ekman layer depth is about 27 m. The maximum depth of the smoothed bathymetry is 4942 m. The rate of these values yields a number of meshes, about 180, that we use in the following simulations.
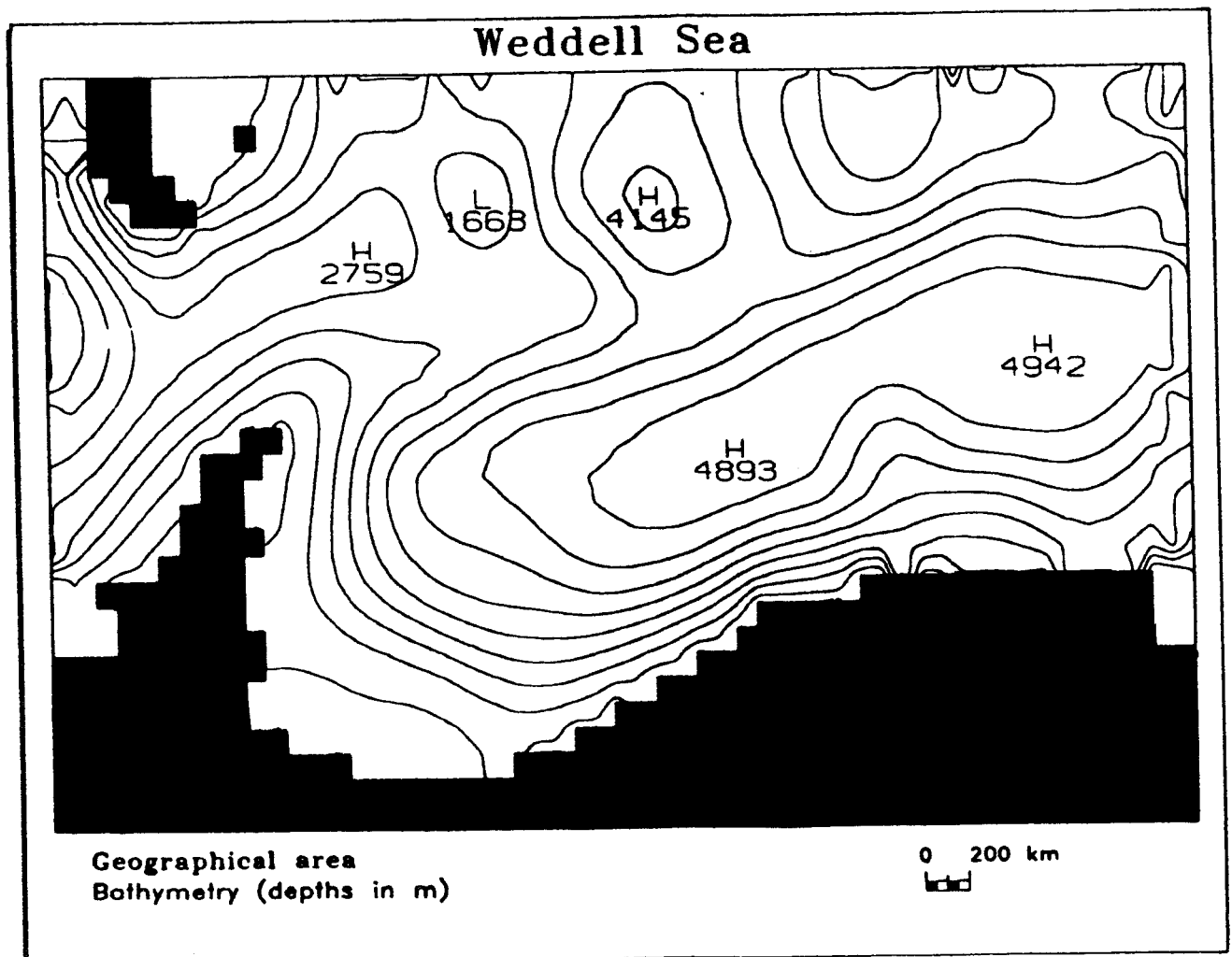
6. time step : $\Delta t = 1800$ s.

Figure 18: Smoothed bathymetry used for the simulation.

The figure 19 shows the typical atmospheric circulation in the Weddell Sea sector in September. The main features of the geostrophic wind circulation remain in the course of the year :

1. between latitude 50°S (north boundary of the model) and 60°S (in the middle of the Drake Passage), the wind blows eastwards with strong velocities (10 ms^{-1});

2. in the Weddell Sea, the wind blows in a clockwise circulation.
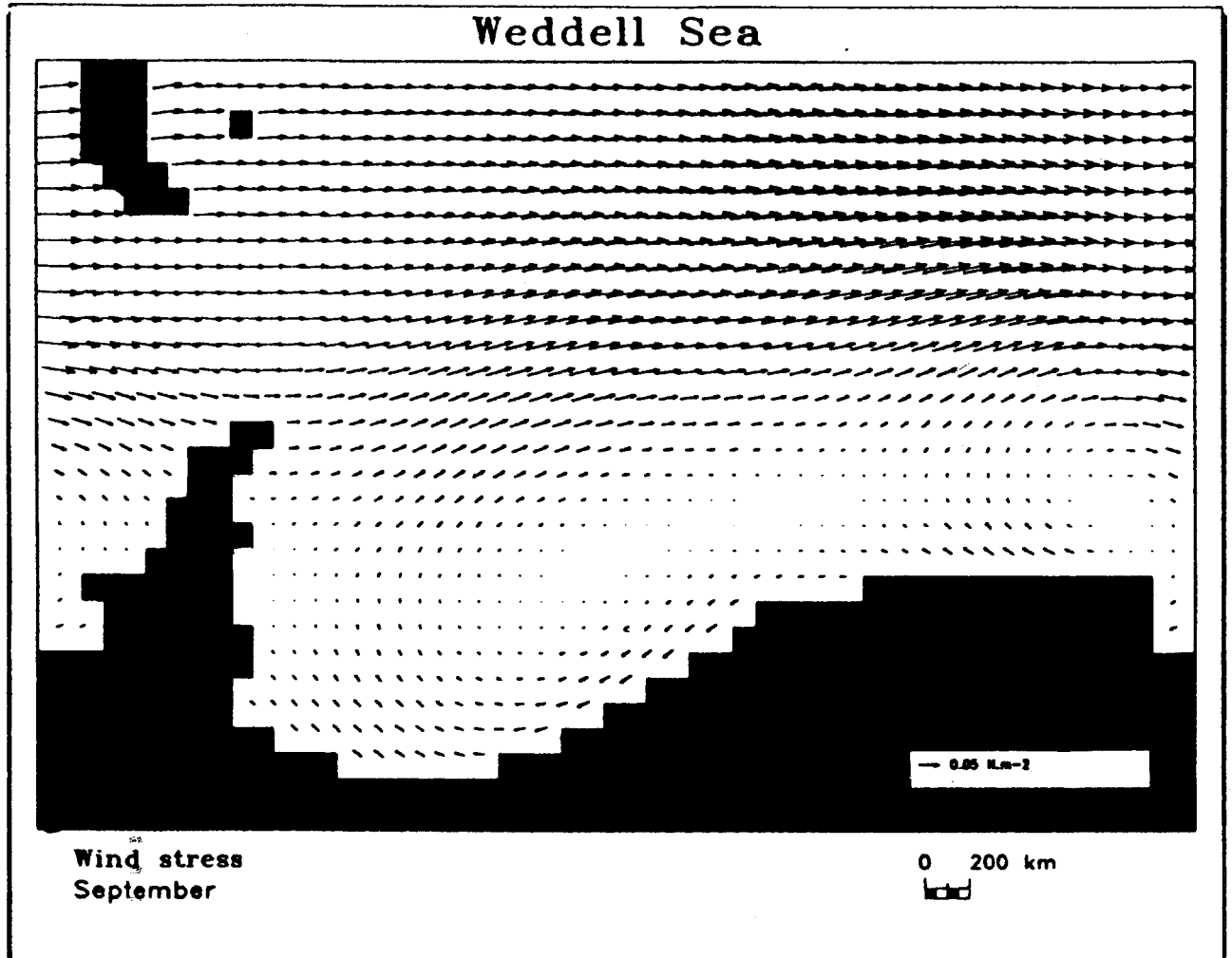

Weddell Sea

Wind stress
September

0   200 km

Figure 19: Wind stress field (Nm^{-2}) in September.

The wind forcing creates a circulation described by the 3D model. The figures 20 and 21 show the surface current in September (this month corresponds about to the maximum of sea ice extent). On the first one, the wind field is corrected along the Antarctic Peninsula with the purpose of taking into account the strong barrier winds due to the Peninsula's steep mountain range (van Ypersele (1986)) : the northward component is increased. On the second one, there is no wind correction. It results in weaker currents along the east coast of the Peninsula. As expected, the surface current tends to flow around the continent in a clockwise movement and

an intense flow exists along the latitude 50°S in a north-east direction, corresponding to the geostrophic balance (surface current directed at 45° on the left of the wind direction in southern hemisphere). The magnitude of the surface current at the center of the Weddell Sea is 0.01 ms^{-1} and 0.15 ms^{-1} along the northern boundary of the oceanic basin.
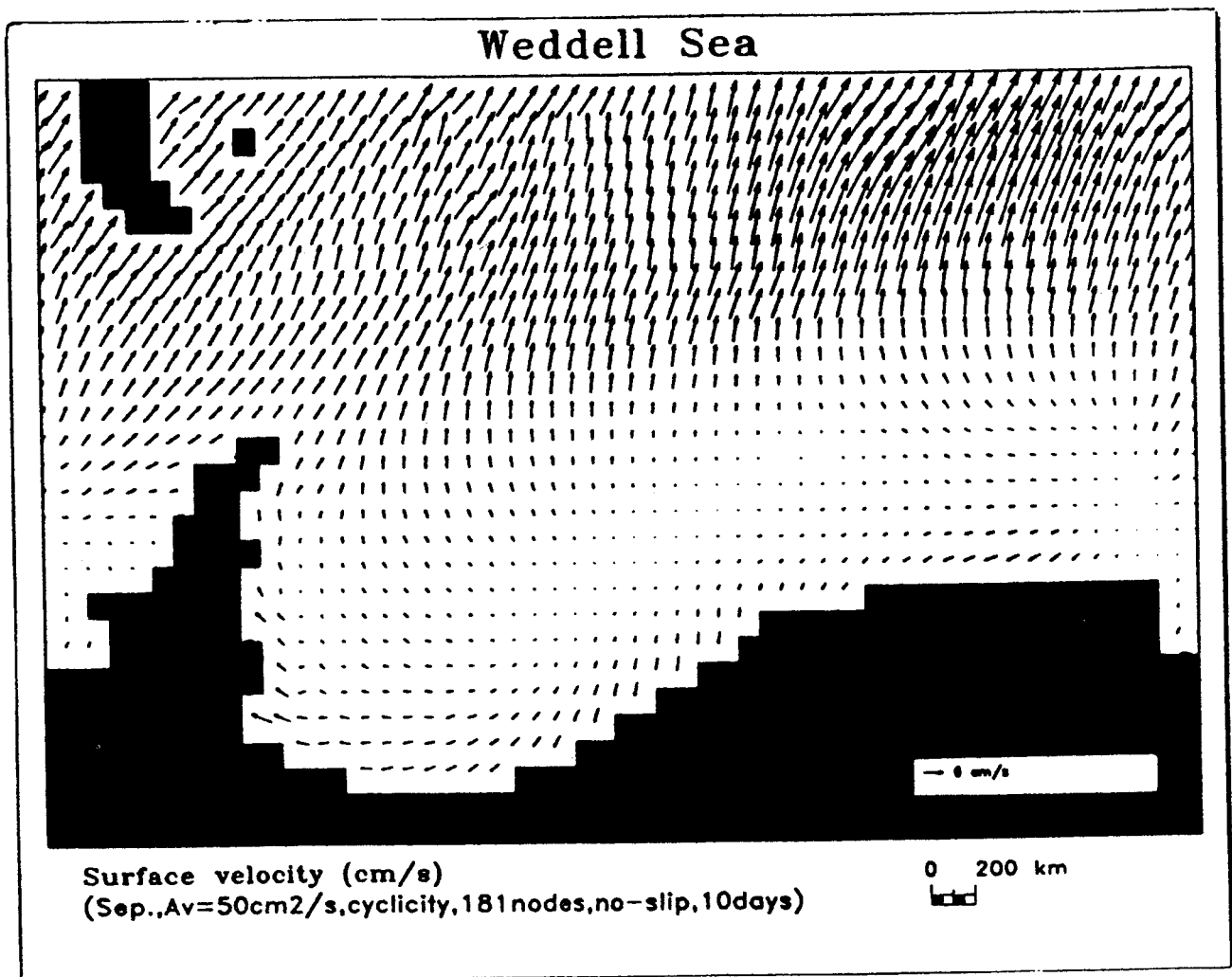

Figure 20: Surface velocity field (cm s^{-1}) in September obtained after a 10-day simulation with wind corrections along the Peninsula.
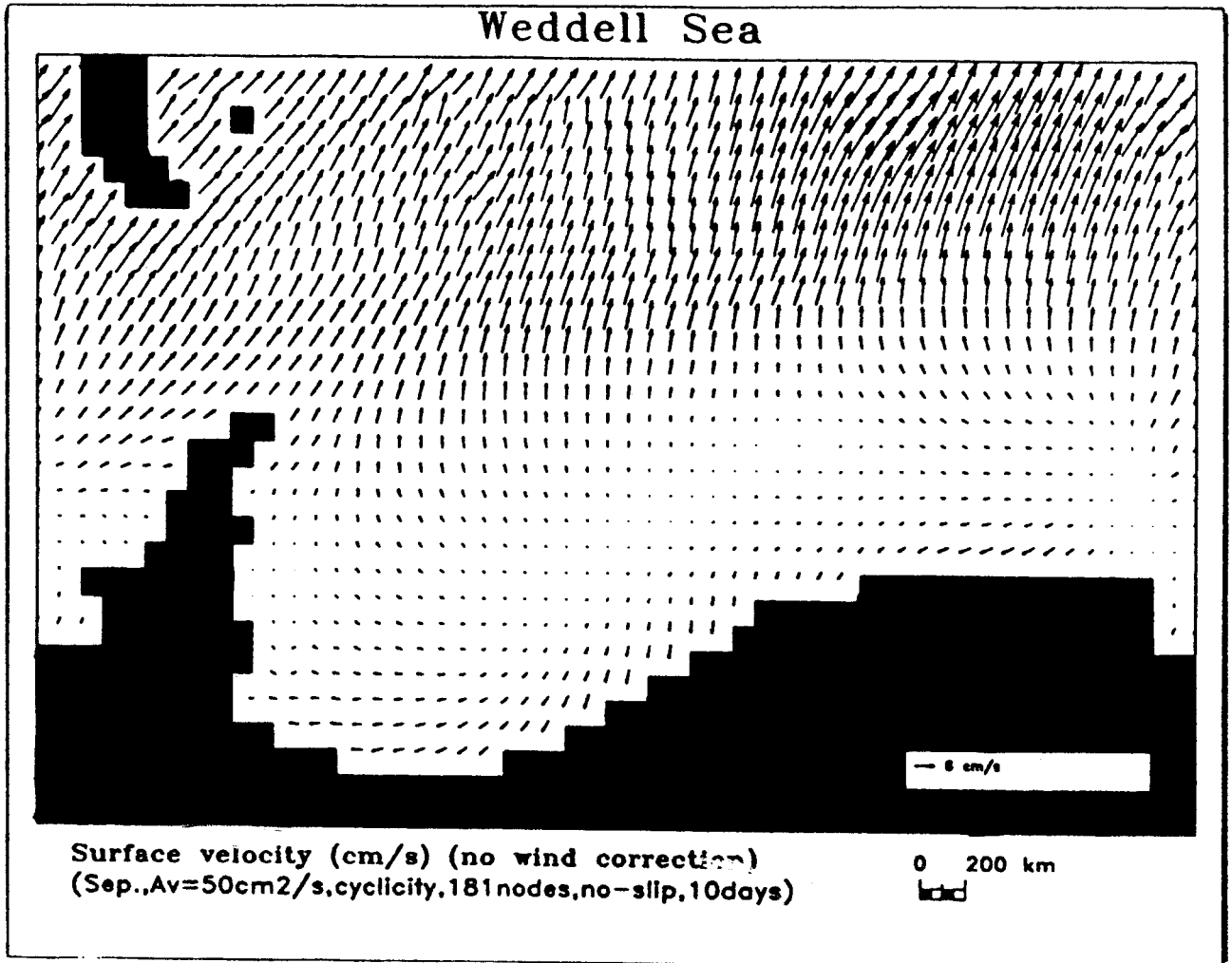
Figure 21: Surface velocity field (cm s^{-1}) in September obtained after a 10–day simulation without wind corrections along the Peninsula.

3.3.5 Application to the sea ice evolution

The surface currents obtained with the 3D model are then used to compute the ice dynamics in the SEAICE model. To allow comparison, the SEAICE model is used in the same configuration as in 2.2.3, more precisely, following the case that we call "thermodynamics and ice transport by wind and currents".

The figures 22 and 23 show the ice thicknesses on Julian day 270 (27 September) obtained with the corrected and the non corrected wind fields after a 5–year simulation. The ice extent is almost the same in the two cases but the position of the "iso-thickness" lines changes. In the first case, the acceleration of the winds and thus of the currents displaces the ice along the east coast of the Peninsula to the tip of this one where the ice is stopped due to the strong currents flowing in the Drake Passage. In the second case, the maximum of ice thickness remains concentrated along the south-east coast of the Peninsula.

4 Conclusions

The goal of this study was the development of a 3D model coupling a thermodynamic sea ice model with an hydrodynamic circulation model. In the first part, we have improved some features of the SEAICE model. The main modifications have been brought in the evolution of the mixed layer. Consequently, the oscillations in the time behaviour of the mixed layer have disappeared.

Different simulations have underlined the sensitivity of the results to the salinity. This is the reason why we have changed the expression of the salt exchanges between the ice and the mixed layer to better respect the conservation of total salt. With this reviewed model, we have made several simulations. The pictures present the time or space evolution of the more representative parametres and prove the good global behaviour of the SEAICE model. An hypothetical atmospheric warming causes the diminution of the ice area.

On the whole, we have thus resolved the problems explained in Demuth (1989) : the thermodynamic part of the SEAICE model is now reliable and ready to be coupled to a complete three-dimensional model.

With the purpose of improving the sea ice dynamics, we have developed two kinds of circulation models.

ANTAR
II/10

The 2.5D model is applied to antarctic conditions. The results are compared to a similar model developed by Fettweis (1990). The velocity profiles obtained when the katabatic wind is blowing are in good agreement with those given by the exact Ekman solution if we use a vertical discretization sufficiently accurate.

Then, we have extended the 2.5D model to a 3D one. The three-dimensional model is applied to simulate the wind driven circulation in the Weddell Sea sector. It reproduces the clockwise circulation of the Weddell Sea and the strong north-east currents in the northern part of the Drake Passage. The use of these currents in the SEAICE model yields satisfying ice thicknesses and ice extent.

Acknowledgments

References

Arakawa, A., 1972. Design of the UCLA general circulation model. Numerical Simulation of Weather and Climate. Dept of Meteorology, Univ. of California, Los Angeles, Tech. Rep. 7, 116 pp.

Demuth, C. and J.-P. van Ypersele, 1989. Simulations of the annual sea ice cover in the Weddell Sea. Belgian Scientific Research Programme on Antarctica. Scientific Results of Phase One (Oct.85–Jan.89). Volume III : glaciology and climatology. Services of the Prime Minister – Science Policy Office.

Demuth, C., 1990. Modélisation de la circulation océanique. Programme de recherches scientifiques sur l'Antarctique. Contrat ANTAR/II/10. Rapport particulier des résultats.

Ekman, V. W., 1905. On the influence of the Earth's rotation on ocean currents. Ark. Mat. Astron. Fys., 2 (11).

Fettweis, M., Yu, C. S., Petit, B., Ozer, J., Demuth, C. and H. Gallée, 1991. Comparison of two 2.5D ocean models forced by a katabatic wind. Report Antar 01, 02 and 03/II contracts, Belgian Scientific Research Programme on Antarctica, Services of the Prime Minister – Science Policy Office, 52 pp.

Fichefet, Th. and Ph. Gaspar, 1988. A model study of upper ocean-sea ice interactions. J. Phys. Oceanogr., 18, 181–195.

Gallée, H., Berger, A., Schayes, G., Fichefet, T., Marsiat, J., Tricot, C. and J.-P. van Ypersele. Numerical study of the air sea interactions in the Antarctic coastal zone and their implications on deep sea formation in the case of katabatic wind. Belgian Scientific Research Programme on Antarctica. Scientific Results of Phase One (Oct.85–Jan.89). Volume III : glaciology and climatology. Services of the Prime Minister – Science Policy Office.

Gaspar, Ph., 1981. Modelling the seasonal cycle of the upper ocean. J. Phys. Oceanogr., 18, 161–180.

Gordon, A. L. and Baker, T. N., 1982. Objective contouring and grid point data set. Southern Ocean Atlas, Columbia Univ. Press, New York, 11 pp., 233 plates.

Gordon, A. L., C. T. A. Chen and W. G. Metcalf, 1984. Winter mixed layer entrainment of Weddell Deep Water. J. Geophys. Res., 89, 637–640.

Jamart, B. M., R. Milliff, W. Lick and J. Paul, 1982. Numerical studies of the wind driven circulation in the Santa Barbara Channel. Final Report to Exxon Production Research Company, 126 pp.

ANTAR II/10

Kitada, T., 1987. Effect of non-zero divergence wind fields on atmospheric transport calculations. Atmospheric Environment, **21**, 4, pp. 785–788.

Paul, J. F. and W. J. Lick, 1981. A numerical model for three-dimensional variable density hydrodynamics flows. U.S. Environmental Protection Agency Report, 150 pp.

Raymond, W. H. and A. Garder, 1988. A spatial filter for use infinite area calculations. Mon. Wea. Rev., **116**, 209–222.

Semtner, A. J. Jr., 1976. A model for the thermodynamics growth of sea ice in numerical investigations of climate. J. Phys. Oceanog., **6**, 379–389.

Taljaard, J. J., van Loon, H., Crutcher, H. L. and R. L. Jenne, 1969. Climate of the Upper Air, I, Southern Hemisphere, Vol.1. Temperatures, Dew Points and Heights at Selected Pressure Levels. NAVAIR 50–1C-55, U.S. Naval Weather Service, Washington, D.C., 135 pp.

van Ypersele de Strihou, J.-P., 1986. A numerical study of the response of the Southern Ocean and its sea ice to a CO_2 – induced atmospheric warming. Cooperative Thesis NCAR CT99, Université Catholique de Louvain, Belgium, and National Center for Atmospheric Research, U.S.A., 135 pp.

Zwally, H. J., Comiso, J. C., Parkinson, C. L., Campbell, W. J., Carsey, F. D. and P. Gloersen, 1983. Antarctic Sea Ice 1973–76. National Aeronautics and Space Administration (NASA), Washington, D.C., 206 pp. (Supt. of Doc., USGPO, Washington).